Biodesign for conformational adaptability and guest recognition in crystalline frameworks

Universitat de València

Instituto de Ciencia Molecular (ICMOL)

****

Memoria presentada por José Navarro Sánchez para aspirar al Grado de Doctor en Nanociencia y Nanotecnología

****

Dirigida por:

Dr. Carlos Martí Gastaldo

Dra. Neyvis Almora Barrios

****

Septiembre 2021

"The only good is knowledge
and the only evil is ignorance."

Acknowledgements

En primer lugar, me gustaría nombrar en este apartado a Carlos Martí, por todo lo aprendido y haberse dedicado personalmente a enseñarme desde el principio. Esto empezó hace ya casi 6 años con la tesis de Máster y siempre ha estado disponible para las ideas nuevas y las dudas absurdas, entendido que este Doctorado ha sido un vuelco a mi formación y un salto al vacío. También agradezco por la ayuda a todos los miembros del FuniMat, a los que se han ido y a los que permanecen, todavía recuerdo cuando el grupo consistía en tres personas y una bomba de vacío.

Esta tiempo no habría sido tan ameno sin contar con los compañeros del UIMM, ha sido curioso ver cómo durante las comidas en la cafería he pasado de ser el más nuevo (con Cella, Elena, José C., Roger, Alberto, Alexis y Néstor) a ser uno de los veteranos. Gracias por los consejos que me dabais al inicio de mi tesis de cómo esconderme de mi tutor o reciclar presentaciones, y por adelantarme la montaña rusa anímica que sería después la tesis. Qué razón teníais, al final todos pasamos por los mismos altibajos. En un tiempo más reciente, me gustaría incluir a gente que entró conmigo y a la gente más nueva. Entre ellos a Eugenia, Víctor, Alejandro, Javi López, Isaac, Iván y muchos más que me dejo. Estar en un ambiente tan positivo hace que el trabajo y los sinsabores de la tesis se hagan mucho más ligeros.

De una forma más personal, me gustaría agradecer a algunas personas con las que he congeniado especialmente. A Néstor, porque aunque hayas desaparecido sin dejar rastro, todavía nos reímos con tus anécdotas terriblemente exageradas y desproporcionadas. A Katia, porque creo que somos muy parecidos y siempre tienes una sonrisa para las situaciones más absurdas. A Ramón, porque fuera de todas las bromas, hemos pasado alguno de los momentos más divertidos de mi estancia (principalmente en congresos). A Roger, porque siempre me saca una sonrisa por muy mal que me salgan los experimentos cuando me entero de que lleva un yogur para comer, y se sabe (o cree saber) mejor que yo lo que pone en mi Scopus. A Jose Alberto, creo que siempre hemos tenido tema de conversación ameno y espero que te vaya genial en la nueva etapa que estás emprendiendo.

Para acabar, y como suele suceder, de forma más importante me gustaría agradecer todo el apoyo recibido por mi familia. A los que están y a los que ya no, sin todo ese apoyo incondicional no habría podido superar todas las adversidades. Bea, sin ti esta tesis no había sido posible, gracias por estar siempre disponible para hacerte consultas o ahogar las penas. También agradezco a nuestra compañera de piso Sira, aunque no puedas leer esto (por ser un perro) te mereces aparecer aquí simplemente por aguantar horas de ensayos y de leer en voz alta, siempre poniendo cara de atención y de entender todo.

Abbreviations

1D	1-dimensional
2D	2-dimensional
3D	3-dimensional
ABTS	2,2'-azino-bis(3-ethylbenzothiazoline-6-sulfonic acid
Ala	Alanine
Car	Carnosine
CD	Circular Dichroism
CSP	Chiral Stationary Phases
CUS	Coordinatively Unsaturated Sites
Cyt c	Cytochrome c
DAC	Diamond Anvil Cell
DFT	Density Functional Theory
DLS	Dynamic Light Scattering
DMF	N,N'-Dimethylformamide
EGFP	Enhanced Green Fluorescent Protein
EP	Ephedrine
FT-IR	Fourier-Transform Infrared Spectroscopy
GCMC	Gran Canonical Monte Carlo
Glu	Glutamic acid
Gly	Glycine
Gly-Thr	Glycine-Threonine
Gly-Tyr	Glycil-L-tyrosine
GOx	Glucose Oxidase
HPLC	High-Performance Liquid Chromatography
HP-PXRD	High-Pressure X-Ray Diffraction

HRP	Horseradish Peroxidase
Ile	Isoleucine
Leu	Leucine
MA	Methamphetamine
MMM	Mixed matrix membranes
MOF	Metal-Organic Framework
MP-11	Microperoxidase-11
Phe	Phenylalanine
PSM	Post-Synthetic Modification
PTM	Pressure Transmitting Medium
PXRD	Powder X-ray Diffraction
RMSD	Root-mean-square deviation
SBU	Secondary building units
SEH	Soybean epoxide hydrolase
SEM	Scanning Electron Microscopy
SPE	Solid-phase extraction
TATB	Triaminotrinitrobenzene
TGA	Thermogravimetric analysis
Trp	Triptophan
Tyr	Tirosine
Tyr	Tyrosine
UV-Vis	Ultraviolet–visible
Val	Valine

Abstract

This thesis intends to tackle some of the most common drawbacks in the synthesis and applications of metal-organic frameworks (MOFs) through the use of biologically-derived molecules. Using the Central Dogma of the Biology a study of all the components from DNA to proteins was carried out, implementing them in the design and applications of MOFs.

Chapter 1 provides an overview of the different biologically-based frameworks reported to date, their structural variety and the different synthetic strategies used to create them. Special attention was given to the increase in complexibility that goes from nucleotide to peptide and then to the incorporation of enzymes. Posteriorly, there was a description of some of the most relevant applications of these systems, and the importance in them of their biologic counterpart.

Chapter 2 studies the structural response to pressure-induced stress into a peptide-based MOF. This type of external stimulus can make the structure collapse, potentially affecting the function and producing adverse effects. However, the inclusion of flexible peptides into the structure of these systems proportionate them with a response to the pressure, which can be predicted. We use a “dense” MOF in order to study the progressive change of the structure with X-ray diffraction.

Chapter 3 continues the exploration of flexible peptide-based MOFs, using a more complex system for enantiomeric discrimination of recreational drugs: methamphetamine and ephedrine. This type of materials are able to provide a chiral recognition framework, allowing at the same time structural stability and porosity. Moreover, we used theoretical simulations in order to predict the separation output, being afterwards corroborated experimentally.

Chapter 4 was developed to proportionate a new immobilization of enzymes inside MOFs, different to what was already reported. Previous works are centered on the scaffold and not the content, modifying or altering the MOF considering the enzyme as an immobile element. However, far from this point of view, the enzymes are in constant movement between energetically favorable conformations. Based on this concept, we developed a procedure that allowed the enzyme to partially unfold into a temporary conformation that would allow it to enter to the pore of the MOF through smaller windows. The native structure could be then regained, which functionality was confirmed through catalytic studies.

This Ph.D. thesis is expected to represent a significant advancement in the development of biologically-based MOFs, intending to provide a more biological approach to a problem that has been studied mostly from the chemical point of view.

Publications

José Navarro-Sánchez, Ana I. Argente-García, Yolanda Moliner-Martínez, Daniel Roca-Sanjuán, Dmytro Antypov, Pilar Campíns-Falcó, Matthew J. Rosseinsky, Carlos Martí-Gastaldo. Peptide Metal–Organic Frameworks for Enantioselective Separation of Chiral Drugs. *J Am Chem Soc* **139**, 4294–4297 (2017).

José Navarro-Sánchez, Ismael Mullor-Ruíz, Catalin Popescu, David Santamaría-Pérez, Alfredo Segura, Daniel Errandonea, Javier González-Platas, Carlos Martí-Gastaldo. Peptide metal–organic frameworks under pressure: flexible linkers for cooperative compression. *Dalton T* **47**, 10654–10659 (2018).

Víctor Rubio-Giménez, Marta Galbiati, Javier Castells-Gil, Neyvis Almora-Barrios, José Navarro-Sánchez, Garin Escorcia-Ariza, Michele Mattera, Thomas Arnold, Jonathan Rawle, Sergio Tatay, Eugenio Coronado, Carlos Martí-Gastaldo. Bottom-Up Fabrication of Semiconductive Metal–Organic Framework Ultrathin Films. *Adv Mater* **30**, 1704291 (2018).

José Navarro-Sánchez, Neyvis Almora-Barrios, Belén Lerma-Berlanga, J. Javier Ruiz-Pernía, Victor A. Lorenz-Fonfria, Iñaki Tuñón, Carlos Martí-Gastaldo. Translocation of enzymes into a mesoporous MOF for enhanced catalytic activity under extreme conditions. *Chem Sci* **10**, 4082–4088 (2019).

Table of contents

Chapter 1:

MOFs based on biological components: design and applications

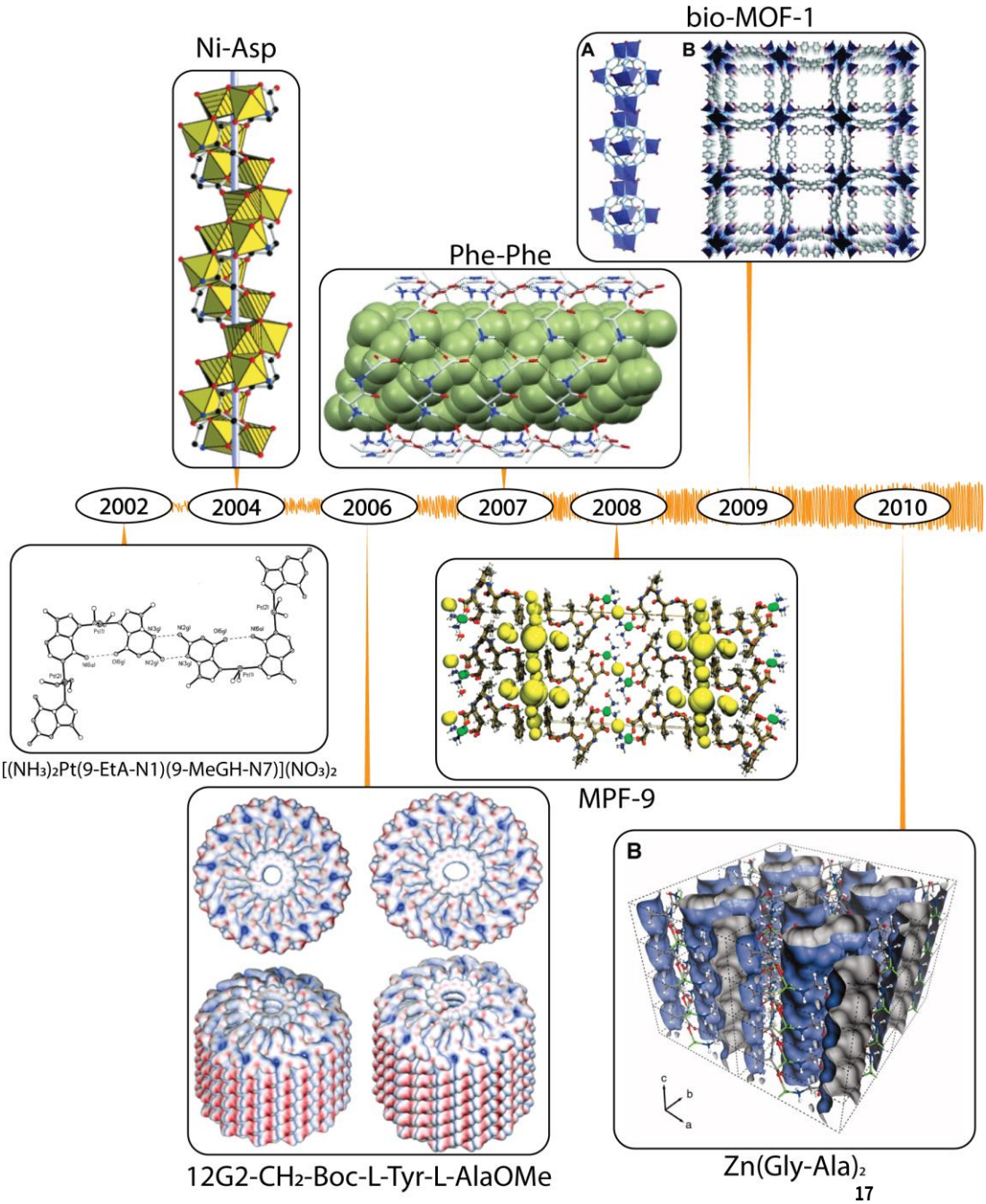
Ni-Asp
bio-MOF-1
A
B
Phe-Phe
2002
2004
2006
2007
2008
2009
2010
[(NH3)2Pt(9-EtA-N1)(9-MeGH-N7)](NO3)2
MPF-9
B
12G2-CH2-Boc-L-Tyr-L-AlaOMe
Zn(Gly-Ala)2

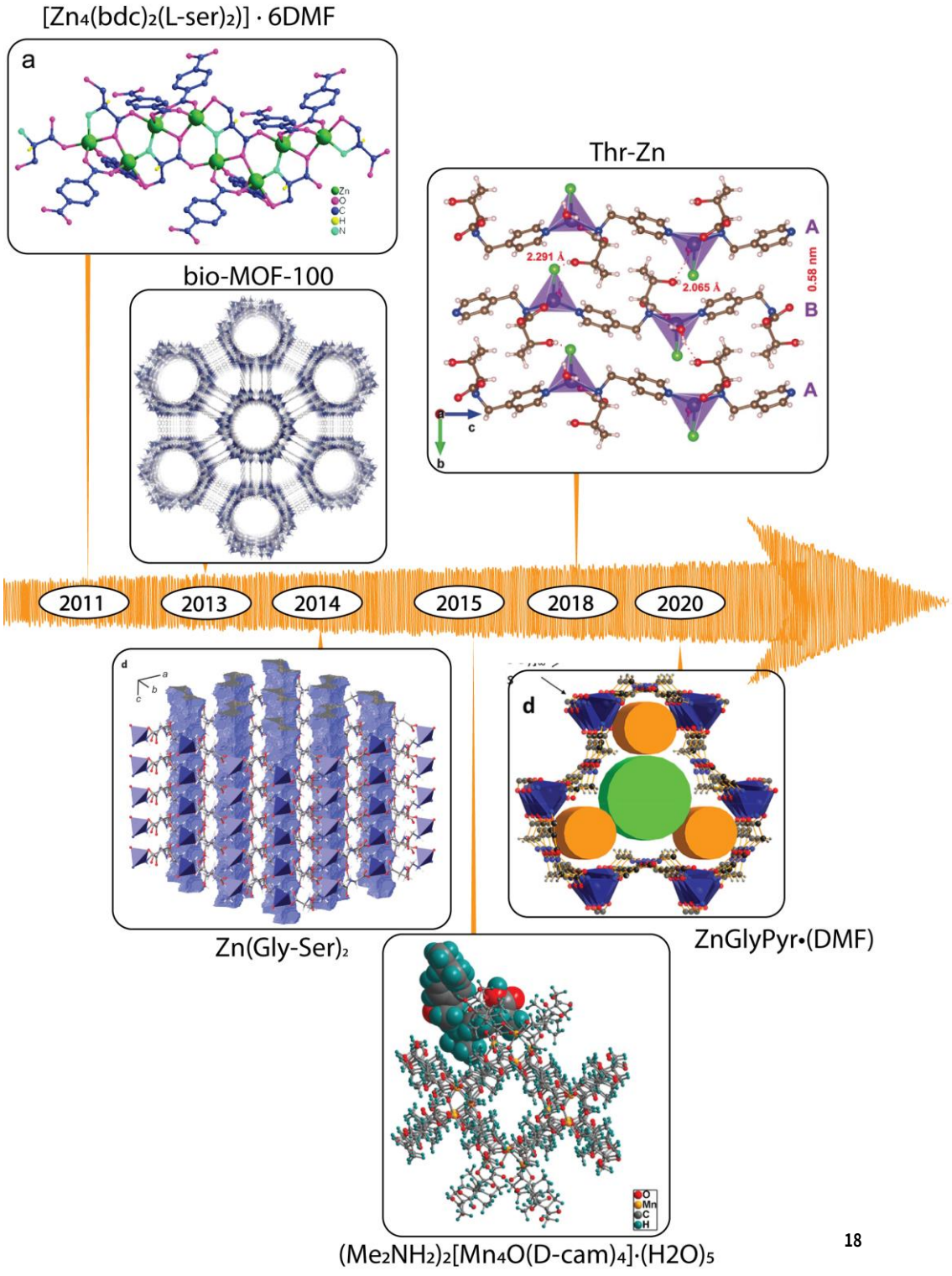
[Zn4(bdc)2(L-ser)2] · 6DMF
a
Zn
O
C
H
N
bio-MOF-100
Thr-Zn
2.291 Å
2.065 Å
0.58 nm
A
B
A
c
b
2011
2013
2014
2015
2018
2020
d
a
b
c
Zn(Gly-Ser)2
d
ZnGlyPyr•(DMF)
O
Mn
C
H
(Me2NH2)2[Mn4O(D-cam)4]·(H2O)5

1. Building blocks

Supramolecular chemistry was born from the inspiration that biology provides for the organization of simple units, into a vast range of intricate and structures with complex and efficient functions. Although many of the synthetic materials had been discovered by accident, rational synthesis started playing an increasingly important role in the 90s.[1] The problem with trying to make such materials was that the products of solid-state reactions were predictable only in a very limited sense, like the example shown in **Figure 1a**. Moreover, to calculate the properties the basis had to be known or theoretically simulated, that caused that predicting the most stable structure for a given composition of matter was more an art than a science.[2]

From the very early days of crystal chemistry it was recognized that the structures of complex crystals could be described in terms of various units called building units. Some time after, it was realized that the assembly of building blocks yields extended structures with designed properties.[3,4] Considerable attention was then given to factors such as solvent composition, catalytic action, cluster formation in solution, and interaction with solvent or other molecules that may serve as guests. This is in sharp contrast to the "shake and bake" of the early days of solid state chemistry, giving birth to the design of organic and particularly metal-organic extended solids.[5–7] Special emphasis was based on low-density ("open framework"), porous solids constructed by combining molecular clusters that have well-defined linking sites with linking groups that may be linear or branched. In many cases that property is absent because passage was hindered by solvent molecules or counterions which form strong interactions with the framework, being necessary to maintaining the integrity of the crystal structure. Solid-state reactions that take place at low temperatures offer the advantage that either inorganic or organic structural elements can be preserved in the transformation from reactant to product. In this way, new metastable structure types could be arrived at by rational means through a series of mechanistically well understood steps.

One particular approach proposed in order to build frameworks was based on the expectation that if molecular "building blocks" with a chemical functionality and a stereochemistry can be devised, then simply allowing these specifically organized components to react together in the correct proportions may lead to the spontaneous assembly of the intended network.[8] A building block is the minimum assembly of atoms, ions, or molecules which can give rise to the final solid and they act as bricks for the edification of the structures and their size can be completely different with the considered solid. Pauling helped in defining the origin of the concept, when he defined the coordination polyhedral for the description of structures.[9] Some of the

steps being taken by chemists as they attempt to increase the rationality of their synthetic work by employing both innovative building block approaches and gentler synthetic techniques which allow the use of such molecular chemistry concepts as kinetic control and polyatomic building blocks, as done later by Meier and Olson for zeolitic structures.[10] General lack of control over the character of solids produced from the traditional synthetic methods is directly related to the fact that the starting entities do not maintain their structure during the reactions, leading to poor correlation between reactants and products. The concept of building unit initially implied thermodynamically stable states, the final compound representing the ultimate step of the formation of the solid whatever the mechanism of formation. This is why they were originally just a tool for the description of structures.

Férey defined the importance of the building units and emphasized this minimum expression instead of focusing in the solid itself.[11] At the time almost nothing was known of the reactions under hydrothermal conditions (calcinated templates was the most used method, as shown in **Figure 1b**), the drastic change in the properties of the solvent affects the nature of the species in the solution. It was considered a "black box" in which one enters the reagents and observes the products, however, it was known that the building units in the solution were formed by the oligomeric condensation of prenucleation building units.

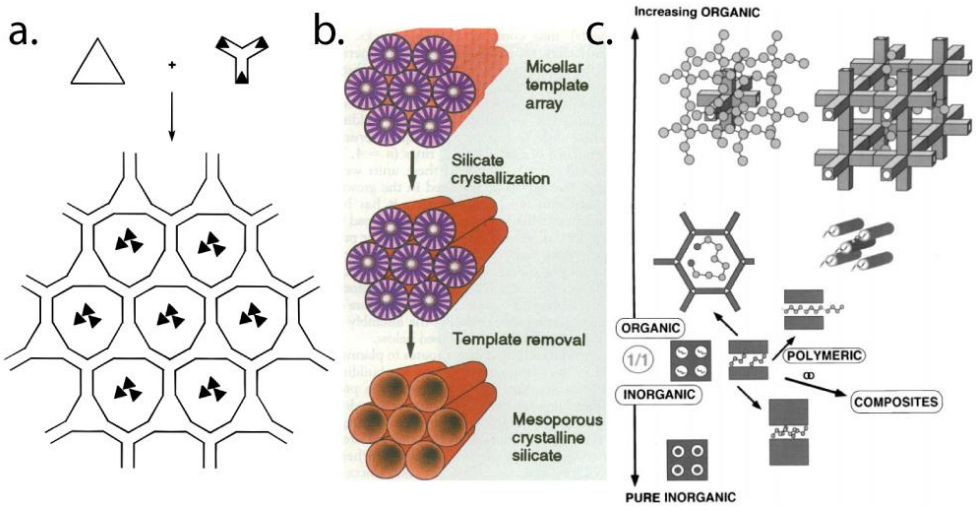

Figure 1. **a**. Condensation-addition polymerization reactions were utilized for the preparation of porous materials from organic molecules, metal clusters, and transition metal ions. **b**. Schematic diagram of the templating mechanism proposed for mesoporous molecular sieves. **c**. Continuum between organic and inorganic frameworks. The latter are shown in dark gray, and the former are represented by spheres and chains. Modified from [1,11,12].

Yaghi's group finally determined the existence of metal-organic carboxylate frameworks, later called MOFs (**Figure 1c**), as crystalline materials with well-defined structures.[12–14] They were interested in the construction of porous materials due to their impact in global economy and the prospects for building complex molecular voids with the possibility selective inclusion and chemical transformations. They found that multidentate linkers such as carboxylates allow for the formation of more rigid frameworks due to their ability to aggregate metal ions into M-O-C clusters. These materials were rigid as the metal ions were locked into their positions by the carboxylates, being able to produce extended frameworks of high structural stability. The frameworks were also neutral, obviating the need for counterions in their cavities. To appreciate the impact of SBUs on pore size and porosity frameworks, they also incorporated long linkers and replaced the vertex of a framework net by a group of vertices. The ability to design their structures allowed the synthesis of compositions with designed pore structure and porosity aspects beyond what the zeolites could achieve.

This kind of reticular synthesis can be described as the process of assembling designed rigid molecular building blocks into predetermined ordered structures, which are held together by strong bonding. The rigidity of the building blocks remains unaltered throughout the construction process – an important aspect that could help to realize the benefits of design in crystalline solid-state frameworks. The adaptability of MOF porosity is limited by both the metal coordination geometry and the degrees of freedom available to the linkers. When the geometry of the metal coordination is fixed, MOFs built from rigid linkers are limited to configurations that can be accessed by uniaxial rotations,[15] and displacement of the linkers. In contrast, proteins are characterized by an adaptable response to their environment, produced by conformational selection of an appropriate functional structure from a large ensemble of energetically low-lying and kinetically accessible states. Biological systems have evolved highly-efficient solutions to the current problems of sustainable energy and transformations. Bioinspiration and biomimetics thus offer new possibilities for the develop of chemical systems.[16]

Many biomolecules, such as amino acids, oligopeptides, proteins and nucleobases are commonly employed ligands and have already been successfully incorporated into coordination polymers. However, some restrictions generally prevent these biomolecules from being good candidates as MOF constituents.

1.1 Nucleobases

Nucleobases are the key constituents of nucleic acids and are involved in base-pairing: adenine binds to thymine or uracil with the help of two H-bonds, and guanine specifically recognizes cytosine through three H-bonds. Purines and pyrimidines are the simplest building blocks of nucleic acids. They contain multiple nitrogen donor atoms that make them attractive ligands for coordination-driven assembly of discrete complexes. One of the basic ideas of the MOF creation is that the packing of rigid building units with rigid linkers would lead to an inefficient occupation of space, as it would be unable to adapt to its contents. For that reason, as a response of the huge necessity towards the incorporation of flexible linkers the nucleobases were evaluated as suitable ligands for the construction of biomimetic compounds.

On that line, there has been a substantial increase in their use as they can provide a stable molecular linker outfitted with many positions able to coordinate to metal centers. They also stablish complementary hydrogen bonding interactions, leading to the formation of accessible voids within the crystal structure making them suitable for the design and synthesis of porous biologically-derived MOFs. One of the reasons for them being marvelous bridges is that they are very versatile metal ligands.[17–21] With excellent metal coordination power in general, each type of nucleobase has its own metal binding preference. Nucleobases can be divided into two groups: purines and pyrimidines (**Figure 2a**), and this also affects to the metal connectivity and difficulty to obtain structures. Purine nucleobases make better bridging ligands than the pyrimidinic ones thanks to their greater heteroatom number (**Figure 2b**). Moreover, hydrogen bonding donor/acceptor positions of the purine nucleobases surpass that of the pyrimidinic ones and make them more appropriate for interacting with other entities. For that reason, suitable systems that would fulfill all the above described requirements for obtaining MOFs are discrete metal-nucleobase systems, especially those based on purine nucleobases. These ligands provide the advantage of the increased rigidity of the supramolecular building block due to the coordination through multiple positions, also presenting many edges capable of establishing complementary hydrogen bonding interactions that provide rigid and predictable synthons. For example, the intrinsically low symmetry and limited length of adenine molecules makes it difficult to obtain three-dimensional (3D) scaffolds using a single adenine ligand, thanks to accessible nitrogen and oxygen electron lone pairs that allow these molecules to act as multidentate organic ligands as shown in **Figure 2c**.

Even though there existed previously some coordination polymer that incorporated nucleobases,[22] the first example of a MOF based on a purine nucleobase coordination mode was a zeolitic type framework with large cavities

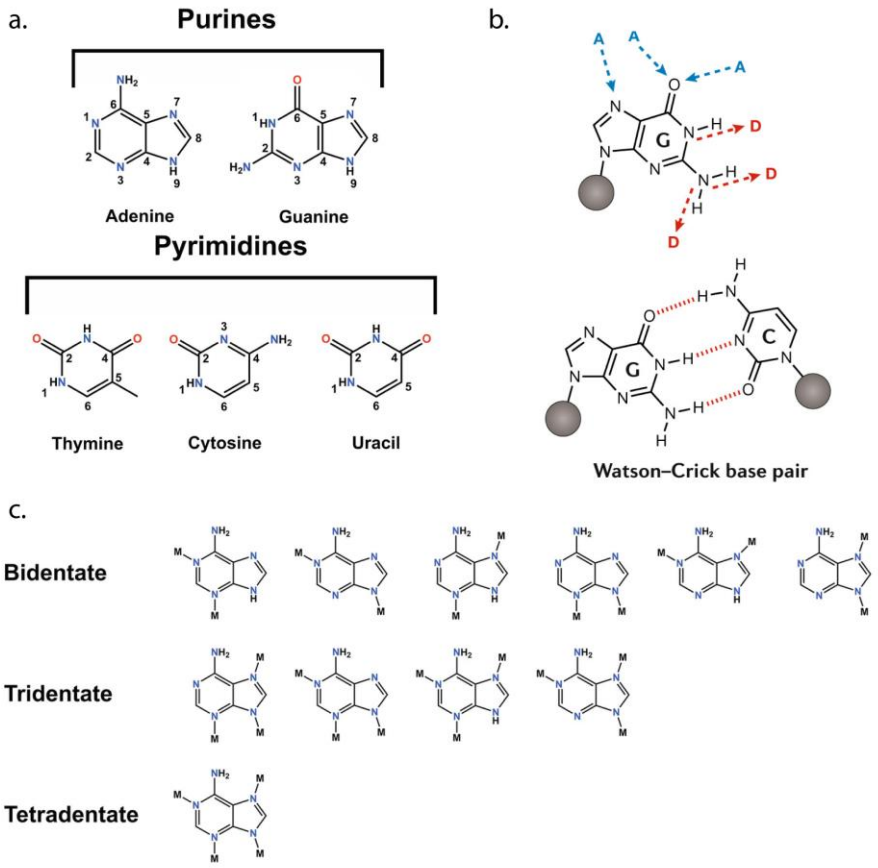

Figure 2 a. Chemical structures of natural nucleobases. **b**. Nucleobases shine by its hydrogen-bond donating/accepting capability, with three acceptors (A) and three donors (D) sites (in the case of the guanine). **c**. Possible coordination modes of adenine when binding to at least two metal ions. Modified from references [30,32].

surrounding smaller pore apertures, indicating a strong interaction between the framework and H_2 / CO_2 molecules.[23] This was an eager approach to the incorporation of biologically derived, flexible linkers to an imidazolate structure. The abundant proportion of amino groups that provide the nucleobases allow the MOFs formed by them exceptional abilities to selectively adsorb gases like CO_2,[24,25] store hydrocarbons,[26] control drug-release,[27] and even logic circuits.[28] However, the guanine is able to form G-quadruplexes that serve as intrinsic electron donors linking planar aromatic electron acceptors.[29] The guanine shines above the other options by its hydrogen-bond (H-bond) donating/accepting capability, with three acceptor (A) and three donor (D) sites, which enables both Watson-Crick and Hoogsteen faces to participate in the creation of a broad array of H-bond networks.[30] Other related

nucleobases like the hypoxanthine and the xanthine are less commonly employed as they are more difficult to incorporate in frameworks.[31] For that reason, MOFs constructed from adenine have been more thoroughly studied.[32]

The first zinc-adenylate vertices on a MOF were developed by Rosi *et al*. in 2012, constructing the bio-MOF-100 with enormous mesoporous cavities and its variants showed in ***Figure 3a***.[33] This was the first MOF material that exclusively exhibited mesopores based on constructing large metal-organic vertices (instead of metal-carboxylate cluster vertices) and periodically linking these large building units together with inexpensive commercially available organic linkers. In addition to this work, Li at al. determined that isoreticular analogues of bio-MOF-100 could be prepared by replacing shorter dicarboxylate linkers with longer molecules.[34,35] The ligand could be interchanged to obtain bio-MOF-102 and bio-MOF-103 (**Figure 3b**). This change produced a sharp increase in the unit cell by 6.34 Å for the 102 and unit cell dimensions a=b=c=82.25 Å for the bio-MOF-103 (**Figure 3c**) consequently increasing the pore size.

Some other great examples are the PNU-21 and PNU-22,[36] two adenine-based MOFs with rigid and robust architectures with coordinately unsaturated metal environments for CO_2 cycloaddition. They showed good catalytic performances and recyclability thanks to their Lewis acidic metal centers and basic functional groups,

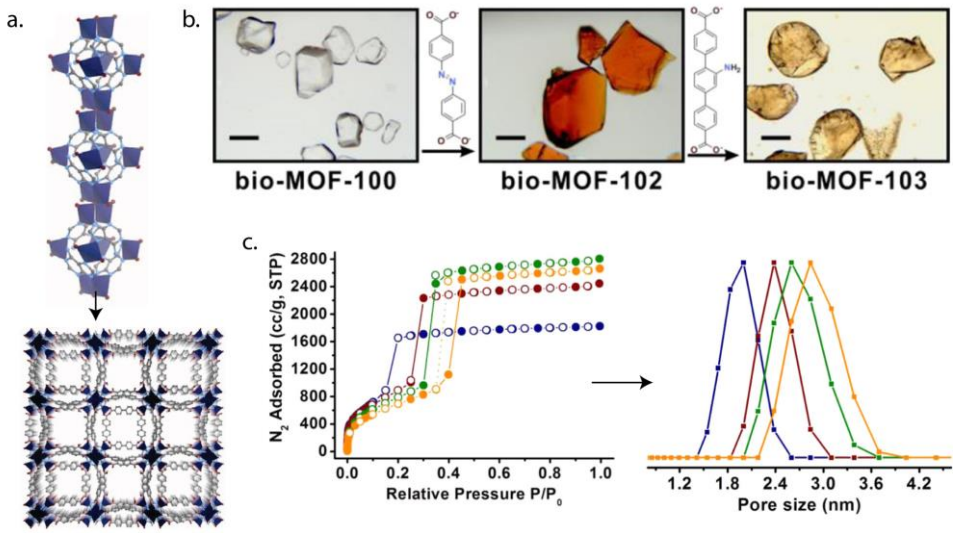

Figure 3. **a**. The crystal structure of bio-MOF-1 consists con zinc-adenylate columns which are linked together into a 3D framework. **b**. Light microscope images of the crystalline MOFs, obtained via ligand exchange. **c**. N2 adsorption isotherms (left) and normalized pore distribution (right) of bio-mof-100 (red), 102 (green), 103 (orange) at 77K. Modified from reference [27,34].

making them efficient heterogeneous catalysts. In this line, Ya-Qian Lan and coworkers created other two adenine-based MOFs for CO_2 photoconversion named AD-MOF-1 and AD-MOF-2.[37] The auxochromic -NH_2 and hydrophobic alkyl groups on the organic linkers made them responsive to visible light, allowing a high HCOOH production rate. Experimental results correlated with theoretical calculations indicated that the CO_2RR formation mainly occurred at the activated aromatic nitrogen atom of adenine with assistance from the *o*-amino group.

As a conclusion, for a single nucleobase it is possible for metal ions to coordinate with almost any site of the molecules. They have the potential to form numerous interactions and their multifunctionality and variety of binding modes within a structure can give rise to structural flexibility as seen in biological molecules such as proteins and peptide-based frameworks.

1.2 Amino acids and Peptides

Amino acids are organic ligands containing both a carboxyl (-COOH) and amino (-NH_2) group that dominate their functional and physical properties. Amino acids link together via amide bonds to form peptides and proteins that serve important biological functions. They are also excellent organic ligands and may coordinate metal ions through both their carboxylate and amino groups. The organic side chain of amino acids can impart hydrophobic or hydrophilic character, with the presence of a polar or non-polar side chain, which is important for the formation of protein structures. Their rich coordination chemistry makes them an attractive class of organic ligands for the formation of extended MOF structures. Carboxyl groups can also form metal-carboxylic clusters or bridge with metal ions to increase the rigidity and stability of the frameworks. Adjacent amino and carboxyl groups with special angles connect metal ions in a certain direction to obtain unique extended network structures. Notably, amino and carboxyl groups can also be used as H-bond acceptor and receptors in the study of host-guest chemistry.

MOFs are able to reduce the gap with enzymes through the incorporation of peptide moieties inside the MOF cavities, thereby providing a typical apoenzyme environment, this type of systems are known as artificial metalloenzymes.[38] Most are constructed by mixing amino acids of modified amino acids with organic ligands. The nature of the amino acid ligand determines the potential chirality of this type of MOFs. In addition, the porosity of the frameworks has special applications for the recognition of some special molecules and selective separation, particularly for enantiomers. Usually, they are either constructed from metal ions and natural amino acids or metal ions and chemically-modified natural amino acids. The first remarkable example of

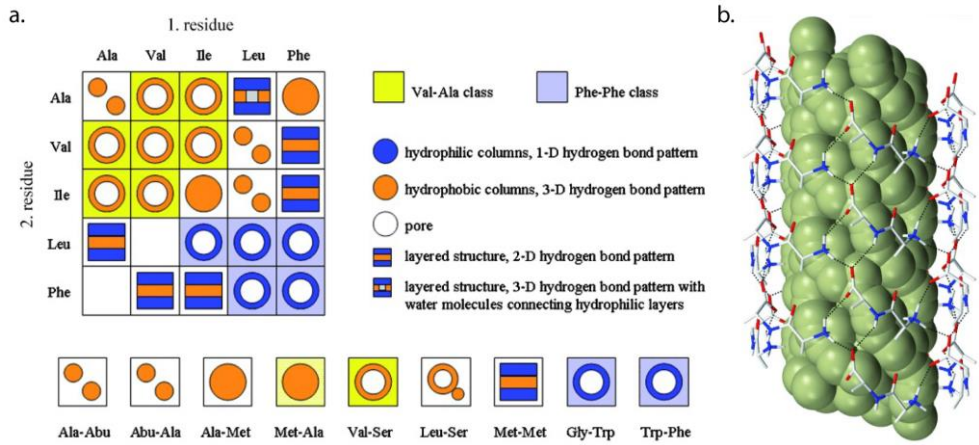

Figure 4. **a**. Table representing the general description of the structures of hydrophobic dipeptides showing pattern for separation between hydrophobic and hydrophilic moieties and the presence of pores. **b**. Water positions (with van der Waals surface) inside a channel of the Phe-Phe structure. Modified from [43].

MOF with amino acid as ligand was presented by Jacobson in 2004,[39] with a nickel aspartate oxide one-dimensional compound with an extended helical subnetwork. The important detail was that this was the first compound that demonstrated the potential of hydrolysis-favoring synthesis conditions for the preparation of novel, structurally complex, chiral compound with amino acids (this was further developed in the following years).[40] Apart from this, some interesting 3D chiral coordination polymers were also being described.[41,42]

However, one of the first reviews that deepened in this relation of amino acid and determined that the dipeptides were useful building blocks for building materials was not a MOF. In 2007 Görbitz made a systematic survey of structures derived from single-crystal X-ray diffraction studies that revealed the existence of two large classes of structures, differing in the dimensionality of the hydrogen-bonding patterns in the crystal and the nature of the channels.[43] Supramolecular self-assembly of the rather small building blocks is dictated by stringent demands on the hydrogen-bond formation by the peptide main chains and the aggregation of hydrophobic entities in the side chains, as can be resumed in **Figure 4a**. With both carboxylate and amino metal binding sites, amino acids tend to form discrete complexes through an O,N-chelating mode, forming a five-membered glycinate chelate ring. However, in some cases coordination of the a-carboxylate group to the metal ions can occur either through bi- or tri-dentate bridging modes creating extended frameworks.[44] One-dimensional coordination networks are commonly formed when pure amino acids are used (**Figure 4b**). Increasing dimensionality can

be achieved using both amino acids and additional organic ligands or inorganic anion/clusters that act as linkers.

In 2007 the Li team reported three Phe (Phenylalanine) and Tyr (Tyrosine) derivatives as ligands to construct four kinds of novel MOFs.[45] On the basis of previous amino acid and metal conjugation systems with Trp and His, they chose the first two aromatic amino acids as candidates because they both have conjugated rings, which may provide rigid trunks in their coordination networks and can be modified easily. The size and the shape of the grids in the two-dimensional (2D) layers could be mediated through rational design by adjusting the "depth" and the "width" of the ligands. The inclusion of the MOF structure was the modification of the aromatic amino acids by organic synthesis. On the same year, McDonald's team developed a new mercury-alanine complex also pointing the relation between identity of the amino acid and the structure of the MOF formed.[46]

Even if the possibility of forming 3D-structured MOFs was suggested, it was still a difficult experimental reality to attain. As Rosseinsky's group pointed in 2010,[47] the simple two-component systems based upon amino acids and metal centers were generally dense, lacking any accessible pore voids. This was due to the flexibility in the amino acid backbone and the preferred mode of binding to metal center. The most common procedure to obtain some kind of porosity was to coordinate the functional groups with one or more phenyl rings. In their first work tackling this problem, they used 4,4'-bipyridyl linkers of variable length and rigid metal-amino acid systems to obtain porous materials. This work highlighted the crucial role that rigid organic pillars had in generating porosity in metal-amino acid derived extended structures.[48] One of the solutions presented in 2014 was the preparation of a homochiral Zn-containing MOF based on a one-pot synthesis of 2-aminoterephtalic acid and L-lactic acid. Similar to the already reported IRMOF-3, the free NH_2 was functionalized with chiral L-proline through a post-synthetic modification (depicted in **Figure 5a**).[49] However, as Canivet and Farrusseng demonstrated priorly[50] and published one year later,[51] the use without purification of a material would obviously contain components from the reaction mixture, invalidating any posterior result. Moreover, the amide formation between the amino groups at the MOF walls and an amino acid would never occur under the conditions described. That same year they proposed an interesting microwave-assisted procedure that would yield excellent results,[52] as the organic-mediated functionalization were much slower.[53]

Returning to the one-pot synthesis of MOFs based on amino acids, the group of Zhang developed in that same year two enantiomorphic MOFs based on an enantiopure alanine ligand, with an interesting SOD topology.[54] From this stepping stone they reported in 2017 a new approach to construct with amino acid and tetrazolate derivatives homochiral MOFs (**Figure 5b**).[55] These materials showed

permanent microporosity and enantioselective recognition ability. Although the efforts devoted until that day, it remained highly challenging to construct homochiral MOFs with zeolitic topology.

All these approaches have been developed separately through the years. The group of Wan reported in 2018 a homochiral zeolitic imidazolate framework membrane, L-His-ZIF-8 (represented in **Figure 6a**) after incorporating the Histidine through a contra diffusion method. [56] The chiral environment in this framework made it the first chiral ZIF membrane capable of chiral separation. With the same application as a goal, the group of Zhou in 2020 prepared a chiral MOF possessing an open amphiphilic channel from a dicarboxylate ligand derived from an amino acid (**Figure 6b**).[57] The remarkable selectivity of this material in the enantiosorption and separation motivated the investigators to try to achieve a single-crystal structure with no success. The excellent performance may arise from the combination of chiral

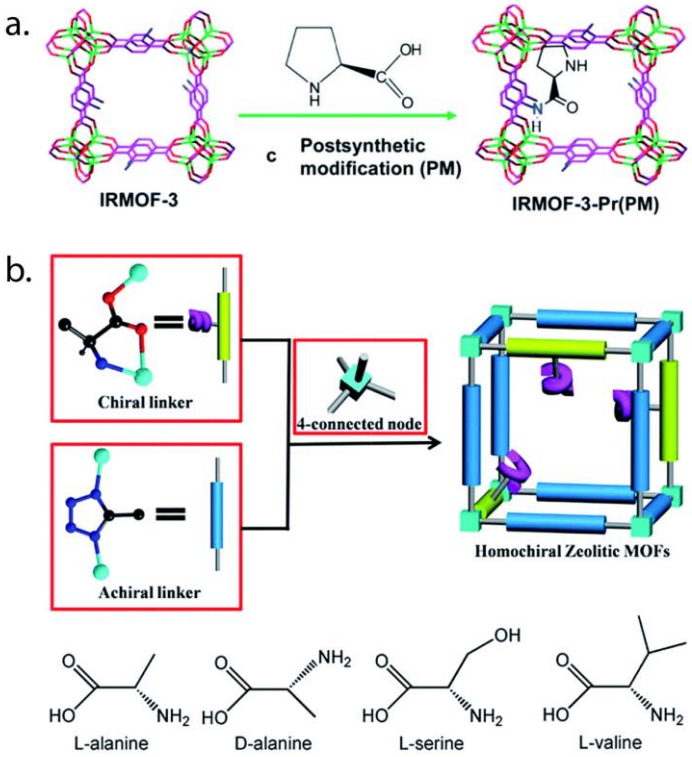

Figure 5. **a**. Synthesis of IRMOF-3-Pr(PM) **b**. The synthesis strategy of the homochiral MOFs. Modified from [49] and [55].

channels of appropriate sizes and the amphiphilic inner surface, which is lined up with hydrophilic amide groups and hydrophobic benzyl groups. This combination allows for bioanalogous interaction of the host framework with adsorbate species during the inclusion process. As a last example of the application of amino acids into MOF structures, Manna's group reported a strategy to develop heterogeneous single-site enantioselective catalysts based on naturally occurring amino acids and earth-abundant metals for eco-friendly asymmetric catalysis. The grafting of amino acids within the pores of the MOF is detailed in **Figure 6c**, followed by post-synthetic metalation afforded high enantioselectivity.[58]

One fundamental property of the amino acids is that two or more can couple and form a chain called peptide. Peptides are polymeric biomolecules composed of the 20 naturally amino acids (or the infinite modifications), each with its own unique size

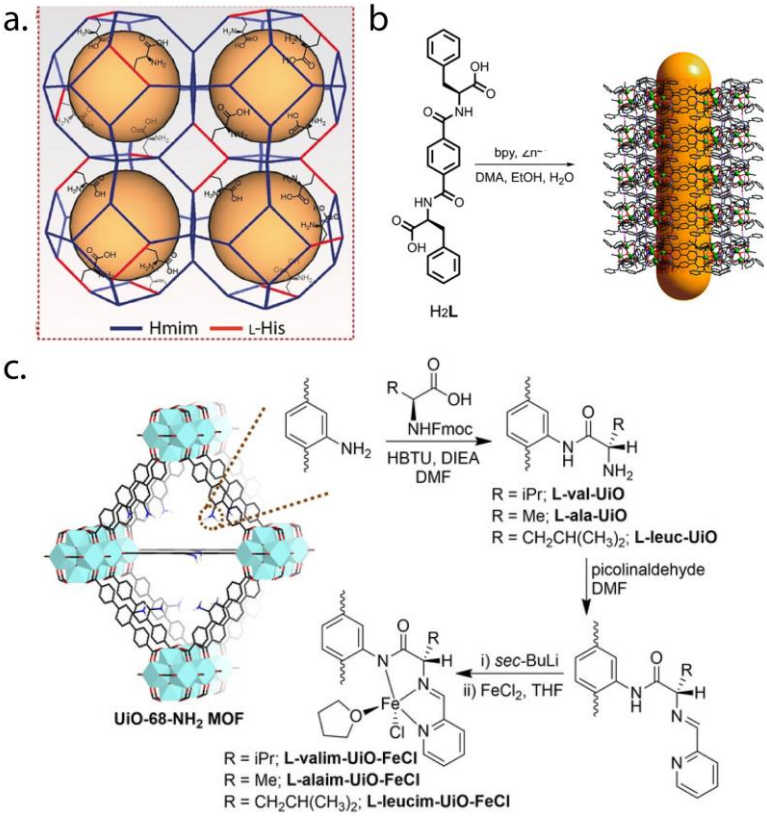

Figure 6. **a**. Representation of L-His-ZIF-8 with the Histidine **b**. Connection of Zn_4O clusters with L ligands and 4,4'-bipyridine and the 1D nanotube highlighted as an orange stick generated from the interlayer hydrogen-bonding. **c**. Synthesis of amino acid-derived chiral MOFs and their metalation with $FeCl_2$. Modified from [56–58].

and functionality. Peptides are capable of performing self-assembly, which makes them useful as building blocks for directing the growth and assembly of inorganic structures, some of the most employed combinations are depicted in **Figure 7a**. Various molecules can be attached to peptides to affect their self-assembly properties directing their assembly into particular desired structures. One of the first in using dipeptides for the assembly of nanoporous materials was Görbitz in 2005.[59,60] Followed by some more exhaustive studies years later,[43,44] starting with hydrophobic residues of Ala (Alanine), Val (Valine), Ile (Isoleucine), Leu (Leucine) and Phe. The Val-Ala materials had a 3D structure due to a hydrogen bonding with

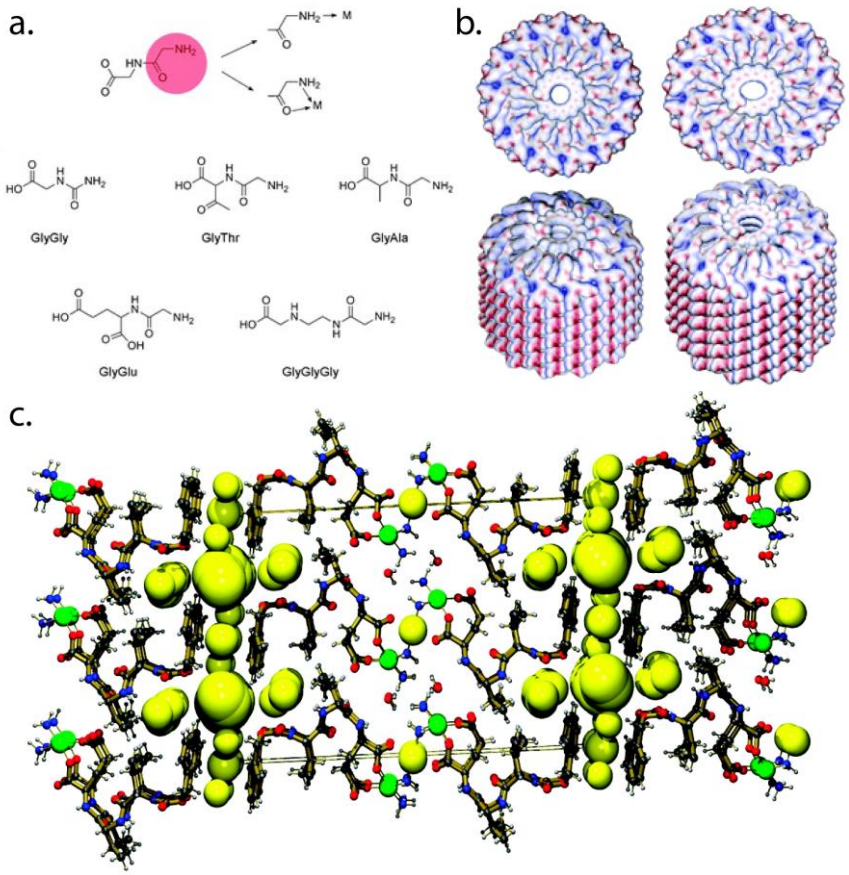

Figure 7. **a**. Potential coordination modes of the terminal amino group of peptides: monodentate and five-membered chelate mode. **b**. Top view of one layer of the circular column, together with top and side views of the porous column. **c**. Packing diagram of MPF-9. Yellow balls indicate the voids. Modified from [61–63]

hydrophobic pores. Another example was presented by Heiney in 2006,[61] as they synthetized dendritic dipeptides that self-assembled into porous elliptical and circular columns that self-organized into periodic arrays. It was possible to make the transition from elliptical to circular columns with a temperature arrange, showing the structural flexibility of the system (**Figure 7b**).

The first report of a peptide-based MOF was made by the Taubert group in 2008.[62] It was constructed from Val and Glu (Glutamic acid) with Cu^{2+} and Ca^{2+} as metals. The system was formed due to the self-assembling properties of the peptide and specific metal-peptide interactions, constituting a stable and porous material. The one-dimensional (1D) channel architecture with two different pore sizes was a fine example of what could be achieved with the introduction of chiral small peptides as ligands (the structure is shown in **Figure 7c**).[63]

In 2010, inspired by the adaptable response of the proteins to their environment (and with a backbone on amino acids), Rosseinsky reported a peptide-based porous material with adaptable porosity. In there, a simple dipeptide linker (Gly-Ala) was arranged in a regular array by coordination to metal centers.[64] The experimental isotherms and desorption simulations of the peptide-linked framework showed that the pores blocked when there were no present guests, and open cooperatively when they were triggered by small molecules with polar bonds (**Figure 8a**). This adaptable porosity is a direct consequence of the peptide linkers. The low-energy states that characterize this deformation of the host are defined by cooperative minimums, composed by coordination with the metal center and hydrogen bond formations. This suggests a cooperative sorption mechanism analogous to the conformational selection in proteins, indicating the presence of an energy landscape with low-energy positions of the peptide unit that control the responses. As a demonstration, they also prepared a Gly-Thr (Glycine-Threonine) MOF with a 2D layered structure that displays 1D porosity and retains crystallinity upon solvent removal.[65] With this they showed that the compromise between flexibility and structural stability can be achieved by precise control of the coordination modes and supramolecular interactions enabled by the peptide. Both MOFs showed differences as Gly-Ala is more flexible whereas the Gly-Thr behaves as a rigid connector and locks the conformational flexibility by forming a chelate with the Zn^{2+} ion, stablishing an additional H-bonding interaction. This work suggests a fine compromise between robustness and flexibility correlative to that of proteins. Some years later, in 2014,[66] they reported a MOF consisting of glycyl-serine dipeptides coordinated to metal centers (the third one with only a change in one amino acid), with a structure capable of conformational changes and compared it with the ones of Thr and Ala. Using Gly-Ser as the linker they observed an ordered torsional change in the resulting framework and displacement on guest loss obtaining a similar effect to the closure of the pores. The Ser side-chain retains the -OH functionality of Thr, but the change

from a secondary to a primary alcohol is sufficient to produce this dramatic change in guest response.

The torsional degrees of freedom of the Gly-Ser dipeptide reposition the OH-bearing side chain of the Ser residue to enable a large translational displacement of the peptide (**Figure 8b**). Whereas the $Zn(Gly\text{-}Ala)_2$ MOF does not offer a unique closure path upon the loss of hydrogen bonding to the guest, the $Zn(Gly\text{-}Ser)_2$ does driven by a conformational change with a translationally symmetric closed state (**Figure 8c**). The strength of the resulting hydrogen bond makes the structure with Ser openable only by polar guests, in contrast to the Ala and Thr (**Figure 8d**). This demonstrates the changes in function associated with a difference In one amino acid residue. This functional control can be compared to a single-point mutation for proteins, as a single amino acid change can radically alter the structure and function.

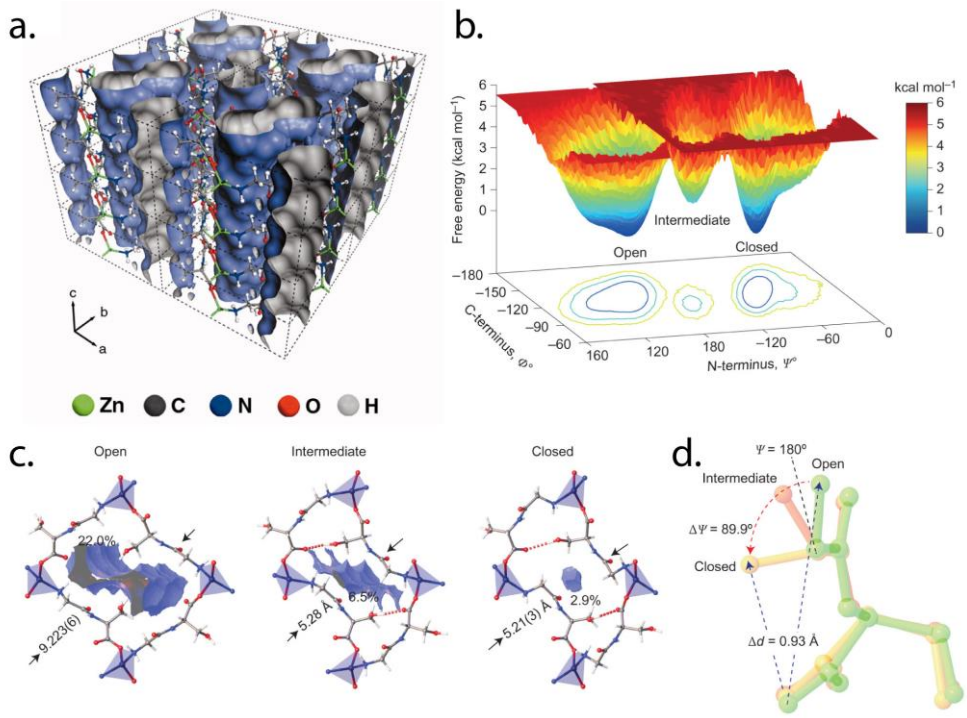

Figure 8. **a**. Perspective view of the Zn(Gly-Ala) channels **b**. Overlaid free-energy profiles calculated from MD simulations of the closed and open phases in equilibrium. There is a single minimum in the open and closed phase. **c**. Comparison of the structure of the open, intermediate and closed states that displays the folding of the peptide. Open and closed states correspond to SCXR-VT experiments coupled with MD simulations. **d**. Structural changes of the Ser MOF on ordered open-intermediate-closed closure. Modified from [64,66].

These examples clearly show how diverse the structures can be and the strong control of adsorption based on small changes in the peptide unit. However, these materials were limited to form 2D structures and low porosity materials. Following the idea that the peptide identity greatly affects the final MOF structure, they created a new MOF based on a natural dipeptide named carnosine (Car) which is formed by Ala and His. The peptidic chain of carnosine contains an extra CH_2 group, and the histidine incorporates the imidazole moiety that could serve as extra metal binding site, giving this peptide two extra linking points. They formed a 3D framework compound in which each carnosine molecule links to four tetrahedral Zn cations. The structure is flexible and displays 1D, higher porosity and a strong binding affinity for small molecules. ZnCar is an analogue of ZIFs where the involvement of the imidazole ring of the histidine side chain affords the chemical stability of the framework in water, retaining its flexibility and conferring structural adaptability on the framework in the presence of guest molecules. Interestingly, the following year they added an additional layer of complexity to this question, demonstrating how the use of longer tripeptides permits increasing the pore metrics in isoreticular peptide-based open frameworks with 3D pores.[67] The combination of structural stability of these materials remains limited by their rich conformational flexibility of the connectors as they undergo structural collapse when desolvated. The interaction of the guest molecules with the scaffold via H-bond interactions triggers a recovery of the porous architecture, being a sorption-driven restructuring. These porous hosts have conformational energy landscapes with certain analogies to those of protein structures and perform chemical functions in response to changes in their pore content. This comparison with proteins is not accidental as, similar to the polypeptide MOF, navigate between multiple metastable structure using bonds rotations in their search for the minimum energetic configuration (in **Figure 9a** there is a comparison between a common, rigid MOF and this possibility).[68] These structural changes are realized through the mechanisms of *conformational selection* (where a higher-energy minimum characteristic of the protein is stabilized by small-molecule binding) and *induced fit* (where a small molecule imposes a structure on the protein that is not a minimum in the absence of that molecule). They show that rotation about covalent bonds in a peptide linker can change a flexible MOF to afford nine distinct crystal structures revealing a conformational energy landscape that is characterized by multiple structural minima. For each of the nine experimentally observed systems, they optimized the host structure, observing that they converged to one of three calculated empty structures (the difference between two of them are represented with (Density Functional Theory) DFT calculations in **Figure 9b**): S-ZnGGH for the straight conformation cluster, T-ZnGGH for the twisted and F-ZnGGH for the folded. These local minima are characteristic of the ZnGGH framework itself and they are separated by energy barriers associated with the large conformational changes

within the host that characterize the three different clusters. Transition paths computed between the three calculated structures show that folding and twisting of the straight linker conformation requires crossing barriers similar on proteins. As a conclusion, the uptake of small-molecule guests by the MOF can be chemically triggered inducing the peptide to perform a conformational change. This transforms the material from a minimum on the landscape that is inactive for guest sorption to an active one. Chemical control of the conformation of a flexible organic linker offers a route to modifying the pore geometry and internal surface chemistry and thus the function of open-framework materials.

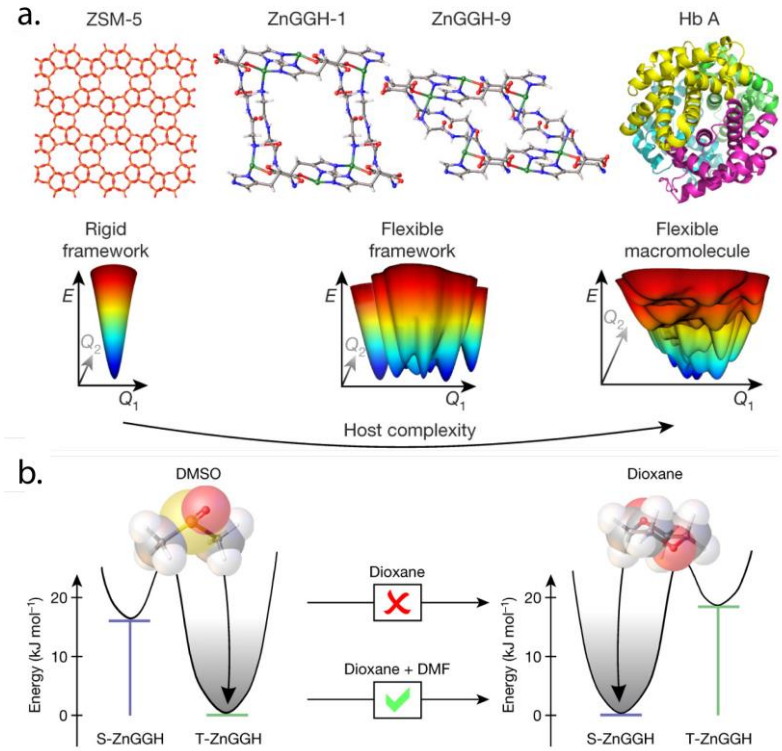

Figure 9. **a**. ZSM-5 is a rigid framework, with one minimum energy landscape, corresponding to a single conformation (left). The GGH MOF displays multiple minima, being a flexible framework it can adopt multiple conformations depending on the solvent (center). The protein HbA is a flexible macromolecule, which adopts a range of conformations to perform its biological function (right). All energy landscape are hypothetical illustrations. **b**. Calculated relative energies per linker for GGH with DMSO and dioxane in the pores. DMSO has the minimum energy in S-ZnGGH (for the straight conformation cluster) and dioxane has it on T-ZnGGH (for the twisted). Modified from [68].

There is the necessity to overcome the limits on the structural and compositional diversity of the linkers to just the natural peptides. The coordination chemistry of the terminal carboxylate and amino group prevents the formation of many well-known SBUs and restricts the number and nature of accessible topologies. On a posterior line, they have recently explored a family of linkers with an amino acid and a pyrazole to facilitate the formation of a variety of SBUs.[69] As one would expect in this type of materials, the linker addition reconfigures the global pore shape and relocates the amino acid to maximize the interaction with the guests. The family developed of flexible MOFs is the "ZnXPyr", being X= Gly, Ala. They have an unusual trefoil-shaped porosity where a pinch point connects a central channel to three peripheral pockets. Inside these pores, there is a restructuration through a linker conformational adjustment, with the objective of fit and be fitted by the guest packing. As they show in their study, the contrast in host volume change and guest uptake between solvents shows how the host-guest chemistry precisely controls the response of the whole system. This points an opportunity to construct flexible MOFs capable of strong bonding with the guest thanks to the pore reconfiguration, directing the function. Recently, the use of modified peptide chain flexibility has been recently exploited, with plenty of examples to form new flexible cavities, as macrocycles,[70] surface functionalization,[71] antimicrobial resistance[72] or to obtain new structures.[73,74]

For example, in the separation field the group of Zhang *et al*. in 2011 decided to tackle common challenges from a more biological perspective.[75] In order to improve the CO_2 capacity and selectivity there are some peptide-specific groups like -OH, -COOH or -NH_2 that can dramatically help on this task. One specific amino acid containing these groups is the serine, and they proved that the incorporation of this molecule into a MOF contributes to this aim. The two serine-based MOF that they developed proved a high selectivity and storage capacity for CO_2 over N_2 and CO at

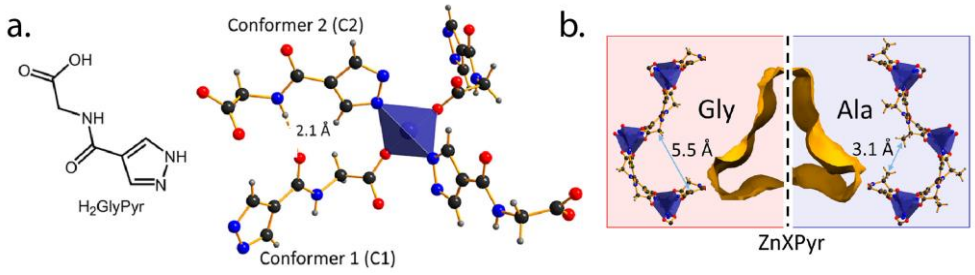

Figure 10. **a**. The linker H_2GlyPyr and the tetrahedral ZnO_2N_2 coordination environment of the Zn(II) ions in the ZnGlyPyr framework. **b**. Schematic constructed from the left-hand side of one pore of ZnGlyPyr and the right-hand side of one pore of ZnAlaPyr, illustrating the narrowing of the pinch point between the central channel and pockets produced by the Ala methyl side chain. Modified from [69].

ambient conditions. On 2020, Rosseinsky's group materialized this research in gas separation preparing a family of flexible MOFs with the structure ZnXPyr (X = Gly, Ala) (**Figure 10a**) that could selectively absorb gas molecules.[69] Possessing a structure formed by a central channel with three peripheral pockets that restructure through a linker conformational adjustment, they were able to both fit and be fitted by the guest. With some changes in the peptide composition, the structural response of the framework to guests is distinct, allowing to couple their organization in the pockets to the resulting pore volume and the overall number of guests taken (**Figure 10b**). Also, the combination is almost infinite as the linkers could be based on all amino acid residues and could be adapted to the desired molecule to separate. Any change in the linker would reconfigure the global pore shape and locally relocate the side chain to recognize chemically similar guests. They observed interesting changes in their behavior: the second guest-free structure observed only in ZnAlaPyr was stabilized by methyl-methyl interactions, allowing this MOF to absorb more toluene than the ZnGlyPyr, but less benzene. This is a clear analogy of the behavior of proteins, where the peptide composition determines a response in the final structure and to their chemical environment. Both are very similar mechanisms as the amino acid composition of the pockets of the proteins are also usually comprised of up to a few numbers of amino acids.

1.3 Proteins

Proteins are amino acid-based macromolecules that direct or participate in nearly every chemical reaction essential for life. Most proteins found in nature must adopt a specific conformation, called the folded or native state, to function properly *in vivo*. The hallmark of foldedness is the thermodynamic drive of proteins to explore an ensemble of highly structurally similar configurations that are all more or less equally competent to carry out some function by virtue of having the proper three-dimensional shape.[76] A protein's energy derives principally from van der Waals, hydrogen bonding, and electrostatic interactions both within the polypeptide chain and between the chain and its surrounding aqueous solvent. Several key properties enable proteins to participate in such a wide range of functions: (1) Proteins are formed by long polypeptide chains, with the amino acids as their fundamental units. (2) They can display an enormous variety of functional groups on their structure. (3) Proteins can interact with other biological molecules and form complex assembles. (4) Proteins are capable of displaying great flexibility.

Enzymes are a type of protein, known for being the most sophisticated catalyst designed by nature because of their high efficiency and high selectivity. The clue to achieve this result is their structure and how it folds, and it is an energetically driven process that depends on the ambient surrounding the enzyme (**Figure 11a**). Contrary to general belief, proteins are multistate rather than two-state objects.[76–78] As all proteins, they must fold to their active native state when they emerge from the ribosome and when they repeatedly unfold and refold during their lifetime. The folding process is difficult and potentially dangerous, for that reason, this process takes place in energetically favorable successive steps (shown an example in **Figure 11b**). They are composed of separately cooperative building blocks that can be seen

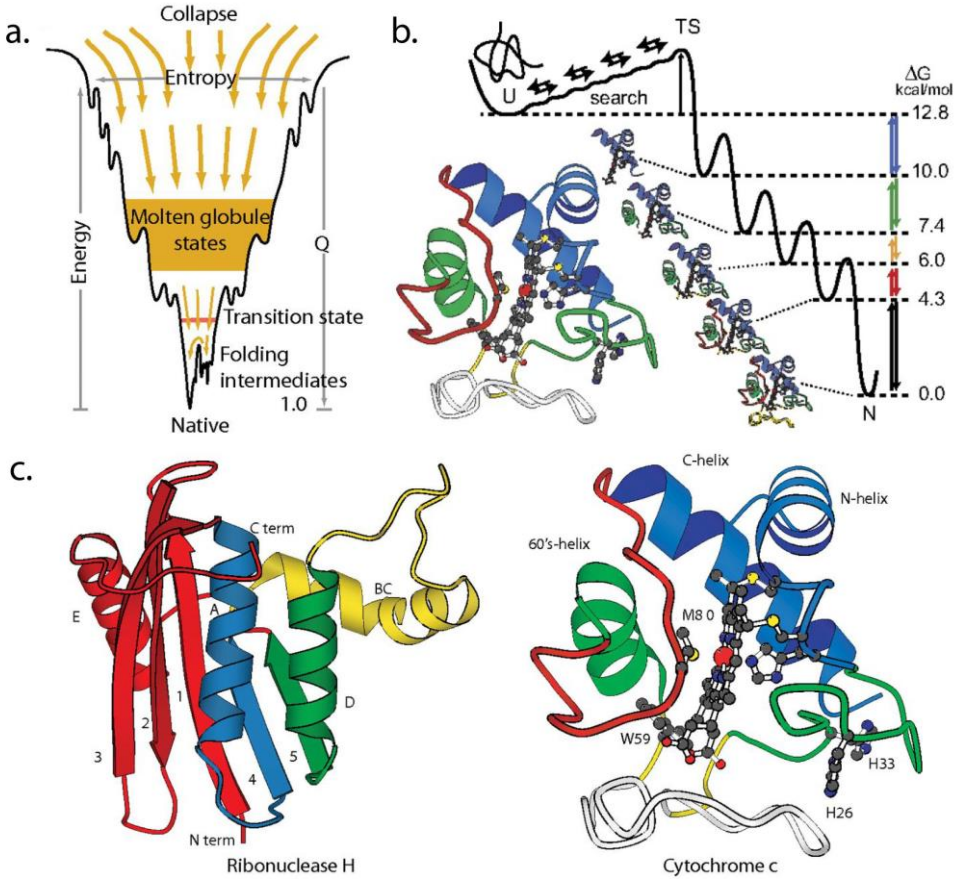

Figure 11. **a**. View of the multiple routes through a funneled landscape. **b**. Experiment shows that, under equilibrium native conditions, Cyt c unfolds by stepping energetically uphill through a ladder of forms that differ one from the next by the unfolding of one more native-like foldon. **c**. The structural composition of Ribonuclease H and Cyt c. The order of folding is blue, green, yellow, red and finally grey. Modified from [77,78].

to repeatedly unfold and refold as units even under native conditions (**Figure 11c**). The inherent drawback of enzymes, such as the difficulty in separation and purification, low tolerances to most organic solvents, poor thermal and long-term stabilities result in the low reusability and high production costs of enzymes.[79] However, because protein structure and folding pathways are energetically determined, they can be manipulated in obvious ways (mutation, solution conditions, confinement in matrix, etc.) in order to compensate or reduce these drawbacks.

For example, making use of their amino acid constituents they acquire the ability to coordinate with metal ions. There are a few examples of extended coordination frameworks constructed from the association of metal ions and enzymes as there lies an enormous difficulty in the control of the complexity and flexibility of their structure. The first examples of self-assembly of proteins with metals in order to form periodic structures involved the collagen peptides. Collagen fibers are composed of bundled triple helices consisting on three repeating Xaa-Yaa-Gly strands, with multiple applications in cells adhesion, tissue regeneration and drug delivery. Chmielewski's group manipulated the structure of collagen peptides to facilitate higher-order organization, through self-assembly strategies involving metal ions.[80–82] They showed that designed radial assembly of collagen peptide triple helices can be realized upon the addition of metal ions. This hierarchical assembly resulted in collagen peptide disks, a structure that has not been observed preiously in other higher-order collagen peptide assemblies. Furthermore, the assembly occurred in the presence of a variety of metal ions and was reversible upon the addition of EDTA.

The potential to incoorporate many design parameters including additional assembly signals for further three-dimensional growth, directed degradation, cell adhesiveness, and release of protein/small molecule therapies resides in the study of protein assembly. Implementing this, in 2014, the group of Jiang reported the synthesis of a protein crystalline framework (PCF).[83] The homotetrameric lectin concanavalin A is crosslinked by predetermined inducing ligands containing monosaccharide and rhodamine groups connected by a spacer. Either interpenetrating or non-interpenetrating frameworks were obtained, and they were controlled by the spacer length of the inducing ligand. Protein crystalline frameworks are attractive for biomimetic and nanothecnological studies because they could augment the useful functionalities of numerous proteins through dense packing and uniform orientation, even if their formation and structural control are challenging aspects. PCFs strongly resemble MOFs, as they both are porous structures with a backbone of functional organic compounds connected with ligand-metal interactions, and have become a growing field in materials science. Crystallographic analysis revealed that the framework formation was promoted by the inducing ligand via dual

supramolecular interactions and that the protein-protein contact within the framework is limited, forming an interpenetrating structure.

Recently, Zhao's group constructed 2D and 3D protein frameworks in solution by using a combination of the relatively weak His-His interaction and Ni^{2+}-participated metal coordination with Glu residues from two adjacent protein nanocages.[84,85] These findings open up a new way of organizing building blocks into 3D protein crystalline frameworks (**Figure 12a-b**). They were interested in the construction of well-organized protein arrays involved by intermolar aromatic interactions such as His-His interactions because they are reversible, chemically tunable, easily designed and engineered. By incorporation of metal coordination between two adjacent protein molecules as guided by the crystal structure of His mutation ferritin, they were able to construct 3D porous protein nanocage arrays in solution (**Figure 12c**). Side chains of amino acid residues located in the exterior surface of protein nanocages are directly involved in protein-protein interactions at

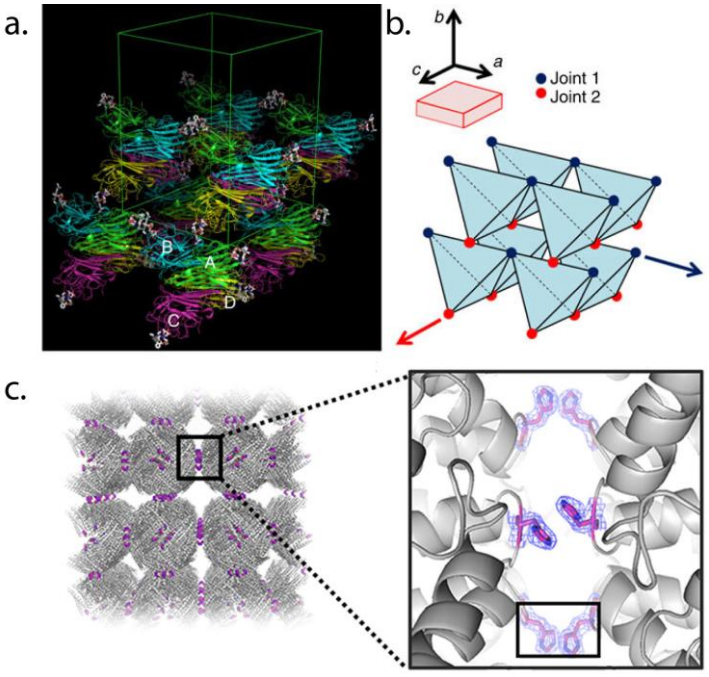

Figure 12. **a**. Packing assembly, the four monomers are represented with different colors. The interaction sites are labelled with letter A-D. **b**. Same packing mode simplified. The selected layer represents the macroscopic form of the assembly, and the coordinate corresponds to that of the metal coordinated packing models. **c**. Assembly of ferritin into simple cubic packing in the crystal structure, and closeup of the four engineered His-induced μ–μ stacking interactions between residues. Modified from [83] and [85].

the interfaces, making biological incorporation of specific amino acids into site-selective protein interfaces an effective method for controlling protein assembly.

There have been some other examples reported by Tezcan's group,[86–88] involving protein-protein interactions through metal coordination, but the complexity of enzymes prove this as a challenge.[88–90] . They recently reported the construction and characterization of a large library of 3D, crystalline protein-MOFs through a combination of three different metallo-ferritin nodes and five synthetic linkers bearing hydroxamate head groups.[91] Their results stablish that the metal ion and the synthetic linker components can be varied in a modular fashion to influence the structural parameters of protein-MOFs. Despite the remarkable size discrepancy between the ferritin nodes and the organic linkers, the self-assembly of the ferritin-MOFs is highly robust, emphasizing the utility of the metal coordination interactions in controlling protein self-assembly. Moreover, by virtue of the flexibility of the linkers and the lability of metal-linker bonds, several ferritin-MOFs have been observed to adopt multiple lattice conformations, which may suggest dynamic behavior. Porous carriers can also have additional benefits for protein stabilization through their immobilization inside their cavities. The concave curvature of the pore increases the contact surface and the binding sites with globular protein structures compared to flat surfaces.[92] Leaching is reduced in porous materials, owing to diffusion restrictions of the proteins out of the pore system. The spatial separation inside the pores prevents the proteins from deactivation by fouling, distortion by gas bubbles, autolysis, and aggregation.[93,94] The immobilization of enzymes can address the inherent drawbacks, as using biocompatible carriers can help shield enzymes from deactivating conditions, and enhance their recyclability.

2. Applications

As stated before, the structural tunability of MOFs allows for precise placement of functional groups in the framework. As a result, tailored pore environments at the molecular level can be attained through judicious choices of building blocks. For that reason, MOFs have been studied for both fundamental interests and practical applications including heterogeneous catalysis, separation, drug delivery and biomedical applications.[95–99] However, when applied into biologically-related fields, biological toxicity should be considered first. The toxicity of MOFs depends on several parameters such as applications, the kinetics of degradation, bio-distribution, accumulation in tissues and organs, excretion from the body, and so on. Many potential applications of MOFs may require them to be constructed from benign building blocks that are biologically and environmentally compatible. Biological

applications usually require non-toxic MOF materials, for example on drug delivery or intracellular imaging. Moreover, most applications will require bulk quantities of MOFs and to reduce their environmental impact bulk MOF should be either environmentally compatible or easily recyclable.

We focused on three of the biggest classifications on biologically MOF applications, being the first based in the catalysis. Catalysts based upon biologically-based MOFs stand out as they not only take advantages of the desirable features of these materials like tunability and regular catalytic sites, but also are capable of remaining robust and effective throughout the process. Besides the high metal content, one of their greatest advantages is that the active sites are rarely different because of the highly crystalline nature of the material. However, despite their rich chemistry, catalysis with this type of MOFs is scarce.

Adsorption is the second big group, and one of the most effective processes to take up specific compounds from liquid or gas phases. It is generally preferred to the other separation methods because of the ease in operation, great efficiency and cost effectiveness. Currently, most commercially used adsorbents include activated carbon, mesoporous silica and zeolites. MOFs have shown huge potential in adsorption-related applications,[100] as hybrids of inorganic and organic materials they are associated with milder synthesis conditions. With a great availability of various configurations and structures, as well as higher porosity and surface area, MOFs are expected to be high-capacity adsorbents. The ability to chemically modify the pore surface of MOFs through pre- and post- synthetic introduction of functional groups, combined with the potential for the formation of open metal coordination sites, can also provide the means to tailor internal surfaces for applications related to gas separation and storage. Compared with other frequently used ligands for MOF synthesis, biologically related ligands offer the potential to utilize multiple coordination sites, and contain a variety of functional groups. In addition to these chemical factors, the geometric features such as pore size and shape, surface area, and pore volume also play important roles in sorption energetics and uptake capacity.

Enzymes are one of the most important and studied macromolecules in nature, far exceeding the efficiency of the artificial catalysts in their ability to catalyze biological processes. For that reason, applying *in vivo* enzymatic transformation to industrial applications is an attractive strategy. However, these possible applications are hindered by the fragile nature, low thermal stability, narrow pH ranges and general instability of the enzymes.[101] For that reason, the third big group of applications is based on producing MOF-enzyme composites. The combination of enzymes and MOFs into one composite can combine both principle properties into one system without compromise. In this system, the MOF will become a stabilizing

microenvironment to protect enzymatic performance by controlling the properties of the pore, allowing the enzyme to perform their function in an improve manner.[102] The high loading capacity and tunable pore environment could dramatically improve enzymatic catalysis, protecting the enzyme from denaturation factor and preventing leaching.

2.1 Biomimetic Catalysis

Just as in all other fields of scientific research, a lot of innovations in catalysis are inspired from nature. Generally, biomimetic catalysis refers to chemical catalysis that mimics key features of enzymes.[103,104] Enzymes are natural catalysts capable of high reactivity, selectivity, and specificity under mild conditions, contributing to green and sustainable processes in chemical, pharmaceutical, and food industries. In a natural enzymatic system the structure of the protein is constructed to precisely control the function, leading to the excellent catalytic efficiency. Therefore, the performance of biomimetic catalysts can rarely keep up with their natural enzyme counterparts due to the low structural tunability and complexity (**Figure 13a**). MOFs are able to mimic the rich pore environment of enzymes and develop that high performance (**Figure 13b**).[105,106]

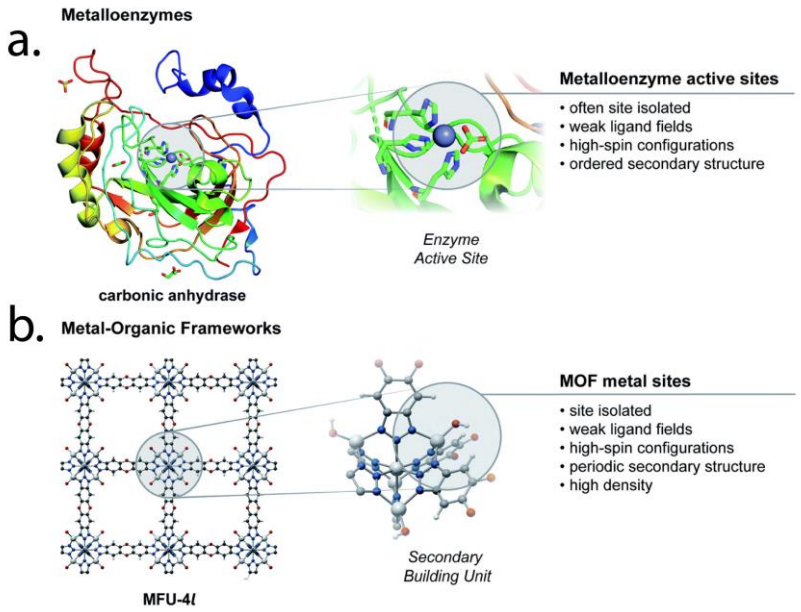

Figure 13. **a** and **b**. Comparison of properties between metalloenzyme actives sites and metal sites in metal–organic frameworks. Modified from [105].

In general there are three types of MOF-based biomimetic catalysts: the first (I) incorporates an uncoordinated site at one of the metal atoms in the inorganic cornerstone, they can also (II) build the active site into the linker mimicking the enzyme active site, and lastly (III) directly incorporate the enzyme inside the MOF. The structural diversity and tunability of MOFs enable all their components (nodes, linkers and pores) to be personalized and adapted to a certain catalytic reaction (depicted in **Figure 14**).[107] The **type I** biomimetic catalysis can be accounted due to the intrinsic nature of the MOFs, as one or more of the coordinative positions around the metallic elements are not usually compromised with the construction of the lattice. Moreover, there are examples of MOFs of almost all di-, tri- or tetrapositive metal ions of the Periodic Table and a large diversity in the structure and binding groups of the organic linker. These "free" positions are typically occupied by solvent molecules and can be frequently evacuated upon heating the MOF at moderate temperatures under vacuum, generating Lewis acid sites and coordinatively unsaturated sites (CUS) around the metal ions.[108] Some studies point UiO-66 as an attractive catalyst for the hydrolysis of methyl paraoxon. This performance can be attributed to the Zr cluster being capable of functionally mimic the binuclear Zn(II) active site of the phosphotriesterase.[109]

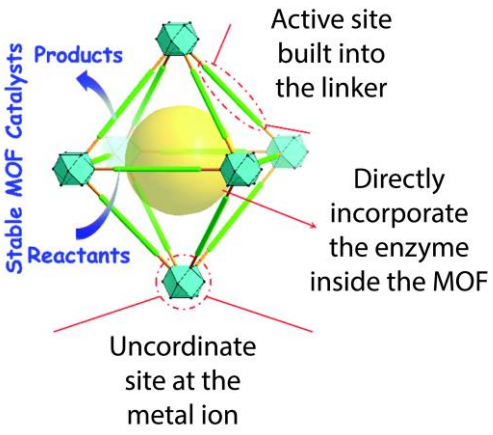

Figure 14. Classification of different positions in MOF materials where catalytic reactions can take place. Modified from [107].

In the **type II** of catalysis, the ligand is used to anchor to the lattice some active sites such as Brönster acid sites[110], basic sites[111] or additional binding centers that can participate in the formation of metallic complexes at peripheral positions respect to the solid lattice that can introduce some specific catalytic activity. A perfect example of this strategy displayed by the group of Hong-Cai Zhou with the use of the PCN-222(Fe) [112], achieving an outstanding peroxidase-like oxidation reaction in which pyrogallol is oxidized to purpurogallin imitating the hydrogen peroxide. Another example used previously was centered on the MOF-818 as a nano-enzyme derivative in order to improve the reaction without the downside of the free enzyme. MOF-818 has good specificity and high catalytic activity as a novel catechol oxidase nanozyme, due to the containing trinuclear copper centers mimicking the active sites of natural catechol oxidase[113]. In **Figure 15a-b** can be seen the use of the enzymes as analogue of metalloenzymes. The type II has long been recognized as there is a great similarity

between MOF SBUs and enzyme active sites, but the practical challenges associated with hydrolytic stability and incorporation of redox active ions at the SBU has impeded this area.[114] Although the similarity between MOF SBUs and enzyme active sites has long been recognized (**Figure 15c**), the use of SBUs for inner-sphere small molecule chemistry is a relatively recent development. Although it is currently not widely used in the context of biomimetic chemistry, changing the secondary structural properties of the MOF through substitution on the organic linker can directly impact the reaction outcome and selectivity.[115,116] One potential benefit of using MOFs to functionally mimic metalloenzymes is the control over environmental components such as hydrophilicity. In principle, bioactive organic ligands such as amino acids[117,118], nucleotides[27,33,118], peptides[117,119] and other molecules[120,121] are also good candidates to serve as the ligands for the synthesis of MOFs with potential favorable features for bio-functions, such as biocatalysis, chirality, and highly selective substrate-binding ability. Usually they are prepared by using non-catalytic

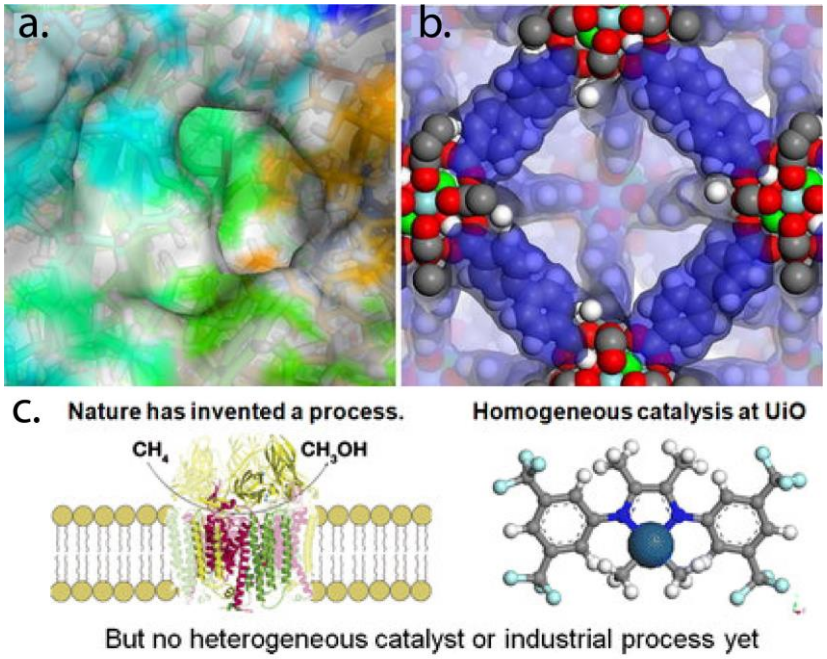

Figure 15. **a**. The cavity around the active site in the anhydrase enzyme. **b**. The surface in the octahedral cage of the UiO-67 MOF structure. The internal surface of MOF based nanoporous materials have more similarities to enzyme surfaces, compared to oxide based surface of zeolites and related oxide based microporous materials. **c**. Soft oxidation of methane to methanol is a reaction that has a known enzyme catalyst (left). Among several homogenous catalysts, the most active metal organic complex for soft activation of methane is depicted (right). Modified from [38].

ligands and using a post-synthetic modification to provide catalytically active sites to them. This also helps to prevent further incompatibility issues with the crystallization, as even minor linker substitutions can prevent or enhance MOF crystallization.[122] One good example in this regard is the PSM (Post-Synthetic Modification) of MIL-101, it is chemically and thermally robust and has big pores. The addition of L-proline was performed, as this aa and its derivatives are well-known asymmetric organocatalysts. This accelerates enantioselective asymmetric organic reactions, like the Michael reactions,[123] showing remarkable catalytic activities in asymmetric aldol reactions including much higher enantioselectivity than the chiral ligand themselves. A more recent use by the Wang group, a Rh-Ru@MIL-101-NH_2 composite where the immobilization using carboxylated functionalized complexes gave rise to enhanced host-guest interactions and prevented the leaching.[124] In a posterior publication, they also demonstrate the use of a proline functionalized NH_2-UiO-66 in order to perform a Suzuki coupling reaction. [125] More recently, Martí-

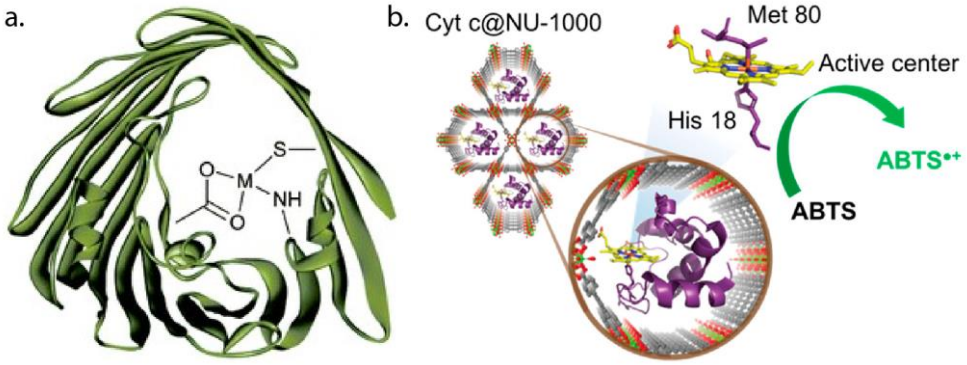

Figure 16. **a**. Schematic of an active site within a metalloenzyme. **b**. Schematic illustration of Cyt c encapsulated in the mesopores of MOF NU-1000 and its oxidation of ABTS. Modified from [127,130].

Gastaldo's group developed a titanium-calcium bimetallic MOF used to direct selective grafting of amines. This enabled the combination of Lewis acid titanium center and amines for cooperative cycloaddition of CO_2 to epoxides, with great efficiency. They achieved a selective grafting of molecules to heterometallic clusters for definitive control of pore chemistry.[126]

Finally, in **type III** of biomimetic catalysts, catalytic species can be encapsulated into MOFs either during the synthesis of MOFs or through PSM. For the one-pot strategy, all the starting materials and the catalytically active components are combined in one reaction system. The catalytic component will be encapsulated into the MOF structure during the crystal formation process. Most commonly, the introduced molecule is a metalloenzyme. They are lengthy proteins that contain a small metal complex in the active site that is coordinated by amino acids from the

protein scaffold. The amino acids stabilize and isolate the metal active-center (as depicted in **Figure 16a**) providing a specific binding pocket for particular substrates to attach.[127]

Understanding the nature and the coordination sphere of the active metal center in a metalloenzyme provides valuable insights for producing functional enzyme mimics. Thus, exposed metal sites can provide relatively strong host-guest interactions whose strengths can be varied through the type of metal ions and MOFs offer a platform for cooperatively binding to one or more guest species. In the first example, the Huo's group tried in 2014 to employ an agarose hydrogel droplet Pickering-stabilized by UiO-66 and magnetite nanoparticles as a template. Around this gel they deposited a hierarchically structure ZIF-8 shell for size-selective biocatalysis. This increased the turnover of the transesterification reactions performed by the lipase immobilized, with a immobilized concentration of up to 30%.[128] In 2019, Farha and coworkers encapsulated a Formate dehydrogenase from yeast inside the NU-1006, enhancing its biological fixation of CO_2.[129] The encapsulated enzyme exhibited enhanced activity for the generation of NAD+ from NADH, a critical step in the CO_2 fixation and also the NADH could be regenerated using a Rh-FTO glass electrode. The coupling of these reactions paves the way for the design of more efficient electro-enzymatic reaction systems. They also encapsulated Cytochrome c in NU-1000 in order to improve the oxidation of ABTS (2,2'-azino-bis(3-ethylbenzothiazoline-6-sulfonic acid)), explained (**Figure 16b**) by an enhanced accessibility of the active center to reaction substrates as a result of that encapsulation.[130]

2.2 Enantioselective Separation

Separation processes play significant roles in industry and daily life and are used for three primary functions: concentration, fractionation and purification.[131] Chiral separations represent one of the most difficult of preparative and analytical separations because enantiomers have identical physical and chemical properties and most separation methods tend to rely on differences in boiling points or solubilities.[132] Enantiomers can be profoundly different by exhibiting exactly opposite biological activities, pharmacology and toxicities. Commercial Chiral Stationary Phases (CSPs) are typically based upon polymer composites that incorporate components with chiral recognition features such as polysaccharide or β-cyclodextrin.[133] Unfortunately, the current generation of CSPs are expensive to manufacture, lack versatility across all types of chiral analytes, and tend to exhibit poor robustness (**Figure 17a**). The modular synthesis and numerous choice of

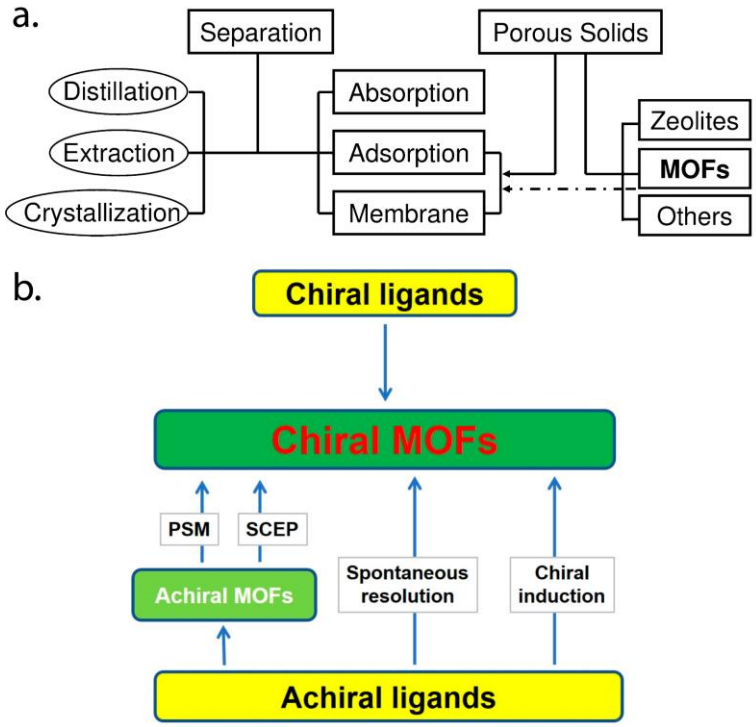

Figure 17. **a**. Separation methods and applications of porous solids acting as the supporting medium in separations. **b**. Schematic representation of the classification of the synthetic strategies of chiral MOFs. Modified from [131,133].

inorganic and organic building blocks make them useful for an unlimited number of separation applications. They are amenable to the introduction of a variety of functional sites, either on the framework or within cavities and channels, to allow a high degree of control over host-guest interactions, sometimes in a cooperative and long-range manner.

Using the same building blocks that give enzymes their rich functionalities, the group of Liu in 2015 synthetized a homochiral MOF based on a D-camphoric acid and a planar Mn_4O cluster for the separation of (±)-ibuprofen.[134] Ibuprofen is an important nonsteroidal anti-inflammatory drug, in which the (+)-ibuprofen has been reported as 160 times more active than its counterpart, thus the separation of both would improve its selectivity and potency. With a hexane-isopropyl alcohol system they confirmed this system to be a suitable mobile phase for enantioseparation, with the retention factor slightly increasing with the column pressure. Besides the D-cam groups, planar Mn_4O clusters having 222 symmetry can also provide homochiral environments. As far as noncovalent interactions are concerned, hydrogen-bonding

and electrostatic interactions should be dominated. Improving the separation of ibuprofen, Galán-Mascarós' group in 2019 developed a porous, robust homochiral MOF named TAMOF-1,[135] built from copper(II) and a linker derived from L-histidine. The scaffold was obtained from the functionalization of the natural amino acid L-histidine with a 4H-1,2,4-triazole moiety, by transformation of its -NH_2 group, yielding an enantiopure ligand that self-assembles with Cu(II) cations in water to build a porous 3D structure. Due to the robust structure that it is capable of display with 1nm-wide channels, TAMOF-1 works as a highly versatile chiral resolutive agent for the separation of organic molecules in either polar or nonpolar solvent conditions, allowing for the alternative/successive use of either of them on HPLC (High-performance liquid chromatography) conditions.

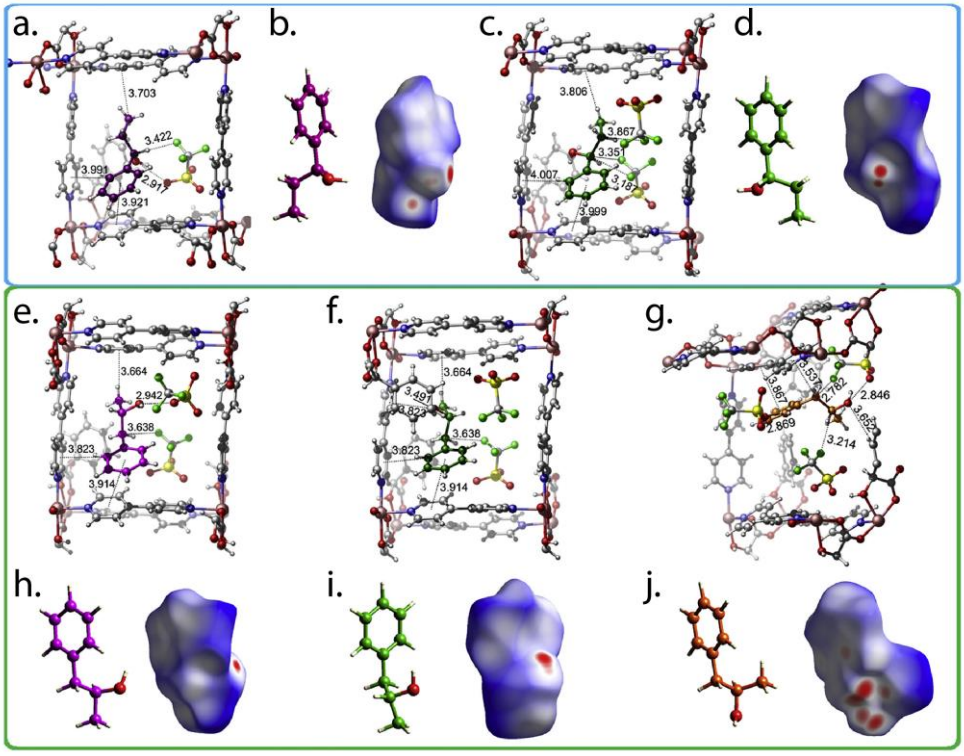

Figure 18. Chiral Binding Sites in CMOM-3S determined by SCXRD. **a**-**d** The binding sites for 1-phenyl-1-propanol and **e**-**j** 1-phenyl-2-propanol, sustained by a plethora of intermolecular interactions. Shown are interactions of position-disordered 1P1P molecules and1P2P molecules in the cavity of CMOM-3S, as well as absolute configuration and corresponding Hirshfeld surface of 1P1P molecules and1P2P molecules. Modified from [137].

Other approach to this problem is to abandon the 3D-based structure and open a new functionality in the form of membranes. Membrane-based separation has emerged as a promising candidate for chiral separation due to its potential advantages including low operating cost, high capacity, and ease of scalability. One of the first examples was developed by Jiang's group, where they created a homochiral Zn-BLD membrane capable of achieving a 33% of enrichment between enantiomers.[136] Experimental and simulation results revealed that the intrinsic separation mechanism of the Zn-BLD membrane is attributed to the different interactions of the two enantiomers with the inner pores. This differential interaction was also studied by the group of Zaworotko in 2017,[137] showing that CMOM-3S serves as a general-purpose CSP and that the adaptable molecular recognition sites are able to mimic enzyme-binding sites (**Figure 18**). The tight stereospecific binding sites are the driving force for chiral and achiral guest molecules. When coupled with the thermal and hydrolytic stability this serves as a CSP more versatile and robust than the current benchmark commercial columns. This outstanding result is also linked to the highly crystalline nature and low-symmetry space group of CMOM-3S that enables determination of the absolute configuration of chiral guest molecules without the need for a reference standard. The better performance is believed to come from the softer character of Fe2+ relative to Mg^{2+}, leading to a stronger interaction with the π electron cloud of the olefin. In this workflow can also be classified by the group of Tang in 2018. [138] Inspired by the classic β-sheet structures assembled by chiral polypeptide chains, they suggest the design of 1D helical metal-organic chains as the basic buildings blocks of a chiral MOF, as the interchain hydrogen-bonding interactions could lead to the formation of 3D layers via weak interlayer foundation. This system was created with chiral amino acids and Zn-$(CH_3COO)_2$ in water to obtain MOF crystals, being chelated with a monodentate carbonate and an amine group from the first chiral linker to from a five-member ring. One H_2O molecule and one chloride ion block the extension along the other axis, maintaining a 2D structure.

Stoddart's CD-MOF-1 was able to act as a separation medium,[139] distinguishing itself from the majority of previous MOFs investigated for their use as stationary-phase materials in separations. In addition to the experimentally observed separations, quantum mechanical calculations and Grand Canonical Monte Carlo (GCMC) simulations were employed in order to predict the possible mechanisms through which this separation takes place. The calculations suggested that the separation of styrene and ethylbenzene may be driven by differences in the noncovalent bonding interactions. Although in the case of larger halogens it is likely that the size limitations imposed by the dimensions of the framework act in such a way as to prevent the achievement of the most favorable orientations for noncovalent bonding interactions. Another similar example with cyclodextrin MOF was developed

by Yan in 2017[140] giving an efficient CSP for HPLC separation of chiral aromatic alcohols. The system provided a good precision, selectivity and resolution for the separation of chiral aromatic alcohols. The quality of the separation highly depended on the environment and the hydrophobic-hydrophilic interactions.

Another approach to this problem is the use of mixed matrix membranes (MMMs) that combine the advantages of a polymeric matrix and the molecular selectivity of microporous materials. Wang in 2019 prepared and characterized a homochiral MIL-53-based MMMs which could generate superior performance for separation of chiral molecules by the simple combination of a L-His-functionalization (process depicted in **Figure 19a**). [141] This system demonstrated enantioselective adsorption for racemic 1-phenylethanol with a peak value of 100% of enantiomeric enrichment during the initial stage of permeation (**Figure 19b**). Analysis of enantioselective adsorption and permeation selectivity of racemic 2-phenyl-ethanol suggests a concentration

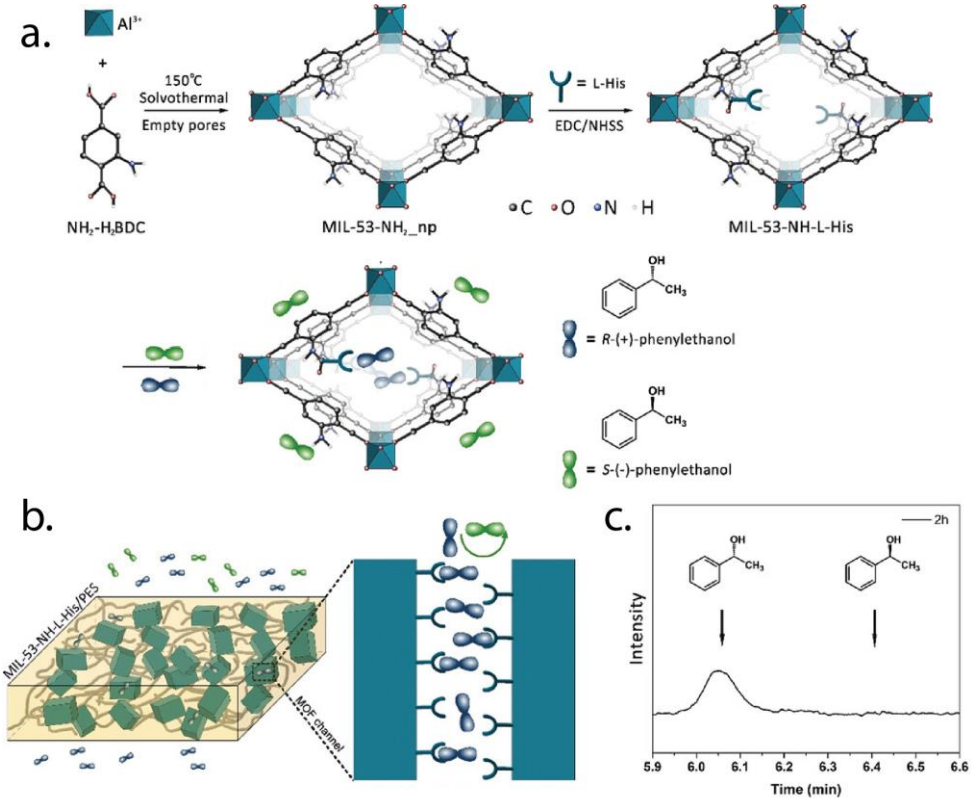

Figure 19. **a**. Fabrication and characterization of amino acid-functionalized MOF nanocrystals. **b**. Schematic illustration of the selective transport of the enantiomers through the MIL-53-NH-l-His channel. **c**. Gas chromatograms of resolved after 2 hours of separation. Modified from [141].

gradient driven facilitated transport mechanism for MIL-53-NH-L-His-based MMMs (**Figure 19c**).

Not only the presence of a linker can affect the separation of molecules, also the defects in the structure can take a part in this matter. As studied by Ladewing in 2017,[142] they introduced missing linker defects into a homochiral MOF based in L-lactic acid and observed an increase in enantiomeric excess for 1-phenylethanol of 35% with the defective frameworks. This showed how the disappearance of part of the linker, which also increases the porosity of the framework, increases partially the pore size and provides a better fit for the guest molecules. Molecules smaller that fitted perfectly in the pristine and defective MOF were not affected in the separation procedure.

2.3 Immobilization

Immobilization of enzymes on a solid support can enhance their stability as well as facilitate ease of separation and recovery for reuse while maintaining activity and selectivity. Great efforts have been made to search suitable supports for enzyme immobilization, and silica materials offering high surface areas and mesopores have attracted the most attention. However, the leaching of the adsorbed enzyme is still often observed during the reaction process due to the weak interactions between molecules and silica supports. The tunable but uniform pore sizes and functionalizable pore walls of porous MOFs may make them appealing to accommodate enzymes for catalytic applications. The designable functionality and excellent thermal stability of MOFs also affords the huge potentials of enzyme@MOF in different applications. Typically, the strategies of enzyme immobilization with MOFs comprise three major categories: **type I** surface immobilization, **type II** post-synthetic infiltration and **type III** in situ encapsulation.

In the **type I** surface immobilization, the most straightforward method, the enzyme is anchored through physical adsorption (van der Waals bonds, pi-pi staking, hydrophobic forces, electrostatic interactions or hydrogen-bonding), being the less time-consuming method. This technique has also the advantage that the chosen MOF does not need to have a characteristic loading capacity,[128,143] also including the chemical cross-linking that attaches covalently to the MOF with a post-synthesis modification.[144] This means that a very broad range of MOFs can be employed as the immobilization matrix due to the non-specific nature of the interactions. Another positive remark is that this method allows the MOFs to be pre-synthesized under conditions that exceed the denaturation ranges of the immobilized enzymes and there is no strict requirement on the pore size of MOFs. One of the first examples of

this type of immobilization was performed by Balkus.[145] They immobilized Microperoxidase-11 (MP-11) in a CuMOF with 17.8 nm pores that adsorbed the protein. They had previously immobilized enzymes in silica,[146] but this was the first example in a MOF, with an adsorption of around 67% of the MP-11 from the solution monitored by UV-Vis spectroscopy. The enzyme retained its activity and was considerably more active.

Enzymes can also be anchored by chemical bioconjugation as demonstrated by Park *et al*. in 2011,[147] using the linking groups in the MOF. Using pendent carboxylate groups present on the surface of MOFs, they activate and modify them for the conjugation to the enzyme. This technique allows the conjugation of proteins to coordination polymers or MOFs indifferently of their structural architectures. As a first choice enhanced green fluorescent protein (EGFP) was selected because its presence and the folding status can be easily tracked by fluorescence microscopy. One year later, the group of Lin also used a similar approach to immobilized a trypsin into the MIL88B-NH_2(Cr) used to digest BSA protein.[144] The preparation of trypsin-FITC@MOF consisted on a simple 30 min vortex-assisted host-guest interaction (**Figure 20a**), and it is a very good example of how quick this type of immobilization can actually be.[143] As said before, the strong point of the surface functionalization resides in the easy binding to the crystalline microporous MOF material, as there is no need for chemical modification of the MOF surface or enzyme macromolecule. Again with a vortex-assisted adsorption, Huan *et al*. formed porcine lipase@MOF particles that provided an exceptional catalytic ability and reusability especially when using carbonized MOFs or hydrophobic MOFs as solid supports.[143]

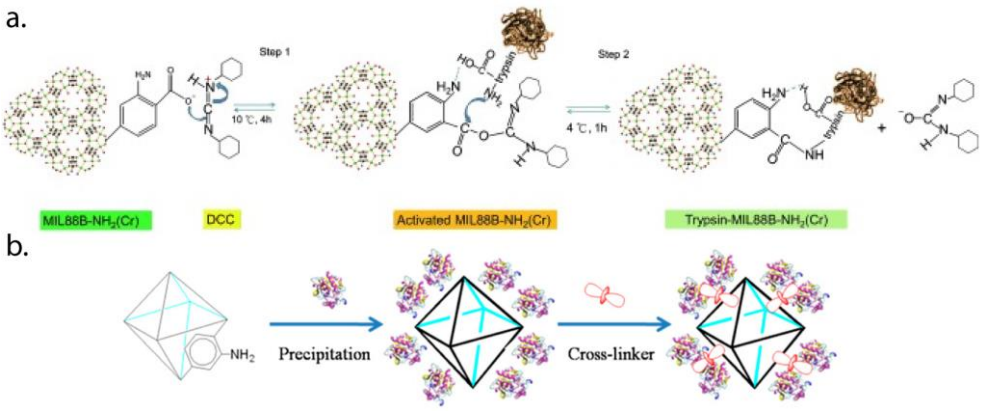

Figure 20. **a** Trypsin immobilization onto DCC-activated MOFs. **b**. Illustration of the synthesis of the Immobilization of SEH onto UiO-66-NH_2. Modified from [144,148].

Lastly, Lou *et al*. immobilized soybean epoxide hydrolase (SEH) in UiO-66-NH_2 (**Figure 20b**) with a high loading of 87.3 mg/g and enzyme activity recovery (88.0%).[148] The novel SEH@UiO-66-NH_2 greatly surpassed the free SHE with respect to pH stability, thermostability, and tolerance to organic solvents. It also manifested markedly enhanced enzyme-substrate affinity and catalytic efficiency compared to free SEH, with a lower Km value and increased $V_{max/km}$ value. The aforementioned works revealed that enzymes adsorbed onto the surface of MOFs have great application potentiality in biocatalysis and biosensors. Although surface immobilization provides a simple and convenient method, it does not take full advantage of the high porosity of MOFs, resulting in low loading efficiency and limited protection against enzymatic denaturation of the obtained enzymes-MOFs materials.

Protein transport is an essential mechanism in living cells. In order for the protein to enter the organelle, it must undergo significant conformational changes during the translocation process. The biological mechanism associated with protein transport through membranes suggests a pathway through which proteins could also be transported through porous solid-state materials,[149] including MOFs. This concept opened the path for the **type II** post-synthetic infiltration of enzymes inside MOFs. It is an efficient approach to incorporate enzymes into MOFs, with minimum chemical and structural disturbance of the enzymes during the immobilization, as well as high loading capacity, resulting from the sufficient use of the high porosity of MOFs. Compared with surface immobilization, enzymes are physically adsorbed into the cavity instead of dangling on the surfaces, contributing to enhanced stability and apparently less leaching of enzymes. It is worth noting that elaborately designed pore structure that complementary to the 3D size of enzymes, is required.

In 2011 Ma *et al.* published one of the earliest enzyme encapsulation examples in MOFs.[150] The immobilization of MP-11 into a mesoporous MOF named Tb-mesoMOF was performed simply mixing both compounds in HEPES buffer in an incubator for 2 days (**Figure 21a**). The change of color of the crystals from white to dark red indicated the saturation of enzyme inside its pores. MP-11 is well-known to conduct peroxidation of organic molecules by the use of hydrogen peroxide. Free MP-11 had a 10 times quicker initial rate of conversion, however it tends to aggregate in solution leading to a less accessibility for the heme, adversely affecting its activity. Immobilization in a suitable host material prevents aggregation, renders the heme more accessible to substrates, and allows a broad range of solution conditions. The immobilization into the MOF also rendered an excellent recyclability property, as the free enzyme only lasted one cycle, the MCM-41@MP-11 for 2 cycles and the Tb-mesoMOF@MP-11 for up to 7 cycles. They also extended this study to the immobilization of myoglobin on Tb-mesoMOF.[151] To study how the proteins are able to enter inside the pores of the MOFs they employed cytochrome c to provide fluorescence microscopy signal.[94] The successful immobilization of Cyt c into the

interior of the Tb-mesoMOF could only take place if the protein underwent a conformational change that reduced the overall dimensions of the protein, allowing migration through the open pores at the crystal surface. The data supported the translocation of the Cyt c into the Tb-mesoMOF in which Cyt c molecules first adsorb onto the surface of the MOF crystals. The partially unfolded protein can adopt a size and an orientation that is more amenable to migration through the surface pore, leading to partitioning of the protein between the surface and the exterior nanopores. At longer incubation times, the protein continues to be partitioned into the interior cavities through the relative small pores of the MOF and is stabilized through the exposure of hydrophobic amino acids from the protein's interior to the hydrophobic interior of the Tb-mesoMOF cavities, resulting in a new protein conformation exhibiting a distinct fluorescence emission. The interactions between the enzyme and MOF are primarily π-π interactions between the heme and conjugated triazine and benzene rings of the TATB (triaminotrinitrobenzene) ligand. These strong interactions prevent the leaching of MP-11 from Tb-mesoMOF.[94] This explains why the enzyme was not leaching from the MOF but it does from the silicas.

More recently, in 2017, they studied how a COF can fit lipase differently in its pores, and how the interior of the pores affects the enzymatic activity.[152] Besides mesoporous MOFs with cage cavities, those possessing very large channel cavities are also used as platforms for enzyme immobilization. Yaghi et. al synthetized a large pore family of MOFs named IRMOF-74 series, by systematically expanding the MOF-74 structure. They have pore apertures ranging from 1.4 to 9.8 nm with non-interpenetrating structures and exhibiting robust architectures, as evidenced by their permanent porosity with high thermal stability. The large choice of building blocks means that the structures and pore characteristics of the metal-organic frameworks can be tuned relatively easily, however it remains a challenge to prepare frameworks specifically tailored for particular applications. Using computational modelling on a well-know NU-1000,[153] the Feng's group brought the immobilization of enzymes into gradually bigger pores of MOFs. With a number of strategies including creation of open metal sites and implantation of Lewis base sites, they were able to tune host-guest interactions.[154] In addition to these chemical factors, the geometric features such as pore size and shape, surface area, and pore volume also play important roles in sorption energetics and uptake capacity.

Mesoporous MOFs with even larger hierarchical mesoporous cavities have been rationally designed and prepared for more complicated enzyme immobilization.[155] Zhou's group published first in 2015 the use of the MOF PCN-333 for the encapsulation of three enzymes with different sizes, horseradish peroxidase (HRP), cytochrome c (Cyt c) and microperoxidase-11 (MP-11).[156] PCN-333 exhibited one of the highest void volumes among all reported MOFs (example in **Figure 21b**). This system was the result of a detailed work that the group had been making in previous

years and it has an extraordinarily large pore size and excellent chemical stability.[104,157] The free enzyme reacts more quickly than the encapsulated enzymes, though it requires significantly more concentration of substrate to reach its peak rate, under carefully controlled conditions designed to prevent it from being aggregated or denatured. After the completion of each catalytic reaction, the immobilized enzymes were then recycled by a simple centrifuge. The catalytic reactivity remains almost unchanged for all enzymes after several cycles. The main reason for the good recyclability is that there is almost no leaching, this rate is thermodynamically related

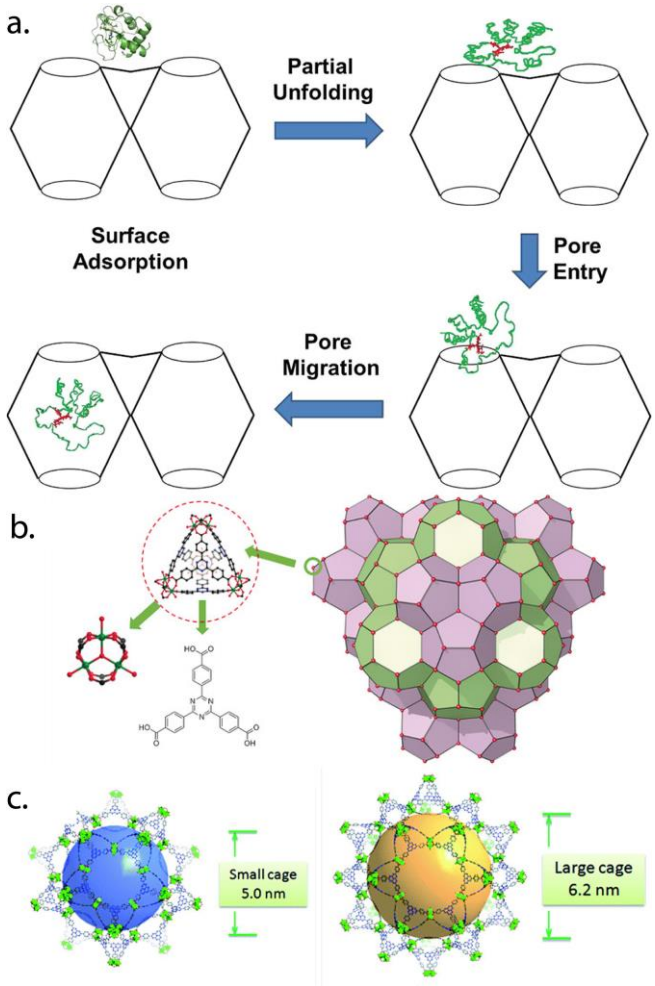

Figure 21. **a**. Mechanism for the Translocation of Cyt c into the Cavities of Tb-mesoMOF. **b**. Structure of PCN-333. **c**. The small cage and large cage of PCN-888 composed of the super tetrahedron in a vertex sharing manner. Modified from [93,159,161].

to the interaction strength between the enzyme and the support.[158] Physisorption is usually much weaker than covalent immobilization. However, when there are many interaction sites such as in the case of encapsulation, the overall interaction strength can be stronger than a single covalent bond. This concept was improved with the PCN-888 with the coupling of two different enzymes to form a tandem nanoreactor.[159] In this work the same design approach is applied with a much more sophisticated problem – coupling two enzymes in a tandem manner with a precise control of the distribution of each enzyme in the nanoreactor. The smallest cage is too compact for either enzyme (**Figure 21c**), thus It is left empty as a diffusion pathway for substrates and products. PCN-888 also lacks leaching of enzyme, whereas the catalytic activity of the encapsulated enzymes is well maintained. This nanoreactor also shows a convincing reusability and outstanding stability against the digestion of trypsin, indicating its potential applications for *in vitro* or *in vivo* studies. The largest cage and the medium cage can only accommodate one molecule of GOx (Glucose Oxidase) and HRP, respectively, indicating that a stepwise encapsulation procedure with a specific order (GOx first, then HRP) is a key operation to achieve the coupling. Control experiments demonstrate that bi-enzyme coupling failed to be established with a reversed encapsulation order. The high catalytic efficiency of the PCN-888 nanoreactor, good cycling performance as well as the protective effect of PCN-888 on the immobilized enzymes against trypsin digestion indicates that cage-MOF tandem nanoreactors have the potential to be applied in more complex systems.

The enzyme-MOF nanoreactor can be a highly efficient activator for cancer therapy coupled with a prodrug. Encapsulated enzymes are well protected by MOFs in proteolytic conditions and in acidic environments, wherein free enzymes would quickly lose activity. The prodrug can be efficiently activated by the enzyme-MOF nanoreactor,[160] thus generating a cytotoxic compound which inhibits cell proliferation and induces apoptosis/necrosis by promoting oxidative stress. *In vivo* experiment shows a 2.5-time regression of tumor volume after a single treatment.[161] This effort in increasing the ligand size and studying the metal chemistry converged in the use of PCNs to encapsulate a nerve agent detoxifying enzyme,[162] and the use of the NU series to encapsulate a formate dehydrogenase[129].

Biomineralization is a natural process whereby inorganic materials (biomaterials) are grown on living organisms. Inspired by nature, scientist have explored and developed an understanding of biomineralization strategies in the laboratory. This gave rise to the **type III** *in situ* encapsulation. As the coating is porous, MOF can function as a perm-selective barrier for the transport of biologically relevant substrates to its interior or act as a matrix to encapsulate enzymes.[163–165] By taking advantage of the extremely mild synthetic conditions of some of those MOFs (for example ZIFs) in aqueous solutions, enzymes can be immobilized in situ during the synthetic process. This methodology allows for the inclusion of guest molecule

(whose size is larger than the pore openings) into the MOF structure, where the MOFs acts as a protective coating.[166] Falcaro *et al*. showed that proteins, enzymes and DNA rapidly induce the formation of protective MOF coatings under physiological condition by concentrating the framework building blocks and facilitating crystallization around the biomacromolecules (**Figure 22a**).[167] In this process, the biomacromolecules regulate the crystal size, morphology and crystallinity while encapsulating itself within the porous crystal and generating new cavities that both tightly surround the biomacromolecules and form bonding interactions with the protein backbone. The controlled release of the biomacromolecules as a bioactive cargo from its protective MOF coating can be achieved via simple pH modification. They confirmed that the MOF coating acts as a protective layer for the enzyme that allows diffusion of the substrates through the ZIF-8 pore cavities while preventing the entry of the proteolytic agent trypsin. Urease and horseradish peroxidase protected within a MOF shell are found to retain bioactivity after being treated at 80°C and boiled in dimethylformamide, when they usually denature above 45°C in biological conditions. The resulting biocomposite is thus stable under conditions that would normally decompose many biological macromolecules.

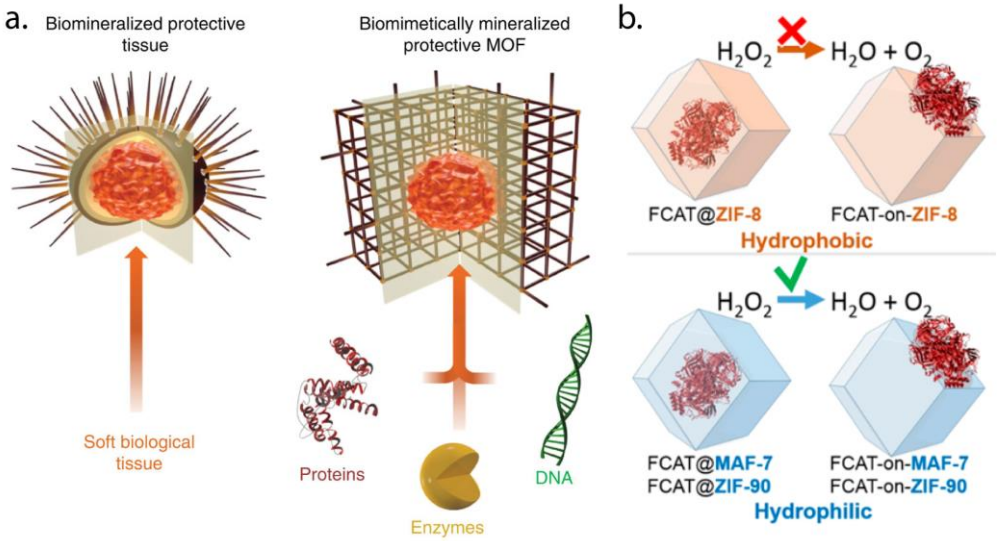

Figure 22. **a**. Schematic of a sea urchin; a hard porous protective shell that is biomineralized by soft biological tissue **b**. Schematic of a MOF biocomposite showing a biomacromolecule, encapsulated within the porous, crystalline shell. **c**. Schematic representations of the different FCAT/ZIF biocomposites formed by encapsulation of enzyme molecules via biomimetic mineralization or surface adsorption within/on hydrophobic (orange) or hydrophilic (blue) frameworks. Modified from [167,171].

Tsung *et al*. developed a similar concept with other MOF, ZIF-90 achieving a 5 wt% loading.[168] ZIF-90 has high chemical stability, and the linkers can be post-synthetically modified, which provides a potential way to modulate the physicochemical interaction between the enzyme and MOF. They previously reported a synthetic protocol to make it in aqueous phase.[169] The ZIF-90 support provides an interesting size-sheltering function to catalase and protects it from the inhibitor. The process is complex, but it is known that proteins tend to have a greater affinity for hydrophobic surfaces and that hydrophobic interactions often engender conformational changes that denature the protein and lead to loss of activity.[170] They continued this first step and tried to display the importance of the polarity of the MOF used.[171] Highlighting the importance of the chemistry of the ZIF and at the ZIF/biointerface, it facilitates and preserves the biological function of an encapsulated enzyme. They show that enzymes encapsulated within MAF-7 retain a significant degree of enzymatic activity. In contrast, topologically identical ZIF-8 essentially deactivates catalase upon encapsulation of surface adsorption. Recent reports encourage the idea that optimizing hydrophobic/-philic interactions between enzymes and polymers is essential for the effective encapsulation is essential for the effective encapsulation and stabilization of biomolecules (**Figure 22b**).

4. References

1. A. Stein, S. W. Keller, T. E. Mallouk, Turning Down the Heat: Design and Mechanism in Solid-State Synthesis. *Science*. 259, 1558–1564 (1993).

2. J. Maddox, Crystals from first principles. *Nature*. 335, 201–201 (1988).

3. O. M. Yaghi, M. O'Keeffe, M. Kanatzidis, Design of Solids from Molecular Building Blocks: Golden Opportunities for Solid State Chemistry. *J Solid State Chem*. 152, 1–2 (2000).

4. S. Kitagawa, M. Kondo, Functional Micropore Chemistry of Crystalline Metal Complex-Assembled Compounds. *B Chem Soc Jpn*. 71, 1739–1753 (1998).

5. O. M. Yaghi, Z. Sun, D. A. Richardson, T. L. Groy, Directed Transformation of Molecules to Solids: Synthesis of a Microporous Sulfide from Molecular Germanium Sulfide Cages. *J Am Chem Soc*. 116, 807–808 (1994).

6. M. F. Hawthorne, Z. Zheng, Recognition of Electron-Donating Guests by Carborane-Supported Multidentate Macrocyclic Lewis Acid Hosts: Mercuracarborand Chemistry. *Accounts Chem Res*. 30, 267–276 (1997).

7. R. H. Cayton, M. H. Chisholm, J. C. Huffman, E. B. Lobkovsky, Metal-metal multiple bonds in ordered assemblies. *J Am Chem Soc*. 113, 8709–8724 (1991).

8. S. R. Batten, R. Robson, Interpenetrating Nets: Ordered, Periodic Entanglement. *Angewandte Chemie Int Ed*. 37, 1460–1494 (1998).

9. L. Pauling, The principles determining the structure of complex ionic crystals. S. *J Am Chem Soc*. 51, 1010–1026 (1929).

10. J. R. Katzer, Atlas of zeolite structure types. W. M. Meier, and D. H. Olson, 2nd rev. ed., Butterworth, 1987. *Aiche J*. 35, 875–875 (1989).

11. G. Férey, Building Units Design and Scale Chemistry. *J Solid State Chem*. 152, 37–48 (2000).

12. O. M. Yaghi, H. Li, C. Davis, D. Richardson, T. L. Groy, Synthetic Strategies, Structure Patterns, and Emerging Properties in the Chemistry of Modular Porous Solids. *Accounts Chem Res*. 31, 474–484 (1998).

13. M. Eddaoudi, D. B. Moler, H. Li, B. Chen, T. M. Reineke, M. O'Keeffe, O. M. Yaghi, Modular Chemistry: Secondary Building Units as a Basis for the Design of Highly Porous and Robust Metal−Organic Carboxylate Frameworks. *Accounts Chem Res*. 34, 319–330 (2001).

14. M. O'Keeffe, M. Eddaoudi, H. Li, T. Reineke, O. M. Yaghi, Frameworks for Extended Solids: Geometrical Design Principles. *J Solid State Chem*. 152, 3–20 (2000).

15. E. B. Winston, P. J. Lowell, J. Vacek, J. Chocholoušová, J. Michl, J. C. Price, Dipolar molecular rotors in the metal–organic framework crystal IRMOF-2. *Phys Chem Chem Phys*. 10, 5188–5191 (2008).

16. D. D. Boehr, R. Nussinov, P. E. Wright, The role of dynamic conformational ensembles in biomolecular recognition. *Nat Chem Biol*. 5, 789–796 (2009).

17. S. Verma, A. K. Mishra, J. Kumar, The Many Facets of Adenine: Coordination, Crystal Patterns, and Catalysis. *Accounts Chem Res*. 43, 79–91 (2010).

18. J. A. R. Navarro, B. Lippert, Molecular architecture with metal ions, nucleobases and other heterocycles. *Coordin Chem Rev*. 185, 653–667 (1999).

19. H. Sigel, R. Griesser, Nucleoside 5′-triphosphates: self-association, acid–base, and metal ion-binding properties in solution. *Chem Soc Rev*. 34, 875–900 (2005).

20. B. Lippert, Multiplicity of metal ion binding patterns to nucleobases. *Coordin Chem Rev*. 200, 487–516 (2000).

21. W. Zhou, R. Saran, J. Liu, Metal Sensing by DNA. *Chem Rev*. 117, 8272–8325 (2017).

22. J. P. García-Terán, O. Castillo, A. Luque, U. García-Couceiro, P. Román, L. Lezama, An Unusual 3D Coordination Polymer Based on Bridging Interactions of the Nucleobase Adenine. *Inorg Chem*. 43, 4549–4551 (2004).

23. H. Hayashi, A. P. Côté, H. Furukawa, M. O'Keeffe, O. M. Yaghi, Zeolite A imidazolate frameworks. *Nat Mater*. 6 (2007).

24. J. An, S. J. Geib, N. L. Rosi, High and Selective CO2 Uptake in a Cobalt Adeninate Metal−Organic Framework Exhibiting Pyrimidine- and Amino-Decorated Pores. *J Am Chem Soc*. 132, 38–39 (2010).

25. P. S. Nugent, V. L. Rhodus, T. Pham, K. Forrest, L. Wojtas, B. Space, M. J. Zaworotko, A Robust Molecular Porous Material with High CO 2 Uptake and Selectivity. *J Am Chem Soc*. 135, 10950–10953 (2013).

26. H.-R. Fu, J. Zhang, Flexible Porous Zinc–Pyrazole–Adenine Framework for Hysteretic Sorption of Light Hydrocarbons. *Cryst Growth Des*. 15, 1210–1213 (2015).

27. J. An, S. J. Geib, N. L. Rosi, Cation-Triggered Drug Release from a Porous Zinc−Adeninate Metal−Organic Framework. *J Am Chem Soc*. 131, 8376–8377 (2009).

28. J. Zhu, L. Zhang, T. Li, S. Dong, E. Wang, Enzyme-Free Unlabeled DNA Logic Circuits Based on Toehold-Mediated Strand Displacement and Split G-Quadruplex Enhanced Fluorescence. *Adv Mater*. 25, 2440–2444 (2013).

29. Y.-L. Wu, N. E. Horwitz, K.-S. Chen, D. A. Gomez-Gualdron, N. S. Luu, L. Ma, T. C. Wang, M. C. Hersam, J. T. Hupp, O. K. Farha, R. Q. Snurr, M. R. Wasielewski, G-quadruplex organic frameworks. *Nat Chem*. 9, 466–472 (2017).

30. L. Stefan, D. Monchaud, Applications of guanine quartets in nanotechnology and chemical biology. *Nat Rev Chem*. 3, 1–19 (2019).

31. D. K. Patel, A. Domínguez-Martín, M. del P. Brandi-Blanco, D. Choquesillo-Lazarte, V. M. Nurchi, J. Niclós-Gutiérrez, Metal ion binding modes of hypoxanthine and xanthine versus the versatile behaviour of adenine. *Coordin Chem Rev*. 256, 193–211 (2012).

32. Z. M. Schulte, N. L. Rosi, Metal-Organic Frameworks in Biomedical and Environmental Field, 291–320 (2021).

33. J. An, O. K. Farha, J. T. Hupp, E. Pohl, J. I. Yeh, N. L. Rosi, Metal-adeninate vertices for the construction of an exceptionally porous metal-organic framework. *Nat Commun*. 3, 604 (2012).

34. T. Li, M. T. Kozlowski, E. A. Doud, M. N. Blakely, N. L. Rosi, Stepwise Ligand Exchange for the Preparation of a Family of Mesoporous MOFs. *J Am Chem Soc*. 135, 11688–11691 (2013).

35. T. Li, D.-L. Chen, J. E. Sullivan, M. T. Kozlowski, J. K. Johnson, N. L. Rosi, Systematic modulation and enhancement of CO 2 :N 2 selectivity and water stability in an isoreticular series of bio-MOF-11 analogues. *Chem Sci*. 4, 1746–1755 (2013).

36. Y. Rachuri, J. F. Kurisingal, R. K. Chitumalla, S. Vuppala, Y. Gu, J. Jang, Y. Choe, E. Suresh, D.-W. Park, Adenine-Based Zn(II)/Cd(II) Metal–Organic Frameworks as Efficient Heterogeneous Catalysts for Facile CO 2 Fixation into Cyclic Carbonates: A DFT-Supported Study of the Reaction Mechanism. *Inorg Chem*. 58, 11389–11403 (2019).

37. N. Li, J. Liu, J. Liu, L. Dong, Z. Xin, Y. Teng, Y. Lan, Adenine Components in Biomimetic Metal–Organic Frameworks for Efficient CO2 Photoconversion. *Angewandte Chemie Int Ed*. 58, 5226–5231 (2019).

38. K. P. Lillerud, U. Olsbye, M. Tilset, Designing Heterogeneous Catalysts by Incorporating Enzyme-Like Functionalities into MOFs. *Top Catal*. 53, 859–868 (2010).

39. E. V. Anokhina, A. J. Jacobson, [Ni 2 O(l -Asp)(H 2 O) 2]·4H 2 O: A Homochiral 1D Helical Chain Hybrid Compound with Extended Ni−O−Ni Bonding. *J Am Chem Soc*. 126, 3044–3045 (2004).

40. E. V. Anokhina, Y. B. Go, Y. Lee, T. Vogt, A. J. Jacobson, Chiral Three-Dimensional Microporous Nickel Aspartate with Extended Ni−O−Ni Bonding. *J Am Chem Soc*. 128, 9957–9962 (2006).

41. J. He, G. Zhang, D. Xiao, H. Chen, S. Yan, X. Wang, J. Yang, E. Wang, Helicity controlled by the chirality of amino acid: two novel enantiopure chiral 3D architectures containing fivefold interwoven helices. *Crystengcomm*. 14, 3609 (2012).

42. C. D. L. Saunders, L. E. Longobardi, N. Burford, M. D. Lumsden, U. Werner-Zwanziger, B. Chen, R. McDonald, Comprehensive Chemical Characterization of Complexes Involving Lead-Amino Acid Interactions. *Inorg Chem*. 50, 2799–2810 (2011).

43. C. H. Görbitz, Microporous Organic Materials from Hydrophobic Dipeptides. *Chem - European J*. 13, 1022–1031 (2007).

44. C. H. Görbitz, F. Rise, Template-directed supramolecular assembly of a new type of nanoporous peptide-based material. *J Pept Sci*. 14, 210–216 (2008).

45. Y. Xie, Z. Yu, X. Huang, Z. Wang, L. Niu, M. Teng, J. Li, Rational Design of MOFs Constructed from Modified Aromatic Amino Acids. *Chem - European J*. 13, 9399–9405 (2007).

46. C. D. L. Saunders, N. Burford, U. Werner-Zwanziger, R. McDonald, Preparation and Comprehensive Characterization of [Hg 6 (Alanine) 4 (NO 3) 4]·H 2 O. *Inorg Chem*. 47, 3693–3699 (2008).

47. J. A. Gould, J. Bacsa, H. Park, J. B. Claridge, A. M. Fogg, V. Ramanathan, J. E. Warren, M. J. Rosseinsky, Nanoporous Amino Acid Derived Material Formed via In-Situ Dimerization of Aspartic Acid. *Cryst Growth Des*. 10, 2977–2982 (2010).

48. T. KUNDU, R. BANERJEE, Structural diversity in serine derived homochiral metal organic frameworks. *J Chem Sci*. 126, 1399–1408 (2014).

49. L. Lili, Z. Xin, R. Shumin, Y. Ying, D. Xiaoping, G. Jinsen, X. Chunming, H. Jing, Catalysis by metal–organic frameworks: proline and gold functionalized MOFs for the aldol and three-component coupling reactions. *Rsc Adv*. 4, 13093–13107 (2014).

50. J. Canivet, S. Aguado, G. Bergeret, D. Farrusseng, Amino acid functionalized metal-organic frameworks by a soft coupling-deprotection sequence. *Chem Commun Camb Engl*. 47, 11650–2 (2011).

51. J. Canivet, D. Farrusseng, Proline-functionalized metal–organic frameworks and their use in asymmetric catalysis: pitfalls in the MOFs rush. *Rsc Adv*. 5, 11254–11256 (2015).

52. J. Bonnefoy, A. Legrand, E. A. Quadrelli, J. Canivet, D. Farrusseng, Enantiopure Peptide-Functionalized Metal–Organic Frameworks. *J Am Chem Soc*. 137, 9409–9416 (2015).

53. H. Hintz, S. Wuttke, Postsynthetic modification of an amino-tagged MOF using peptide coupling reagents: a comparative study. *Chem Commun*. 50, 11472–11475 (2014).

54. E. Yang, L. Wang, F. Wang, Q. Lin, Y. Kang, J. Zhang, Zeolitic Metal–Organic Frameworks Based on Amino Acid. *Inorg Chem*. 53, 10027–10029 (2014).

55. M.-Y. Li, F. Wang, Z.-G. Gu, J. Zhang, Synthesis of homochiral zeolitic metal–organic frameworks with amino acid and tetrazolates for chiral recognition. *Rsc Adv*. 7, 4872–4875 (2017).

56. J. Y. Chan, H. Zhang, Y. Nolvachai, Y. Hu, H. Zhu, M. Forsyth, Q. Gu, D. E. Hoke, X. Zhang, P. J. Marriot, H. Wang, Incorporation of Homochirality into a Zeolitic Imidazolate Framework Membrane for Efficient Chiral Separation. *Angewandte Chemie Int Ed*. 57, 17130–17134 (2018).

57. H. Tang, K. Yang, K.-Y. Wang, Q. Meng, F. Wu, Y. fang, X. Wu, Y. Li, W. Zhang, Y. Luo, C. Zhu, H.-C. Zhou, Engineering a homochiral metal–organic framework based on an amino acid for enantioselective separation. *Chem Commun*. 56, 9016–9019 (2020).

58. R. Newar, N. Akhtar, N. Antil, A. Kumar, S. Shukla, W. Begum, K. Manna, Amino Acid-Functionalized Metal-Organic Frameworks for Asymmetric Base–Metal Catalysis. *Angewandte Chemie Int Ed*. 60, 10964–10970 (2021).

59. C. H. Görbitz, E. Gundersen, l-Valyl-l-alanine. *Acta Crystallogr Sect C Cryst Struct Commun*. 52, 1764–1767 (1996).

60. C. H. Görbitz, Peptide-based organic microporous materials. *Acta Crystallogr Sect Found Crystallogr*. 61 (2005).

61. M. Peterca, V. Percec, A. E. Dulcey, S. Nummelin, S. Korey, M. Ilies, P. A. Heiney, Self-Assembly, Structural, and Retrostructural Analysis of Dendritic Dipeptide Pores Undergoing Reversible Circular to Elliptical Shape Change. *J Am Chem Soc*. 128, 6713–6720 (2006).

62. A. Mantion, L. Massüger, P. Rabu, C. Palivan, L. B. McCusker, A. Taubert, Metal−Peptide Frameworks (MPFs): "Bioinspired" Metal Organic Frameworks. *J Am Chem Soc*. 130, 2517–2526 (2008).

63. J. Baek, B. Rungtaweevoranit, X. Pei, M. Park, S. C. Fakra, Y.-S. Liu, R. Matheu, S. A. Alshmimri, S. Alshehri, C. A. Trickett, G. A. Somorjai, O. M. Yaghi, Bioinspired Metal–Organic Framework Catalysts for Selective Methane Oxidation to Methanol. *J Am Chem Soc*. 140, 18208–18216 (2018).

64. J. Rabone, Y.-F. Yue, S. Y. Chong, K. C. Stylianou, J. Bacsa, D. Bradshaw, G. R. Darling, N. G. Berry, Y. Z. Khimyak, A. Y. Ganin, P. Wiper, J. B. Claridge, M. J. Rosseinsky, An Adaptable Peptide-Based Porous Material. *Science*. 329, 1053–1057 (2010).

65. C. Martí-Gastaldo, J. E. Warren, K. C. Stylianou, N. L. O. Flack, M. J. Rosseinsky, Enhanced Stability in Rigid Peptide-Based Porous Materials. *Angewandte Chemie Int Ed*. 51, 11044–11048 (2012).

66. C. Martí-Gastaldo, D. Antypov, J. E. Warren, M. E. Briggs, P. A. Chater, P. V. Wiper, G. J. Miller, Y. Z. Khimyak, G. R. Darling, N. G. Berry, M. J. Rosseinsky, Side-chain control of porosity closure in single- and multiple-peptide-based porous materials by cooperative folding. *Nat Chem*. 6, 343–351 (2014).

67. C. Martí-Gastaldo, J. E. Warren, M. E. Briggs, J. A. Armstrong, K. M. Thomas, M. J. Rosseinsky, Sponge-Like Behaviour in Isoreticular Cu(Gly-His-X) Peptide-Based Porous Materials. *Chem - European J*. 21, 16027–16034 (2015).

68. A. Katsoulidis, D. Antypov, G. Whitehead, E. Carrington, D. Adams, N. Berry, G. Darling, M. Dyer, M. Rosseinsky, Chemical control of structure and guest uptake by a conformationally mobile porous material. *Nature*. 565, 213–217 (2019).

69. Y. Yan, E. J. Carrington, R. Pétuya, G. F. S. Whitehead, A. Verma, R. K. Hylton, C. C. Tang, N. G. Berry, G. R. Darling, M. S. Dyer, D. Antypov, A. P. Katsoulidis, M. J. Rosseinsky, Amino Acid Residues Determine the Response of Flexible Metal–Organic Frameworks to Guests. *J Am Chem Soc* (2020).

70. R. Miyake, C. Kuwata, Y. Masumoto, Selective CO 2 gas adsorption in the narrow crystalline cavities of flexible peptide metallo-macrocycles. *Dalton T*. 44, 2993–2996 (2015).

71. G. Fan, C. M. Dundas, C. Zhang, N. A. Lynd, B. K. Keitz, Sequence-Dependent Peptide Surface Functionalization of Metal–Organic Frameworks. *Acs Appl Mater Inter*. 10, 18601–18609 (2018).

72. W. Li, F. Separovic, N. M. O'Brien-Simpson, J. D. Wade, Chemically modified and conjugated antimicrobial peptides against superbugs. *Chem Soc Rev* (2021).

73. T. Schnitzer, E. Paenurk, N. Trapp, R. Gershoni-Poranne, H. Wennemers, Peptide–Metal Frameworks with Metal Strings Guided by Dispersion Interactions. *J Am Chem Soc*. 143, 644–648 (2021).

74. S. Dey, R. Misra, A. Saseendran, S. Pahan, H. N. Gopi, Metal-Coordinated Supramolecular Polymers from the Minimalistic Hybrid Peptide Foldamers. *Angew Chem-ger Edit*. 133, 9951–9956 (2021).

75. Y.-X. Tan, Y.-P. He, J. Zhang, Serine-Based Homochiral Nanoporous Frameworks for Selective CO 2 Uptake. *Inorg Chem*. 50, 11527–11531 (2011).

76. J. L. England, G. Haran, Role of Solvation Effects in Protein Denaturation: From Thermodynamics to Single Molecules and Back. *Annu Rev Phys Chem*. 62, 257–277 (2011).

77. S. W. Englander, L. Mayne, The nature of protein folding pathways. *Proc National Acad Sci*. 111, 15873–15880 (2014).

78. S. W. Englander, L. Mayne, The case for defined protein folding pathways. *Proc National Acad Sci*. 114, 8253–8258 (2017).

79. J. F. Darby, A. P. Hopkins, S. Shimizu, S. M. Roberts, J. A. Brannigan, J. P. Turkenburg, G. H. Thomas, R. E. Hubbard, M. Fischer, Water Networks Can Determine the Affinity of Ligand Binding to Proteins. *J Am Chem Soc*. 141, 15818–15826 (2019).

80. D. E. Przybyla, J. Chmielewski, Metal-Triggered Collagen Peptide Disk Formation. *J Am Chem Soc*. 132, 7866–7867 (2010).

81. D. E. Przybyla, J. Chmielewski, Metal-Triggered Radial Self-Assembly of Collagen Peptide Fibers. *J Am Chem Soc*. 130, 12610–12611 (2008).

82. M. M. Pires, J. Chmielewski, Self-assembly of Collagen Peptides into Microflorettes via Metal Coordination. *J Am Chem Soc*. 131, 2706–2712 (2009).

83. F. Sakai, G. Yang, M. S. Weiss, Y. Liu, G. Chen, M. Jiang, Protein crystalline frameworks with controllable interpenetration directed by dual supramolecular interactions. *Nat Commun*. 5, 4634 (2014).

84. K. Zhou, J. Zang, H. Chen, W. Wang, H. Wang, G. Zhao, On-Axis Alignment of Protein Nanocage Assemblies from 2D to 3D through the Aromatic Stacking Interactions of Amino Acid Residues. *Acs Nano*. 12, 11323–11332 (2018).

85. X. Tan, H. Chen, C. Gu, J. Zang, T. Zhang, H. Wang, G. Zhao, Converting histidine-induced 3D protein arrays in crystals into their 3D analogues in solution by metal coordination cross-linking. *Commun Chem*. 3, 151 (2020).

86. P. A. Sontz, J. B. Bailey, S. Ahn, F. A. Tezcan, A Metal Organic Framework with Spherical Protein Nodes: Rational Chemical Design of 3D Protein Crystals. *J Am Chem Soc*. 137, 11598–11601 (2015).

87. R. J. Radford, F. A. Tezcan, A Superprotein Triangle Driven by Nickel(II) Coordination: Exploiting Non-Natural Metal Ligands in Protein Self-Assembly. *J Am Chem Soc*. 131, 9136–9137 (2009).

88. E. N. Salgado, J. Faraone-Mennella, F. A. Tezcan, Controlling Protein−Protein Interactions through Metal Coordination: Assembly of a 16-Helix Bundle Protein. *J Am Chem Soc*. 129, 13374–13375 (2007).

89. J. D. Brodin, A. Medina-Morales, T. Ni, E. N. Salgado, X. I. Ambroggio, F. A. Tezcan, Evolution of Metal Selectivity in Templated Protein Interfaces. *J Am Chem Soc*. 132, 8610–8617 (2010).

90. E. N. Salgado, R. A. Lewis, J. Faraone-Mennella, F. A. Tezcan, Metal-Mediated Self-Assembly of Protein Superstructures: Influence of Secondary Interactions on Protein Oligomerization and Aggregation. *J Am Chem Soc*. 130, 6082–6084 (2008).

91. J. B. Bailey, L. Zhang, J. A. Chiong, S. Ahn, F. A. Tezcan, Synthetic Modularity of Protein–Metal–Organic Frameworks. *J Am Chem Soc*. 139, 8160–8166 (2017).

92. P. Wang, S. Dai, S. D. Waezsada, A. Y. Tsao, B. H. Davison, Enzyme stabilization by covalent binding in nanoporous sol-gel glass for nonaqueous biocatalysis. *Biotechnol Bioeng*. 74, 249–255 (2001).

93. Y. Chen, V. Lykourinou, C. Vetromile, T. Hoang, L.-J. Ming, R. W. Larsen, S. Ma, How Can Proteins Enter the Interior of a MOF? Investigation of Cytochrome c Translocation into a MOF Consisting of Mesoporous Cages with Microporous Windows. *J Am Chem Soc*. 134, 13188–13191 (2012).

94. Y. Chen, S. Han, X. Li, Z. Zhang, S. Ma, Why Does Enzyme Not Leach from Metal–Organic Frameworks (MOFs)? Unveiling the Interactions between an Enzyme Molecule and a MOF. *Inorg Chem*. 53, 10006–10008 (2014).

95. L. Ma, C. Abney, W. Lin, Enantioselective catalysis with homochiral metal–organic frameworks. *Chem Soc Rev*. 38, 1248–1256 (2009).

96. J.-R. Li, R. J. Kuppler, H.-C. Zhou, Selective gas adsorption and separation in metal–organic frameworks. *Chem Soc Rev*. 38, 1477–1504 (2009).

97. J. Lee, O. K. Farha, J. Roberts, K. A. Scheidt, S. T. Nguyen, J. T. Hupp, Metal–organic framework materials as catalysts. *Chem Soc Rev*. 38, 1450–1459 (2009).

98. K. Sumida, D. L. Rogow, J. A. Mason, T. M. McDonald, E. D. Bloch, Z. R. Herm, T.-H. Bae, J. R. Long, Carbon dioxide capture in metal-organic frameworks. *Chem Rev*. 112, 724–81 (2011).

99. T. Simon-Yarza, A. Mielcarek, P. Couvreur, C. Serre, Nanoparticles of Metal-Organic Frameworks: On the Road to In Vivo Efficacy in Biomedicine. *Adv Mater*. 30, e1707365 (2018).

100. B. V. de Voorde, B. Bueken, J. Denayer, D. D. Vos, Adsorptive separation on metal–organic frameworks in the liquid phase. *Chem Soc Rev*. 43, 5766–5788 (2014).

101. X. Lian, Y. Fang, E. Joseph, Q. Wang, J. Li, S. Banerjee, C. Lollar, X. Wang, H.-C. Zhou, Enzyme–MOF (metal–organic framework) composites. *Chem Soc Rev*. 46, 3386–3401 (2017).

102. X. Wang, P. C. Lan, S. Ma, Metal–Organic Frameworks for Enzyme Immobilization: Beyond Host Matrix Materials. *Acs Central Sci*. 6, 1497–1506 (2020).

103. J. T. Hupp, Towards artificial enzymes. *Nat Chem*. 2, 432–433 (2010).

104. D. Zhao, D. J. Timmons, D. Yuan, H.-C. Zhou, Tuning the Topology and Functionality of Metal−Organic Frameworks by Ligand Design. *Accounts Chem Res*. 44, 123–133 (2011).

105. J. R. Bour, A. M. Wright, X. He, M. Dincă, Bioinspired chemistry at MOF secondary building units. *Chem Sci*. 11, 1728–1737 (2020).

106. L. Ma, W. Lin, Functional Metal-Organic Frameworks: Gas Storage, Separation and Catalysis. *Top Curr Chem*. 293, 175–205 (2009).

107. J.-S. Qin, S. Yuan, C. Lollar, J. Pang, A. Alsalme, H.-C. Zhou, Stable metal–organic frameworks as a host platform for catalysis and biomimetics. *Chem Commun*. 54, 4231–4249 (2018).

108. A. Dhakshinamoorthy, Z. Li, H. Garcia, Catalysis and photocatalysis by metal organic frameworks. *Chem Soc Rev*. 47, 8134–8172 (2018).

109. M. J. Katz, J. E. Mondloch, R. K. Totten, J. K. Park, S. T. Nguyen, O. K. Farha, J. T. Hupp, Simple and Compelling Biomimetic Metal–Organic Framework Catalyst for the Degradation of Nerve Agent Simulants. *Angew Chem-ger Edit*. 126, 507–511 (2014).

110. J. Jiang, O. M. Yaghi, Brønsted Acidity in Metal–Organic Frameworks. *Chem Rev*. 115, 6966–6997 (2015).

111. L. Zhu, X.-Q. Liu, H.-L. Jiang, L.-B. Sun, Metal–Organic Frameworks for Heterogeneous Basic Catalysis. *Chem Rev*. 117, 8129–8176 (2017).

112. D. Feng, Z. Gu, J. Li, H. Jiang, Z. Wei, H. Zhou, Zirconium-Metalloporphyrin PCN-222: Mesoporous Metal–Organic Frameworks with Ultrahigh Stability as Biomimetic Catalysts . *Angew Chem-ger Edit*. 124, 10453–10456 (2012).

113. M. Li, J. Chen, W. Wu, Y. Fang, S. Dong, Oxidase-like MOF-818 Nanozyme with High Specificity for Catalysis of Catechol Oxidation. *J Am Chem Soc*. 142, 15569–15574 (2020).

114. S. Yuan, L. Feng, K. Wang, J. Pang, M. Bosch, C. Lollar, Y. Sun, J. Qin, X. Yang, P. Zhang, Q. Wang, L. Zou, Y. Zhang, L. Zhang, Y. Fang, J. Li, H. Zhou, Stable Metal–Organic Frameworks: Design, Synthesis, and Applications. *Adv Mater*. 30, 1704303 (2018).

115. D. J. Xiao, J. Oktawiec, P. J. Milner, J. R. Long, Pore Environment Effects on Catalytic Cyclohexane Oxidation in Expanded Fe 2 (dobdc) Analogues. *J Am Chem Soc*. 138, 14371–14379 (2016).

116. M. Kalaj, S. M. Cohen, Postsynthetic Modification: An Enabling Technology for the Advancement of Metal–Organic Frameworks. *Acs Central Sci*. 6, 1046–1057 (2020).

117. J. Bonnefoy, A. Legrand, E. A. Quadrelli, J. Canivet, D. Farrusseng, Enantiopure Peptide-Functionalized Metal–Organic Frameworks. *J Am Chem Soc*. 137, 9409–9416 (2015).

118. B. Mohapatra, Pratibha, S. Verma, Directed adenine functionalization for creating complex architectures for material and biological applications. *Chem Commun*. 53, 4748–4758 (2017).

119. A. P. Katsoulidis, K. S. Park, D. Antypov, C. Martí-Gastaldo, G. J. Miller, J. E. Warren, C. M. Robertson, F. Blanc, G. R. Darling, N. G. Berry, J. A. Purton, D. J. Adams, M. J. Rosseinsky, Guest-Adaptable and Water-Stable Peptide-Based Porous Materials by Imidazolate Side Chain Control. *Angew Chem-ger Edit*. 126, 197–202 (2014).

120. S. S. Nadar, L. Vaidya, S. Maurya, V. K. Rathod, Polysaccharide based metal organic frameworks (polysaccharide–MOF): A review. *Coordin Chem Rev*. 396, 1–21 (2019).

121. D. J. Levine, T. Runčevski, M. T. Kapelewski, B. K. Keitz, J. Oktawiec, D. A. Reed, J. A. Mason, H. Z. H. Jiang, K. A. Colwell, C. M. Legendre, S. A. FitzGerald, J. R. Long, Olsalazine-Based Metal–Organic Frameworks as Biocompatible Platforms for H2 Adsorption and Drug Delivery. *J Am Chem Soc*. 138, 10143–10150 (2016).

122. A. Schaate, P. Roy, A. Godt, J. Lippke, F. Waltz, M. Wiebcke, P. Behrens, Modulated Synthesis of Zr-Based Metal–Organic Frameworks: From Nano to Single Crystals. *Chem - European J*. 17, 6643–6651 (2011).

123. M. Banerjee, S. Das, M. Yoon, H. J. Choi, M. H. Hyun, S. M. Park, G. Seo, K. Kim, Postsynthetic Modification Switches an Achiral Framework to Catalytically Active Homochiral Metal−Organic Porous Materials. *J Am Chem Soc*. 131, 7524–7525 (2009).

124. X. Wang, F. M. Wisser, J. Canivet, M. Fontecave, C. Mellot-Draznieks, Immobilization of a Full Photosystem in the Large-Pore MIL-101 Metal–Organic Framework for CO2 reduction. *Chemsuschem*. 11, 3315–3322 (2018).

125. L. Cheng, K. Zhao, Q. Zhang, Y. Li, Q. Zhai, J. Chen, Y. Lou, Chiral Proline-Decorated Bifunctional Pd@NH 2 -UiO-66 Catalysts for Efficient Sequential Suzuki Coupling/Asymmetric Aldol Reactions. *Inorg Chem*. 59, 7991–8001 (2020).

126. E. López-Maya, N. M. Padial, J. Castells-Gil, C. R. Ganivet, A. Rubio-Gaspar, F. G. Cirujano, N. Almora-Barrios, S. Tatay, S. Navalón, C. Martí-Gastaldo, Selective Implantation of Diamines for Cooperative Catalysis in Isoreticular Heterometallic Titanium–Organic Frameworks. *Angew Chem-ger Edit*. 133, 11975–11980 (2021).

127. D. J. Xuereb, R. Raja, Design strategies for engineering selectivity in bio-inspired heterogeneous catalysts. *Catal Sci Technol*. 1, 517–534 (2011).

128. J. Huo, J. Aguilera-Sigalat, S. El-Hankari, D. Bradshaw, Magnetic MOF microreactors for recyclable size-selective biocatalysis. *Chem Sci*. 6, 1938–1943 (2014).

129. Y. Chen, P. Li, H. Noh, C. Kung, C. T. Buru, X. Wang, X. Zhang, O. K. Farha, Stabilization of Formate Dehydrogenase in a Metal–Organic Framework for Bioelectrocatalytic Reduction of CO2. *Angew Chem-ger Edit*. 131, 7764–7768 (2019).

130. Y. Chen, F. Jiménez-Ángeles, B. Qiao, M. D. Krzyaniak, F. Sha, S. Kato, X. Gong, C. T. Buru, Z. Chen, X. Zhang, N. C. Gianneschi, M. R. Wasielewski, M. O. de la Cruz, O. K. Farha, Insights into the Enhanced Catalytic Activity of Cytochrome c When Encapsulated in a Metal–Organic Framework. *Journal of the American Chemical Society*. 142 (2020),

131. J.-R. Li, J. Sculley, H.-C. Zhou, Metal–Organic Frameworks for Separations. *Chem Rev*. 112, 869–932 (2012).

132. A. M. Stalcup, Chiral Separations. *Annu Rev Anal Chem*. 3, 341–363 (2010).

133. S. Bhattacharjee, M. Khan, X. Li, Q.-L. Zhu, X.-T. Wu, Recent Progress in Asymmetric Catalysis and Chromatographic Separation by Chiral Metal–Organic Frameworks. *Catalysts*. 8, 120 (2018).

134. R. Hailili, L. Wang, J. Qv, R. Yao, X.-M. Zhang, H. Liu, Planar Mn 4 O Cluster Homochiral Metal–Organic Framework for HPLC Separation of Pharmaceutically Important (±)-Ibuprofen Racemate. *Inorg Chem*. 54, 3713–3715 (2015).

135. M. N. Corella-Ochoa, J. B. Tapia, H. N. Rubin, V. Lillo, J. Gonzalez-Cobos, J. L. N. Rico, S. R. G. Balestra, N. Almora-Barrios, M. Lledos, A. Guell-Bara, J. Cabezas-Giménez, E. C. Escudero-Adán, A. Vidal-Ferran, S. Calero, M. M. Reynolds, C. Marti-Gastaldo, J. R. Galan-Mascaros, Homochiral metal-organic frameworks for enantioselective separations in liquid chromatography. *J Am Chem Soc* (2019),

136. W. Wang, X. Dong, J. Nan, W. Jin, Z. Hu, Y. Chen, J. Jiang, A homochiral metal-organic framework membrane for enantioselective separation. *Chem Commun Camb Engl*. 48, 7022–4 (2012).

137. S.-Y. Zhang, C.-X. Yang, W. Shi, X.-P. Yan, P. Cheng, L. Wojtas, M. J. Zaworotko, A Chiral Metal-Organic Material that Enables Enantiomeric Identification and Purification. *Chem*. 3, 281–289 (2017).

138. J. Guo, Y. Zhang, Y. Zhu, C. Long, M. Zhao, M. He, X. Zhang, J. Lv, B. Han, Z. Tang, Ultrathin Chiral Metal–Organic-Framework Nanosheets for Efficient Enantioselective Separation. *Angew Chem-ger Edit*. 130, 6989–6993 (2018).

139. K. J. Hartlieb, J. M. Holcroft, P. Z. Moghadam, N. A. Vermeulen, M. M. Algaradah, M. S. Nassar, Y. Y. Botros, R. Q. Snurr, J. F. Stoddart, CD-MOF: A Versatile Separation Medium. *J Am Chem Soc*. 138, 2292–2301 (2016).

140. C.-X. Yang, Y.-Z. Zheng, X.-P. Yan, γ-Cyclodextrin metal–organic framework for efficient separation of chiral aromatic alcohols. *Rsc Adv*. 7, 36297–36301 (2017).

141. Y. Lu, H. Zhang, J. Y. Chan, R. Ou, H. Zhu, M. Forsyth, E. M. Marijanovic, C. M. Doherty, P. J. Marriott, M. M. B. Holl, H. Wang, Homochiral MOF–Polymer Mixed Matrix Membranes for Efficient Separation of Chiral Molecules. *Angew Chem-ger Edit*. 131, 17084–17091 (2019).

142. B. Slater, Z. Wang, S. Jiang, M. R. Hill, B. P. Ladewig, Missing Linker Defects in a Homochiral Metal–Organic Framework: Tuning the Chiral Separation Capacity. *J Am Chem Soc*. 139, 18322–18327 (2017).

143. W.-L. Liu, S.-H. Lo, B. Singco, C.-C. Yang, H.-Y. Huang, C.-H. Lin, Novel trypsin–FITC@MOF bioreactor efficiently catalyzes protein digestion. *J Mater Chem B*. 1, 928–932 (2013).

144. Y. Shih, S. Lo, N. Yang, B. Singco, Y. Cheng, C. Wu, I. Chang, H. Huang, C. Lin, Trypsin-Immobilized Metal–Organic Framework as a Biocatalyst In Proteomics Analysis. *Chempluschem*. 77, 982–986 (2012).

145. T. J. Pisklak, M. Macías, D. H. Coutinho, R. S. Huang, K. J. Balkus, Hybrid materials for immobilization of MP-11 catalyst. *Top Catal*. 38, 269–278 (2006).

146. J. F. Diaz, F. Bedioui, E. Briot, J. Devynck, K. J. Balkus, Immobilization of Cobalt Complexes on Mesoporous MCM-41 Support Materials. *Mrs Online Proc Libr*. 431, 89–94 (1996).

147. S. Jung, Y. Kim, S.-J. Kim, T.-H. Kwon, S. Huh, S. Park, Bio-functionalization of metal–organic frameworks by covalent protein conjugation. *Chem Commun*. 47, 2904–2906 (2011).

148. S.-L. Cao, D.-M. Yue, X.-H. Li, T. J. Smith, N. Li, M.-H. Zong, H. Wu, Y.-Z. Ma, W.-Y. Lou, Novel Nano-/Micro-Biocatalyst: Soybean Epoxide Hydrolase Immobilized on UiO-66-NH 2 MOF for Efficient Biosynthesis of Enantiopure (R)-1, 2-Octanediol in Deep Eutectic Solvents. *Acs Sustain Chem Eng*. 4, 3586–3595 (2016).

149. M. Hartmann, D. Jung, Biocatalysis with enzymes immobilized on mesoporous hosts : the status quo and future trends. *J Mater Chem*. 20, 844–857 (2009).

150. V. Lykourinou, Y. Chen, X.-S. Wang, L. Meng, T. Hoang, L.-J. Ming, R. L. Musselman, S. Ma, Immobilization of MP-11 into a Mesoporous Metal–Organic Framework, MP-11@mesoMOF: A New Platform for Enzymatic Catalysis. *J Am Chem Soc*. 133, 10382–10385 (2011).

151. Y. Chen, V. Lykourinou, T. Hoang, L.-J. Ming, S. Ma, Size-Selective Biocatalysis of Myoglobin Immobilized into a Mesoporous Metal–Organic Framework with Hierarchical Pore Sizes. *Inorg Chem*. 51, 9156–9158 (2012).

152. Q. Sun, C.-W. Fu, B. Aguila, J. Perman, S. Wang, H.-Y. Huang, F.-S. Xiao, S. Ma, Pore Environment Control and Enhanced Performance of Enzymes Infiltrated in Covalent Organic Frameworks. *J Am Chem Soc*. 140, 984–992 (2018).

153. O. K. Farha, A. Ö. Yazaydın, I. Eryazici, C. D. Malliakas, B. G. Hauser, M. G. Kanatzidis, S. T. Nguyen, R. Q. Snurr, J. T. Hupp, De novo synthesis of a metal–organic framework material featuring ultrahigh surface area and gas storage capacities. *Nat Chem*. 2, 944–948 (2010).

154. Q.-G. Zhai, X. Bu, X. Zhao, D.-S. Li, P. Feng, Pore Space Partition in Metal–Organic Frameworks. *Accounts Chem Res*. 50, 407–417 (2017).

155. X. Xu, S. Li, Q. Liu, Z. Liu, W. Yan, L. Zhao, W. Zhang, L. Zhang, F. Deng, H. Cong, H. Deng, Isolated π-Interaction Sites in Mesoporous MOF Backbone for Repetitive and Reversible Dynamics in Water. *Acs Appl Mater Inter*. 11, 973–981 (2018).

156. D. Feng, T.-F. Liu, J. Su, M. Bosch, Z. Wei, W. Wan, D. Yuan, Y.-P. Chen, X. Wang, K. Wang, X. Lian, Z.-Y. Gu, J. Park, X. Zou, H.-C. Zhou, Stable metal-organic frameworks containing single-molecule traps for enzyme encapsulation. *Nat Commun*. 6, 5979 (2015).

157. M. Zhang, Y.-P. Chen, H.-C. Zhou, Structural design of porous coordination networks from tetrahedral building units. *Crystengcomm*. 15, 9544–9552 (2013).

158. S. Hudson, J. Cooney, E. Magner, Proteins in mesoporous silicates. *Angewandte Chemie Int Ed Engl*. 47, 8582–94 (2008).

159. X. Lian, Y.-P. Chen, T.-F. Liu, H.-C. Zhou, Coupling two enzymes into a tandem nanoreactor utilizing a hierarchically structured MOF. *Chem Sci*. 7, 6969–6973 (2016).

160. H. Deng, S. Grunder, K. E. Cordova, C. Valente, H. Furukawa, M. Hmadeh, F. Gándara, A. C. Whalley, Z. Liu, S. Asahina, H. Kazumori, M. O'Keeffe, O. Terasaki, J. F. Stoddart, O. M. Yaghi, Large-Pore Apertures in a Series of Metal-Organic Frameworks. *Science*. 336, 1018–1023 (2012).

161. X. Lian, Y. Huang, Y. Zhu, Y. Fang, R. Zhao, E. Joseph, J. Li, J. Pellois, H. Zhou, Enzyme-MOF Nanoreactor Activates Nontoxic Paracetamol for Cancer Therapy. *Angewandte Chemie Int Ed*. 57, 5725–5730 (2018).

162. P. Li, S.-Y. Moon, M. A. Guelta, S. P. Harvey, J. T. Hupp, O. K. Farha, Encapsulation of a Nerve Agent Detoxifying Enzyme by a Mesoporous Zirconium Metal–Organic Framework Engenders Thermal and Long-Term Stability. *J Am Chem Soc*. 138, 8052–8055 (2016).

163. J. Livage, T. Coradin, C. Roux, Encapsulation of biomolecules in silica gels. *J Phys Condens Matter*. 13, R673–R691 (2001).

164. K. Liang, J. Richardson, C. Doonan, X. Mulet, Y. Ju, J. Cui, F. Caruso, P. Falcaro, An Enzyme-Coated Metal-Organic Framework Shell for Synthetically Adaptive Cell Survival. *Angew Chem-ger Edit*. 129, 8630–8635 (2017).

165. K. Liang, J. J. Richardson, J. Cui, F. Caruso, C. J. Doonan, P. Falcaro, Metal–Organic Framework Coatings as Cytoprotective Exoskeletons for Living Cells. *Adv Mater*. 28, 7910–7914 (2016).

166. K. Liang, C. J. Coghlan, S. G. Bell, C. Doonan, P. Falcaro, Enzyme encapsulation in zeolitic imidazolate frameworks: a comparison between controlled co-precipitation and biomimetic mineralisation. *Chem Commun*. 52, 473–476 (2016).

167. K. Liang, R. Ricco, C. M. Doherty, M. J. Styles, S. Bell, N. Kirby, S. Mudie, D. Haylock, A. J. Hill, C. J. Doonan, P. Falcaro, Biomimetic mineralization of metal-organic frameworks as protective coatings for biomacromolecules. *Nat Commun*. 6, 7240 (2015).

168. F.-K. Shieh, S.-C. Wang, C.-I. Yen, C.-C. Wu, S. Dutta, L.-Y. Chou, J. V. Morabito, P. Hu, M.-H. Hsu, K. C.-W. Wu, C.-K. Tsung, Imparting Functionality to Biocatalysts via Embedding Enzymes into Nanoporous Materials by a de Novo Approach: Size-Selective Sheltering of Catalase in Metal–Organic Framework Microcrystals. *J Am Chem Soc*. 137, 4276–4279.

169. F. Shieh, S. Wang, S. Leo, K.- Wu, Back Cover: Water-Based Synthesis of Zeolitic Imidazolate Framework-90 (ZIF-90) with a Controllable Particle Size (Chem. Eur. J. 34/2013). *Chem - European J*. 19, 11456–11456 (2013).

170. T. Zoungrana, G. H. Findenegg, W. Norde, Structure, Stability, and Activity of Adsorbed Enzymes. *J Colloid Interf Sci*. 190, 437–448 (1997).

171. W. Liang, H. Xu, F. Carraro, N. K. Maddigan, Q. Li, S. G. Bell, D. M. Huang, A. Tarzia, M. B. Solomon, H. Amenitsch, L. Vaccari, C. J. Sumby, P. Falcaro, C. J. Doonan, Enhanced Activity of Enzymes Encapsulated in Hydrophilic Metal–Organic Frameworks. *J Am Chem Soc*. 141, 2348–2355 (2019).

Chapter 2:

Pressure-mediated structural study of peptide-based MOFs

1. Motivation

When this PhD started back in 2016, the group had a big background on flexible peptide-based materials based on dipeptides.[1,2] Peptides have proved to be a particularly diverse set of candidates for linkers thanks to the diversity of their side-chain chemistries and the role of that group in controlling their behavior.[3,4] However, one of the disadvantages of the flexible MOFs based on biological ligands is that their "soft" mechanical properties can lead to pore collapsing or structural distortion when pressure is applied. Any structural deformation leads to an alteration of the guest-binding properties of the MOF, directly affecting to its function. Structural flexibility opens the path to a very rich and diverse array of pressure-induced mechanical responses in MOFs, which need a proper study to be really understood.[5]

Previous structural studies of the flexibility of peptide MOFs do not state the origin of this particular feature,[6–10] and current methodologies do not allow for easy discrimination between the two main sources of changes: the presence of non-coordinating groups and the capacity of the peptide of establishing supramolecular interactions.[9,11] In this regard, their structural adaptability is usually assigned to the torsional flexibility of the peptidic chain, however, the presence of non-coordinating groups in the backbone of the peptide capable of establish interactions is equally important. It has not been properly studied, as there is a fundamental problem in the inexistence of a crystallographic methodology that allows for an easy discrimination between both of them. Moreover, this method is exclusively used for porous materials where the guest interactions also take part.

2. Summary of key results

The findings of this work were published in "Navarro-Sánchez, I. Mullor-Ruíz, C. Popescu, D. Santamaría-Pérez, A. Segura, D. Errandonea, J. González-Platas, C. Martí-Gastaldo. Peptide metal–organic frameworks under pressure: flexible linkers for cooperative compression. *Dalton T* **47**, 10654–10659 (2018)". In this publication we demonstrate how through high-pressure coupled with X-ray diffraction it is possible to study a peptidic-based flexible MOF, priorly discarting all the meddling of the solvent and any changes in the structure associated to the inclusion of guest molecules.

In order to study how pressure affects flexible MOFs we employed the $Zn(GlyTyr)_2$ (**Figure 23a**) system, reported as a "dense" peptide-based material.[1] The structure of this particular system is ideal to study the elasticity of the dipeptide connector with external pressure, as the absence of solvent entry enormously simplifies the refinement of High-Pressure X-Ray Diffraction (HP-PXRD) data. The

synthesis of the system is based on a solvothermal reaction of zinc(II) nitrate with enantiopure GlyTyr at 85°C, on a mixture of methanol and toluene. After cooling to room temperature, crystals with sizes close to 50 µm were obtained and thoroughly washed with abundant methanol. The structure of the dipeptide is based on hydrogen bonding interactions between layers (showed in **Figure 1b**), producing a non-porous solid. The internal structure of this layer is derived from the family of materials like $Zn(GlyAla)_2$,[4] $Zn(GlySer)_2$[1] or $Zn(GlyThr)_2$[2]. The supramolecular interactions involve phenol units of the tyrosine and (O3) and the C=O (O4) and NH (N1) groups from the dipeptide bond. The election of this packing system helps to highlight the importance of sidechain chemistry in directing the structure of metal-peptide coordination polymers. Even if this system is considered non-porous or

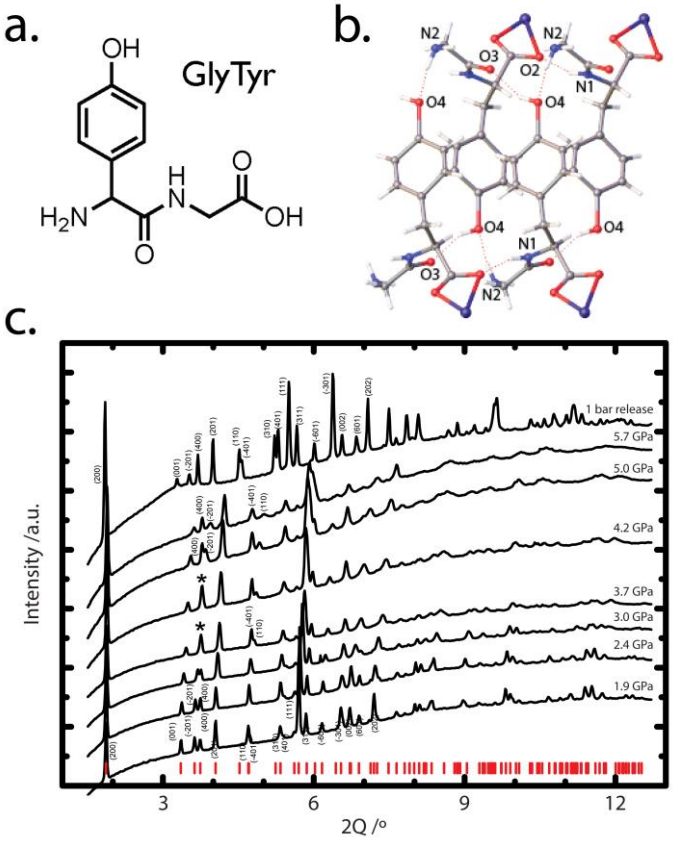

Figure 23. **a**. Structure of glycyl-L-tyrosine (GlyTyr). **b**. View of the H-bonding that controls the packing, specific to the dipeptide. **c**. HP-PXRD of $Zn(GlyTyr)_2$ in methanol:water (3:1). The pointed peaks (-201 and 400) are separated between 1.9 and 2.4 GPA, merging as the pressure increases. This is a clear indication of anisotropic compression.

"dense", the compressibility of $Zn(GlyTyr)_2$ is substantially higher than the majority of zeolite-type materials. Also, these last display smaller changes in the volume cell at the higher pressures studied (below 10%). The material consisted of a pure phase, confirmed by Elemental Analysis, FT-IR (Fourier-transform infrared spectroscopy), SEM (Scanning electron microscope), TGA (Thermogravimetric analysis) and PXRD (Powder diffraction). The homochirality of the dipeptide was studied by CD (Circular Dichroism), presenting a negative cotton effect in the UV-Vis spectrum.

With the objective of discerning which technique and medium use for the experiments, we first employed a Pressure Transmitting Medium (PTM) inside a Diamond Anvil Cell (DAC).[12,13] This technique allows to apply a constant and homogeneous force to all the parts of the crystal.[5,6,11] In order to enable a high-quality data collection avoiding amorphization at the same time, we first decided to start with simple PXRD experiments. The crystalline sample and one ruby crustal (used for reference) were gasketed inside the DAC equipped with a 500 um diamond culet. We immersed the crystals in fluorinert, methanol, ethanol, DMF and methanol:water (3:1) as quasi-hydrostatic liquids.[14,15] For all these materials, we recollected HP powder diffraction of up to 8GP and then back to atmospheric pressure for reference. The only noticeable difference in the sample was a merge and posterior split of two peaks as can be appreciated in **Figure 23c**, at [100] and [-401]. However, there was one medium that showed discrepancies, as the methanol:water medium possessed an additional peak merging of [-201] and [400] into one peak at 3.7 GPa with inversion frown low to high pressures. All these changes were reversible upon pressure release, and thanks to the characteristic absence of porosity of the MOF there was no pressure media penetrating inside its pores. Moreover, all the experiments showed a common broadening of the diffraction beyond the 4 GPa mark. The explanation to this phenomenon lies in the intrinsic deterioration of the quasi-hydrostatic conditions of the different PTMs used. Crystallinity is retained upon removal of the pressure to the highest point covered by the experiments, in particular, the broadening was less acute for the fluorinert and the methanol:water. This fact suggested that these were more adequate PTMs for single-crystal studies, being the next step analyzing the effect of pressure in a single-crystal for more precise structural information. In **Figure 2a** there is a representation of the volume change of the MOF cell in MeOH:EtOH:H_2O as the pressure increases. The unit cell shows a continuous compression down to 87% of the original value at 3.95 GPa, while remaining crystalline. The evolution of the unit cell parameters when compressed remains different depending on the orientation, and it is not the same for all the cell volume.

For the single-crystal HP-XRD experiments, structures were refined as pressure increased, using previous results as starting point on F2 by full-matrix least-squares refinement using the SHELXL program. The DAC imposed some structural

limitations as there is a small window where we only could obtain around 30% of the total reflections. For that reason, we employed structural refinements with isotropic displacement parameters for all atoms except the zinc, which was refined with anisotropic. We did not use any restrains in the simulations, and hydrogen atoms were included posteriorly.

These structural changes can be observed in the curves in **Figure 2b** where a slope change of around 2GPa clearly shows a differential change in phase, indicating an isostructural second-order phase transition. The space group of the crystal does not varies with pressure increase and also the cell volume does not show any discontinuity. Even though there is a decrease in the intensity of the diffraction as the pressure increases, the transformation does not seem compromise

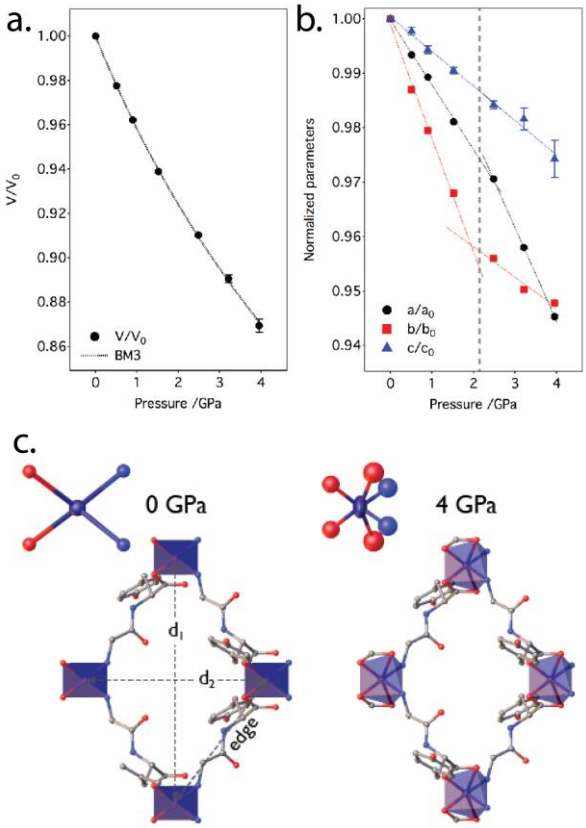

Figure 24. **a**. Unit cell volume compression with pressure. Dashed line stands for the EoS model fit. **b**. Evolution of the unit cell parameters with increasing pressure showing a discontinuity above 2 GPa. **c**. Structural changes in $Zn(GlyTyr)_2$ at high-pressure. Comparison of the structure at 0 and 4 GPa to show changes in coordination geometry and internal structure of the grid-like layer along the [101] direction.

in any way the integrity of the crystal, allowing us to refine the data sets and obtain precise structural information. This information made clear that $Zn(GlyTyr)_2$ displays a highly anisotropic resistance to compression. Concretely, once the structures for each pressure were resolved, we found that the direction [-101] displayed a high resistance to the compression due to the high density of atoms in this direction. However, the softest compression took place along in the [010] direction, as there lays the reorganization of phenyl rings, π-π interactions and hydrogen bonds.

The most characteristic changes from 0 to 4 GPa are summarized in **Figure 2c**, the phase transition of the system proceeds with a cooperative bond rearrangement of the coordination sphere of Zn(II) centers. This phenomenon is controlled by the coordination of the Gly carboxylate group, making the metallic cluster evolve from a four-fold distorted trigonal pyramidal geometry at room pressure into a six-fold distorted trigonal prismatic geometry. The change of the overall connectivity of the system occurs simultaneously on all the MOF, and upon the relaxation of its internal structure of layers, depending on adjustments in the supramolecular interactions on the peptide. This information points to the real responsible for the compressibility, the two amino acids in the peptide, as the main response to pressure is to shorten the H-bond distances that separate the interlayer. The peptide is the responsible for the cooperative changes in the MOF, being the Tyr the most important amino acid in relaxing the structure and retaining the crystallinity. There is a also a sharp decrease in the distance separating neighboring aromatic rings between Tyr, although this is not playing as much as an important role in directing the structural transformation. Overall, the conformations accessible thanks to the peptide combined with the non-covalent interactions allow this MOF to have a compressible cushion, allowing to accommodate there the large distortions that we provoked whilst avoiding amorphization. Moreover, thanks to the dense characteristic of the MOF, we can ascertain that this behavior is not affected by host/guest interactions allowing a real evaluation of the elasticity of the system without tampering.

3. References

1. C. Martí-Gastaldo, D. Antypov, J. E. Warren, M. E. Briggs, P. A. Chater, P. V. Wiper, G. J. Miller, Y. Z. Khimyak, G. R. Darling, N. G. Berry, M. J. Rosseinsky, Side-chain control of porosity closure in single- and multiple-peptide-based porous materials by cooperative folding. *Nat Chem*. **6**, 343–351 (2014).

2. C. Martí-Gastaldo, J. E. Warren, K. C. Stylianou, N. L. O. Flack, M. J. Rosseinsky, Enhanced Stability in Rigid Peptide-Based Porous Materials. *Angewandte Chemie Int Ed*. **51**, 11044–11048 (2012).

3. A. P. Katsoulidis, K. S. Park, D. Antypov, C. Martí-Gastaldo, G. J. Miller, J. E. Warren, C. M. Robertson, F. Blanc, G. R. Darling, N. G. Berry, J. A. Purton, D. J. Adams, M. J. Rosseinsky, Guest-

Adaptable and Water-Stable Peptide-Based Porous Materials by Imidazolate Side Chain Control. *Angew Chem-ger Edit*. **126**, 197–202 (2014).

4. J. Rabone, Y.-F. Yue, S. Y. Chong, K. C. Stylianou, J. Bacsa, D. Bradshaw, G. R. Darling, N. G. Berry, Y. Z. Khimyak, A. Y. Ganin, P. Wiper, J. B. Claridge, M. J. Rosseinsky, An Adaptable Peptide-Based Porous Material. *Science*. **329**, 1053–1057 (2010).

5. C. L. Hobday, R. J. Marshall, C. F. Murphie, J. Sotelo, T. Richards, D. R. Allan, T. Düren, F. Coudert, R. S. Forgan, C. A. Morrison, S. A. Moggach, T. D. Bennett, A Computational and Experimental Approach Linking Disorder, High-Pressure Behavior, and Mechanical Properties in UiO Frameworks. *Angew Chem-ger Edit*. **128**, 2447–2451 (2016).

6. K. J. Gagnon, C. M. Beavers, A. Clearfield, MOFs Under Pressure: The Reversible Compression of a Single Crystal. *J Am Chem Soc*. **135**, 1252–1255 (2013).

7. A. Celeste, A. Paolone, J.-P. Itié, F. Borondics, B. Joseph, O. Grad, G. Blanita, C. Zlotea, F. Capitani, Mesoporous Metal–Organic Framework MIL-101 at High Pressure. *J Am Chem Soc*. **142**, 15012–15019 (2020).

8. M. Andrzejewski, N. Casati, A. Katrusiak, Reversible pressure pre-amorphization of a piezochromic metal–organic framework. *Dalton T*. **46**, 14795–14803 (2017).

9. A. Worthy, A. Grosjean, M. C. Pfrunder, Y. Xu, C. Yan, G. Edwards, J. K. Clegg, J. C. McMurtrie, Atomic resolution of structural changes in elastic crystals of copper(II) acetylacetonate. *Nat Chem*. **10**, 65–69 (2018).

10. X. Zhou, Y. Miao, K. S. Suslick, D. D. Dlott, Mechanochemistry of Metal–Organic Frameworks under Pressure and Shock. *Accounts Chem Res* (2020).

11. K. W. Chapman, G. J. Halder, P. J. Chupas, Guest-Dependent High Pressure Phenomena in a Nanoporous Metal−Organic Framework Material. *J Am Chem Soc*. **130**, 10524–10526 (2008).

12. Y. Hu, Z. Liu, J. Xu, Y. Huang, Y. Song, Evidence of Pressure Enhanced CO2 Storage in ZIF-8 Probed by FTIR Spectroscopy. *J Am Chem Soc*. **135**, 9287–9290 (2013).

13. J. Sotelo, C. H. Woodall, D. R. Allan, E. Gregoryanz, R. T. Howie, K. V. Kamenev, M. R. Probert, P. A. Wright, S. A. Moggach, Locating Gases in Porous Materials: Cryogenic Loading of Fuel-Related Gases Into a Sc-based Metal–Organic Framework under Extreme Pressures. *Angewandte Chemie Int Ed*. **54**, 13332–13336 (2015).

14. M. J. P. Brugmans, W. L. Vos, Competition between vitrification and crystallization of methanol at high pressure. *J Chem Phys*. **103**, 2661–2669 (1995).

15. S. Klotz, J.-C. Chervin, P. Munsch, G. L. Marchand, Hydrostatic limits of 11 pressure transmitting media. *J Phys D Appl Phys*. **42**, 075413 (2009).

Publication 1:

Peptide metal–organic frameworks under pressure: flexible linkers for cooperative compression

Dalton Trans., 2018,47, 10654-10659

Dalton Transactions

PAPER

View Article Online
View Journal | View Issue

Cite this: *Dalton Trans.*, 2018, **47**, 10654

Peptide metal–organic frameworks under pressure: flexible linkers for cooperative compression†

José Navarro-Sánchez,[a] Ismael Mullor-Ruíz,[a,e] Catalin Popescu,[b] David Santamaría-Pérez,[c] Alfredo Segura,[c] Daniel Errandonea,[c] Javier González-Platas[d] and Carlos Martí-Gastaldo*[a]

Received 2nd May 2018,
Accepted 10th May 2018

DOI: 10.1039/c8dt01765d

rsc.li/dalton

We investigate the structural response of a dense peptide metal–organic framework using *in situ* powder and single-crystal X-ray diffraction under high-pressures. Crystals of $Zn(GlyTyr)_2$ show a reversible compression by 13% in volume at 4 GPa that is facilitated by the ability of the peptidic linker to act as a flexible string for a cooperative response of the structure to strain. This structural transformation is controlled by changes to the conformation of the peptide, which enables a bond rearrangement in the coordination sphere of the metal and changes to the strength and directionality of the supramolecular interactions specific to the side chain groups in the dipeptide sequence. Compared to other structural transformations in Zn(II) peptide MOFs, this behaviour is not affected by host/guest interactions and relies exclusively on the conformational flexibility of the peptide and its side chain chemistry.

Introduction

Metal–Organic Frameworks (MOFs) are crystalline, porous materials built from the interconnection of metal ions or clusters and organic linkers to produce porous architectures. Based on their unlimited chemical/structural versatility combined with fine control over porosity metrics, MOFs found rapid application as storage media and selective sieves for gases like carbon dioxide (clean energy and environmental protection), methane and hydrogen (energy storage) or as heterogeneous catalysts.[1,2] These applications involve subjecting MOFs to chemical/physical pressure and mechanical stress, which demands further understanding of their mechanical and structural response with applied pressure in order to optimize their performance. However, the number of works attempting to clarify this question remains still scarce. To date, most representative high-pressure crystallographic studies available include those on archetypical frameworks as HKUST-1,[3,4] zeolitic imidazolate frameworks (ZIF) – including the dense ZIF-4[5] and porous ZIF-8,[6,7] MOF-5,[8] MIL-53,[9] UiO[10] and more recently the retrofitting studies in MOF-520.[11] All these works are exclusively based on MOFs built from rigid polyaromatic connectors. Hence, structural transformations are limited to the relative displacement of organic and inorganic components of the net, contraction of coordination bonds or occasional tilting of the linker, which undergoes very small changes in its internal structure. Alternative linkers featuring a richer conformational landscape might result in more elastic frameworks for which the availability of multiple low-energy conformational states for the linker would enable reversible deformation under stress.[12] This is the case of oligopeptides based on short sequences of amino acids (aa's). Previous studies demonstrate that peptide MOFs feature unprecedented structural flexibility. They can accommodate their structure to environmental changes like solvent removal, guest exchange or pore filling with a manifold of responses that include: inelastic changes,[13] cooperative closure of porosity,[14] sponge-like behaviour,[15] guest inclusion[16] and adaptable porosity.[17]

Although this structural adaptability is often ascribed to the torsional flexibility of the peptidic chain, the presence of sidechain non-coordinating groups in the backbone of the peptide capable of establishing supramolecular interactions might be equally important in directing structural transform-

[a]*Universidad de Valencia (ICMol), Catedrático José Beltrán-2, 46980 Paterna, Spain. E-mail: carlos.marti@uv.es*
[b]*CELLS-ALBA Synchrotron Light Facility, Cerdanyola, Barcelona 08290, Spain*
[c]*Departamento de Física Aplicada-ICMUV, Universidad de Valencia, MALTA Consolider Team, Edificio de Investigación, C/Dr. Moliner 50, 46100 Burjassot, Valencia, Spain*
[d]*Departamento de Física, Universidad de La Laguna, 38204 La Laguna, Tenerife, Spain*
[e]*Department of Bioengineering. Imperial College London, London SW7 2 AZ, UK*

† Electronic supplementary information (ESI) available. CCDC 1588160–1588166. For ESI and crystallographic data in CIF or other electronic format see DOI: 10.1039/c8dt01765d

ations. The crystallographic studies available do not allow for easy discrimination between these two sources of changes to their structures. They are based exclusively on porous materials, for which framework/guest (solvent or gas molecules) interactions might be equally responsible for reversible changes in the structure. We hypothesised that this could be better understood with high-pressure X-ray diffraction studies of a dense peptide MOF. The effect of high pressures over the compressibility of this family of materials remains still unexplored and this would allow for neglecting the effect of pore filling and the changes associated with guest inclusion, generally responsible for pressure-induced transformations. In this way, structural response would be limited only to internal changes in the framework associated with inter-peptide supramolecular interactions and peptide–metal coordination bonds, to enable direct evaluation of the elasticity of this type of connectors and the frameworks built from them.

Results and discussion

Synthesis and structure of $Zn(GlyTyr)_2$

$Zn(GlyTyr)_2$ (GlyTyr = glycyl-L-tyrosine; Scheme 1) was synthesised by the solvothermal reaction of zinc(II) nitrate with enantiopure GlyTyr at 85 °C in a mixture of methanol and toluene. Controlled cooling results in the quantitative formation of colourless, prismatic crystals with sizes close to 50 μm (Fig. SI2†). $Zn(GlyTyr)_2$ crystallizes in the monoclinic, polar space group *I*2. Homochirality is confirmed by the Flack parameter value of 0.014(13) (Table SI1†). It is built from the four-fold coordination of Zn(II) centers by C-terminal Tyr carboxylate groups and N-terminal Gly amino groups of two GlyTyr molecules. These last act as bridges to form a neutral grid-like layer (Fig. 1a). The internal structure of this layer is reminiscent of other peptide-based porous materials like $Zn(GlyAla)_2$,[17] $Zn(GlySer)_2$[14] or $Zn(GlyThr)_2$[13] (Fig. SI7†). However, the solid packs into a dense structure with no empty space available for accommodating solvent molecules (Fig. 1b). Packing is controlled by H-bonding interactions between neighbouring layers that interleave them to produce a non-porous solid. As shown in Fig. 1c, supramolecular interactions involve the phenol units specific to the aa Tyr (O3) and the C=O (O4) and NH (N1) groups from the peptide bond (Table SI2†). As suggested by previous examples,[13,14,16,17] this highlights the importance of sidechain chemistry in directing the structure of metal–peptide coordination polymers. The structure of $Zn(GlyTyr)_2$ makes it ideal to study the intrinsic elasticity of the dipeptide connector with external pressure. Besides neglecting the effect of host/guest interactions over the structural response of the solid, the absence of solvent is also expected to simplify the refinement of High-Pressure X-Ray Diffraction (HP-XRD) data.

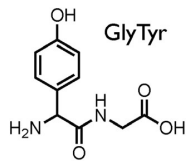

Scheme 1 Structure of glycyl-L-tyrosine (GlyTyr).

High-pressure powder X-ray diffraction and effect of the pressure transmitting medium

Previous works suggest that the Pressure Transmitting Medium (PTM) used for the hydrostatic regime affects the structural response and amorphization pressure of metal–organic hybrids.[4,10,18] In order to define which was the most suitable medium to enable high-quality data collection at high-pressures whilst avoiding amorphization, we first carried out powder XRD experiments. As shown in SI2,† phase purity of the bulk material was first confirmed by CHN, FT-IR, Scanning Electron Microscopy (SEM), thermogravimetric analysis and powder X-ray diffraction (PXRD). Homochirality

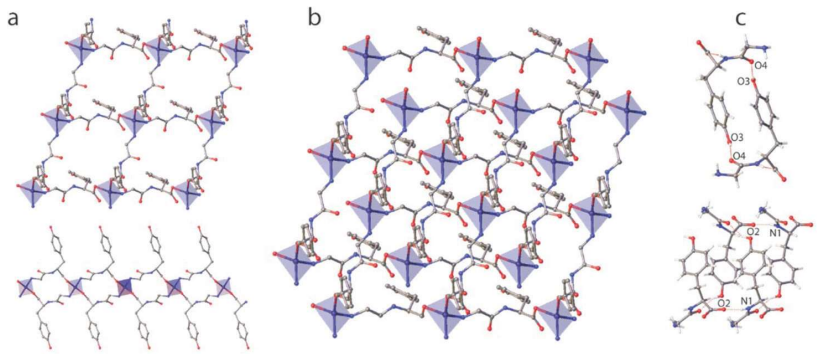

Fig. 1 Structure of $Zn(GlyTyr)_2$. (a) View of the peptide metal grid-like layer along [1 1 1] (top) and [0 1 0] (bottom) directions. (b) The solid crystallizes as a dense material due to interweaving of neighbouring layers. (c) Packing is controlled by inter-layer H-bonding interactions specific to the Tyr sidechain (top) and the peptide bond (bottom).

was also confirmed with circular dichroism (CD), which presents a negative Cotton effect in the UV-Vis spectrum below 300 nm due to Zn(II) complexation with enantiopure glycil-L-tyrosine (Fig. SI6†). Polycrystalline samples and ruby crystals, for pressure calibration, were loaded into a gasketed Diamond Anvil Cell (DAC) equipped with a 500 μm diamond culet. Next, in different experiments, they were immersed in Fluorinert (FC-70), methanol, ethanol, dimethylformamide (DMF) and a mixture of methanol and water (3 : 1 in volume) as quasi-hydrostatic liquids. HP powder diffraction was collected on increasing pressures up to a maximum of 8 GPa and then back to ambient pressure for reference. For all of them we found a qualitatively similar behaviour. Bragg peaks evolve towards higher angles under compression with different pressure dependences, which is a consequence of the anisotropic compression of the solid. As result, a few peaks merge under compression and others, like [100] and [−401], split. There is no evidence of the pressure media penetrating into the MOF. There are some changes in the relative intensities of Bragg peaks due to preferential orientations, which get amplified because of the focused X-ray beam used. All the experiments show a broadening of the diffraction beyond 4 GPa due to the deterioration of quasi-hydrostatic conditions of the different PTMs used.[19,20] However, crystallinity is retained up to the highest pressure covered by the experiments. The peak broadening was more acute for the experiments performed in MeOH, EtOH and DMF (Fig. SI8–SI10†). In turn, the quality of the PXRD patterns in FC-70 (Fig. SI11†) and MeOH : H_2O (Fig. 2) experiments is comparatively higher, suggesting that these were the more adequate PTMs for single-crystal studies. This last shows an anisotropic compression that accounts for the differential pressure evolution of Bragg peaks. This is confirmed by the merging of [−201] and [400] into one peak at 3.7 GPa and their inversion from low to high pressures. All the changes observed were reversible upon pressure release.

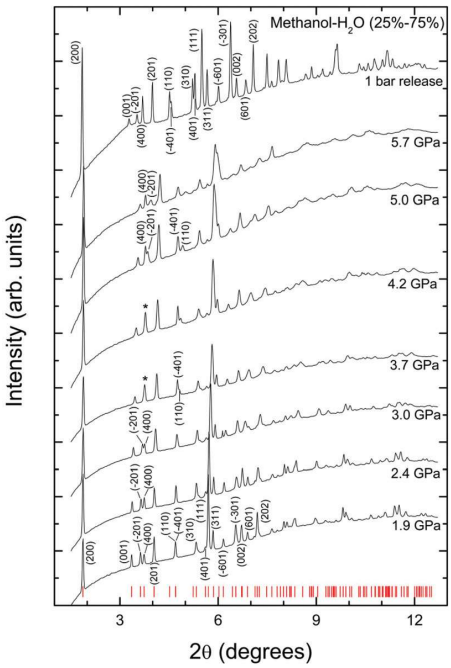

Fig. 2 HP-PXRD of $Zn(GlyTyr)_2$ in methanol : water (3 : 1). The merging of the diffraction lines [−201] and [400], which stand for anisotropic compression, is highlighted.

High-pressure structural transformation in a single crystal

With this information in hand we decided to analyse the effect of pressure in a single-crystal for more precise structural information. Fig. 3a represents the evolution of the volume cell of $Zn(GlyTyr)_2$ in MeOH : EtOH : H_2O (16 : 3 : 1) on increasing pressure. The unit cell shows a continuous compression down to 87% of the original value at 3.95 GPa, while remaining crystalline. It is worth noting that this variation is equivalent to the reversible compression described above for the polycrystalline solid by using MeOH : H_2O as PTM (Fig. SI14†). This denotes a resilient material with a large pressure response that lies close to the maximum volume changes reported for other molecule-based crystalline materials like ZAG-4 (27%, 7 GPa)[18] or the family $LnFe(CN)_6$ (20%, 1 GPa).[21] We used the EosFit7-GUI program[22] to calculate the equation of state (EoS) using a third-order Birch–Murnaghan function (Fig. SI14 and Table SI3†). This provides a value of V_0 of 1082.00(6) Å^3 and a bulk modulus of K_0 = 21.9(9) GPa and K' = 4.2(8). All refinements of EoS yield $\omega\chi^2 < 1$ due to over-estimation of $\sigma(P)$, but none of the fits show any systematic variation of $P_{obs} - P_{calc}$ with pressure, ensuring that the calculated parameters are consistent with the experimental data. For comparison, molecular solids generally present bulk moduli below 30 GPa.[23] In particular, MOFs often present a lower resistance to compression that scales down with increasing porosity and lower density. Although higher K values have been reported, these are not directly related to the compression of the framework but to the penetration of the PTM into the pores that increases the stability of the system at low-P regimes.[24] When it comes to non-porous (dense) MOFs, the compressibility of $Zn(GlyTyr)_2$ is substantially higher than those reported for very stable zeolite-type materials like $Zn(Im)_2$-zni (14 GPa)[23] and $LiB(Im)_4$ (16.6 GPa).[25] Also, these last display smaller changes in the volume cell at the higher pressures studied (below 10%).

The evolution of unit cell parameters upon compression is different from that of the unit cell volume (Fig. 3b). The curves show a slope change above 2 GPa that suggests a possible phase transition. We argue that this can be classified as an isostructural second-order phase transition as there is no change in the space group and the compression of the cell volume does not show any discontinuity in the range of pressures evaluated. To our surprise, apart from decreasing diffraction intensity, this transformation takes place without compromising the integrity of the crystal thus enabling refinement of all data sets for precise structural information. As earlier suggested by HP-PXRD experiments, $Zn(GlyTyr)_2$ displays a highly aniso-

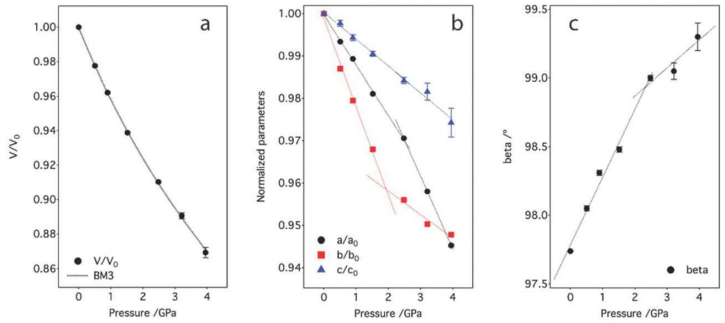

Fig. 3 HP cell contraction of single-crystals of Zn(GlyTyr)2 in methanol : ethanol : water. (a) Unit cell volume compression with pressure. Dashed line stands for the EoS model fit. Error bars are smaller than their respective size symbols. (b) Evolution of the unit cell parameters and (c) beta angle with increasing pressure showing a discontinuity above 2 GPa. Solid lines are only a guide to the eye.

tropic resistance to compression. As shown in Fig. SI16,† the direction [−101] displays a high resistance to the compression for negligible changes close to 1% due to the high density of atoms in this direction while the softest compression takes place along in the [010] direction (or [101] after 3 GPa) on account of the reorganization of phenyl rings and therefore pi–pi interactions and some hydrogen bonds. This is often observed for layered covalent crystals, for which intralayer distances are less compressible than those between layers.[26] Fig. 4 summarises the most characteristic changes to the structure of the peptide MOF with pressure. The phase transition proceeds *via* cooperative bond rearrangement in the coordination sphere of Zn(II) centers controlled by the coordination mode of the C-term Gly carboxylate group, which evolves from a four-fold distorted trigonal pyramidal (η^1) geometry at room pressure into a six-fold distorted trigonal prismatic geometry (η^2). As pointed out before, according to our HP-PXRD data (Fig. SI12†), this transformation proceeds reversibly. This change to the overall connectivity of the network is not isolated and proceeds upon the relaxation of the structure. This is enabled by cooperative changes to the internal structure of the layers, the conformation of the dipeptide and adjustments to

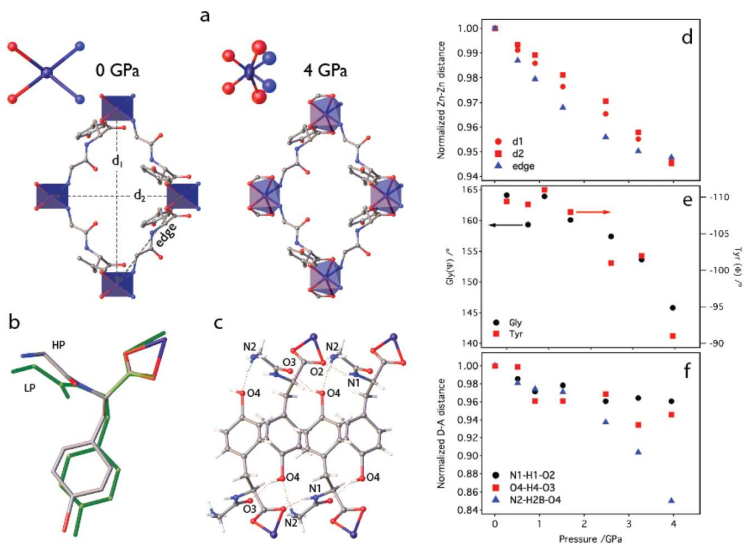

Fig. 4 Structural changes in $Zn(GlyTyr)_2$ at high-pressure. Comparison of the structure at 0 and 4 GPa to show changes in: (a) coordination geometry and internal structure of the grid-like layer along the [101] direction. Variations in the distance separating Zn(II) has been measured for the edge and diagonals (d1 and d2) of the rhomboid; (b) changes to the peptide conformation. For clarity, the LP phase is highlighted in green. (c) Formation of additional H-bonds at 4 GPa. Evolution of the most relevant structural parameters with pressure: (d) Zn–Zn distance, (e) peptide internal dihedral angles (Ψ and Φ) and (f) selected H-bond distances along the [100] direction. For clarity, changes have been normalized to the value at room pressure. See Table SI5† for the absolute values.

the directionality and strength of interlayer supramolecular interactions. As shown in Fig. 4a and d, the grid-like layers feature an isotropic compression. The edge and diagonal distances (d_1 and d_2) separating the metal nodes display an equivalent compression regime and decrease by close to 6% of the original value. This is coupled to a change in the dihedral angles of the peptide backbone. Ψ shows a clear closure trend from 164.1(3) to 146(6)° whereas Φ changes from −109.4(3) to −91(8)°. This suggests that the response of the linker to stress is controlled by the cooperative rotation of the two amino acids in the peptide. The solid also shortens the H-bond distances that dictate the interlayer separation for accommodating the change in pressure. This results in a compression of the bonds O4···O3 and N1···O2 down to 2.50(9) and 2.72(6) Å for a change of 3.9 and 5.4%, respectively (Fig. 4f). More important is the formation of an additional H-bond N2···O4 between the nitrogen in the amide bond and the –OH group in Tyr that becomes relatively strong (2.54(14) Å) after compressing close to 15% of its original value (Fig. 4c, Table SI5†). This highlights the importance of supramolecular interactions in controlling cooperative changes in peptide MOFs. Just like $Zn(GlySer)_2$, in which the –OH groups intrinsic to Ser are key to enable cooperative closure of the structure upon the formation of intralayer H-bonds,[14] the phenol units in Tyr seem to play an important role in relaxing the structure and retaining crystallinity up to very high pressures. As for the π–π interactions between neighbouring units, we also identify a clear decrease in the distance separating the aromatic rings in Tyr (Fig. SI18†). However, they are not short enough to consider them playing an important role in directing the structural transformation.

Conclusions

In summary, we have carried out a crystallographic study to unveil the structural response of peptide MOFs to high-pressures for the first time. Crystals of $Zn(GlyTyr)_2$ can be compressed reversibly by 13% in volume at 4 GPa, whilst maintaining long-range order. The peptide, acting as a metal connector, behaves as a flexible string and facilitates a cooperative response of the structure to mechanical strain. The relaxation of the structure is controlled by the internal rotation of the two amino acids in the peptide that modify its conformation and trigger a bond rearrangement at the coordination sphere of the metal coupled to changes in the strength and directionality of H-bonds. Overall, the landscape of conformations accessible to the peptide combined with the directional nature of non-covalent interactions provides a compressible cushion that allows for accommodating large distortions in the framework whilst avoiding amorphization. Compared to other structural transformations reported for peptide MOFs based on tetrahedral Zn(II) nodes,[14] this behaviour is not affected by host/guest interactions and relies exclusively on the conformational flexibility of the peptide and its side chain chemistry.

Conflicts of interest

There are no conflicts to declare.

Acknowledgements

This work was supported by the EU (FEDER funds) and the Spanish MINECO (MDM-2015-0538, MAT2015-71070-REDC, MAT2016-75586-C4-4-P, MAT2016-75586-C4-1-P & CTQ2017-83486-P). C. M.-G. and D. S.-P. thank the Spanish MINECO for a Ramón y Cajal Fellowship (RyC-2012-10894 and 2014-15643). J. G.-P. thanks the X-ray General Service (SIDIX) at La Laguna University. HP experiments were performed at the MSPD beamline at ALBA Synchrotron with the collaboration of in-line staff.

Notes and references

1 H. Furukawa, K. E. Cordova, M. O'Keeffe and O. M. Yaghi, *Science*, 2013, **341**, 1230444–1230444.
2 K. Adil, Y. Belmabkhout, R. S. Pillai, A. Cadiau, P. M. Bhatt, A. H. Assen, G. Maurin and M. Eddaoudi, *Chem. Soc. Rev.*, 2017, **46**, 3402–3430.
3 A. Graham, J. Tan and D. Allan, *Chem. Commun.*, 2012, **48**, 1535–1537.
4 K. W. Chapman, G. J. Halder and P. J. Chupas, *J. Am. Chem. Soc.*, 2008, **130**, 10524–10526.
5 T. D. Bennett, P. Simoncic, S. A. Moggach, F. Gozzo, P. Macchi, D. A. Keen, J.-C. Tan and A. K. Cheetham, *Chem. Commun.*, 2011, **47**, 7983–7985.
6 C. L. Hobday, T. D. Bennett, D. Fairen-Jimenez, A. J. Graham, C. A. Morrison, D. R. Allan, T. Düren and S. A. Moggach, *J. Am. Chem. Soc.*, 2018, **140**, 382–387.
7 S. A. Moggach, T. D. Bennett and A. K. Cheetham, *Angew. Chem., Int. Ed.*, 2009, **48**, 7087–7089.
8 A. J. Graham, D. R. Allan, A. Muszkiewicz, C. A. Morrison and S. A. Moggach, *Angew. Chem., Int. Ed.*, 2011, **50**, 11138–11141.
9 P. Serra-Crespo, E. Stavitski, F. Kapteijn and J. Gascon, *RSC Adv.*, 2012, **2**, 5051–5053.
10 C. L. Hobday, R. J. Marshall, C. F. Murphie, J. Sotelo, T. Richards, D. R. Allan, T. Düren, F.-X. Coudert, R. S. Forgan, C. A. Morrison, S. A. Moggach and T. D. Bennett, *Angew. Chem., Int. Ed.*, 2016, **128**, 2447–2451.
11 E. A. Kapustin, S. Lee, A. S. Alshammari and O. M. Yaghi, *ACS Cent. Sci.*, 2017, **3**, 662–667.
12 A. Worthy, A. Grosjean, M. C. Pfrunder, Y. Xu, C. Yan, G. Edwards, J. K. Clegg and J. C. McMurtrie, *Nat. Chem.*, 2017, **20**, 5834.
13 C. Marti-Gastaldo, J. E. Warren, K. C. Stylianou, N. L. O. Flack and M. J. Rosseinsky, *Angew. Chem., Int. Ed.*, 2012, **51**, 11044–11048.
14 C. Martí-Gastaldo, D. Antypov, J. E. Warren, M. E. Briggs, P. A. Chater, P. V. Wiper, G. J. Miller, Y. Z. Khimyak,

G. R. Darling, N. G. Berry and M. J. Rosseinsky, *Nat. Chem.*, 2014, **6**, 343–351.
15 C. Martí-Gastaldo, J. E. Warren, M. E. Briggs, J. A. Armstrong, K. M. Thomas and M. J. Rosseinsky, *Chem. – Eur. J.*, 2015, **21**, 16027–16034.
16 A. P. Katsoulidis, K. S. Park, D. Antypov, C. Martí-Gastaldo, G. J. Miller, J. E. Warren, C. M. Robertson, F. Blanc, G. R. Darling, N. G. Berry, J. A. Purton, D. J. Adams and M. J. Rosseinsky, *Angew. Chem., Int. Ed.*, 2014, **53**, 193–198.
17 J. Rabone, Y. F. Yue, S. Y. Chong, K. C. Stylianou, J. Bacsa, D. Bradshaw, G. R. Darling, N. G. Berry, Y. Z. Khimyak, A. Y. Ganin, P. Wiper, J. B. Claridge and M. J. Rosseinsky, *Science*, 2010, **329**, 1053–1057.
18 K. J. Gagnon, C. M. Beavers and A. Clearfield, *J. Am. Chem. Soc.*, 2013, **135**, 1252–1255.
19 M. J. P. Brugmans and W. L. Vos, *J. Chem. Phys.*, 1998, **103**, 2661–2669.
20 S. Klotz, J. C. Chervin, P. Munsch and G. Le Marchand, *J. Phys. D: Appl. Phys.*, 2009, **42**, 075413.
21 S. G. Duyker, V. K. Peterson, G. J. Kearley, A. J. Studer and C. J. Kepert, *Nat. Chem.*, 2016, **8**, 270–275.
22 J. Gonzalez-Platas, M. Alvaro, F. Nestola and R. Angel, *J. Appl. Crystallogr.*, 2016, **49**, 1377–1382.
23 E. C. Spencer, R. J. Angel, N. L. Ross, B. E. Hanson and J. A. K. Howard, *J. Am. Chem. Soc.*, 2009, **131**, 4022–4026.
24 S. C. McKellar and S. A. Moggach, *Acta Crystallogr., Sect. B: Struct. Sci., Cryst. Eng. Mater.*, 2015, **71**, 587–607.
25 T. D. Bennett, J.-C. Tan, S. A. Moggach, R. Galvelis, C. Mellot-Draznieks, B. A. Reisner, A. Thirumurugan, D. R. Allan and A. K. Cheetham, *Chem. – Eur. J.*, 2010, **16**, 10684–10690.
26 D. Errandonea, D. Martínez-García, A. Segura, J. Haines, E. Machado-Charry, E. Canadell, J. C. Chervin and A. Chevy, *Phys. Rev. B: Condens. Matter Mater. Phys.*, 2008, **77**, 045208.

Supplementary information

Peptide Metal-Organic Frameworks under pressure: flexible linkers for cooperative compre

José Navarro-Sánchez, Ismael Mullor-Ruíz, Catalin Popescu, David Santamaría-Pérez, Alfredo Segura, Daniel Errandonea, Javier González Platas and Carlos Martí-Gastald

Table of Contents

SI1. General considerations: starting materials and characterization

Materials and reagents

All reagents and solvents used were of commercially available grade and were used without any additional purification. The dipeptide H-Gly-Tyr-OH and the metal salt $Zn(NO_3)_2.6H_2O$ was purchased from Sigma®. Methanol and toluene were supplied by Scharlau. Ultrapure water was obtained from a Nanopure II (Sybron) system

Physical and chemical characterizatio

- Carbon, nitrogen and hydrogen contents were determined by microanalytical procedures using a LECO CHNS
- Infrared spectra were recorded in an Agilent Cary 630 FTIR Spectrometer directly with KBr pellets
- Thermogravimetric analysis was carried out with a Mettler Toledo TGA/SDTA 851e apparatus between 25 and 800 °C under ambient conditions (10 °C·min^{-1} scan rate and an air flow $^{-1}$)
- Powder XRD patterns were collected in a PANalytical X'Pert PRO diffractometer using copper radiation (Kα = 1.5418 Å) with an X'Celerator detector, operating at 40 mA and 45 kV. Profiles were collected in the 2° < 2θ < 40 range with a step size of 0.017°.
- Single-crystal XRD data at room pressure was collected in a Rigaku SuperNOVA diffractometer equip ATLAS detector (CCD) and Cu radiation micro-source (C Kα = 1.54184 Å)
- Angle dispersive powder HP-XRD were performed at MSPD beamline of Alba synchrotron light source using monochromatic beam (λ=0.4246 Å). The 2D patterns were collected using a Rayonix SX165 CCD detector locate 350 mm away from the sample and then integrated using FIT2D. The typical acquisition time was 20 s.
- Single-crystal HP-XRD was performed at MSPD beamline of Alba synchrotron light source with a wavelen λ=0.3185 Å focused down to 20x20 μm^2 (FWHM). The diffraction images were collected by 0.2^0 ω scanning using a Rayonix SX165 CCD detector placed 170 mm away from the sample.
- NIKON Eclipse LV-100 Optical microscope equiped with a digital camera: Nikon, D7000 AF-S DX NiKKOR 18-105mm f/3.5-5.6G ED VR was used for taking pictures of the crystals
- Chiral dichroism (CD) UV-Vis spectrum was collected with a spectropolarim

SI2. Synthesis and characterization of $Zn(GlyTyr)_2$

Synthesis of Zn(GlyTyr $_2$. 47.6 mg of Gly-Tyr (0.2 mmol) are dissolved in 7.6 mL of $Zn(NO_3)_2.6H_2O$ 0.13M methanolic solution in a 12 mL scintillation vial. The mixture is hand shaken to render a colourless solution followed by addition of 4 mL of toluene. The mixture is mechanically stirred for 15 minutes and then transferred to an oven and heated at 85ºC for two minutes. This results on the formation of colourless crystals tha
filtration, washed thoroughly with methanol and left to stand at room temperature for dr
This protocol was repeated 5 times to produce a total of 270 mg (30% yield calculated for zinc).
Analysis. calc. for $Zn(C_{15}H_{20}O_4N_2)$ (Mw: 357.71) Calc. C: 48.95 H: 4.85 N: 10.38. Found: C:47.98 H:5.01 N: 10.2

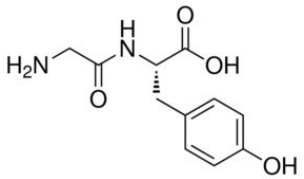

Glycil-L-tyrosine (Gly-Tyr)

Figure SI1. Optical microscope and of as-made crystals of Zn(Gly-T $_2$.

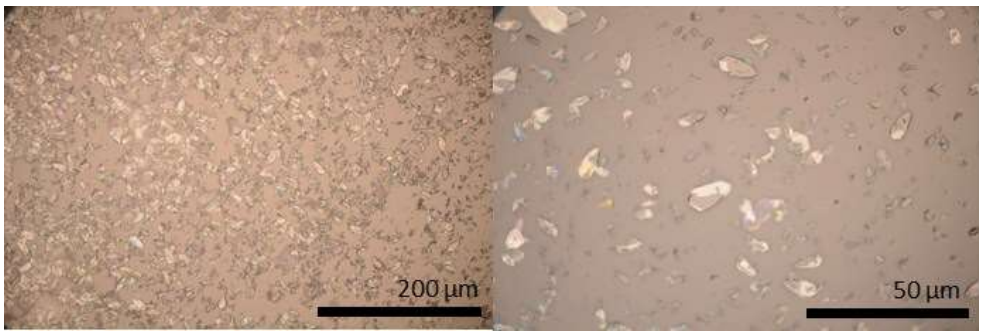

Figure SI2. Scanning Electron Microscopy (SEM) images. Particle morphologies and dimensions were studied with a Hitachi S-4800 scanning electron microscope at an accelerating voltage of 20 keV, over metalized samples with a mixture of gold and palladium during 30

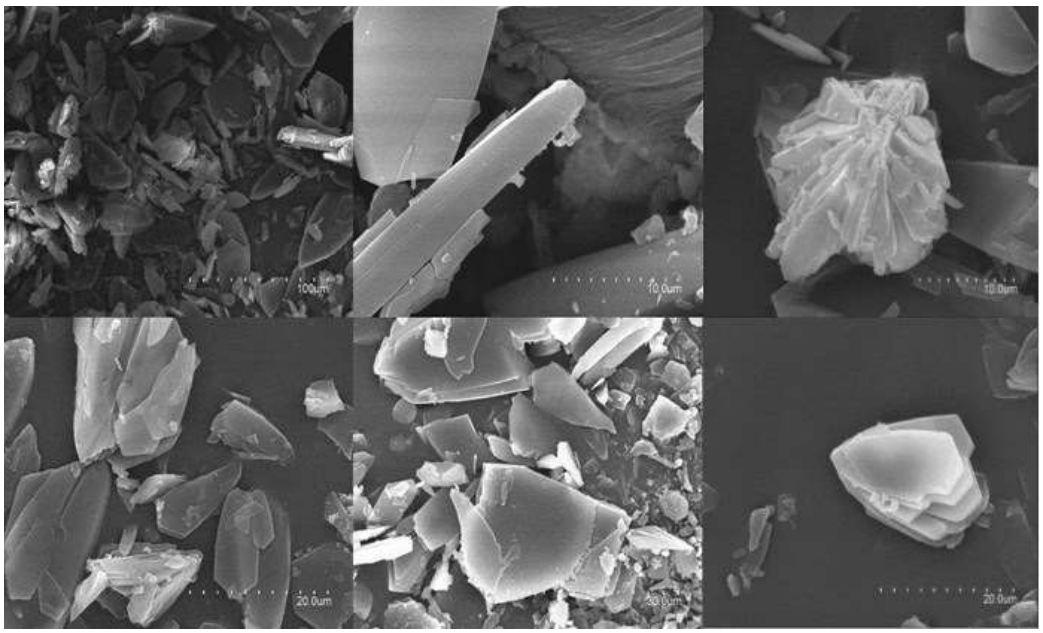

Figure SI3. FT-IR of $Zn(Gly\text{-}Tyr)_2$ collected in a FT-IR Nicolet 5700 spectrometer in the 4000–400 cm^{-1} range from ground crystals diluted in a KBr pellet.

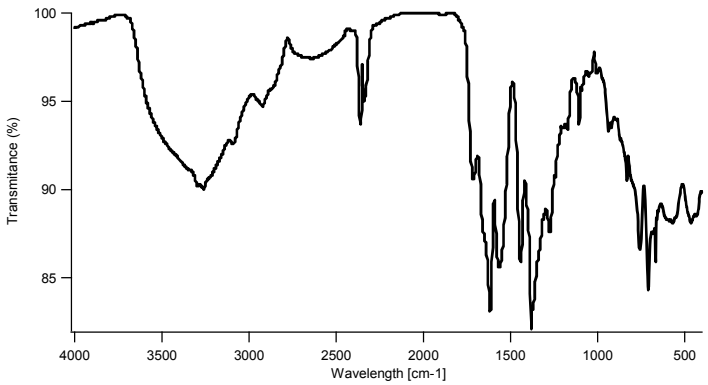

(KBr, [cm-1]): 300 (m), 610 (m), 1200 (m), 1400 (m), 1600 (m), 2400 (w), 2900 (w), 2450 (sr, br), 3700

Figure SI4. Thermogravimetric analysis of $Zn(Gly\text{-}Tyr)_2$ between 25 and 800 °C under a 5 °C.min^{-1} scan rate and an air flow o 30 mL.mi $^{-1}$ by using a a Mettler Toledo TGA/SDTA 851.

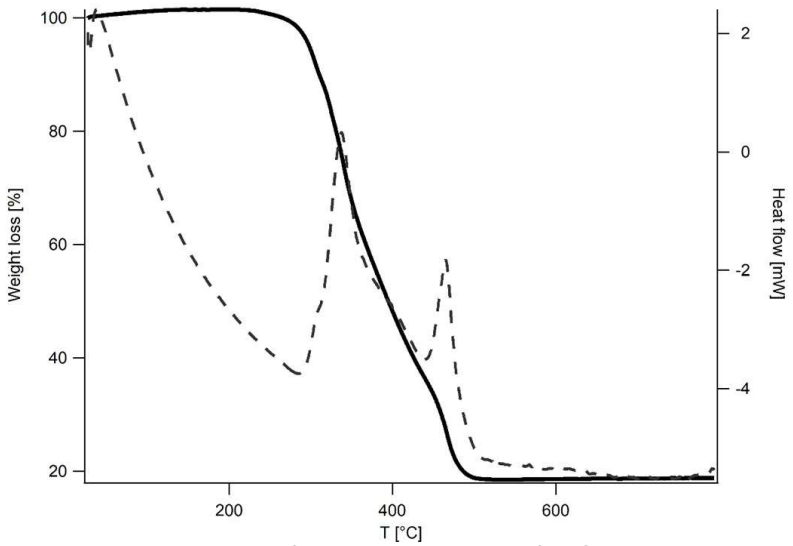

There is no weight loss at low temperature that confirms the dense structure of $Zn(GlyTyr)_2$.

Figure SI5. Experimental PXRD (red line), calculated (blue line), difference plot [(Iobs−Icalcd)] (black line, bottom panel) and Bragg positions (green dashed line) for the unit cell refinement of experimental diffraction data of Zn(Gly-Tyr)2 collected at room temperature by using experimental single-crystal data as starting parameters.1 PXRD patterns were collected in a PANalytical X'Pert PRO diffractometer using copper radiation (Kα = 1.5418 Å) with an X'Celerator detector, operating at 40 mA and 45 kV. Profiles were collected in the 2° < 2θ < 60° range with a step size of 0.0

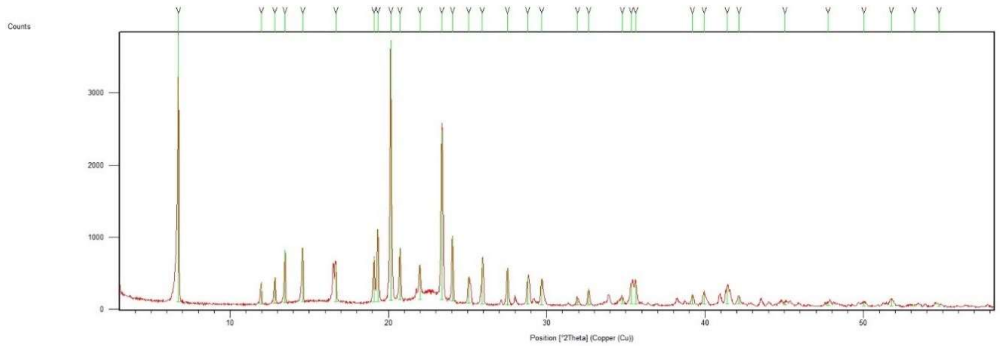

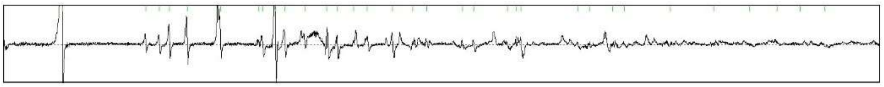

Monoclinic, I 2; a =7.4716(5), b = 5.4271(3), c = 26.6069(14) Å; V = 1068.21 Å^3. X^2 = 1.529E-06. Snyder's FOM = 4.789

Figure SI6. Chiral dichroism (CD) UV-Vis spectrum of Gly-Tyr (blue) and Zn(Gly-Tyr)2 (green). Solution used for th measurements was prepared by diluting ground crystals of the MOF in ultrapure water. Spectra was collected wit spectropolarimeter Jasco J-810 and recorded at a temperature of 25°C. Ellipticity values were recorded every 0.5 nm at wavelength scanning speed of 100 nm/min. The response time was set to 1 s and the bandwidth was set to 1 nm. The final spectrum represented the accumulated average of ten consecutive scans with baseline correction. As the free dipeptide gives a shift in the area of the peptidic bond (displays a negative Cotton effect in the UV region linked to the presence of enantiop dipeptide), the other one has a negative adsorption due to Zn (II) complexatio

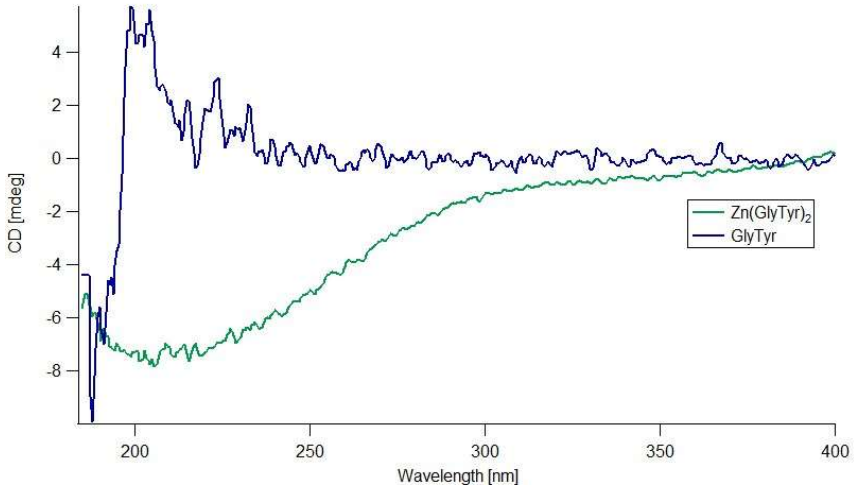

SI3. X-Ray diffraction and structure of Zn(Gly 2

X-ray diffraction (XRD) measurement was collected at room temperature by using a Rigaku SuperNOVA diffractometer equipped with an EOS detector (CCD) and Mo radiation micro-source (λ=0.71073Å) and CrysAlisPro softwar [1] was used to process the data. The structure of the compound at rt was determined by a dual-space algorithm using t [2] and refinement was performed using SHELXL [3] against F^2 by full-matrix least-squares refinement. All non-hydrogen atoms were refined anisotropically and hydrogen atoms were included in the model at calculated positions, and refined with a rigid model with their U_{iso} value to 1.2U_{eq} of their parent atoms. The PLATON program[4] has been used for geometric calculation

Crystallographic data for the structures reported in this contribution have been deposited with the Cambridge Crystallographic Data Centre as supplementary publication. Copies of the data can be obtained free of charge on applic Cambridge, U.K. (http://www.ccdc.cam.ac.uk/).

Table SI1. Crystal data and structure refinement for Zn(GlyTyr $_2$ at environmental pressure.

Identification c	1588160
Empirical formu	$C_{22}H_{26}N_4O_8Zn$
M	539.84
Cryst. Syst.	Monoclinic
Space grou	I2
a, Å	7.4908 (2)
b, Å	5.4877 (2)
c, Å	26.5634 (10)
α, °	90
β, °	97.740 (3
γ, °	90
V, Å^3	1082.00 (6
Z	2
D_c/g cm^{-3}	1.657
F(000)	560
μ(Mo Kα), mm^{-1}	2.109
Reflections (collected/un (Rint))	4430/2206/0.019
Data/restrains/paramet ers	2206/1/160
R1, wR [$F^2>2\sigma(F^2)$]	0.025/0.065
Goodness-of-f [2]	1.048
Largest diff. peak and hole (e Å^{-3})	0.27/-0.21
Flack paramet	0.014(13)

Refinement model description: number of restraints – 0; number of constraints – 0.

Figure SI7. Ortep representation (50% probability) of the asymmetric unit of Zn(GlyTy $_2$.

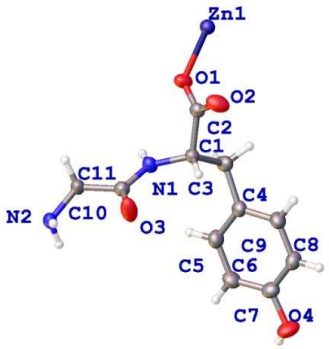

Table SI2. Hydrogen bonds for $Zn(GlyTyr)_2$.

D	H	A	d(D-H)/Å	d(H-A)/Å	d(D-A)/Å	D-H-A/°
N1	H1	O2(i)	0.86	1.98	2.831(4)	169
N2	H2B	O4(ii)	0.89	2.23	2.987(3)	143
O4	H4	O3(ii)	0.82	1.89	2.643(4)	152
N2	H2A	O3	0.89	2.46	2.789(4)	102

(i) x,1+y,z (ii) 3/2-x,1/2+y,3/2-z

Figure SI8. Structure of (a) Zn(GlyAl $_2$,[5] (b) Zn(GlyS $_2$,[6] and (c) $Zn(GlyThr)_2$.[7] Neutral layers are represented along parallel (top) and perpendicular directions (bottom).

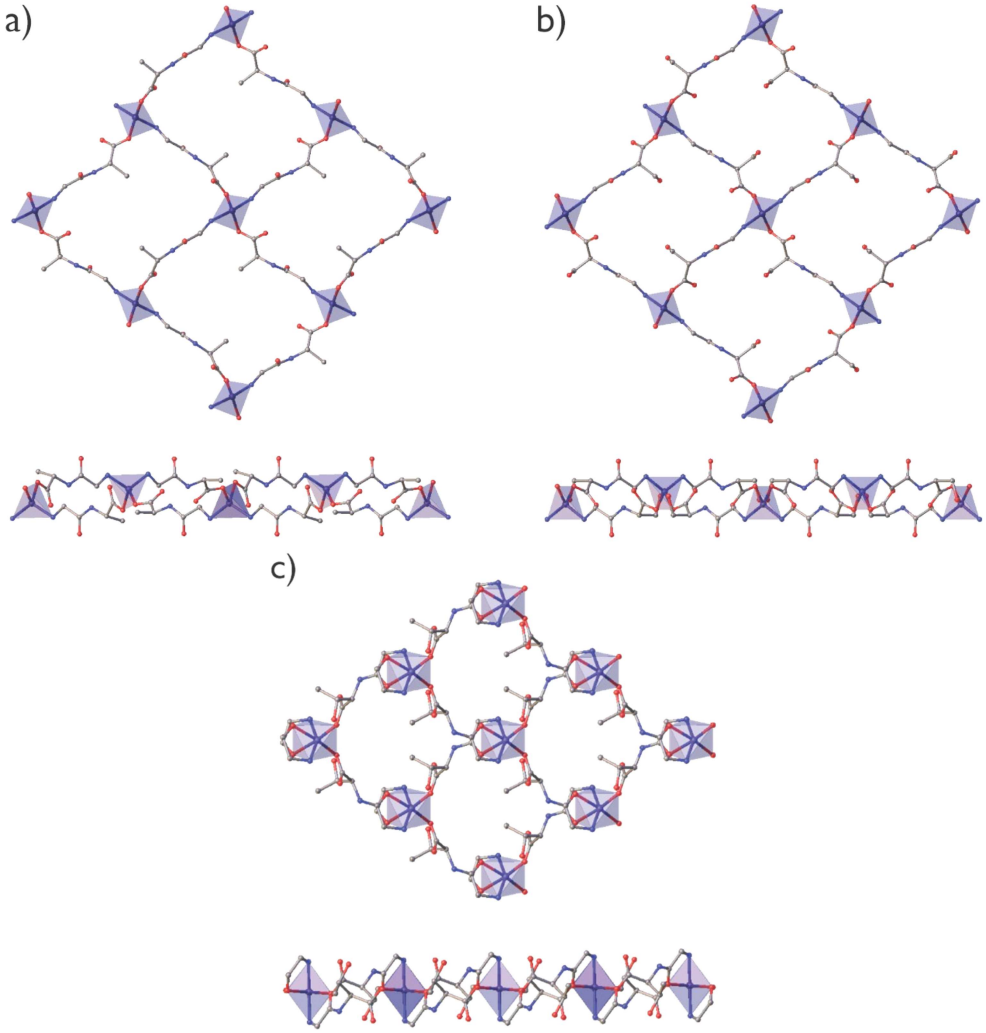
a)
b)
c)

SI4. Powder High-Pressure X-Ray diffraction and effect of Pressure Transmitting Media over structural re

Five series of synchrotron-based powder XRD experiments under compression were performed using different pressure media: Fluorinert FC-70 (Figure SI8), methanol (Figure SI9), ethanol (Figure SI10), dimethylformamide (Figure SI11) and methanol a water 3:1 in volume (Figure 2 in the text). The maximum pressure reached was 10 GPa, but due to peak broadening and par amorphization we only show the data below 6 GPa. Angle-dispersive XRD experiments were carried out using diamond-an cells (DAC) with diamond culets of 500 and 700 μm. The pressure chamber was a 200-3 μm hole drilled on a 40-μm pre indented Inconel gasket. Pressure was determined by using ruby fluorescence.[8] Particular attention was paid to avoid sample bridging between the diamond anvils [9] Experiments were performed at the materials science and powder diffraction (MSPD) beamline of the ALBA synchrotron.[10] A monochromatic beam (λ = 0.4246 Å) focused to a beam size down to 20 μm x 20 μm (FWHM) using Kirkpatrick-Baez mirrors. The two-dimensional XRD patterns were collected using a Rayonix SX165 C detector and integrated with FIT2D[11] , while structural analyses were performed with GSAS.[12]

Figure SI9. High-pressure powder diffraction data in methan

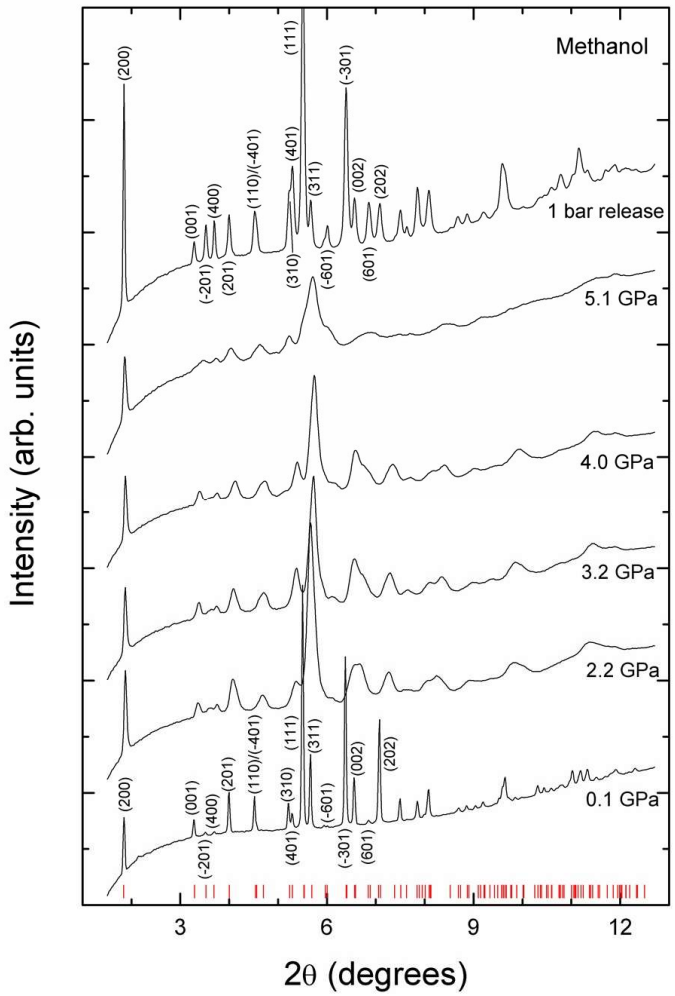

Figure SI10 High-pressure powder diffraction data in eth

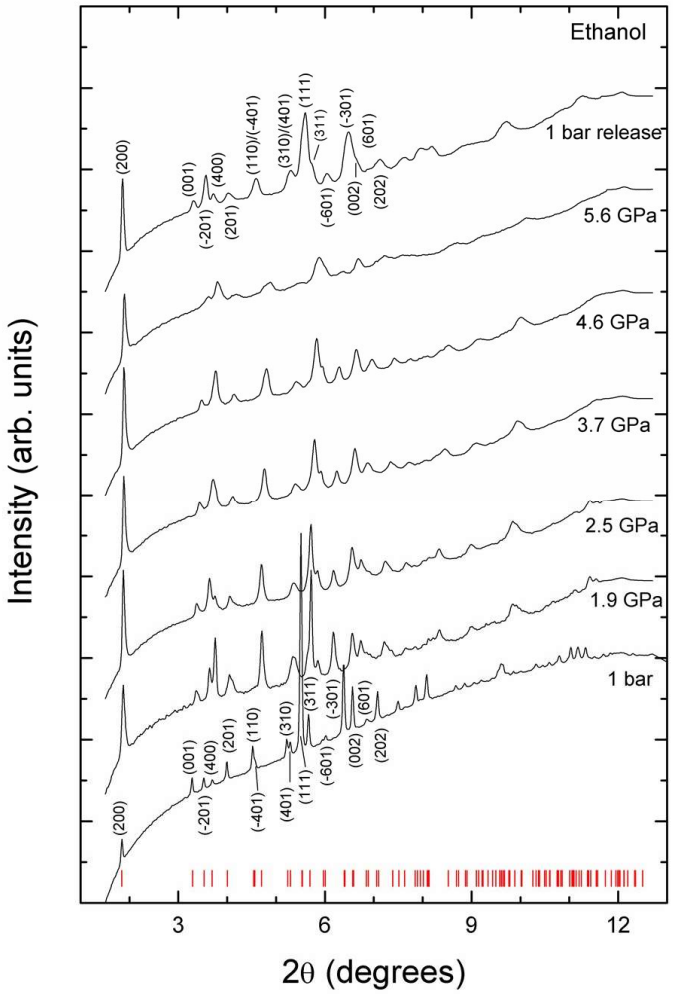

Figure SI11. High-pressure powder diffraction data in dimethylformamide. The two new diffraction lines observed at low angles correspond to Bragg peaks of DMF.

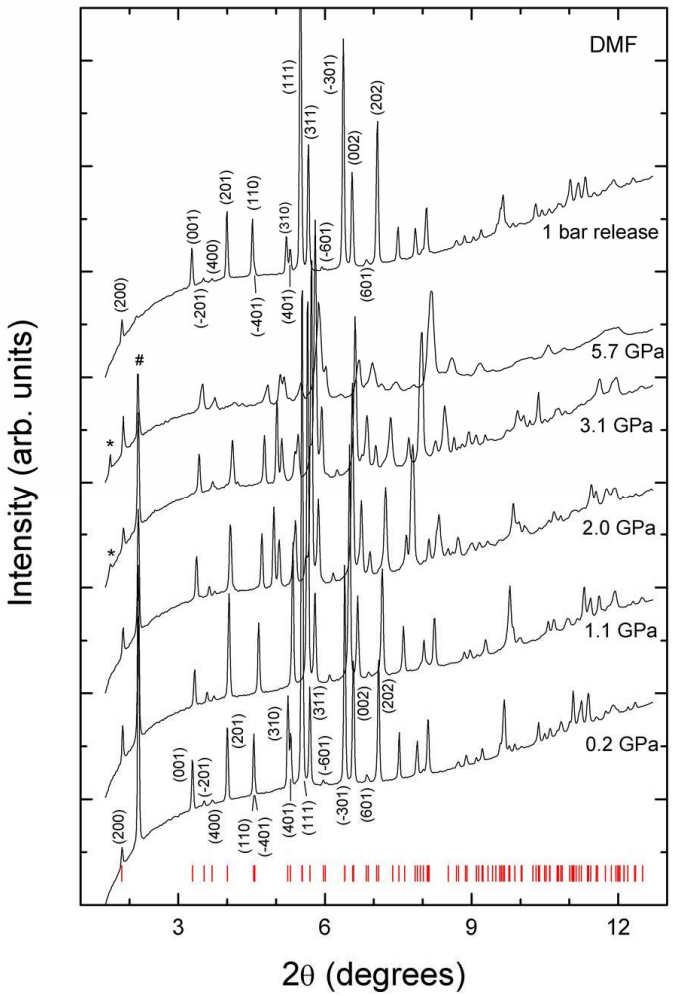

Figure SI12. High-pressure powder diffraction data in Fluorinert (FC-7

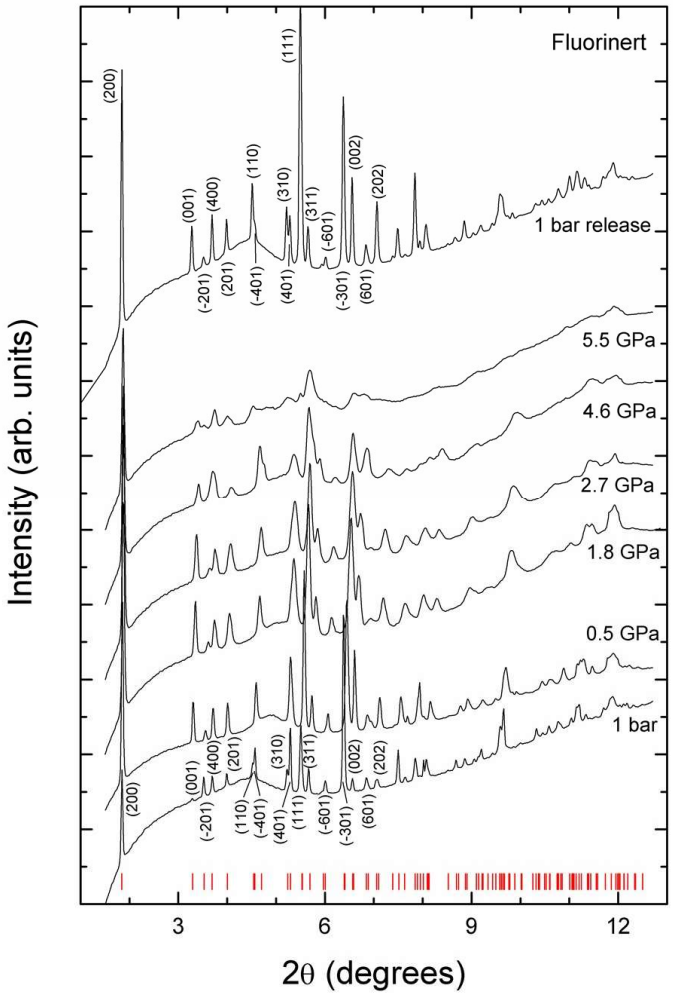

Figure SI13. Evolution of the unit cell parameters with pressure for the HP-PXRD experiments performed in MeOH:water (25:75). From left to right changes in: volume, cell axis and beta values. Solid symbols stand for the first set of experiments upon increasing pressure. Empty symbols were obtained after releasing pressure. The coincidence between increasing decreasing pressures suggest that the compression of the material proceeds reve

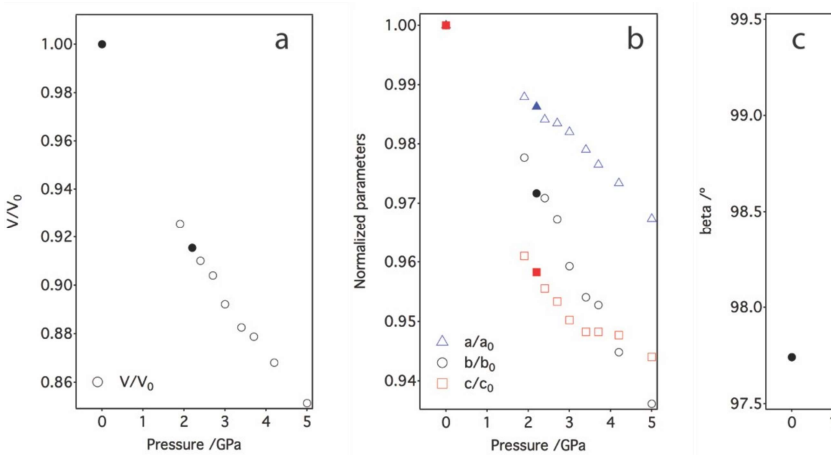

SI5. Single-crystal High-Pres

Single-crystal HP-XRD experiments. For high-pressure measurements, we have used a Diacell Bragg-Mini diamond anvil cell (DAC) from Almax-EasyLab, with an opening angle of 85º and anvil culets of 500μm diameter, fitted with a stai containing a hole of 200μm diameter a 50μm depth. A mixture of methanol-ethanol-water (16:3:1 in volume) was use pressure-transmitting medium, which remains hydrostatic in the range of pressure used in [13,1] in order to minimize deviatoric stresses which can cause incorrect values for bulk modul [15] The sample was placed on o diamonds anvils (diffraction side) together with a small ruby sphere as pressure sensor. The single-crystal XRD experiment was performed at MSPD beamline wi λ = 0.3185 Å determined from the La absorption K-edge (38.92 keV). The sample-detector distance (170 mm) and the beam centre position were calibrated using the FIT2D software from L$_6$ diffraction data measured at exactly the same conditions as the sample. The exploration of the reciprocal space was performed by rotation the DAC aroun Φ axis and performing small scans (Δω=0.2^0, time/frame=0.5 s) covering an ω range between -3 ^{0} and +30^0.The structure was refined, for each pressure, using previous results as starting point, on F^2 by full-matrix least-squares refinement using the SHELXL program. Due to limitations of the opening angle of our DAC it is only possible to c 20-30% of the total reflections present in a full dataset at ambient conditions. In this situation, structure refinements were performed with isotropic displacement parameters for all atoms except for zinc atom that was refined with anisotropic displacement parameters whenever it did not become non-positive definite. Hydrogen atoms were included in the fina procedure in the same way as for ambient conditions. No restraints were used during this p

Crystallographic data for the structures reported in this contribution have been deposited with the Cambridge Crystallographic Data Centre as supplementary publication 1588161-1588166. Copies of the data can be obtained free of charge on applicat to the CCDC, Cambridge, U http://www.ccdc.cam.ac.uk/).

Figure SI14. (*left*) Variation of the unit cell volume of Zn(GlyTy$_2$ with increasing pressure. Error bars are smaller than their respective size symbols. The curve was fit to a third-order Birch-Murnaghan function. Dashed line corresponds to the EoS model fit. (*right*) Plot of normalized pressure *vs* data strain (Ff) confirms that model used is consistent with the experimental data.

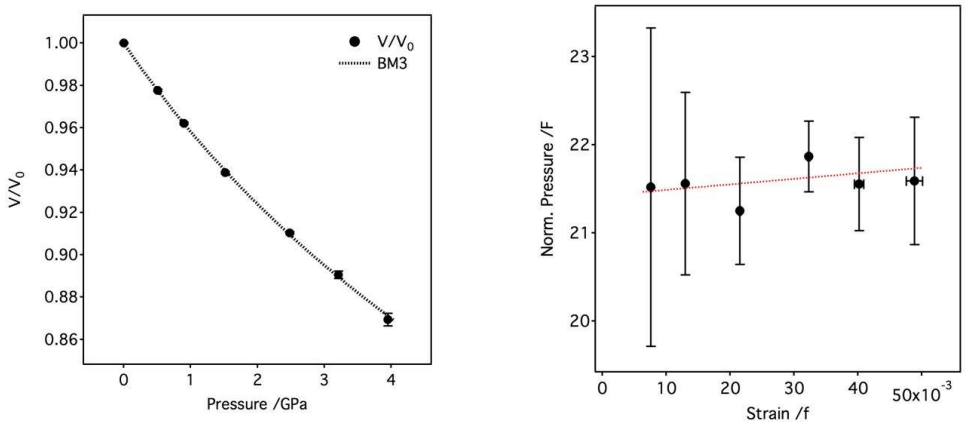

Table SI3. BM3 EoS parameters for single crystal Zn(GlyTyr)$_2$.

Parameters	Value
V_0 /Å^3	1082.00(6)
K_0 /GPa	21.9(9)
K'	4.2(7)

The bulk modulus obtained for Zn(GlyT$_2$ is typical for organometallic compound (10-30 GPa)[16,1] and we can associate thi lower value to the deformability of the intermolecular interactions. The evolution of unit cell parameters is completely

respect to the behavior of the volume when the pressure increase (Figure 3 in the text). In general, the curves show a slop change around 2.2GPa that in general, means a possible phase

Figure SI15. Comparison of the variation of the volume, cell parameters and beta angle with pressure for the HP-SCXR experiments performed in MeOH:EtOH:water (filled symbols) and the PXRD experiments performed in MeOH:water (empty symbols). Lines are only for eye guide. Changes in the PTM or the use of polycrystalline sample or single crystals do no seem to affect the evolution in the unit cell parameters that follow the s

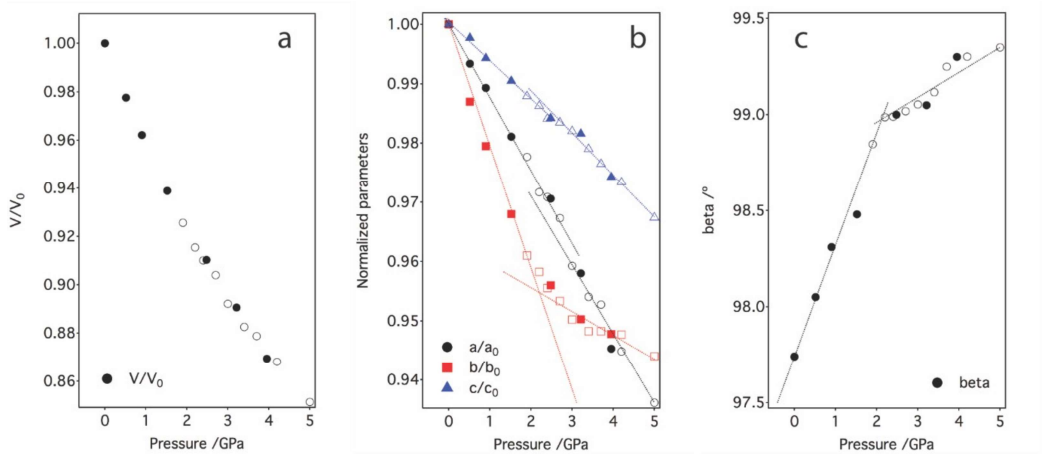

Variation of the cell parameters with pressure suggest that this compound presents an isostructural second-order phase transition. The space group does not change and the evolution of the volume cell does not show any discontinuity w pressure increase in the range evaluated in this s

Table SI4. Crystal data and HP structure refinement for Zn(GlyTy $_2$ between 0.51 and 3.95 GP

Pressure	0.51 GPa	0.90 GPa	1.52 GPa
Identificatio	1588161	1588162	1588163
Empirical formu	$C_{22}H_{26}N_4O_8Zn$	$C_{22}H_{26}N_4O_8Zn$	$C_{22}H_{26}N_4O_8Zn$
M	539.84	539.84	539.84
Cryst. Syst.	Monoclinic	Monoclinic	Monoclinic
Space group	I2	I2	I2
a, Å	7.4416(6)	7.4106(6)	7.3494(5)
b, Å	5.4166(4)	5.3751(4)	5.3119(4)
c, Å	26.503(17)	26.411(17)	26.310(16)
α, °	90	90	90
β, °	98.046(18)	98.306(18)	98.483(17)
γ, °	90	90	90
V, Å^3	1057.8(7)	1041.0(7)	1015.9(6)
Z	2	2	2
D_c/g cm^{-3}	1.695	1.722	1.765
F(000)	560	560	560

μ(- Kα), mm^{-1}	0.651	0.661	0.678
Reflections (collected/unique, (Rint))	675/571/0.029	651/570/0.024	564/512/0.018
Data/restrains/parameters	571/1/60	570/7/61	512/7/61
R1, wR [$F^2>2\sigma(F^2)$]	0.079/0.214	0.063/0.162	0.063/0.169
Goodness-of-fit on F^2	1.05	1.07	1.09
Largest diff. peak and hole (e $Å^{-3}$)	0.37/-0.41	0.29/-0.32	0.41/-0.31

Pressure	2.48 GPa	3.21 GPa	3.95 GPa
Identificati	1588164	1588165	1588166
Empirical for	$C_{22}H_{26}N_4O_8Zn$	$C_{22}H_{26}N_4O_8Zn$	$C_{22}H_{26}N_4O_8Zn$
M	539.84	539.84	539.84
Cryst. Syst.	Monoclinic	Monoclinic	Monoclinic
Space grou	I2	I2	I2
a, Å	7.2705(5)	7.1762(14)	7.0813(19)
b, Å	5.2464(4)	5.2148(8)	5.2012(10)
c, Å	26.144(18)	26.07(5)	25.88(10)
α, °	90	90	90
β, °	99.00(2)	99.05(6)	99.31(10)
γ, °	90	90	90
V, $Å^3$	985.0(7)	963.5(19)	941(4)
Z	2	2	2
D_c/g cm^{-3}	1.820	1.861	1.905
F(000)	560	560	560
μ(- Kα), mm^{-1}	0.699	0.714	0.732
Reflections (collected/unique, (Rint)	539/477/0.016	465/435/0.016	387/367/0.020
Data/restrains/parameters	477/7/61	435/7/61	367/8/49
R1, wR [$F^2>2\sigma(F^2)$]	0.060/0.160	0.067/0.177	0.084/0.242
Goodness-of-fit on F^2	1.11	1.07	1.08
Largest diff. peak and hole (e $Å^{-3}$)	0.39/-0.32	0.27/-0.23	0.26/-0.21

Figure SI16. Comparison of the variation of the cell changes normalized to their value at ambient pressure for the crystallographic directions [-101], [010] and [101]. Overlaid structures of $_2$ for each direction is show page.

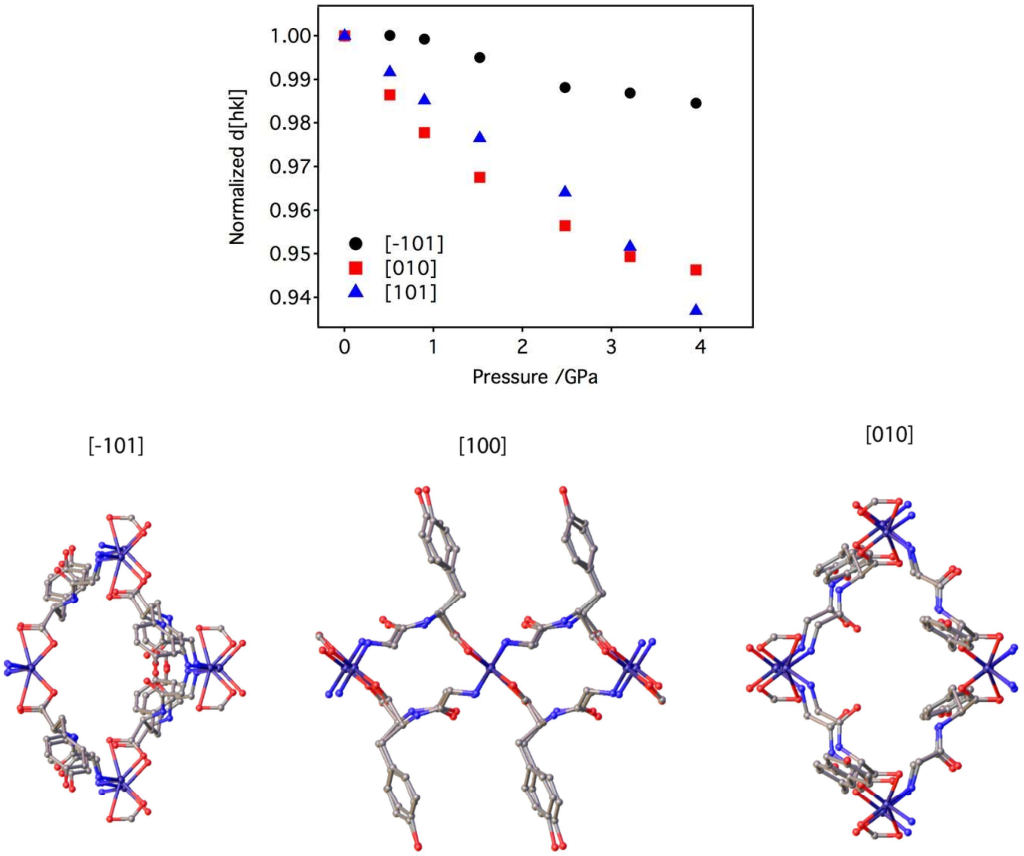

Figure SI17. Changes in the distance π-π interactions between 0-3.95 GPa defined as the distance between the centroid of neighbouring aromatic rings in the sidechain of

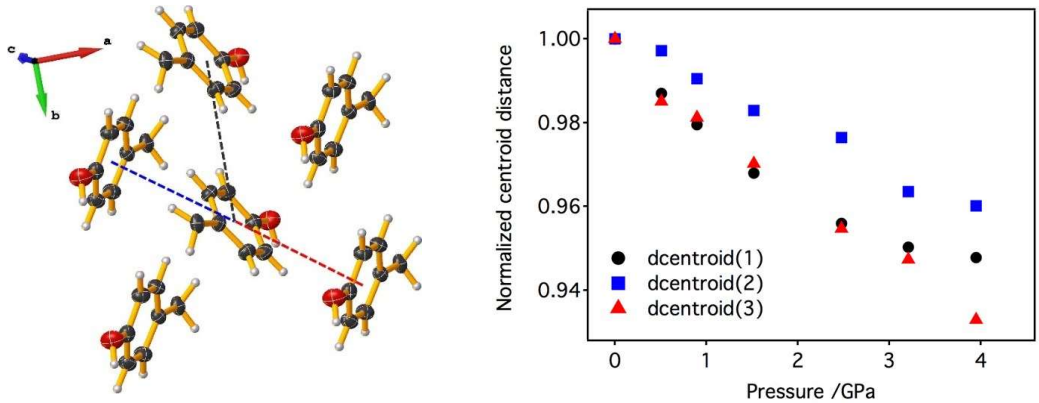

Table SI5. Summary of the evolution of the parameters used for analysing the structural changes in $Zn(GlyTyr)_2$ at HP. For clarity, the figures included in the text represent the variation of volume and distances normalised to their respective values ambient pressure by using the data below.

Evolution of the neighbouring Zn(II) sites across the MOF layer defined as diagonal 1 $_1$), diagonal 2 $_2$) and edge (Figure 4d):

Pressure /GPa	d_1 /Å	d_2 /Å	edge /Å
0.0001(1)	14.9816(4)	10.9754 (3	9.2858(3)
0.51(4)	14.8832(14)	10.8332 (8)	9.2042(8)
0.90(4)	14.8212(14)	10.7502 (15)	9.1547(11)
1.52(4)	14.6988(12)	10.6238 (15)	9.0681(11)
2.48(4)	14.5410(13)	10.4928 (6	8.9658(7)
3.21(4)	14.352(4)	10.4296 (1	8.871(2)
3.95(4)	14.163(6)	10.4024(1)	8.786(2)

Conformational changes of the peptide defined as the torsion angles of the glycyl C-terminus Ψ) and threonine N-terminu (Φ), that stand respectively for the dihedral angles (Figure 4

Pressure /GPa	Ψ /° N2-C11-C10-N1	Φ /° C2-C1-N1-C10
0.000(1)	164.1(3)	-109.4(3)
0.51(4)	159(3)	-109(4)
0.90(4)	164(3)	-111(3)
1.52(4)	160(3)	-108(4)
2.48(4)	157(3)	-101(4)
3.21(4)	154(4)	-102(5)
3.95(4)	146(6)	-91(8)

Hydrogen bond distances and angles (Figure 4f)

Pressure /GPa	D-H-A = N1-H1-O2(i)			
	d(D-H)/Å	d(H-A)/Å	d(D-A)/Å	D-H-A/°
0.000(1)	0.86	1.98	2.831(4)	169
0.51(4)	0.86	1.94	2.79(3)	168
0.90(4)	0.86	1.93	2.75(2)	158
1.52(4)	0.86	1.92	2.77(2)	173
2.48(4)	0.86	1.86	2.72(2)	177
3.21(4)	0.86	1.88	2.73(3)	170
3.95(4)	0.86	1.90	2.72(6)	160

(i) x,1+y,

Pressure /GP	D-H-A = O4-H4-O3(ii)			
	d(D-H)/Å	d(H-A)/Å	d(D-A)/Å	D-H-A/°

0.000(1)	0.82	1.89	2.643(4)	152
0.51(4)	0.82	1.88	2.64(4)	148
0.90(4)	0.82	2.09	2.54(3)	115
1.52(4)	0.82	2.00	2.54(4)	122
2.48(4)	0.82	2.10	2.56(4)	120
3.21(4)	0.82	2.05	2.47(4)	118
3.95(4)	0.82	1.99	2.50(9)	110

(ii) 3/2-x,1/2+y,3/2

Pressure /GPa	D-H-A = N2-H2B-O4(ii			
	d(D-H)/Å	d(H-A)/Å	d(D-A)/Å	D-H-A/°
0.0001(1)	0.89	2.23		143
0.51(4)	0.89	2.16		144
0.90(4)	0.89	2.17		140
1.52(4)	0.89	2.17		139
2.48(4)	0.89	2.23		102
3.21(4)	0.90	1.96		138
3.95(4)	0.90	1.85		133

(ii) 3/2-x,1/2+y,3/2-z

Distances of t π-π interactions between the centroids of neighbouring aromatic rings (Figure SI15

Pressure /GPa	Cg-Cg(i) /Å	Cg-Cg(ii) /Å	Cg-Cg(iii) /Å
0.0001(4)	5.488(4)	4.6125(4)	4.672(4)
0.51(4)	5.42(3)	4.60(3)	4.60(3)
0.90(4)	5.37(2)	4.57(2)	4.58(2)
1.52(4)	5.31(3)	4.52(2)	4.53(2)
2.48(4)	5.25(3)	4.51(2)	4.46(2)
3.21(4)	5.21(3)	4.45(3)	4.43(3)
3.95(4)	5.20(3)	4.43(3)	4.36(3)

(i)x, y-1, z (black); (ii)1/2-x,-1/2+y,3/2-z (blue); (iii)3/2-x,1/2+y,3/2-z

SI6. References

[1] Rigaku Oxford Diffra **2017**, *CrysAlisPro Software system, version 1.171.38.46*, Rigaku Corporation, Oxford, UK
[2] Sheldrick, G. M. *Acta Cryst.* **2015***, A71*, 3-8.
[3] Sheldrick, G. M. *Acta Cryst.* **2008**, *A64*, 112-122
[4] Spek, A. L. *Acta Cryst* **2009**, *D65*, 148-155
[5] J. Rabone, Y. F. Ye, S. Y. Chong, K. C. Stylianou, J. Bacsa, D. Bradshaw, G. R. Darling, N. G. Berry, Y. Z Khimyak, A. Y. Ganin, P. Wiper, J. B. Claridge, M. J. Rosseinsky, *Science* **2010**, *329*, 1053.
[6] C. Martí-Gastaldo, D. Antypov, J. E. Warren, M. E. Briggs, P. A. Chater, P. V. Wiper, G. J. Miller, Y. Z. Khimyak, G. R. Darling, N. G. Berry, M. J. Rosseinsky, *Nat. Chem.* **2014**, *6*, 343
[7] C. Marti-Gastaldo, J. E. Warren, K. C. Stylianou, N. L. O. Flack, M. J. Rosseinsky, *Angew. Chem. Int. Ed* **2012**, *51*, 11044.
[8] Mao, H. K.; Xu, J.; Bell, P. M. *J. Geophys.* **1986**, *91*, 4673.
[9] Errandonea *Cryst. Res. Technol.* **2015**, *50*, 7
[10] Fauth, F.; Peral, I.; Popescu, C.; Knapp, M. *Synchrotron Powder Diffr.* **2013**, 28, S360.
[11] Hammersley, A. P.; Svensson, S. O.; Hanfland, M.; Fitch, A. N.; Häusermann, D. *High Press.* **1996**, *14*, 235.
[12] Larson, A. C.; von Dreele, R. B. GSAS: General Structure Analysis S *Los Alamos National Labor Report* **2000**, 86-748.
[13] Angel, R. J.; Bujak, M.; Zhao, J.; Gatta, G.D.; Jacobsen, S. D. *J. Appl. Crystallogr.* **2007**, *40*, 26-32.
[14] Klotz, S.; Chervin, J.; Munsch, P.; Le Marchand, G. *J. Phys. D. Appl. Phys.* **2009**, *42*, 75413, 200
[15] Errandonea, D.; Muñoz, A.; Gonzalez-Platas, J. *J. Appl. Phys.* **2014**, 115, 216101:1-3

Chapter 3:

Enantioselective simulations to predict separation of chiral drugs with a peptidic MOF

1. Motivation

Separation of chiral molecules with biological activity is one of the most important applications in MOFs. Many relevant drugs are dosed in racemic mixtures, tampering their effectivity and leading to a loss in activity or even to adverse reactions. The irruption of chiral MOFs permitted rapid separation of individual adsorbents, as it was based on chiral recognition rather than shape/size selectivity. In recent years there has been an increasing interest in the development of homochiral MOFs incorporating enantiomerically pure linkers as ligands in their structure.[1–3] These are usually derived from chiral templates, post synthetic linker exchange, functionalization, or direct synthesis.[4,5] Concretely, the incorporation of chiral peptides as adsorbents can proportionate the scaffold with the benefits of a intrinsically enantioselective recognition.[6] With a precise selection of enantiomers, this system would originate a specific enantioselective recognition, originated from the different host-guest intermolecular interactions.[7–9]

In this context, a number of di- and tripeptides was explored by Rosseinsky 's group.[10–12] These materials can show a robustness, chemical stability, and porous response that can be effectively modulated by the choice of amino acids added to the chain. The distinct behavior of the systems is controlled by the conformational flexibility, chemistry of the amino acids and their sequence. For that reason, we tried to take advantage of this defined conduct in order to separate enantiomers with one of these systems, the Gly-L-His-Gly (GlyHisGly) tripeptide with Cu(II).[13]

2. Summary of key results

The finding of this approach we took were published in "J. Navarro-Sánchez, A. I. Argente-García, Y. Moliner-Martínez, D. Roca-Sanjuán, D. Antypov, P. Campíns-Falcó, M. J. Rosseinsky, C. Martí-Gastaldo. Peptide Metal–Organic Frameworks for Enantioselective Separation of Chiral Drugs. *J Am Chem Soc* **139**, 4294–4297 (2017)". In this publication we reported the enantiomerical separation of two relevant drugs: methamphetamine (MA) and ephedrine (EP). Both are chiral compounds used as recreational drugs and at the same time components in pharmaceutical preparations with a therapeutic use. All these structures are shown in **Figure 1a**. We report the ability of a chiral Cu(II) 3D MOF based on the tripeptide GlyHisGly for an enantioselective enrichment, providing theoretical simulations that reveal how intermolecular interactions between the drugs and the peptide backbone guide chiral recognition. In order to corroborate that the inherent flexibility of the MOF would be able to deliver a tailored response to the enantiomers, we employed the program Materials Studio Simulator to perform Monte Carlo simulations. This allowed us to

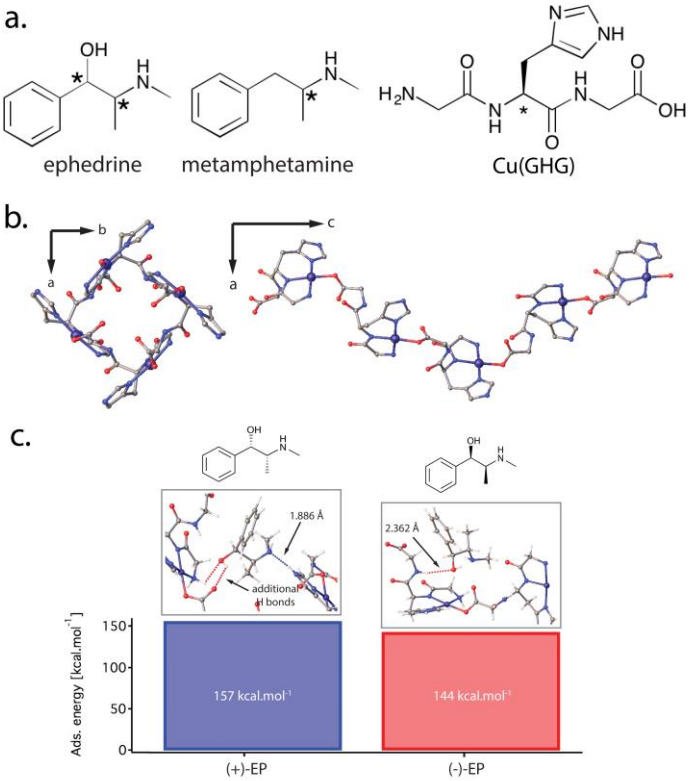

Figure 25. **a**. Structures of Cu(GHG), EP and MA. **b**. Structure of helicoidal chains in Cu(GHG) MOF (left) and the functional groups in the peptidic backbone decorating the surface of the pores (right). **c**. Representative MC binding geometries of (+,-) EP enantiomers and the energetic values of their absolute adsorption values. Most relevant H bonds are represented, indicating the distances.

understand the role played by the peptide in performing a preferential adsorption for the most favorable binding site. The two enantiomers (+,-) of MA and EP were inserted into the structure of the Cu(GlyHisGly) priorly depleted of solvent molecules (shown in **Figure 1b**). Most stable conformations of MA and EP were randomly explored changing the torsion angles in order to determine the most stable conformation within the pore. **Figure 1c** summarizes the EP adsorption energies and the preferential binding sites for the most energetically stable location in the MOF pore. In order to obtain this structure we performed discrete models of the MOF and classic-chemical calculations, being chosen for each step the most energetically favorable and at least 4 kcal/mol stronger than those accessible by interaction with other functional groups in the pocket. While the accuracy of the force-field model and

the difficulty of replicating experimental solvation effects do not allow for quantitative prediction of chiral selectivity, this simulations we performed suggest that more effective enantioselective recognition is to be expected for EP as result of cooperative supramolecular interactions. The adsorption of the (+)-EP is indeed preferential thanks to the establishment of additional H-bond. It is the strength and number of H-bonds that translate into a bigger difference in adsorption energies close to 13 kcal/mol. Even if these results look promising, there was the need for actual experimental evidence of the capacity of the Cu(GlyHisGly) to separate enantiomers.

The MOF was synthetized by controlled layering of ethanol onto an aqueous solution containing glycyl-L-histidylglycine and Cu(II) acetate, in a 1:1 ratio at room temperature one night.[13] Cu(GlyHisGly) crystallizes in a tetragonal $P4_12_12$ space group to produce an open 3D framework. The porosity of the system arises from the interconnection of 1D empty channels that account for a solvent-accessible volume close to 60% of the total volume. The use of peptides as ligands to connect the metal allowed a decoration of the surface of the empty space with carboxylate, amide and imidazole groups pointing into the channels. One of the key limitations of flexible MOFs is their poor stability without solvent that could result in the pore collapsing upon its removal. Fortunately, chiral recognition is a dynamic process, and solvent removal is not necessary as the solvent molecules occupying the pores can be progressively exchanged with the chiral guests in solution. For that reason, the MOF employed for the separation experiments was not evacuated of solvent and was employed as-synthesized to preserve its structural integrity (it was abundantly cleaned with solvent prior to use).

In order to perform a quick test of the separative capacities of the MOF, we first decided to test the MA and EP in solution. To a solution of 10 mg of fresh solid we added racemic mixtures, and the solvent was analyzed chromatographically. As shown in **Figure 2a**, the adsorption of (-)-MA and (-)-EP was almost negligible. However, the (+)-MA and (+)-EP enantiomers were preferentially absorbed. We attribute the long recognition times of up to 4 hours to the highly polar mixture of solvents used. This stabilizes the chiral drugs in solution inside the pores, preventing fast diffusion into the porous chiral medium for a slow recognition process with long equilibration times. Concretely, there is approximately a 30% of excess for the (+)-MA and 37% for the EP after 4 and 2 hours, respectively. The experiment agrees well with the MC simulations that support preferential interaction of (+)-enantiomers in the chiral pocket, linked to the specific conformations that the molecules adopt inside the pores. Theoretical simulations also predict a more favorable separation of EP enantiomers over those of MA, which indeed is shown in the results.

Peptide-based MOFs have many limitations as stationary phases due to their poor stability and particle heterogeneity. This limits the range of mobile phases available for polar analytes, and increases the difficulty of truly obtaining an efficient packing of the particles in the column, which relies on narrow distributions in size and shape for reproducible sorption/desorption kinetics. A lack of control over these variables can result in high retention times, low chromatographic performance and longer separations. For that reason, and inspired by the promising results, we decided to test one of the most relevant separation techniques in industry called solid-phase extraction (SPE). In contrast to normal columns, the SPE enables isolation of the enantiomers rather than only providing a measure of the enantiomeric purity of a mixture. SPE allows for a more efficient chromatographic analysis by removal of interferences, increase of trace concentration and sample simplification.

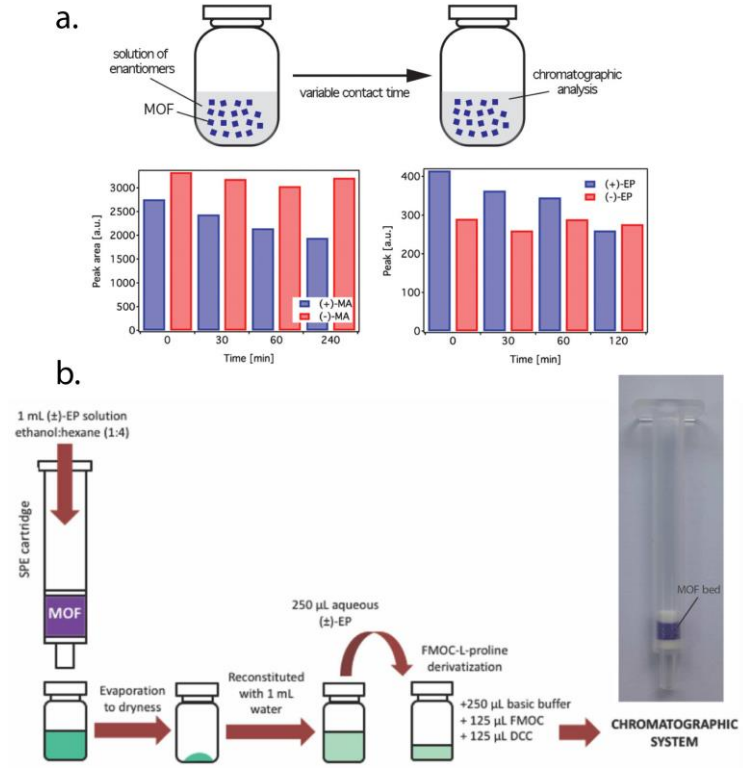

Figure 26. **a**. Evolution of the retention of MA and EP as time increases for (left) MA and (right) EP. Chiral adsorption was evaluated from chromatographic analysis of the supernatant solution. **b**. Scheme of the experimental setup employed for the enantiomeric separation of the EP racemate, showing the actual polypropylene SPE tube after the incorporation of the chiral MOF bed (right).

We used this technique with the MOF as bed, packing 50 mg of Cu(GlyHisGly) in a polypropylene SPE cartridge and eluded a racemic mixture of EP inside. The full procedure of extraction is showed in **Figure 2b**. In this second part of the experimental we focused mainly on EP over MA based in our preliminary results, which suggested faster and more efficient recognition for the first one. As predicted, the tests the chiral column allowed for a 54% of (+)-EP separation from equimolar mixtures of the enantiomers in just 4 min, with satisfactory precision and relatively short retention times. This results obtained suggest that Cu(GlyHisGly) offers high performance in terms of stereoselective recognition and time efficiency, for a high-speed chiral separation column. Finally, in order to act as control we tested the separation of a ground mixture of GlyHisGly and Cu(II) acetate in the same proportion as present in the MOF without obtaining measurable chiral recognition. This proved that the periodic distribution of chiral channels in the MOF scaffold was key for the proper separation of enantiomers. To sum up, peptide MOFs are particularly well suited for enantioselective recognition and this feature can be incorporated to separation techniques. The chiral pockets inside their structure can be manipulated for maximizing host-guest intermolecular interactions for a specific enantiomer simply by suitable choice of the peptide sequence. This combination of theory and experimental holds great potential for the chiral recognition field, and opens the way for the production of more complex chemical environments in which supramolecular interactions can be tuned for the maximization of their separation.

3. References

1. Y. Lu, H. Zhang, Y. Zhu, P. J. Marriott, H. Wang, Emerging Homochiral Porous Materials for Enantiomer Separation. *Adv Funct Mater*, 2101335 (2021).

2. J. Liu, S. Mukherjee, F. Wang, R. A. Fischer, J. Zhang, Homochiral metal–organic frameworks for enantioseparation. *Chem Soc Rev* (2021).

3. S. Liang, X.-L. Wu, J. Xiong, M.-H. Zong, W.-Y. Lou, Metal-organic frameworks as novel matrices for efficient enzyme immobilization: An update review. *Coordin Chem Rev*. **406**, 213149 (2020).

4. T. Duerinck, J. F. M. Denayer, Metal-organic frameworks as stationary phases for chiral chromatographic and membrane separations. *Chem Eng Sci*. **124**, 179–187 (2015).

5. C. Kutzscher, P. Müller, S. Raschke, S. Kaskel, The Chemistry of Metal-Organic Frameworks: Synthesis, Characterization, and Applications: Synthesis, Characterization, and Applications, 387–419 (2016).

6. J. Rabone, Y.-F. Yue, S. Y. Chong, K. C. Stylianou, J. Bacsa, D. Bradshaw, G. R. Darling, N. G. Berry, Y. Z. Khimyak, A. Y. Ganin, P. Wiper, J. B. Claridge, M. J. Rosseinsky, An Adaptable Peptide-Based Porous Material. *Science*. **329**, 1053–1057 (2010).

7. J. Y. Chan, H. Zhang, Y. Nolvachai, Y. Hu, H. Zhu, M. Forsyth, Q. Gu, D. E. Hoke, X. Zhang, P. J. Marriot, H. Wang, Incorporation of Homochirality into a Zeolitic Imidazolate Framework Membrane for Efficient Chiral Separation. *Angewandte Chemie Int Ed*. **57**, 17130–17134 (2018).

8. M. N. Corella-Ochoa, J. B. Tapia, H. N. Rubin, V. Lillo, J. Gonzalez-Cobos, J. L. N. Rico, S. R. G. Balestra, N. Almora-Barrios, M. Lledos, A. Guell-Bara, J. Cabezas-Giménez, E. C. Escudero-Adán, A. Vidal-Ferran, S. Calero, M. M. Reynolds, C. Marti-Gastaldo, J. R. Galan-Mascaros, Homochiral metal-organic frameworks for enantioselective separations in liquid chromatography. *J Am Chem Soc* (2019).

9. Y. Lu, H. Zhang, J. Y. Chan, R. Ou, H. Zhu, M. Forsyth, E. M. Marijanovic, C. M. Doherty, P. J. Marriott, M. M. B. Holl, H. Wang, Homochiral MOF–Polymer Mixed Matrix Membranes for Efficient Separation of Chiral Molecules. *Angew Chem-ger Edit*. **131**, 17084–17091 (2019).

10. A. P. Katsoulidis, K. S. Park, D. Antypov, C. Martí-Gastaldo, G. J. Miller, J. E. Warren, C. M. Robertson, F. Blanc, G. R. Darling, N. G. Berry, J. A. Purton, D. J. Adams, M. J. Rosseinsky, Guest-Adaptable and Water-Stable Peptide-Based Porous Materials by Imidazolate Side Chain Control. *Angew Chem-ger Edit*. **126**, 197–202 (2014).

11. C. Martí-Gastaldo, J. E. Warren, K. C. Stylianou, N. L. O. Flack, M. J. Rosseinsky, Enhanced Stability in Rigid Peptide-Based Porous Materials. *Angewandte Chemie Int Ed*. **51**, 11044–11048 (2012).

12. C. Martí-Gastaldo, D. Antypov, J. E. Warren, M. E. Briggs, P. A. Chater, P. V. Wiper, G. J. Miller, Y. Z. Khimyak, G. R. Darling, N. G. Berry, M. J. Rosseinsky, Side-chain control of porosity closure in single- and multiple-peptide-based porous materials by cooperative folding. *Nat Chem*. **6**, 343–351 (2014).

13. C. Martí-Gastaldo, J. E. Warren, M. E. Briggs, J. A. Armstrong, K. M. Thomas, M. J. Rosseinsky, Sponge-Like Behaviour in Isoreticular Cu(Gly-His-X) Peptide-Based Porous Materials. *Chem - European J*. **21**, 16027–16034 (2015).

Publication 2:

Peptide Metal–Organic Frameworks for Enantioselective Separation of Chiral Drugs

J. Am. Chem. Soc. 2017, 139, 12, 4294–4297

JACS
JOURNAL OF THE AMERICAN CHEMICAL SOCIETY

Communication

pubs.acs.org/JACS

Peptide Metal–Organic Frameworks for Enantioselective Separation of Chiral Drugs

José Navarro-Sánchez,[†,⊥] Ana I. Argente-García,[‡,⊥] Yolanda Moliner-Martínez,[‡] Daniel Roca-Sanjuán,[†] Dmytro Antypov,[§] Pilar Campíns-Falcó,[‡] Matthew J. Rosseinsky,[§] and Carlos Martí-Gastaldo*[,†]

[†]Instituto de Ciencia Molecular, Universidad de Valencia, 46980 Paterna, Spain

[‡]MINTOTA Research Group, Departament de Química Analítica, Facultat de Química, Universitat de Valencia, 46100 Burjassot, Spain

[§]Department of Chemistry, University of Liverpool, Liverpool L697ZD, U.K.

Supporting Information

ABSTRACT: We report the use of a chiral Cu(II) 3D metal–organic framework (MOF) based on the tripeptide Gly-L-His-Gly (GHG) for the enantioselective separation of metamphetamine and ephedrine. Monte Carlo simulations suggest that chiral recognition is linked to preferential binding of one of the enantiomers as a result of either stronger or additional H-bonds with the framework that lead to energetically more stable diastereomeric adducts. Solid-phase extraction of a racemic mixture by using Cu(GHG) as the extractive phase permits isolating >50% of the (+)-ephedrine enantiomer as target compound in only 4 min. To our knowledge, this represents the first example of a MOF capable of separating chiral polar drugs.

Metal–organic frameworks (MOFs) are crystalline, porous materials built from the interconnection of metal ions or clusters and organic linkers to produce porous architectures. Besides other applications like catalysis or sensing, their unlimited structural/chemical flexibility enables rational tailoring of the chemical function and pore dimensions for more efficient and selective separation of gases,[1] hydrocarbons,[2] or aromatic compounds.[3] In this context, separation of chiral molecules with biological activity is also very relevant. A large number of drug compounds are often dosed as racemic mixtures. Enantiomers generally display different pharmacological and/or toxicological properties which can lead to a loss in activity or even to undesired side reactions. Discovery of chiral adsorbents that permit rapid separation of individual enantiomers is of utmost importance in the early stages of drug research in the pharmaceutical industry. This type of separation relies on chiral recognition rather than shape/size selectivity. Hence, preferential interaction of one of the enantiomers with the homochiral adsorbent must lead to the formation of a transient diastereomeric adsorbate, whose free energy shall be sufficiently different for enantiomeric separation to take place.

Compared to classical adsorbents like zeolites or activated carbons, MOFs are arguably more promising candidates for chiral separation. They can be more easily engineered to deploy a periodic array of chiral channels that are accessible to guest sorption and can be modified in size, shape, and chemical function to optimize mass-transfer rates and chiral recognition. However, the application of MOFs in enantioselective separation is still limited by the small number of homochiral, microporous phases available.[4] These are typically prepared either by using chiral templates that drive enantiomeric resolution, by post-synthetic linker exchange for partial grafting of chiral linkers in the metal struts at the expense of accessible porosity, or by direct synthesis from enantiopure linkers.[4a] This last route is compatible with the use of naturally occurring chiral linkers like camphoric and tartaric acid, amino acids (aa's), or oligopeptides. Among these, peptides are well suited to producing functional, chiral MOFs whose robustness, chemical stability, and porous response can be effectively modulated by suitable choice of aa's in the peptidic sequence.[5] The broad choice of side-chain groups available from proteinogenic aa's can be also used to engineer the chiral pockets in their structure with specific functions. Due to their crystalline nature, peptide MOFs are also well suited for theoretical modeling of the enantiomer interactions in a confined space, which is important to accelerate screening of materials already available and guide the design of more efficient systems.

Metamphetamine (MA) and ephedrine (EP) (Scheme 1) are chiral compounds used as recreational drugs, but also as components in pharmaceutical preparations of therapeutic use as bronchodilators and respiratory stimulants. Both compounds possess a chiral center and exist as a pair of enantiomers which may differ in their pharmacological activity as well as in their metabolic and pharmacokinetic characteristics. Separation of MA or EP enantiomers is frequently required in clinical, forensic, and toxicology laboratories. We report the ability of a chiral Cu(II) three-dimensional (3D) MOF based on the tripeptide Gly-L-His-Gly (GHG) for their separation and provide clear insights on the experimental stereoselectivity by theoretical simulations that

Scheme 1. Structures of MA and EP

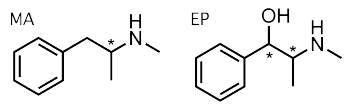

Received: January 9, 2017
Published: March 9, 2017

DOI: 10.1021/jacs.7b00280
J. Am. Chem. Soc. 2017, 139, 4294–4297

reveal how intermolecular interactions between the drugs and the peptide backbone guide chiral recognition. We are confident that our results might guide the development of efficient porous media for enantioselective applications.

Cu(GHG) was synthesized by slow diffusion of glycyl-L-histidylglycine and Cu(II) acetate to produce prismatic, micrometric blue crystals by following a synthetic procedure recently reported by some of us.[6] As shown in Figures SI1−S4, phase purity was studied by CHN, FT-IR, scanning electron microscopy (SEM), thermogravimetric analysis, and powder X-ray diffraction (PXRD). Analysis of the room-temperature PXRD is consistent with the single-crystal data available, thus confirming the isolated solid is isostructural with the phase reported.[6] Homochirality of the solid was also confirmed by solid-state circular dichroism (CD), which displays a positive Cotton effect in the UV/vis spectrum of the MOF at 610 cm^{-1} linked to Cu(II) complexation with enantiopure glycyl-L-histidylglycine (Figure SI5).

Cu(GHG) crystallizes in the tetragonal, polar space group $P4_12_12$ to produce an open 3D framework, built from the interconnection of 4-fold helicoidal Cu-peptide-Cu chains by μ_2-carboxylate bridges in C-terminal Gly (Figure 1a). Porosity arises from the interconnection of 1D empty channels that account for a solvent-accessible volume close to 60% of the total volume. Use of peptides as metal connectors allows us to decorate the surface of the empty space with carboxylate, amide, amino, and imidazole groups pointing into the channels (Figure 1b). This renders chemically versatile channels featuring a manifold of interaction sites for modulating framework/guest interactions (Figure 1c). Study of the porosity metrics with Zeo++ yields diameters of the largest included (D_i) and free spheres (D_f) above 2 nm, big enough to accommodate small drugs like EP or MA (Figure SI6). For these guests, recognition can potentially be triggered by preferential sorption in the chiral pockets of the MOF rather than interactions at the surface of the solid.

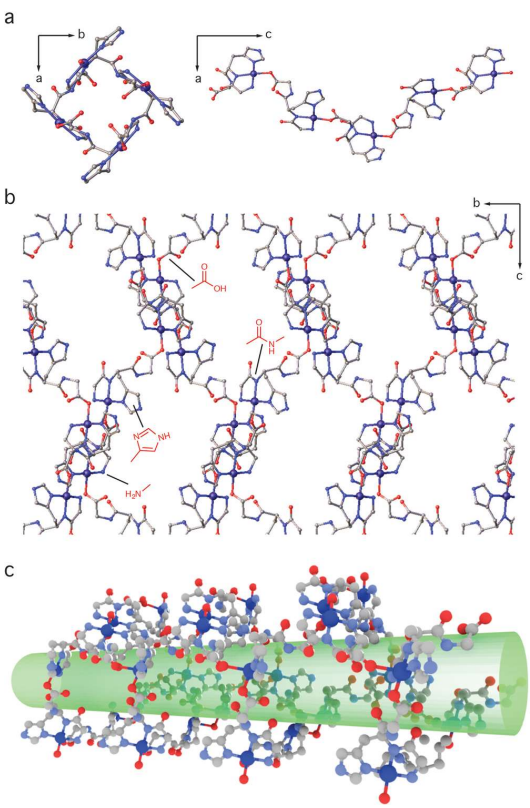

Figure 1. (a) Structure of helicoidal chains in Cu(GHG) MOF. (b) Functional groups in the peptidic backbone decorating the surface of the pores. (c) 1D channels in Cu(GHG) are surrounded by functional sites prone to establish supramolecular interactions, well suited for chiral recognition and discrimination.

Monte Carlo (MC) simulations were used to gain a better understanding of the role played by the functional groups from the peptide in controlling preferential adsorption for more favorable binding sites. We simulated the adsorption of the two enantiomers (+,−) of MA and EP (Figure 2). The structure of Cu(GHG) (CCDC 961607) was first prepared for the theoretical study by removal of solvent molecules occupying the pores. Most stable conformations of MA and EP enantiomers were explored by randomly changing the torsion angles. Next, MC computations were carried for each enantiomer to determine their most stable locations within the MOF upon sorption (see Supporting Information, SI2, for details). Figure 2 summarizes the adsorption energies and preferential binding sites for the most representative host−guest adducts calculated. Adsorption of both MA enantiomers is preferentially directed by the formation of H-bonds between the amine and the imidazole group in His side chain. We have used discrete models of the MOF and quantum-chemistry calculations to confirm that this interaction is energetically most favorable, at least 4 kcal/mol stronger than those accessible by interaction with other functional groups in the pocket involving C-terminal and N-terminal Gly (Figure SI7, Table SI1). Regarding enantiomeric recognition, (+)-MA is accommodated closer to the pocket for a stronger interaction via an imidazole H-bond. This elongates from 1.87 Å for (+)-MA to 2.03 Å when interacting with (−)-MA, due to small changes in the adsorption configurations of the enantiomers (Figure 2). The higher binding energy observed for (+)-MA mainly arises from stronger van der Waals interactions due to a better fit to the shape of the pocket. This agrees well with the energy variation for increasing H-bond distances calculated by quantum-chemistry methods for short-range imidazole−dimethylamine interactions (Figure SI8). While the accuracy of the force-field model and the difficulty of replicating experimental solvation effects do not allow for quantitative prediction of chiral selectivities, our simulations suggest that more effective enantioselective recognition is expected for EP as result of cooperative supramolecular interactions. As shown in Figure 2, adsorption of (−)-EP is solely directed by the formation of a weak elongated H-bond (2.36 Å) with the amide bond in C-terminal Gly. In contrast, (+)-EP combines short His-EP H-bonds (1.89 Å), equivalent to that with (+)-MA, with auxiliary bonds with the carboxylate and amino groups (2.09 and 2.40 Å) in the C-terminal and N-terminal Gly aa's of Cu(GHG) for more favorable adsorption. It is the strength and number of H-bonds—EP has two H-bonding groups capable of interacting synergically with the environment of the peptide MOF—that translate into a bigger difference in adsorption energies close to 13 kcal/mol.

MC simulations suggest that Cu(GHG) might display stereoselectivity, in particular for EP enantiomers, associated with the control of non-covalent interactions over their binding geometries. This promising result prompted us to attempt actual

DOI: 10.1021/jacs.7b00280
J. Am. Chem. Soc. 2017, 139, 4294−4297

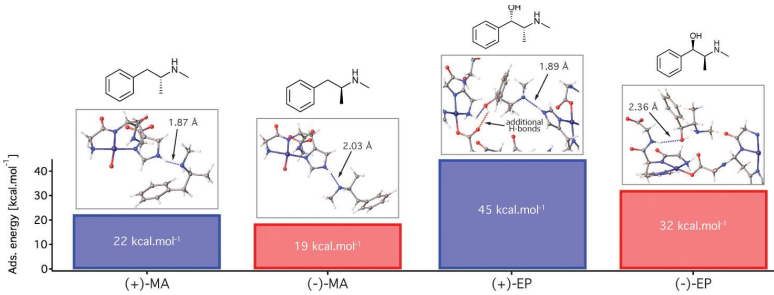

Figure 2. Representative MC binding geometries of (+,−) MA and EP enantiomers within the structure of Cu(GHG) and corresponding adsorption energies as absolute values calculated with respect to gas phase. Most relevant H-bonds in directing guest binding are annotated in each case. See Figure SI9 for an overall view of geometries and more favorable binding sites in the framework. Dotted lines represent H-bonds with N−H (blue) and O−H (red) donor groups.

separation experiments from solutions of the racemates. One of the key limitations of flexible MOFs is their poor mechanical robustness that results in collapse of the structure upon solvent removal. This is also the case for Cu(GHG), which displays sponge-like behavior with a crystalline-to-amorphous transformation after activation that can be reverted to the original state in the presence of polar solvents.[6] Though this is a key limitation for gas storage, which requires the porous material to be activated prior to gas sorption, chiral recognition is a dynamic process, and prior filling of the pores is not imperative since the solvent molecules occupying the pores can be progressively exchanged with the chiral guests in solution. Hence, all separation experiments were carried out by using non-evacuated, as-synthesized materials to preserve their structural integrity. First, we studied the ability of Cu(GHG) to recognize selectively enantiomers from solution by soaking 10 mg of fresh solid in racemic mixtures of MA and EP (40 μg/mL in ethanol:water 75:25). Enantioselective recognition was evaluated chromatographically as a function of contact time (see Supporting Information, SI3, for experimental conditions and methodology). As shown in Figure 3, adsorption of (−)-MA and (−)-EP can be considered negligible, whereas 30 ± 3% of (+)-MA and 37 ± 3% of (+)-EP are preferentially adsorbed after 4 and 2 h, respectively. We attribute the long recognition times to the highly polar mixture of solvents used. This will stabilize the chiral drugs in solution, preventing fast diffusion into the porous chiral medium for a slow recognition process with long equilibration times. This experiment agrees well with the MC simulations that support preferential interaction of (+)-enantiomers in the chiral pocket linked to specific conformations that enable H-bond formation with the histidine side chain. As described above, theoretical predictions are also consistent with more favorable separation of EP enantiomers over those of MA based on the energy differences for enantiomer interaction with Cu(GHG), which are higher for the former. We also performed a control experiment by using a ground mixture of GHG and Cu(II) acetate in the same proportion present in the MOF. Individual components do not show measurable chiral recognition (Figure SI11), suggesting that the periodic distribution of chiral channels in the MOF scaffold is key for enantiomeric separation. To confirm the stability of the solid in the experimental conditions, we collected UV/vis spectra of dispersions of Cu(GHG) at variable times. As shown in Figure SI15, spectra remained constant and there is no signature of Cu(II) leaching that might account for partial dissolution. As for the MOF structure, PXRD of the solid after the experiment confirms the structure remains intact (Figure SI16a), with only minor variations in the relative intensities of some Bragg's reflections ascribed to preferential orientation of the crystals or changes in the nature of the species occupying the pores.

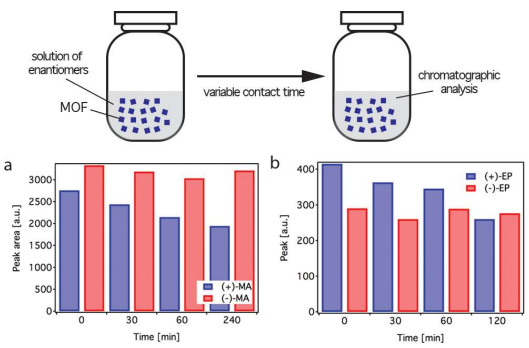

Figure 3. Evolution of the enantioselective recognition of Cu(GHG) for chiral drugs in ethanol:water 75:25 solution with contact time for (a) MA and (b) EP. Chiral adsorption was evaluated from chromatographic analysis of the supernatant solution. See Figure SI10 for more details.

Recent reports highlight the potential of chiral MOFs for the development of chiral stationary phases (CSPs) in the form of packed columns for high-performance liquid chromatography (HPLC) enantioselective separation.[7] However, the limited number of tests available suggests that the main limitations of MOFs as stationary phases are their poor stability and particle heterogeneity. This limits the range of mobile phases available, in particular for polar analytes, and makes it difficult to achieve efficient packing of the particles in the column, which relies on narrow distributions in size and shape for reproducible sorption/desorption kinetics. Lack of control over these variables can result in high retention times, low chromatographic performance, and energy-consuming separations. MOFs might be instead better fitted for solid-phase extraction (SPE) separation technologies. In contrast to CSP, SPE enables isolation of the enantiomers rather than only providing a measure of the enantiomeric purity of a mixture. SPE can allow for more efficient chromatographic analysis by removal of interferences, increase of trace concentration, or sample simplification, but use of chiral MOFs in this context remains unexplored. To illustrate this concept, we

DOI: 10.1021/jacs.7b00280
J. Am. Chem. Soc. 2017, 139, 4294−4297

packed 50 mg of Cu(GHG) in a polypropylene SPE cartridge and eluded a racemic mixture of (±)-EP in hexane:ethanol 75:25 at 0.25 mL/min, followed by HPLC analysis of the resulting extract (Figure 4a). The experimental setup is shown in Figure SI12. We

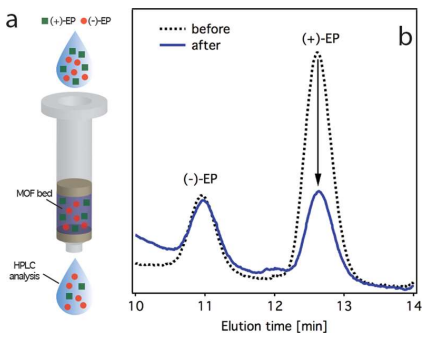

Figure 4. (a) SPE separation of EP in hexane:EtOH 75:25 by using Cu(GHG) as chiral bed. (b) HPLC chromatograms of EP racemate before (dashed line) and after (solid line) passing through the MOF bed. See Supporting Information, SI4, for experimental details.

opted for EP rather than MA based on our preliminary results that suggested faster and more efficient recognition of the former. As shown in Figure 4b, comparison of the chromatograms of the sample before and after SPE/Cu(GHG) separation confirms the ability of the MOF to trap preferentially (+)-EP, in line with our theoretical predictions. While the peak area contribution for (−)-EP remains constant, there is a significant decrease for the (+)-form. Quantitatively, the chiral solid permits separating 54 ± 2% of (+)-EP from equimolar mixtures of the enantiomers in 4 min with a satisfactory precision (RSD = 4%) for the different cartridges tested (Table SI3). HPLC analysis of the solution desorbed from the MOF by elution with fresh solvent confirms that only (+)-EP enantiomers are retained in the separation, confirming enantioselectivity (Figure SI13). Compared to SPE, direct soaking of the crystals in a racemic mixture of (±)-EP in hexane:EtOH 75:25 also leads to enantioselective separation of 44% of (+)-EP in the same time (Figure SI14). MOF cartridges can be used at least for two runs without significant loss of enantioselectivity. PXRD (Figure SI16b−d) and SEM (Figure SI17) studies of the crystals in the MOF bed after separation experiments confirm that both the structure and the morphology of the solid remain unchanged. Hence, we ascribe loss of activity to an inefficient packing of the solid rather than to chemical degradation. Our results suggest that Cu(GHG) offers high performance in terms of stereoselective recognition and time efficiency, for a high-speed chiral separation medium.

Peptide MOFs are particularly well suited for enantioselective recognition. The chiral pockets in their structure can be manipulated for maximizing host−guest intermolecular interactions for a specific enantiomer simply by suitable choice of the peptide sequence. Cu(GHG) is capable of separating >50% of (+)-ephedrine from a racemic mixture in only 4 min when used as a chiral SPE cartridge. This is a promising result, considering the limited availability of SPE cartridges for chiral separation on the market. According to our theoretical simulations, stereoselectivity is driven by preferential non-covalent interactions with specific amino acids, particularly His, in the MOF backbone. This combination of theory and experiment holds great potential and might help in addressing the challenge of chiral recognition by producing more complex chemical environments in which supramolecular interactions can be finely tuned for maximizing enantiomeric resolution for particular drugs.

■ ASSOCIATED CONTENT

Supporting Information

The Supporting Information is available free of charge on the ACS Publications website at DOI: 10.1021/jacs.7b00280.

Synthetic and experimental details, physical characterization, Tables SI1−SI3, and Figures SI1−SI17 (PDF)

■ AUTHOR INFORMATION

Corresponding Author

*carlos.marti@uv.es

ORCID

Pilar Campíns-Falcó: 0000-0002-0980-8298
Matthew J. Rosseinsky: 0000-0002-1910-2483
Carlos Martí-Gastaldo: 0000-0003-3203-0047

Author Contributions

⊥J.N.-S. and A.I.A.-G. contributed equally.

Notes

The authors declare no competing financial interest.

■ ACKNOWLEDGMENTS

This work was supported by the EU (ERC Stg Chem-fs-MOF 714122), Spanish MINECO/FEDER (Project CTQ-2014-53916-P and Unit of Excellence María de Maeztu MDM-2015-0538), and the Generalitat Valenciana (Prometeo 2016/109 and GV/2016/137). C.M.-G. and A.I.A.-G. thank the Spanish MINECO for a Ramón y Cajal Fellowship and FPU Scholarship, respectively.

■ REFERENCES

(1) Nugent, P.; Burd, S. D.; Forrest, K.; Pham, T.; Ma, S.; et al. *Nature* **2013**, *495*, 80.

(2) (a) Bloch, E. D.; Queen, W. L.; Krishna, R.; Zadrozny, J. M.; Brown, C. M.; Long, J. R. *Science* **2012**, *335*, 1606. (b) Cadiau, A.; Adil, K.; Bhatt, P. M.; Belmabkhout, Y.; Eddaoudi, M. *Science* **2016**, *353*, 137.

(3) Warren, J. E.; Perkins, C. G.; Jelfs, K. E.; Boldrin, P.; Chater, P. A.; et al. *Angew. Chem., Int. Ed.* **2014**, *53*, 4592.

(4) (a) Kutzscher, C.; Müller, P.; Raschke, S.; Kaskel, S. *Chiral Linker Systems: Synthesis, Characterization, and Applications*; Wiley: Weinheim, 2016; pp 387−419. (b) Duerinck, T.; Denayer, J. F. M. *Chem. Eng. Sci.* **2015**, *124*, 179.

(5) (a) Martí-Gastaldo, C.; Antypov, D.; Warren, J. E.; Briggs, M. E.; Chater, P. A.; et al. *Nat. Chem.* **2014**, *6*, 343. (b) Katsoulidis, A. P.; Park, K. S.; Antypov, D.; Martí-Gastaldo, C.; Miller, G. J.; et al. *Angew. Chem., Int. Ed.* **2014**, *53*, 193. (c) Marti-Gastaldo, C.; Warren, J. E.; Stylianou, K. C.; Flack, N. L. O.; Rosseinsky, M. J. *Angew. Chem., Int. Ed.* **2012**, *51*, 11044. (d) Rabone, J.; Yue, Y. F.; Chong, S.; Stylianou, K.; Bacsa, J.; et al. *Science* **2010**, *329*, 1053.

(6) Martí-Gastaldo, C.; Warren, J. E.; Briggs, M. E.; Armstrong, J. A.; Thomas, K. M.; Rosseinsky, M. J. *Chem. - Eur. J.* **2015**, *21*, 16027.

(7) (a) Hartlieb, K. J.; Holcroft, J. M.; Moghadam, P. Z.; Vermeulen, N. A.; Algaradah, M. M.; et al. *J. Am. Chem. Soc.* **2016**, *138*, 2292. (b) Hailili, R.; Wang, L.; Qy, J.; Yao, R.; Zhang, X.-M.; Liu, H. *Inorg. Chem.* **2015**, *54*, 3713. (c) Peng, Y.; Gong, T.; Zhang, K.; Lin, X.; Liu, Y.; Jiang, J.; Cui, Y. *Nat. Commun.* **2014**, *5*, 4406. (d) Zhang, M.; Pu, Z.-J.; Chen, X.-L.; Gong, X.-L.; Zhu, A.-X.; Yuan, L.-M. *Chem. Commun.* **2013**, *49*, 5201. (e) Das, M. C.; Guo, Q.; He, Y.; Kim, J.; Zhao, C.-G.; et al. *J. Am. Chem. Soc.* **2012**, *134*, 8703. (f) Padmanaban, M.; Müller, P.; Lieder, C.; Gedrich, K.; Grünker, R.; et al. *Chem. Commun.* **2011**, *47*, 12089.

DOI: 10.1021/jacs.7b00280
J. Am. Chem. Soc. 2017, 139, 4294−4297

Supplementary Information

Peptide Metal-Organic Frameworks for enantioselective separation of chiral drugs

José Navarro-Sanchez[a‡], Ana I. Argente-García[b‡], Yolanda Moliner-Martínez[b], Daniel Roca-Sanjuán[a], Dmytro Antypov[c], Pilar Campíns-Falcó,[b] Matthew J. Rosseinsky[c] and Carlos Martí-Gastaldo*[a]

[a]Universidad de Valencia (ICMol), Catedrático José Beltrán-2, 46980, Paterna (Spain)
[b]MINTOTA research group. Departament de Química Analítica, Facultat de Química, Universitat de Valencia, Doctor Moliner, 50, 46100 Burjassot, (Spain).
[c]Department of Chemistry, University of Liverpool. Crown Street, Liverpool, L697ZD (UK)

Table of contents

Materials and reagents. All reagents and solvents used were of commercially available grade and were used without any additional purification. The tripeptide H-Gly-L-His-Gly-OH was purchased from Bachem®. Acetonitrile, methanol, ethanol and hexane were supplied by Scharlau. Methamphetamine (MA) enantiomers, Ephedrine (EP) enantiomers, 9-fluorenylmethyl chloroformate-L-proline (FMOC-L-Pro) and dicyclohexylcarbodiimide (DCC) were all purchased from Sigma Aldrich. Sodium hydrogencarbonate (Probus) was also used. Ultrapure water was obtained from a Nanopure II (Sybron) system.

SI 1. Synthesis of Cu(GHG). [Cu(Gly-L-His-Gly)] (Gly-L-His-Gly = $C_{12}H_{16}N_6O_5^{2-}$) was prepared by following the synthesis previously described by one of us. [1] 24.2 mg of the peptide (90 μmol) were dissolved in 300 μL of an aqueous solution of $Cu(OAc)_2 \cdot 2H_2O$ 0.3 M (90 μmol) in a 4 mL glass vial to produce a blue solution. The solution was manually stirred followed by sequential addition of 1.26 mL of absolute ethanol and 200 μL of water. The mixture was then left to stand in a temperature controlled chamber at 25ºC for the formation of blue coloured prismatic crystals. After 48 hours, crystals were filtered, washed with absolute ethanol and stored at 4ºC (75% yield, calculated for the metal). Analysis. calc. for $[Cu(C_{12}H_{16}N_6O_5)] \cdot (H_2O)_6$ (Mw = 495.93): C, 29.06; N, 16.95; H, 5.69. Found: C, 28.85; N, 16.85; H, 5.51.

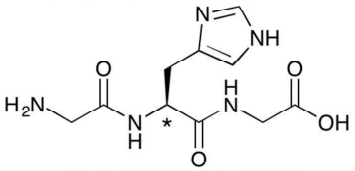

Glycil-L-histidylglicine (GHG)

Figure SI1. Optical microscope (left) and Scanning Electron Microscopy (SEM) images (right) of as-made crystals of Cu(GHG). Particle morphologies and dimensions were studied with a Hitachi S-4800 scanning electron microscope at an accelerating voltage of 20 keV, over metalized samples with a mixture of gold and palladium during 30 s.

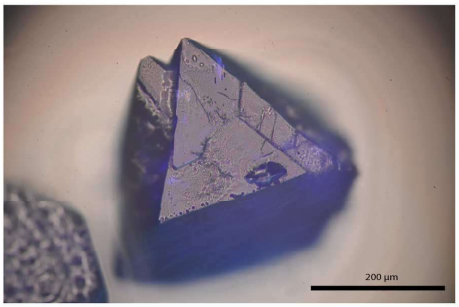

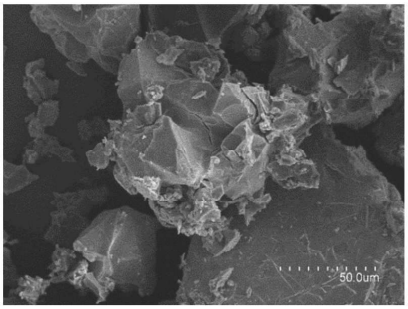

Figure SI2. FT-IR of Cu(GHG) collected in a FT-IR Nicolet 5700 spectrometer in the 4000–400 cm^{-1} range from ground crystals diluted in a KBr pellet.

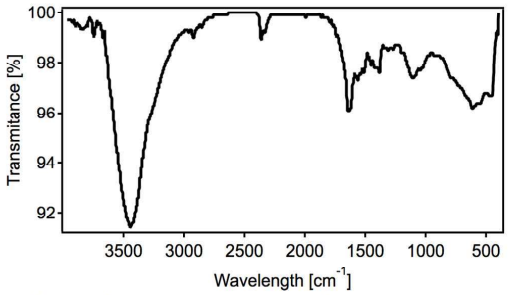

(KBr, [cm^{-1}]): 300 (m), 610 (m), 1200 (m), 1400 (m), 1600 (m), 2400 (w), 2900 (w), 2450 (sr, br), 3700 (w)

Figure SI3. Thermogravimetric analysis of Cu(GHG) between 25 and 800 °C under a 10 °C.min^{-1} scan rate and an air flow of 30 mL.min^{-1} by using a a Mettler Toledo TGA/SDTA 851.

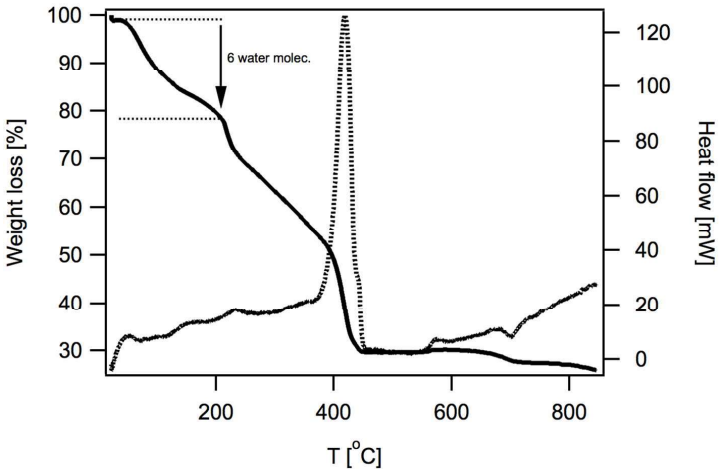

The weight loss of 22% from room temperature to close to 200 ºC corresponds to the removal of close to 6 water molecules from the pores of Cu(GHG), in good agreement with the solvent content present in the as-made solid.

Figure SI4. Experimental (red dots), calculated (blue line), difference plot [(*I*obs−*I*calcd)] (red line, bottom panel) and Bragg positions (green ticks, bottom panel) for the unit cell refinement of experimental diffraction data of Cu(GHG) collected at room temperature by using single-crystal data available from CCDC931607 as starting parameters.[1] PXRD patterns were collected in a PANalytical X'Pert PRO diffractometer using copper radiation (Cu Kα = 1.5418 Å) with an X'Celerator detector, operating at 40 mA and 45 kV. Profiles were collected in the 2° < 2θ < 60° range with a step size of 0.017°.

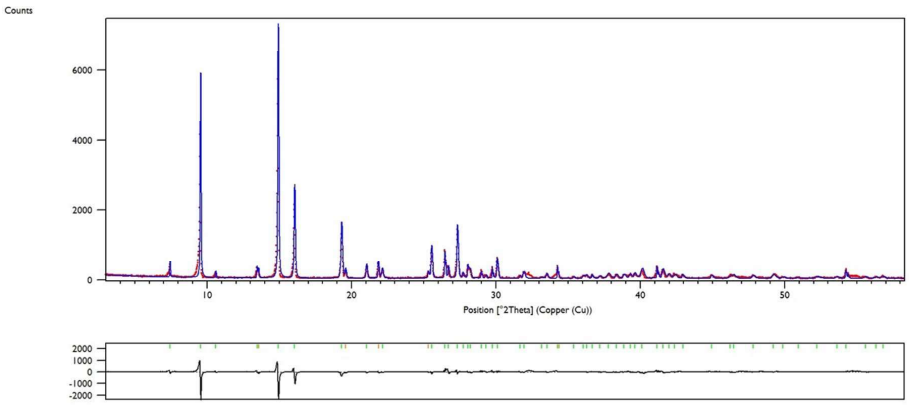

Tetragonal, P4212; a = b = 13.973(6), c = 27.51(2) Å; V = 5370.93Å^3. X^2 = 1.50E-05. Snyder's FOM = 1.90.

Figure SI5. Solid-state chiral dichroism (CD) UV-Vis spectrum of GHG (blue) and Cu –GHG (green). Pellet used for the measurements was prepared by diluting ground crystals of the MOF in a KBr matrix. Spectra was collected with a spectropolarimeter Jasco J-810 and recorded at a temperature of 25°C. Ellipticity values were recorded every 0.1 nm at a wavelength scanning speed of 20 nm/min. The response time was set to 1 s and the bandwidth was set to 1 nm. The final spectrum represented the accumulated

average of five consecutive scans. Whilst CD of GHG displays a positive Cotton effect in the UV region linked to the presence of enantiopure GHG, Cu(GHG) displays a broad absorption band centered at 610 nm as result of Cu(II) complexation.

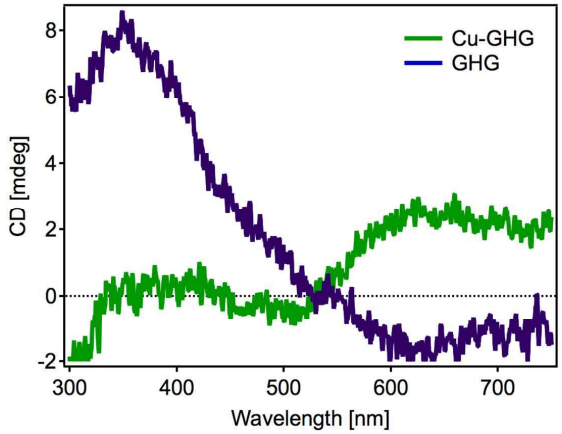

Figure SI6. Pore metrics and molecular dimensions of chiral drugs. a) Diameter of the largest included (Di) and free sphere (Df) in Cu(GHG) as calculated by Voronoi decomposition of the void space with a spherical probe of 1.2 Å by using Zeo++.[2] b) Molecular dimensions of ephedrine and metamphetamine by using the following element radii: C, 1.7; H, 1.09; N, 1.55 and O, 1.52 Å. Default radii source: http://www.ccdc.cam.ac.uk/products/csd/radii.

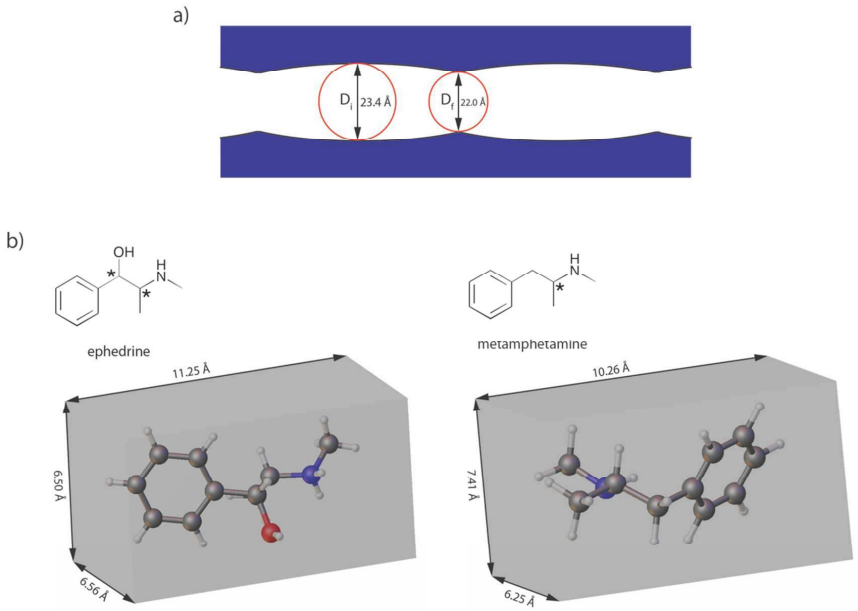

SI 2. Computational details.

Monte Carlo (MC) simulations. Pure component adsorption in Cu(GHG) was simulated by carrying out multiple MC searches of the configurational space of the substrate-adsorbate system, searching for low-energy adsorption sites as the temperature is slowly decreased according to a simulated annealing procedure.[3,4] A single guest molecule was used in the computations. To generate the candidate substrate-adsorbate configurations, a canonical ensemble is used in which the loading of the adsorbate on the rigid substrate and the temperature are fixed. In each step of the MC sampling, a randomly neighboring state is produced. If the energy decreases, the new state will be used for the next step. If the energy increases, the attempt is followed by a decision whether to accept the selected neighboring state or use the current state. The decision is based on the energy difference between the states and the temperature of the system.

One unit cell of Cu(GHG) of 13.97x13.97x27.47 Å (cell volume of 5368.87 $Å^3$) was used for the simulations. The COMPASSII force field was used to model the substrate and adsorbates (MA and EP enantiomers). A cut-off distance of 12.5 Å was used for all Van der Waals interactions. The Ewald summation method was used for the electrostatic interactions. For the MC adsorption simulations, 100000 loading steps were performed, in 5 heating cycles with 50000 steps per cycle. Previously, the geometry of both the adsorbate and the MOF were optimized separately with the same force field, COMPASSII, and charges assigned by the force field. Adsorption energies were computed as the energy difference between the energy of the substrate-adsorbate adduct obtained from the MC simulation and those of the separated components. The reported energy values correspond to the average data obtained for the 10 most stable adducts of each enantiomer. In such manner, we take into account close-lying configurations which might also be important.

Relative adsorption energies for (±)-MA and (±)-EP as calculated from MC simulations:

	(+)-MA	(-)-MA	(+)-EP	(-)-EP
Ads. Energies [kcal.mol^{-1}]	22.46	18.84	44.96	32.48
ΔE (±)-enant.	3.62		12.48	

Quantum-Chemistry computations. We used the Density Functional Theory (DFT) with the B3LYP functional and the 6-31G* basis set in the Gaussian 09 (D.01 revision) software package[5] to roughly estimate the hydrogen bond binding energies between the different functional groups decorating the pores of the MOF (imidazole, amide and amino sites) and those in MA adsorbate. Our purpose here is not to accurately determine the energies, but to provide a semi-quantitative estimation of the relative H-bond strengths with bond distance. For simplicity, we limited the study to the asymmetric unit of Cu(GHG) shown in Figure SI7. Hydrogen bond energies were computed as the difference between the energy of the isolated MOF unit and adsorbate molecules and that of the MOF-guest adduct. The potential energy curve of the dimethylamine···imidazole dimer was also computed with the same methodology upon increasing and decreasing the hydrogen bond distance from the optimized bond length in the equilibrium structure of the dimer. The *Cs* symmetry point group was used in this case to simplify the computation.

Table SI1. Summary of binding energies and H-bond lengths for MA-MOF interactions as estimated by quantum-chemistry calculations.

H-Bond	Binding Energy / kcal.mol^{-1}	Bond Length / Å
(MA)-HN···HN-(imidazole; His)	15.0	1.977
(MA)-HN···H_2N-(amino, Gly; N-term)	10.9	2.054
(MA)-NH···O=C-(amide bond, Gly N-term)	6.3	2.149

Figure SI7. Relevant hydrogen-bond interactions between MA and functional groups in the MOF pocket calculated by DFT: (a) imidazole (Hys), (b) amino group (Gly, N-term) and (c) amide bond (Gly, N-term).

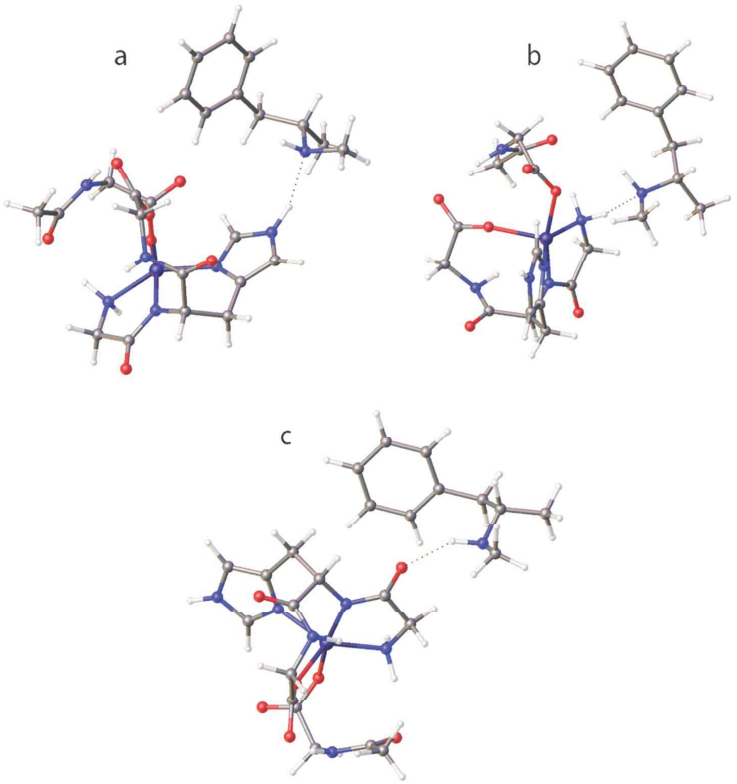

Figure SI8. DFT potential energy curve (ΔE) of the dimethylamine-imidazole dimer upon increasing the hydrogen bond distance (d_{HB}).

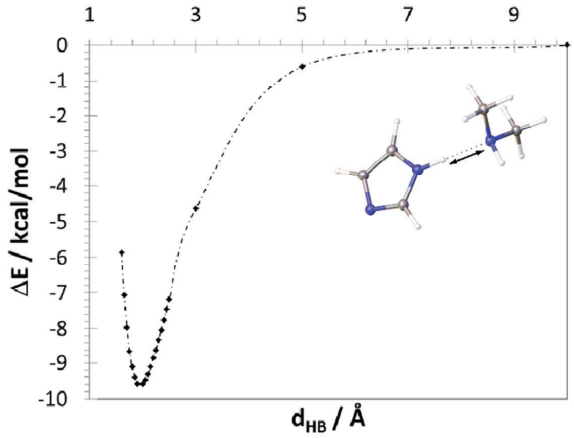

Figure SI9. (a) MC optimized binding geometries of (+,-)-MA (a, top) and EP (d, bottom panel). Enantiomers, and H-bonds specific to the docking, are overlaid for highlighting the different geometries of (+) and (-) forms and represented in orange and turquoise, respectively. Overall view along 100 of the more favorable binding sites of (+)-MA (b), (-)-MA (c), (+)-EP (e) and (-)-EP (f) in the internal cavities of Cu(GHG).

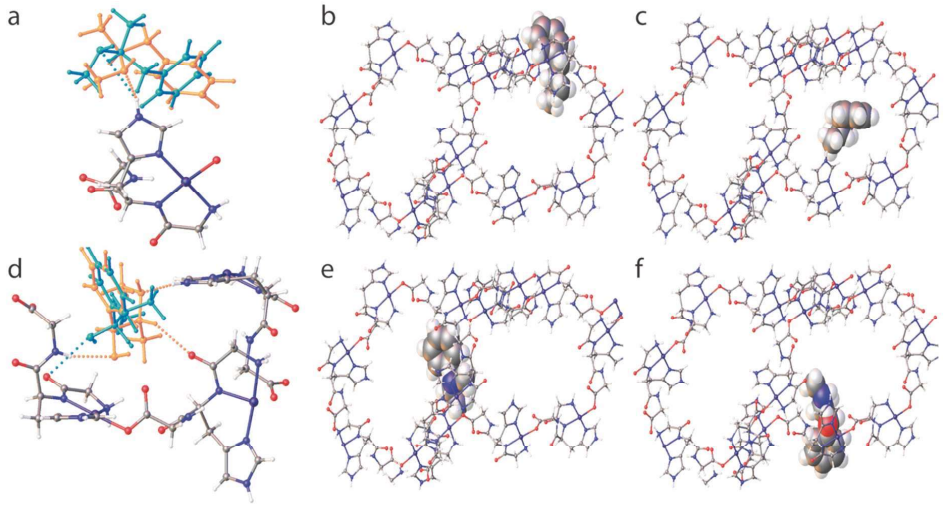

SI 3. Enantioselective separation study.

Enantioselective separation in solution. For a first set of preliminary studies, we examined the enantiomeric recognition of Cu(GHG) in solution. 10 mg of freshly made MOF were soaked in 2 mL of an alcoholic mixture (ethanol:water 75:25) of a racemic mixture of (±)-MA and (±)-EP (40 μg mL^{-1}). Enantioselective separation was evaluated by chromatographic analysis of the solution with time.

Enantioselectivity preliminary studies. The determination of MA and EP by liquid chromatography entails a previous chemical derivatization to make the analytes more amenable for chromatography and to enhance the sensitivity. Conditions for the derivatization of the tested drugs were selected according to our previous work.[6] Aliquots of enantiomer solution (125 μL) were placed into 2 mL glass vials, and mixed with 125 μL of carbonate buffer (0.01 M, pH 10) and with 250 μL of derivatization reagent (0.1 mM of FMOC). The resulting solution was allowed to react for a 5 and 2 min, for methamphetamine and ephedrine, respectively. Finally, 20 μL of the solution were injected onto the analytical column. In order to reduce the analysis time and solvent consumption, the preliminary studies were carried out with a capillary LC (CapLC) using a chromatographic column Zorbax C18 column (35 mm x 0.5 mm i.d., 5 μm particle diameter). The mobile phase was acetonitrile:water 60:40 at a flow rate of 15 μL min-1 at 298 K. The target analytes were monitored at 264 nm. Under these conditions, enantiomers were tested individually.

Figure SI10. Time evolution of HPLC chromatograms of (+,-)-MA and (+,-)-EP after soaking in an alcoholic mixture with 10 mg of Cu(GHG) under static conditions. Inset in the right column highlights the signal specific to each enantiomer.

Time evolution of (-)-MA in solution in contact with Cu(GHG):

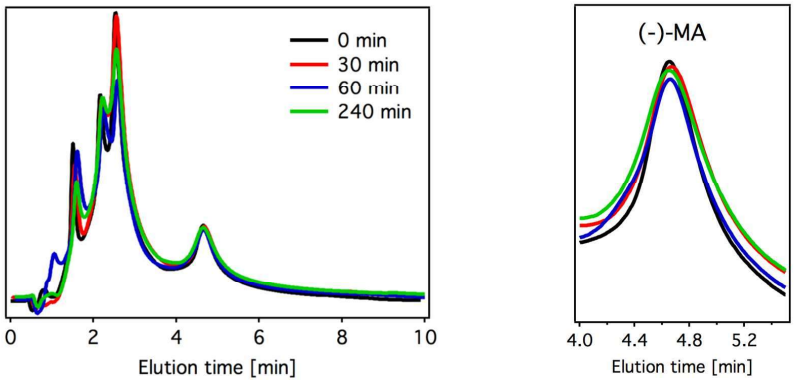

Time evolution of (+)-MA in solution in contact with Cu(GHG):

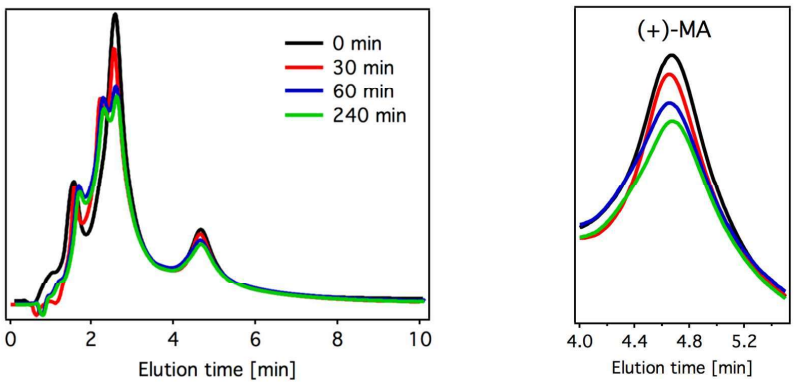

Time evolution of (-)-EP in solution in contact with Cu(GHG):

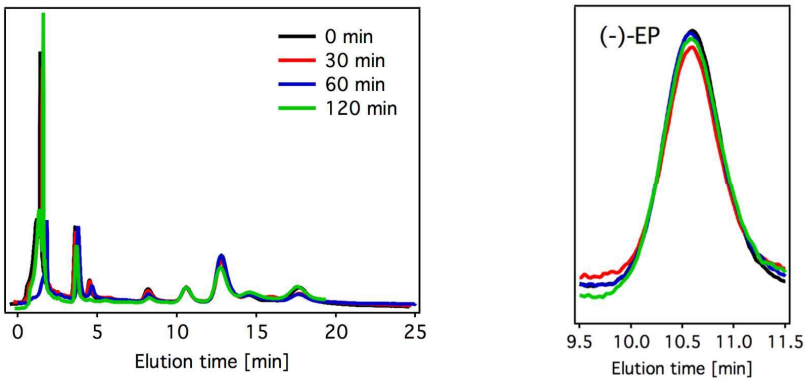

Time evolution of (+)-EP in solution in contact with Cu(GHG):

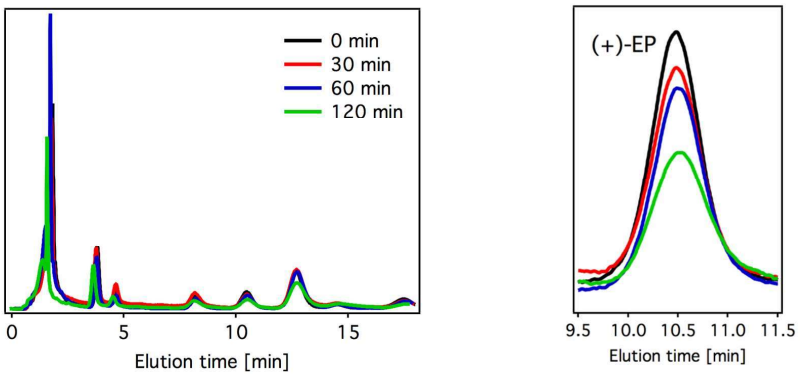

As shown above, time evolution of the peak area for (-)-MA and (-)-EP is almost negligible, ruling out preferential recognition for any of these enantiomers. However, areas for the (+)-MA and (+)-EP signals show a clear decrease for longer contact times with the MOF, which suggests preferential MOF/enantiomer interaction. This is more clearly shown in Fig.3 in the paper that displays the peak area evolution as calculated with Agilent Chemstation© for all species as a function of the time in contact with the MOF in solution.

For clarity, we have defined the enantioselective recognition of Cu(GHG) for (+)-MA and (+)-EP as the ratio between the difference of the peak areas for these enantiomers after 240 and 120 min (minimum signal intensity detected experimentally in each case) and the maximum at 0 min for free enantiomers in solution in absence of the MOF normalized to the peak area of this last. Experiments were repeated two times for confirming reproducibility of the reported behavior, data are summarized in the table below.

Table SI2. Experimental data used for calculation of enantioselective recognition capability of Cu(GHG).

Time [min]	Peak area (+)-MA [a.u.]		
	Test 1	Test 2	Test 3
0 (no MOF)	2828	2694	2750
240 (with MOF)	2092	1812	1914
Enantioselective recognition [%]	26.0	32.7	30.4
Average [%]		**30**	
Standard Deviation (s)		**3**	

Time [min]	Peak area (+)-EP [a.u.]		
	Test 1	Test 2	Test 3
0 (no MOF)	440	392	410
120 (with MOF)	288	234	267
Enantioselective recognition [%]	34.5	40.3	34.9
Average [%]		**37**	
Standard Deviation (s)		**3**	

Figure SI11. Control experiment to confirm the observed chiral recognition is specific to the MOF architecture rather than to any of its components. Below HPLC chromatograms for a physical mixture of GHG and Cu(II) acetate in the same proportion present in the MOF. Evolution of the peak areas for (+) and (-)-MA in a solution of the MOF components rules out measureable enantioselective recognition of any of the enantiomers. Inset in the right column highlights the signal specific to each enantiomer.

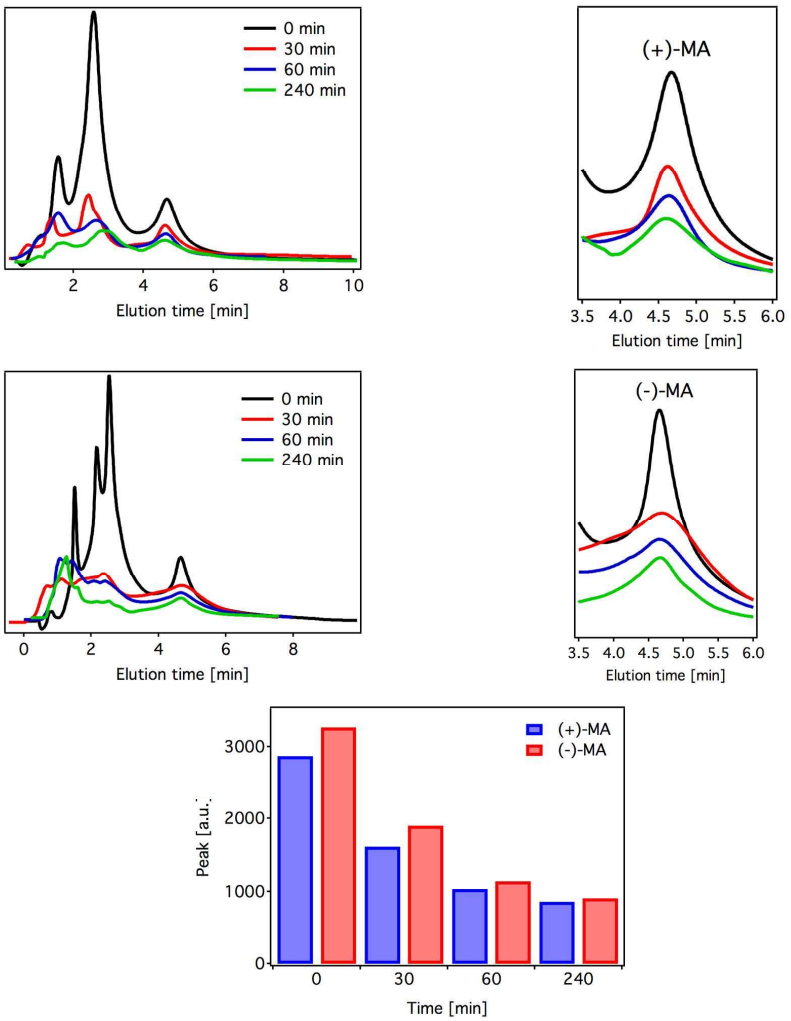

SI 4. SPE enantioseparation with Cu(GHG).

Enantioselective separation with solid phase extraction (SPE). The SPE cartridges were prepared by placing 50 mg of Cu(GHG) as extractive phase into a polypropylene SPE tube (1mL, Supelco) with upper and lower polyethylene frits (20 µm pore size, Supelco). For enantioselective separation experiments we let flow a racemic mixture of ephedrine enantiomers (200 µg mL^{-1} of each enantiomer) in 1 mL of ethanol:hexane (1:4) through the SPE cartridge by gravity (approximately 4 min of contact time between the SPE cartridge and the MOF). Eluted solution was collected and evaporated to dryness using nitrogen. Then, the extract was dissolved in 1 mL of water and derivatized following the procedure above for chiral identification by HPLC. Cyclability of the MOF was evaluated by using the same cartridge for 2 consecutive separation cycles.

Chiral identification. Identification of the enantiomers was carried out by following the procedure described by some of us.[6] Accordingly, 125 µL of FMOC-L-proline (1 mM) and 125 µL of DCC (10 mM) were mixed for 5 min and added to 250 µL of analyte solution, followed by addition of 250 µL of hydrogencarbonate buffer (4% m/v, pH 10.0). The resulting solution was allowed to react for 2 min and then was injected (20 µL) into the HPLC system. The chromatographic system consisted of an isocratic quaternary pump (Jasco, PU-2089 Plus), a high-pressure six-port valve equipped with a 20 µL loop (Rheodyne) and a Hypersil ODS-C18 (250 mm x 4 mm i.d., 5 µm) analytical column. We used a fluorescence detector (Jasco, FP-202 Plus) for enantiomer detection by using excitation and emission wavelengths of 264 nm and 313 nm, respectively. Chiral identification was carried out at ambient temperature using acetonitrile-water 60:40 as the mobile phase at a flow rate of 0.5 $mL.min^{-1}$.

Figure SI12. (a) Scheme of the experimental setup used for SPE enantioseparation and (b) picture of the actual polypropylene SPE tube after incorporation of the chiral MOF bed.

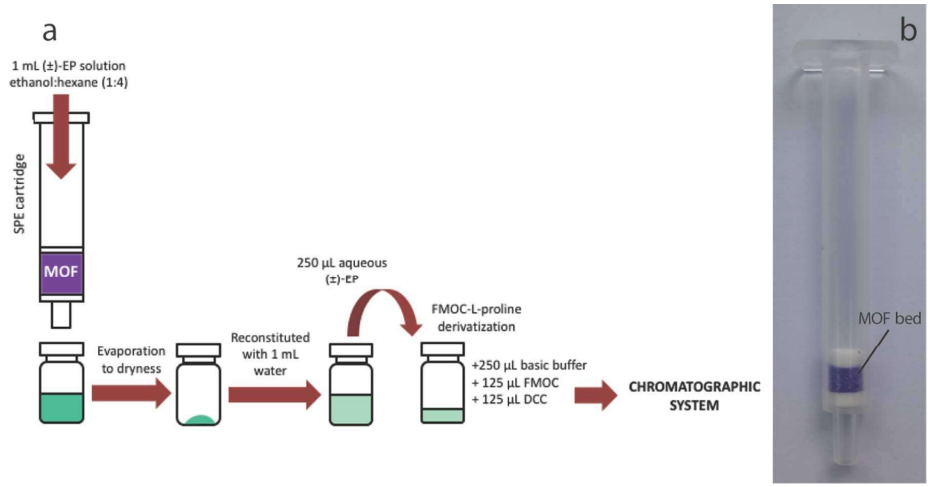

Table SI3. Cartridge to cartridge precision.

Conditions	Peak area (+)-EP [a.u.]		
	Test 1	Test 2	Test 3
no MOF	68103	66451	69391
with MOF	30420	31873	30611
Enantioselective recognition [%]	55.3	52.0	55.9
Average [%]		**54**	
Standard Deviation (s)		**2**	
Relative standard deviation (RSD) [%]		**4**	

Figure SI13. Comparison of HLPC chromatograms of a racemic mixture of (±)-EP in Hexane:EtOH 75:25 after passing through the MOF SPE cartridge (black line, adsorption) and after elution with fresh solvent (desorption). The presence of (-)-EP in the desorbed fraction is negligible whilst only (+)-EP can be detected in the chromatogram in good agreement with the reported enantioselectivity.

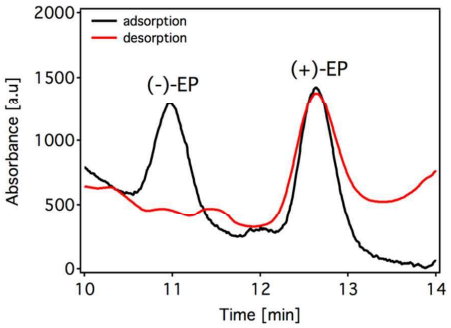

Figure SI14. Control experiment by soaking as-made crystals of CuGHG in a racemic mixture of (±)-EP in hexane:EtOH 75:25. (a) Evolution of the peak areas for (-) and (+)-EP. Adsorption of (-)-EP can be considered negligible whilst close to 44% of (+)-EP is preferentially adsorbed. (b) HPLC chromatograms of EP racemic solution in contact with the MOF before (0 min) and after 4 minutes.

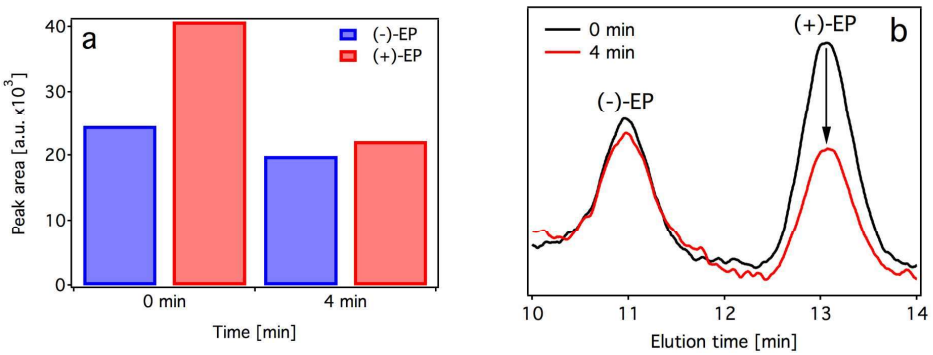

Figure SI15. Time evolution of the UV-Vis spectra at room temperature (Hewlett-Packard HP8452) of a dispersion of as-made 5 mg of Cu(GHG) in 500 µL of EtOH:H_2O (25:75 v%) from 0 to 240 min. All measurements were taken for the same fraction of crystals and solvent to prevent relative differences in light scattering. This set of conditions are equivalent to those used for studying the ability of Cu(GHG) to recognize selectively enantiomers from solution (see SI3 for more details). The system remains constant and no signature of Cu(II) leaching –broad absorption band centered at 600 nm– can be observed, confirming the chemical integrity of the solid in these conditions.

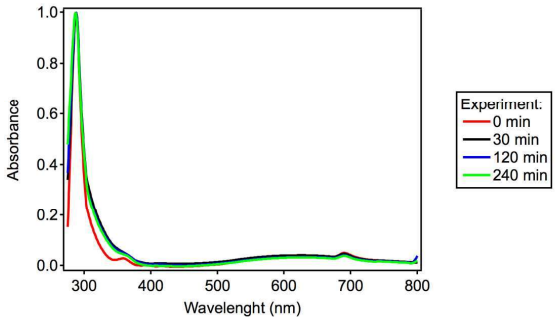

Figure SI16. PXRD of Cu(GHG) after enantioselective separation experiments in solution (a) and packed SPE cartridges (b-d). Variations in the relative intensities of some Bragg's reflections with respect to the PXRD of Cu(GHG) shown in Figure SI4 can be ascribed to the sample preparation procedure (ground solid vs crystals). PXRD patterns were collected in a PANalytical X'Pert PRO diffractometer in transmission mode using copper radiation (Cu Kα = 1.5418 Å) with an X'Celerator detector, operating at 40 mA and 45 kV. Profiles were collected in the 5° < 2θ < 58° range with a step size of 0.013°.Refinement against the unit cell calculated from the atomic positional parameters of the single-crystal data available CCDC961607.[1] Experimental (red dots), calculated (blue line), difference plot [(*I*obs−*I*calcd)] (red line, bottom panel) and Bragg positions (green ticks, bottom panel). Refined cell parameters and zero shift calculated with X'Pert HighScore Plus.

(a) Cu(GHG) exposed to a racemic mixture of MA in EtOH:H_2O (75:25) for 5 days

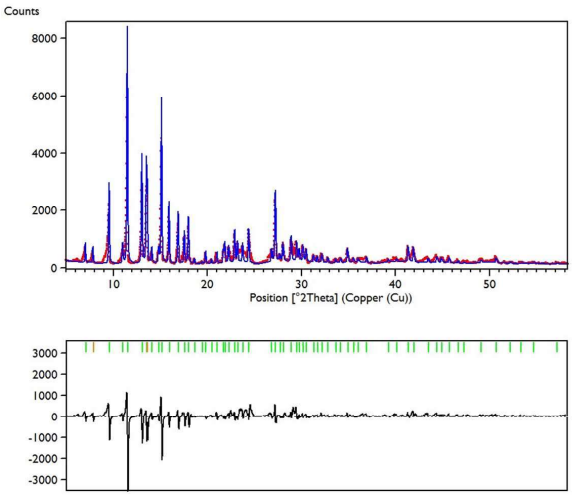

Tetragonal, P4212; a = b = 13.98(3), c = 27.46(4) Å; V = 5367.90Å^3; zero shift = -0.00(6)º; X^2 = 2.11E-05. Snyder's FOM = 1.84.

(b) Cu(GHG) after SPE separation of a racemic mixture of EP in hexane:ethanol (75:25); cartridge 1.

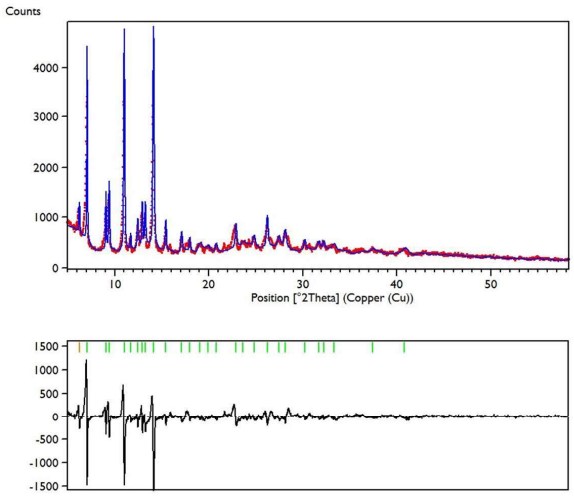

Tetragonal, P4212; a = b = 13.99(4), c = 27.44(9) Å; V = 5370.15Å^3; zero shift = 0.00(8)º; X^2 = 4.47E-06. Snyder's FOM = 2.28.

(c) Cu(GHG) after SPE separation of a racemic mixture of EP in hexane:ethanol (75:25); cartridge 2.

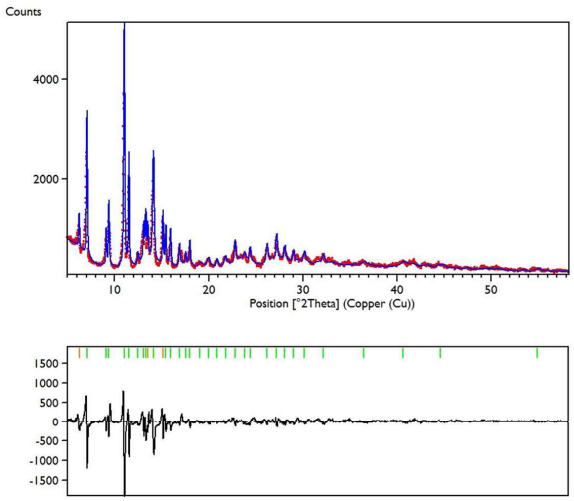

Tetragonal, P4212; a = b = 14.00(3), c = 27.32(6) Å; V = 5354.88Å^3; zero shift = -0.01(6)º; X^2 = 5.91E-06. Snyder's FOM = 1.16.

(d) Cu(GHG) after SPE separation of a racemic mixture of EP in hexane:ethanol (75:25); cartridge 3.

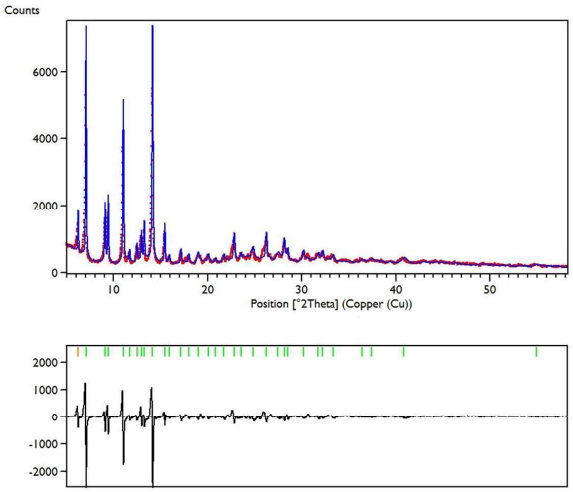

Tetragonal, P4212; a = b = 13.98(3), c = 27.38(5) Å; V = 5349.93Å^3; zero shift = -0.02(6)º; X^2 = 5.54E-06. Snyder's FOM = 1.35.

Figure SI17. SEM pictures of Cu(GHG) before (up) and after (down) SPE separation taken with a Hitachi S-4800 scanning electron microscope at an accelerating voltage of 20 keV. Crystals were metalized with a mixture of gold and palladium during 30 s.

Before:

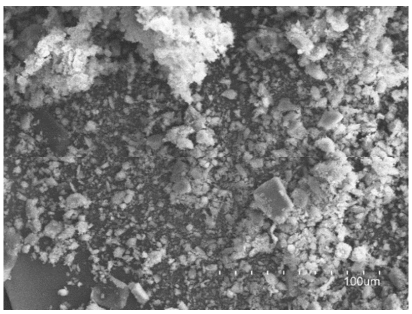

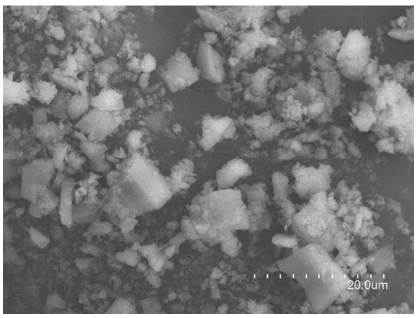

After:

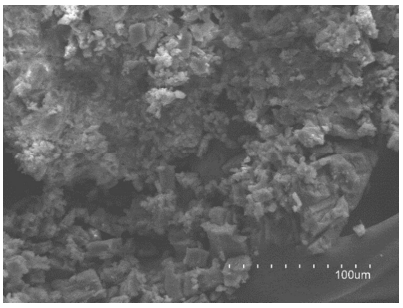

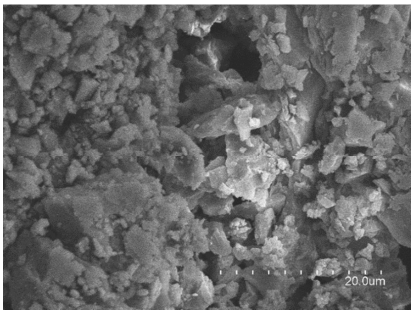

References.

(1) Martí-Gastaldo, C.; Warren, J. E.; Briggs, M. E.; Armstrong, J. A.; Thomas, K. M.; Rosseinsky, M. J. *Chem-Eur J.* **2015**, *21* (45), 16027.

(2) Willems, T. F.; Rycroft, C. H.; Kazi, M.; Meza, J. C.; Haranczyk, M. *Microporous and Mesoporous Materials* **2012**, *149* (1), 134.

(3) Černý, V. *Journal of Optimization Theory and Applications* **1985**, *45* (1), 41.

(4) Kirkpatrick, S.; Gelatt, C. D.; Vecchi, M. P. *Science* **1983**, *220* (4598), 671.

(5) Frisch, M. J.; Trucks, G. W.; Schlegel, H. B.; Scuseria, G. E.; Robb, M. A.; Cheeseman, J. R.; Scalmani, G.; Barone, V.; Mennucci, B.; Petersson, G. A.; Nakatsuji, H.; Caricato, M.; Li, X.; Hratchian, H. P.; Izmaylov, A. F.; Bloino, J.; Zheng, G.; Sonnenberg, J. L.; Hada, M.; Ehara, M.; Toyota, K.; Fukuda, R.; Hasegawa, J.; Ishida, M.; Nakajima, T.; Honda, Y.; Kitao, O.; Nakai, H.; Vreven, T.; Montgomery, J. A., Jr; Peralta, J. E.; Ogliaro, F.; Bearpark, M. J.; Heyd, J.; Brothers, E. N.; Kudin, K. N.; Staroverov, V. N.; Kobayashi, R.; Normand, J.; Raghavachari, K.; Rendell, A. P.; Burant, J. C.; Iyengar, S. S.; Tomasi, J.; Cossi, M.; Rega, N.; Millam, N. J.; Klene, M.; Knox, J. E.; Cross, J. B.; Bakken, V.; Adamo, C.; Jaramillo, J.; Gomperts, R.; Stratmann, R. E.; Yazyev, O.; Austin, A. J.; Cammi, R.; Pomelli, C.; Ochterski, J. W.; Martin, R. L.; Morokuma, K.; Zakrzewski, V. G.; Voth, G. A.; Salvador, P.; Dannenberg, J. J.; Dapprich, S.; Daniels, A. D.; Farkas, Ö.; Foresman, J. B.; Ortiz, J. V.; Cioslowski, J.; Fox, D. J. **2009**.

(6) Herraez-Hernandez, R.; Campins-Falco, P.; Tortajada-Genaro, L. A. *Analyst* **1998**, *123* (10), 2131.

Chapter 4:

Translocation of enzymes as new technique for immobilization in MOFs

1. Motivation

As explained in the Introduction, there are three main choices when trying to immobilize an enzyme inside a MOF, each having their own disadvantages and limitations. In order to provide a fresh view, we decided to explore the problematic from another point of view: the one of the enzyme. One of the most important structural peculiarities of the proteins is the capability some of them have of folding under certain conditions to their ternary structures without assistance. This process is step-wise and allows them to fold into their native state through a energetically downhill at the level of residue-level dynamics.[1,2]

Previous studies have not taken this characteristic into account and use the enzyme as a solid block, incapable of conformational flexibility. The only study made to take profit of this peculiarity was reported in 2012 by Ma,[3] as they described, the immobilization of the protein is based on its translocation.[4,5] This process starts when the protein undergoes a conformational change that changes its dimensions, allowing migration through the open pores at the crystal surface. Inspired by this notable example, we decided to apply this concept on a very special group of proteins: enzymes. Enzymes are a very complex type of protein which difficulties the conformational change that allows the immobilization inside the MOF, as the native structure of the enzyme is fundamental to correctly perform the catalytic activity. Provided that the enzyme could be reverted back to a biological active structure after infiltration, this would result in a very efficient immobilization as the enzyme would remain effectively trapped in the internal cavities of the MOF, avoiding leaching.

For that reason, we decided to employ an enzyme with a notable structural stability and capable of folding by itself under favorable conditions. This technique would allow us to immobilize the enzyme inside a well-fitted pore, with windows that under normal conditions would not allow the entrance of an enzyme of that size. In finding an alternative route that permits overcoming the size limitation, there is an enlargement of the number of MOF-enzyme combinations that could be achieved.

2. Summary of key results

The finding of this work were published in “J. Navarro-Sánchez, N. Almora-Barrios, B. Lerma-Berlanga, J. J. Ruiz-Pernía, V. A. Lorenz-Fonfria, I. Tuñón, C. Martí-Gastaldo, Translocation of enzymes into a mesoporous MOF for enhanced catalytic activity under extreme conditions. *Chem Sci* 2019, **10**, 4082–4088”. In this publication we report the infiltration of a protease, an aspartic proteinase from *Aspergillus saitoi*,[6–8] into the mesoporous cavities of MIL-101(Al)-NH_2. The incubation of the enzyme in an organic medium at mild temperatures forces the enzyme to be partially unfolded, enabling its translocation across the pore windows

of the scaffold (concept represented in **Figure 1a**). This procedure was supported by molecular dynamic simulations and fluorescence spectroscopy, in order to study the conformational changes that the enzyme had undergone.

This enzyme was selected for two reasons, the first based on its relevance for biotechnological applications,[9,10] and the second for being compatible in size with the mesoporous cavities of the MIL-101(Al)-NH_2.[11] On the other hand, the MOF was selected due to several reasons as well. From a structural point of view, it displays a MTN zeotypic three-dimensional extended network that combines two types of mesoporous cavities of 3.6 and 2.9 nm that are interconnected by pentagonal and hexagonal windows of 1.6 and 1.2 nm. This MOF has previously been employed in biologically-compatible conditions and it is capable of adapting to the conditions used for the incubation of enzymes.[12] Dynamic light scattering (DLS) measurements of the protein in TRIS buffer indicated an average distribution size of around 2.85 nm. The pore of the MIL-101-NH_2 was thus selected in order to have a small space between the enzyme and the wall of the MOF, with a ratio of around 1.2. In similar studies this ratio is almost 1,[13–17] and as we hypothesized, this reduced environmental stress is going to improve the conformational regeneration of the enzyme after the translocation. Moreover, we employed the amino-functionalized version of the MOF as the pore decoration that it offers would engage hydrophilicity inside its pores, promoting the formation of H-bond interactions.[18] The increased polarity allows the MOF to show an improved dispersibility in aqueous medium.

In order to allow the enzyme to enter inside the structure of the scaffold, we thought of employing a non-polar solvent and slightly increasing the temperature. This conditions are commonly known to be able to denaturalize the protease, as they reduce the hydrophobic effect and increase the kinetic energy of the system. The new protein arrangement with an altered structure, effectively changes the landscape of energies associated with the array of supramolecular interactions (pi-pi stacking, H-bonds), with the solvent and within the protein affecting its tertiary structure. Thus, in a normal immobilization procedure, we immersed 100 mg of freshly made MIL-101(Al)-NH_2 particles in a 3 mL solution of the protease in TRIS buffer. To this suspension we added 30 mL of anhydrous hexane with a continuous stirring at room temperature. This mixture would be incubated overnight at a temperature of 60°C. After the insertion procedure, the resulting solid was thoroughly washed with the buffer and centrifugated, until there was no measurable protein excess in UV-Vis. Moreover, in order to ensure that the protease was properly fitted inside the pores of the MOF and not bonded in the surface, we carried out two control

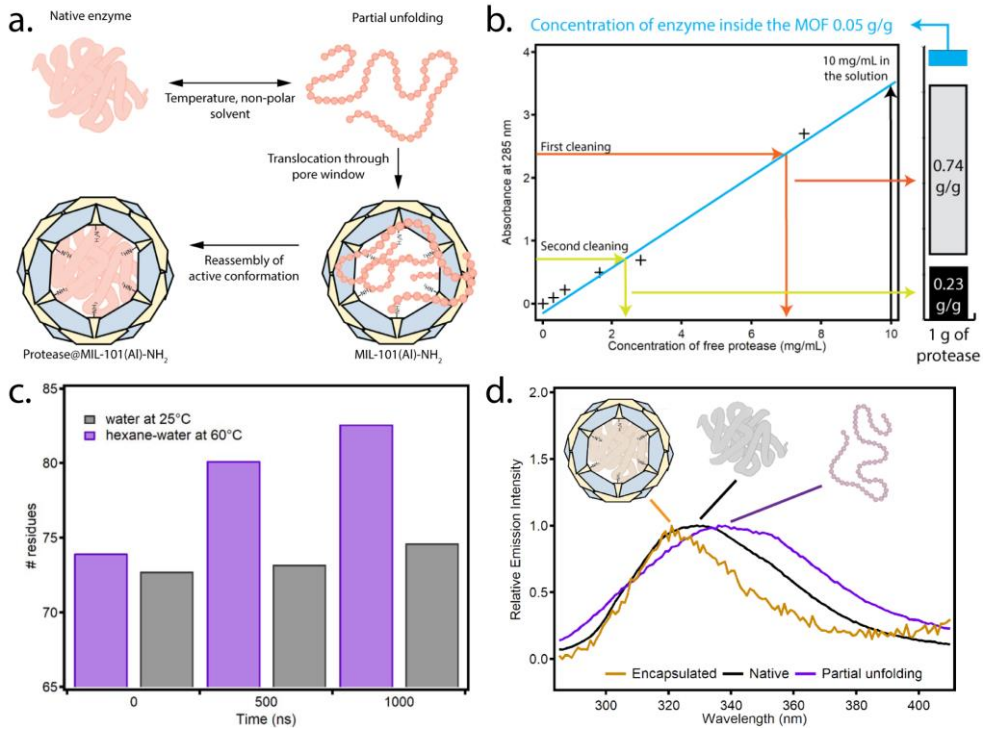

Figure 27. **a**. Scheme of the immobilization process, from the partial denaturalization of the enzyme to the infiltration inside the MOF and the structure regeneration. **b**. Evaluation of enzyme loading by UV-Vis spectroscopy of the supernatant after material washing. **c**. Results of MD simulations of the Aspartic proteinase from *Aspergillus saitoi*. **d**. Fluoresce spectra of free protease (black), protease in non-polar incubation medium at mild temperature (purple) and the protease@MIL-101(Al)-NH_2 (yellow).

experiments. We followed the same enzyme incubation protocol using instead the MIL-101(Cr), lacking a polar environment we did not observe immobilization of the enzyme inside its pores. For the next test we used a commonly known protease substrate, azocasein, with 5 different samples: TRIS buffer (1), TRIS with MOF and protease without incubation (2), MOF incubated with enzyme lacking hexane (3), the protease@MIL-101(Al)-NH_2 prepared as described above (4) and free protease (5). We only observed proteolytic activity in the last two cases, being a corroboration that the enzyme was truly inside the pores of the MOF and the importance of the parameters of the immobilization protocol. The quantity of enzyme immobilized inside the MOF was calculated by UV-Vis, measuring the cleaning medium as shown in **Figure 1b** reaching a 5% w/w. In order to fully understand the innards of this mechanism, we analyzed this process with MD simulations. The *Aspergillus saitoi* protease undergoes a reversible unfolding under the conditions we use on our

experiment. The 1.0 μs MD simulations of the enzyme in the immobilization conditions showed a clear drift from the native structure as time passes, using a standard value of the size of the protein like the root-mean-square deviation (RMSD) we can conclude that there is a partial unfolding. The RMSD continues to increase with time to reach larger values than those of the protein in a polar medium, with 25°C or 60°C. This data confirms that the enzyme is only capable of changing its structure with the combination of the two parameters we use in the immobilization procedure. In a comparison of this new structure with the native one, shows that the protein undergoes an unfolding in the non-polar solution involving the opening of the cleft between two protein lobes. Concretely, the analysis showed a gradual transformation of α-helices and β-sheets into unstructured regions and a progressive increase in amino acids not forming part of a defined secondary structure (**Figure 1c**). The results obtained of the simulations confirm that we are capable of partially unfold the protein in the immobilization conditions.

In order to obtain a direct correlation of the theoretical simulations with the experiment, we used fluorescence spectroscopy to compare the emission spectra of the free protease, the protease in the incubation conditions, and after the translocation (inside the MOF). This particular protease is composed by 16 tyrosine (Tyr) and 3 tryptophan (Trp) residues, capable of emission and thus of being studied.[19] As shown in **Figure 1d**, incubating the free protease on an nonpolar medium with relatively high temperatures shifts the fluorescence maximum emission from 329 to 338 nm. This red shift in the fluorescence is as already reported consequence of the denaturation of proteins, as corresponding to solvent-exposing Tyr and Trp, and reversible. However, when the enzyme is immobilized inside the MOF there is a different change, leading to a blue shift with maximum at 321nm. This could mean that the protein exists in a different folded conformation where Tyr/Trp residues experience a more polar environment than in the native folded state. The immobilization of the enzyme inside the MOF allowed the system to remain stable, as we confirmed by PXRD and SEM. The enzyme could be clearly observed inside the MOF with TGA, Raman spectra, N_2 adsorption experiments and IR. The composite was also stable in the buffer employed in the experiment, TRIS. In other buffers we observed a degradation of the PXRD structure of the MOF to a phase more similar to the MIL-53, with one-dimensional diamond-shaped pores.

In order to corroborate that the enzyme was correctly folded, we performed proteolytic measurements of its activity, as previous reports confirm that proteases can regain their native structure and function after denaturant or thermal-inducing unfolding.[9,10] Concretely, we studied the proteolytic activity of free and immobilized protease to cleave the peptide bond of glycyl-L-tyrosine (Gly-Tyr), and also compared both results in extreme temperature and pH. The free enzyme has a

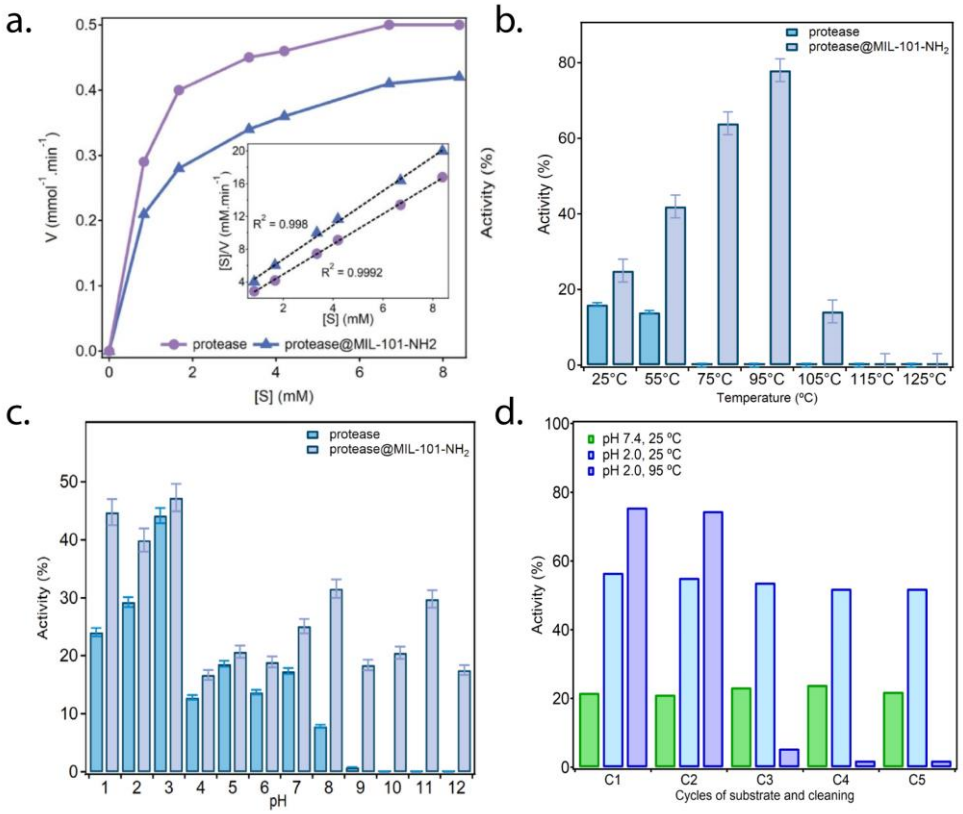

Figure 28. **a**. Study of the proteolytic activity with time as followed by UV-Vis. Comparison of the activity of the free protease and the encapsulated one. **b**. Comparison of the activity of protease before and after encapsulation from 25 to 125°C, pH=7.4. **c**. Same comparison at 25°C, from pH 1 to pH 12. **d**. Activity and recyclability of the composite, stored at room temperature for two weeks, confirming long-term stability and excellent recyclability.

quicker activity under the same conditions (**Figure 2a**) probably due to the more difficult path that the product has to follow to enter inside the MOF, affecting the reaction kinetics. On the other hand, **Figure 2b** shows the evolution of the proteolytic activity maintained after 3 hours at 25°C with changes to the pH between 1 and 12. When compared with the free enzyme, the protease@MIL-101-NH_2 is more active in all cases outside the optimal conditions. Moreover, the composite almost doubles the proteolytic activity of the enzyme at pH 1 and permits retaining the enzymatic activity in a basic medium above pH 8, for which the activity of the free enzyme is completely lost. We also studied a range of high temperatures, as shown in **Figure 2c**, as the kinetic velocity of the catalytic reaction would be increased enormously (providing the preserved integrity of the enzyme). The free enzymes starts showing a decrease in the activity at 55°C to become inactive at higher temperatures. Under

the same conditions, the encapsulated one retains its function in a broader range of temperatures, with a maximum of 78% at 95°C. Heating above this temperature leads to an absolute loss of the activity. We also decided to study how the long-ranged stability would change when the enzyme is unable to lose its structure, being able to be stored at room temperature for two weeks. The system was also able to be recycled after activity up to 5 times, ruling out enzyme leaching or partial denaturation, as shown in **Figure 1d** for all different sets.

Our tests confirm that the MOF-enzyme biocatalyst surpasses the proteolytic activity of the free enzyme in all cases, and its operating range can be extended to extreme conditions of pH and temperature with excellent recyclability and tolerance to competing enzymes.

3. References

1. S. W. Englander, L. Mayne, The nature of protein folding pathways. *Proc National Acad Sci*. **111**, 15873–15880 (2014).

2. S. W. Englander, L. Mayne, The case for defined protein folding pathways. *Proc National Acad Sci*. **114**, 8253–8258 (2017).

3. Y. Chen, V. Lykourinou, T. Hoang, L.-J. Ming, S. Ma, Size-Selective Biocatalysis of Myoglobin Immobilized into a Mesoporous Metal–Organic Framework with Hierarchical Pore Sizes. *Inorg Chem*. **51**, 9156–9158 (2012).

4. Y. Chen, S. Han, X. Li, Z. Zhang, S. Ma, Why Does Enzyme Not Leach from Metal–Organic Frameworks (MOFs)? Unveiling the Interactions between an Enzyme Molecule and a MOF. *Inorg Chem*. **53**, 10006–10008 (2014).

5. Y. Chen, V. Lykourinou, C. Vetromile, T. Hoang, L.-J. Ming, R. W. Larsen, S. Ma, How Can Proteins Enter the Interior of a MOF? Investigation of Cytochrome c Translocation into a MOF Consisting of Mesoporous Cages with Microporous Windows. *J Am Chem Soc*. **134**, 13188–13191 (2012).

6. S. E. Jackson, A. R. Fersht, Folding of chymotrypsin inhibitor 2. 1. Evidence for a two-state transition. *Biochemistry-us*. **30**, 10428–10435 (1991).

7. V. Daggett, Molecular Dynamics Simulations of the Protein Unfolding/Folding Reaction. *Accounts Chem Res*. **35**, 422–429 (2002).

8. F. N. Zaidi, U. Nath, J. B. Udgaonkar, Multiple intermediates and transition states during protein unfolding. *Nat Struct Biol*. **4**, 1016–1024 (1997).

9. T. A. S. e Silva, A. Knob, C. R. Tremacoldi, M. R. Brochetto-Braga, E. C. Carmona, Purification and some properties of an extracellular acid protease from Aspergillusclavatus. *World J Microbiol Biotechnology*. **27**, 2491–2497 (2011).

10. K. Liburdi, I. Benucci, M. Esti, Study of Two Different Immobilized Acid Proteases for Wine Application. *Food Biotechnol*. **24**, 282–292 (2010).

11. N. Bombara, A. M. R. Pilosof, M. C. Añón, Thermal stability of a neutral protease of *Aspergillus Oryzae*. *J Food Biochem*. **18**, 31–41 (1994).

12. F.-X. Qin, S.-Y. Jia, F.-F. Wang, S.-H. Wu, J. Song, Y. Liu, Hemin@metal–organic framework with peroxidase-like activity and its application to glucose detection. *Catal Sci Technol*. **3**, 2761–2768 (2013).

13. P. Li, Q. Chen, T. C. Wang, N. A. Vermeulen, B. L. Mehdi, A. Dohnalkova, N. D. Browning, D. Shen, R. Anderson, D. A. Gómez-Gualdrón, F. M. Cetin, J. Jagiello, A. M. Asiri, J. F. Stoddart, O. K. Farha, Hierarchically Engineered Mesoporous Metal-Organic Frameworks toward Cell-free Immobilized Enzyme Systems. *Chem*. **4**, 1022–1034 (2018).

14. X. Lian, Y. Huang, Y. Zhu, Y. Fang, R. Zhao, E. Joseph, J. Li, J. Pellois, H. Zhou, Enzyme-MOF Nanoreactor Activates Nontoxic Paracetamol for Cancer Therapy. *Angewandte Chemie Int Ed*. **57**, 5725–5730 (2018).

15. P. Li, S.-Y. Moon, M. A. Guelta, S. P. Harvey, J. T. Hupp, O. K. Farha, Encapsulation of a Nerve Agent Detoxifying Enzyme by a Mesoporous Zirconium Metal–Organic Framework Engenders Thermal and Long-Term Stability. *J Am Chem Soc*. **138**, 8052–8055 (2016).

16. W.-L. Liu, S.-H. Lo, B. Singco, C.-C. Yang, H.-Y. Huang, C.-H. Lin, Novel trypsin–FITC@MOF bioreactor efficiently catalyzes protein digestion. *J Mater Chem B*. **1**, 928–932 (2013).

17. D. Feng, T.-F. Liu, J. Su, M. Bosch, Z. Wei, W. Wan, D. Yuan, Y.-P. Chen, X. Wang, K. Wang, X. Lian, Z.-Y. Gu, J. Park, X. Zou, H.-C. Zhou, Stable metal-organic frameworks containing single-molecule traps for enzyme encapsulation. *Nat Commun*. **6**, 5979 (2015).

18. J. L. England, G. Haran, Role of Solvation Effects in Protein Denaturation: From Thermodynamics to Single Molecules and Back. *Annu Rev Phys Chem*. **62**, 257–277 (2011).

19. C. Albrecht, Joseph R. Lakowicz: Principles of fluorescence spectroscopy, 3rd Edition. *Anal Bioanal Chem*. **390**, 1223–1224 (2008).

Publication 3:

Translocation of enzymes into a mesoporous MOF for enhanced catalytic activity under extreme conditions

Chem. Sci. 2019, 10, 4082-4088

Chemical Science

EDGE ARTICLE

View Article Online
View Journal | View Issue

Cite this: *Chem. Sci.*, 2019, **10**, 4082

All publication charges for this article have been paid for by the Royal Society of Chemistry

Translocation of enzymes into a mesoporous MOF for enhanced catalytic activity under extreme conditions†

José Navarro-Sánchez,[a] Neyvis Almora-Barrios,[a] Belén Lerma-Berlanga,[a] J. Javier Ruiz-Pernía,[b] Victor A. Lorenz-Fonfria,[a] Iñaki Tuñón[b] and Carlos Martí-Gastaldo*[a]

Received 6th January 2019
Accepted 27th February 2019

DOI: 10.1039/c9sc00082h

rsc.li/chemical-science

Enzymatic catalysis is of great importance to the chemical industry. However, we are still scratching the surface of the potential of biocatalysis due to the limited operating range of enzymes in harsh environments or their low recyclability. The role of Metal–Organic Frameworks (MOFs) as active supports to help overcome these limitations, mainly by immobilization and stabilization of enzymes, is rapidly expanding. Here we make use of mild heating and a non-polar medium during incubation to induce the translocation of a small enzyme like protease in the mesoporous MOF MIL-101(Al)-NH_2. Our proteolytic tests demonstrate that protease@MIL-101(Al)-NH_2 displays higher activity than the free enzyme under all the conditions explored and, more importantly, its usability can be extended to extreme conditions of pH and high temperatures. MOF immobilization is also effective in providing the biocomposite with long-term stability, recyclability and excellent compatibility with competing enzymes. This simple, one-step infiltration strategy might accelerate the discovery of new MOF-enzyme biocatalysts that meet the requirements for biotechnological applications.

Introduction

Metal–Organic Frameworks (MOFs) have proven to be promising alternatives for enzyme immobilization based on their high surface areas and unparalleled structural and chemical flexibility.[1,2] Compared to other porous supports, MOFs also provide tailorable functionality to gain control over specific interactions with the enzyme that helps mitigating their poor stability at high temperatures or in organic solvents. Accordingly, MOF immobilization can improve the intrinsic properties of the enzyme for superior substrate specificity, catalytic stability under different pH conditions or its susceptibility to autolysis at higher temperatures, modulating and enlarging the range of conditions for which the enzyme can retain its activity.

There are three main different strategies to produce enzyme-immobilized MOF composites depending on the chemical interaction between the enzyme and the solid support.[1,3] Grafting of the enzyme to the external surface of the MOF by covalent linkage,[4] biomimetic co-mineralization of the MOF from direct reaction of its precursors in the presence of the enzyme,[5–7] and direct infiltration of the enzyme into the pores of pre-synthesized MOFs.[8,9] Overall, all these strategies permit producing composites with better catalytic activities and environmental resistance than the free enzyme, but direct infiltration is arguably better fitted to prevent undesirable leaching and self-aggregation. Pore entrapment also renders superior stability due to the physical adsorption in a confined cavity. However, this approach is restricted to a handful of mesoporous materials with big pore apertures compatible with the diffusion of enzymes that typically feature large molecular dimensions.[10–14] Finding alternative routes that permit overcoming this size limitation would permit enlarging the number of MOF-enzyme combinations that can be adapted to this route.

Previous reports confirm the ability of biomolecules to diffuse through comparatively narrow nanopores. By using fluorescence spectroscopy, Ma and co-workers demonstrated that the protein cytochrome c (2.6 × 3.3 × 3.3 nm) undergoes conformational changes due to the interaction with the surface of Tb-mesoMOF.[15] Inspired by this work, we decided to explore if a similar protein translocation mechanism could also be extended to biologically active enzymes. This represents an additional challenge as the catalytic function of the enzyme is intimately linked to its native structure and its translocation into the MOF would need to be compatible with the regeneration of an active state after encapsulation. We presumed this could be demonstrated more easily for small enzymes formed using only one polypeptide chain, more likely to unfold partially

[a]Instituto de Ciencia Molecular (ICMol), Universidad de Valencia, Catedrático José Beltrán-2, Paterna, 46980, Spain. E-mail: carlos.marti@uv.es

[b]Departamento de Química Física, Universidad de Valencia, Doctor Moliner-50, Burjassot, 46100, Spain

† Electronic supplementary information (ESI) available. See DOI: 10.1039/c9sc00082h

and recover its native structure without irreversible changes that could destroy their function.[16–18] Provided the enzyme could be reverted back to a biological active structure after infiltration, this would result in a very efficient immobilization as the enzyme would remain effectively trapped in the internal cavities of the MOF to avoid leaching.

Here we report the infiltration of a protease, an aspartic proteinase from *Aspergillus saitoi* (also known as *Aspergillus phoenicis*), into the mesoporous cavities of MIL-101(Al)-NH_2 (ref. 19) (Fig. 1). Incubation of protease in an organic medium at mild temperatures facilitates partial unfolding of the enzyme, supported by molecular dynamics simulations and fluorescence spectroscopy, to enable its translocation across the pore windows of the host (50% smaller in size). Our tests confirm that the MOF-enzyme biocatalyst surpasses the proteolytic activity of the free enzyme in all cases and its operating range can be extended to extreme conditions of pH and temperature with excellent recyclability and tolerance to competing enzymes.

Results and discussion

Translocation of protease in MIL-101(Al)-NH_2

Among the different candidates possible, we targeted a family of fungal proteases based on their relevance in biotechnological applications.[20–22] Previous reports confirm that proteases can regain their native structure and function after denaturant or thermal-induced unfolding.[23,24] Also important, compared to other common proteins like horseradish peroxidase (HPP, 44 kDa) or lipase (72 kDa), the smaller size of protease (17 kDa) would be compatible with the mesoporous cavities of MIL-101. As for the MOF, we selected MIL-101(Al)-NH_2 due to several reasons. From a structural point of view, it displays a MTN zeotypic three-dimensional extended network that combines two types of mesoporous cavities of 3.6 and 2.9 nm that are interconnected by pentagonal and hexagonal windows of 1.6 and 1.2 nm (Fig. 1a). In principle, these mesoporous cages are large enough to accommodate small enzymes like *Aspergillus saitoi* protease. Dynamic light scattering (DLS) measurements of the protein in a TRIS buffer indicate an average distribution of sizes centered at 2.85 nm (Fig. S1†). The ratio between the diameters of the mesoporous cavity in MIL-101 and the protein is close to 1.2. Compared to other studies in which this value is close to one,[13,25] this reduced environmental stress will result in a higher conformational freedom more likely to favor the regeneration of an active conformation after enzyme translocation. Previous reports confirm the biocompatibility of MIL-101 and its ability to endure the conditions used for the incubation of enzymes (physiological medium, pH, temperature, and prolonged time).[26] Also important, we decided to use the amino functionalized MOF to favor the diffusion of the protease in the polar environment provided by the hydrophilic pores in MIL-101(Al)-NH_2. This surface functionalization was also expected to render better dispersibility in aqueous medium and favor the stabilization of the encapsulated enzyme by formation of H-bond interactions.[27]

Prior to attempting the infiltration experiments, we studied the effect of the buffer used for enzyme incubation on the structural integrity of the framework. MIL-101(Al)-NH_2 was prepared by following a previously reported method,[28] and immersed in TRIS, HEPES, carbonate and PBS buffers (0.1 M). As shown in Fig. S2,† PXRD of the solid recovered after 12 hours confirms that the structural integrity of MIL-101 is only maintained in TRIS whereas other buffers like HEPES and PBS accelerate its transformation into the MIL-53 phase. Accordingly, freshly made MIL-101(Al)-NH_2 particles were immersed in 3 mL of a solution of the protease in TRIS buffer (0.1 M, pH = 7.4) followed by addition of 30 mL of anhydrous hexane with continuous stirring. The mixture was incubated under these conditions at 60 °C overnight. The addition of a non-polar solvent and a higher temperature were expected to favor the denaturation of the protease as result of reducing the hydrophobic effect and increasing kinetic energy of the system. The altered structure of the water in the aqueous polar medium by the presence of hexane, in combination with the increase in temperature, changes the landscape of energies associated with the array of supramolecular interactions (π–π stacking, H-bonds) with the solvent and within the protein that control its secondary structure. This process was analysed by means of MD simulations. As shown in Fig. 2a, the *Aspergillus saitoi* protease undergoes reversible unfolding under the conditions used in the experiment. Our 1.0 μs long MD simulation in a hexane : water mixture at 60 °C shows a continuous drift from the native structure with time. The root-mean-square deviation (RMSD) allows a comparison between the structure of the native folded protein and the corresponding partially or fully unfolded structure. The RMSD measured in the presence of hexane increases continuously with time to reach larger values than those observed for the protein in a polar medium, aqueous solutions at 25 and 60 °C. This confirms that the combination of temperature and an organic solvent can favor partial denaturation of the enzyme. Comparison of the structure of the enzyme in the hexane : water mixture after 1.0 μs simulation with the reported X-ray structure shows that protein unfolding in the non-polar solution involves the opening of the cleft between the two protein lobes (Fig. 2a, insets). As shown in Fig. S3,† analysis of the secondary structure shows a gradual transformation of α-helices and β-sheets into unstructured regions, with a progressive increase of the number of residues belonging to regions

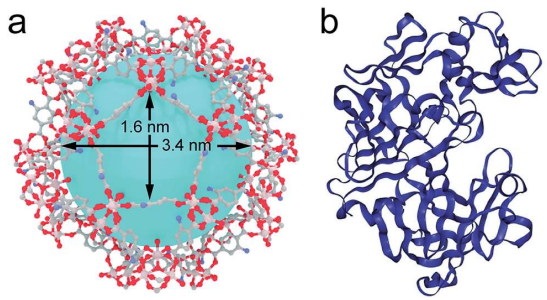

Fig. 1 (a) Structure of MIL-101(Al)-NH_2 highlighting the dimensions of the largest pore windows and mesoporous cages. (b) Crystal structure of the protease used in this work. Files available from CCDC (605510) and PDB (1IBQ).

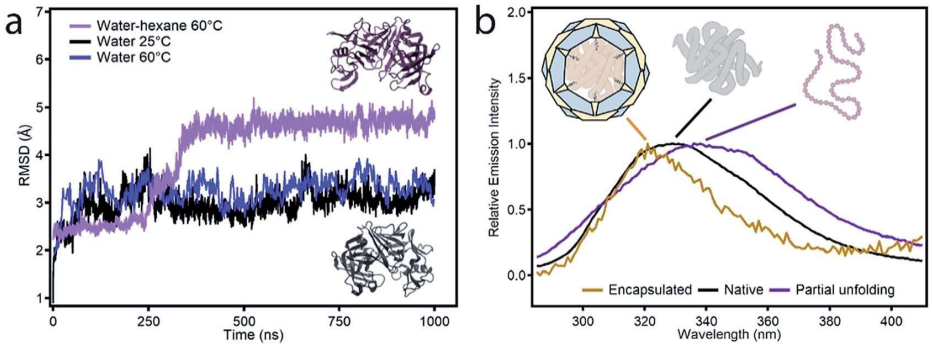

Fig. 2 (a) Representation of the RMSD of the configurations obtained during MD simulations in different media with respect to the reported X-ray structure of protease (PDB code 1IBQ): hexane : water at 60 °C (purple), aqueous solution at 60 °C (blue) and 25 °C (black). The inset highlights the changes in the structure obtained after 1.0 μs of simulation in hexane : water (dark purple) compared to the original structure (black). (b) Fluorescence spectra of free protease (black), protease in the non-polar incubation medium at 60 °C (purple) and protease@MIL-101(Al)-NH_2 (yellow).

without a defined secondary structure. Overall, our MD simulations confirm the potential ability of the enzyme to modify its conformation under the conditions used in the experiments required to translocate across the narrow pore windows in the MOF. For direct correlation with the experiment, we used fluorescence spectroscopy to compare the emission spectra of protease in TRIS buffer – native confirmation, in the incubation medium – partial unfolding – and after translocation into the MOF – encapsulated conformation. Protease presents 16 tyrosine (Tyr) and 3 tryptophan (Trp) residues that account for its emission spectrum. As shown in Fig. 2b incubating the free protease on a water–hexane dispersion under mild temperature conditions shifts the fluorescence emission maximum from 329 to 338 nm, corresponding to solvent-exposed Tyr and Trp.[29] This red shift in fluorescence is a common situation when unfolding soluble proteins,[29] and is fully reversed upon removal of the hexane and cooling down to room temperature (Fig. S4†). In contrast, refolding the protease in the presence of the MOF leads to a composite displaying a fluorescence emission maximum at 321 nm. This blue shift indicates that the protein located within MIL-101(Al)-NH_2 cavities exists in a non-native folded conformation where Tyr/Trp residues experience an environment less polar than in the native folded state. The Raman spectra of free protease and protease@MIL-101(Al)-NH_2 display the characteristics bands of disulphide bonds of cysteine (Fig. S5†). As reported for the encapsulation of microperoxidase in Tb-mesoMOF,[30] the signals at 470 and 2436 cm^{-1} in the enzyme are blue shifted close to 6 and 9 cm^{-1} after encapsulation as result of the interaction with the framework. After the insertion procedure, the resulting solid was thoroughly washed with the buffer and isolated by centrifugation to afford protease@MIL-101(Al)-NH_2. UV-visible spectroscopy was used to ensure complete removal of the excess of non-encapsulated protease upon washing. As shown in Fig. 3a, there was no measurable protease in solution after two rounds. To further confirm that the protease was encapsulated rather than adsorbed on the external surface of the particles, we carried out two control experiments. We followed the same enzyme incubation protocol described above by using MIL-101(Cr). Immobilization is negligible in this case (Fig. S6 and S7†), likely due to the absence of $-NH_2$ groups important in directing the translocation of the enzyme into the MOF. For the next test we made use of azocasein as a protease substrate (Fig. 3a, inset). Azocasein is hydrolysed non-specifically by proteolytic enzymes, releasing the azo dye into the media where it can be detected by its characteristic and intense absorbance at 440 nm. This permits rapid identification of the presence of the enzyme in MOFs incubated under different conditions. We ran five experiments by adding azocasein to five vials that contained: TRIS buffer as a blank sample (1) and dispersions in the same buffer of the MOF incubated with protease at 25 °C with hexane (2), the MOF incubated with protease at 60 °C without hexane (3), the protease@MIL-101(Al)-NH_2 prepared as described above (4) and free protease (5). Samples 2, 3 and 4 where washed at least 3 times with fresh buffer before the test. After addition of azocasein, only samples 4 and 5 gave a positive result of proteolytic activity (yellow color), confirming the importance of temperature and the presence of a non-polar solvent in the incubation medium to facilitate the infiltration of the enzyme.

Enzyme uptake and physicochemical characterization of protease@MIL-101(Al)-NH_2

Comparison of the thermogravimetric (TGA) profile of the MOF before and after encapsulation confirms that protease@MIL-101(Al)-NH_2 displays an additional weight loss at 230 °C that corresponds to the decomposition of the enzyme (Fig. S8†). The amount of protease was calculated to be 5%. The uptake of protease was also evaluated by using UV-vis spectroscopy, by correlating the drop in the absorption of the band intrinsic to protease, at 260 nm, with the concentrations of non-encapsulated enzyme in the supernatants after washing the material (Fig. S9†). The uptake calculated by this experiment is 0.05 g g^{-1}. This value is very close to the content estimated from TGA,

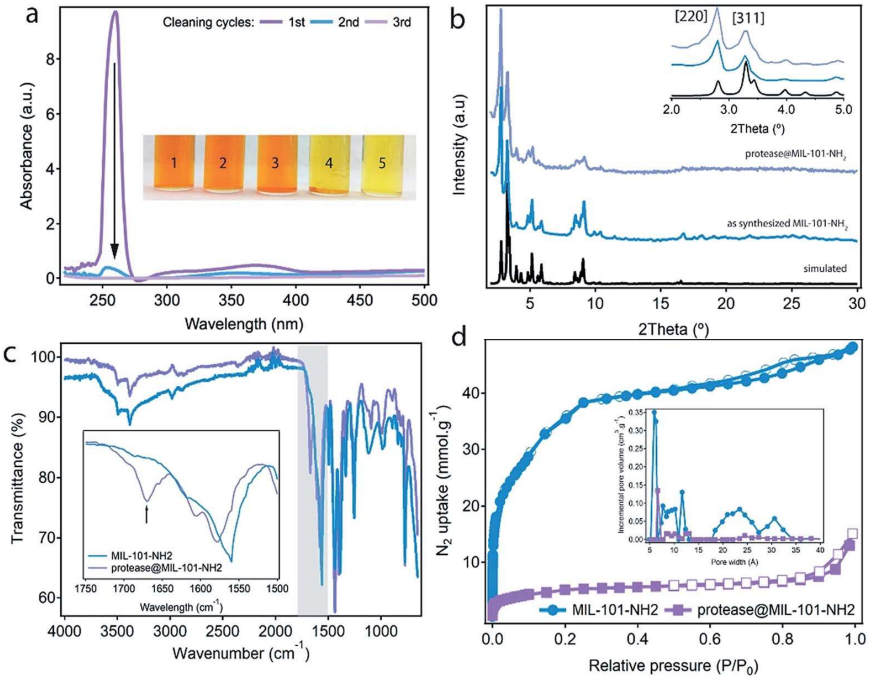

Fig. 3 (a) UV-vis spectra of the supernatant solution, confirming the complete removal of non-encapsulated protease after the second cleaning of protease@MIL-101(Al)-NH_2. Insets show control experiments with addition of azocasein to a TRIS buffer (1; reference), dispersions in the same buffer of the MOF incubated with protease at 25 °C with hexane (2), 60 °C without hexane (3), 60 °C with hexane (4) and the free enzyme (5). (b) PXRDs of MIL-101(Al)-NH_2: simulated (black), the as-synthesized material (blue) and after infiltration of protease (purple). The inset shows most representative Bragg peaks at low-theta values. (c) FT-IR spectra showing the appearance of stretching band characteristic of the enzyme (marked with an arrow) in protease@MIL-101(Al)-NH_2. (d) N_2 isotherms confirming the drop in porosity after encapsulation. The inset shows the PSD of both materials analysed by density functional theory.

and quite similar to the values reported for the encapsulation of other enzymes in mesoporous hosts like Tb-mesoMOF[31] or NTU-1000.[9,12]

Protease@MIL-101(Al)-NH_2 was fully characterized by PXRD, scanning electron microscopy (SEM), FT-IR spectroscopy and adsorption/desorption experiments. As shown in Fig. 3b, the infiltration of the enzyme proceeds without significant changes to the crystallinity of the MOF. After incubation in TRIS, there are no additional diffraction lines that could account for a structural transformation during encapsulation. Only the change in the relative intensity of the Bragg peaks seems to account for the filling of the pores. Phase purity was also confirmed by Le Bail refinement of the PXRDs of the material before and after infiltration (Fig. S10, Table S1†). SEM pictures confirm that the infiltration of protease does not cause changes to the size or morphology of the particles or induce the formation of an amorphous, contaminant phase (Fig. S11†). Infrared (IR) spectroscopy was used to study vibrational differences between the bare MOF and the protease@MIL-101(Al)-NH_2. Fig. 3c shows that some spectral differences exist between them, in particular the presence of a new vibrational band at around 1670 cm^{-1} in protease@MIL-101(Al)-NH_2. This band can be tentatively assigned to the amide I vibration ν(C=O) of the peptide bond of the protease. Encapsulation seems to shift the maximum of this band outside the typical range for folded proteins and peptides in solution (between 1660 and 1630 cm^{-1}).[32,33] We also observe a shift from 1560 to 1580 cm^{-1} in the position of the peak characteristic of δ(N–H) vibrations from the amino groups in the MOF after infiltration of protease, suggesting the presence of weak interactions between the enzyme and the host. However, changes in this frequency range could also be caused by overlapping contributions from the amide II vibration of the peptide bond (~1550 cm^{-1}).[33] N_2 adsorption isotherms were used to confirm the effect of encapsulation on the porosity of the material. MIL-101(Al)-NH_2 displays the reported behaviour with a high uptake capacity for a Brunauer–Emmett–Teller (BET) surface area of 3000 $m^2\ g^{-1}$, that is reduced to 245 $m^2\ g^{-1}$ after encapsulation (Fig. 3d). The analysis of the pore size distribution in MIL-101(Al)-NH_2 and protease@MIL-101(Al)-NH_2 by using density functional theory (DFT) shows that the incremental pore volume corresponding to the mesoporous cages, centered at 2.0–2.5 and 3.0–3.4 nm, drops from 0.08 to 0.005 $cm^3\ g^{-1}$ and 0.06 to 0.001 $cm^3\ g^{-1}$ after the encapsulation of protease. This suggests that the majority of the mesoporous space in MIL-101(Al)-NH_2 is occupied by the protease with a small fraction of microporosity (0.6 nm), still

accessible for substrate diffusion. This behaviour is very similar to the reduction of porosity reported for COFs after encapsulation of lipase.[34]

Enzymatic activity of encapsulated protease

In order to assess the protective effect of the MOF host on the chemical and thermal stability of the enzyme, we studied the proteolytic ability of free and immobilized protease to cleave the peptide bond of glycyl-L-tyrosine (Gly–Tyr) under extreme conditions of pH and temperature (see S5† for more details). Activity data were collected before 3 hours to discard the effect or protease autolysis. Previous studies confirm that this enzyme half-life is retained for at least 14 hours.[35] Fig. 4a shows the evolution of the proteolytic activity maintained after 3 hours at 25 °C with changes to the pH between 1 and 12. Compared to the free enzyme, protease@MIL-101(Al)-NH_2 is more active in all cases even under the optimal conditions of this alkali protease at pH 2–3. Moreover, immobilization almost doubles the proteolytic activity of the enzyme at pH 1 and permits retaining the enzymatic reactivity in a basic medium above pH 8, for which the activity of the free enzyme is completely lost (Fig. S13†). The effect of temperature was studied with equivalent experiments by varying the bath temperature between 25 and 125 °C whilst fixing the pH at 7.4. We hypothesized that temperature would have a positive effect on reactivity due to thermodynamic reasons, provided the integrity of the enzyme was preserved. As shown in Fig. 4b, the free enzyme displays a slight decrease in activity at 55 °C to become inactive at higher temperatures. Under the same conditions, encapsulation permits the enzyme to retain its function in a broader range of temperatures, with a maximum of 78% at 95 °C. Heating above this temperature has a detrimental effect leading to complete loss of activity above 105 °C (Fig. S14†). These assays confirm the beneficial effect of encapsulation on the stability of the enzyme, which can retain enzymatic activity under extreme conditions of pH and temperature during which the free enzyme is denatured.

Encouraged by the chemical and thermal stability of the biocomposite we decided to test its long-term stability and recyclability for recovery after use. One of the key advantages of enzyme encapsulation is the possibility of simplifying the handling, storage or transportation of the biocatalyst whilst retaining its biological function intact.

To investigate this possibility, we dried protease@MIL-101(Al)-NH_2 in a vacuum and stored it at room temperature for two weeks. This sample was used to perform recyclability tests by recovering the sample by centrifugation after each catalytic round. Activity was measured by following the same protocol described above at pH 7.4 and 25 °C after 3 hours. After two weeks the proteolytic activity remained unchanged, with only small deviations with respect to the freshly prepared material

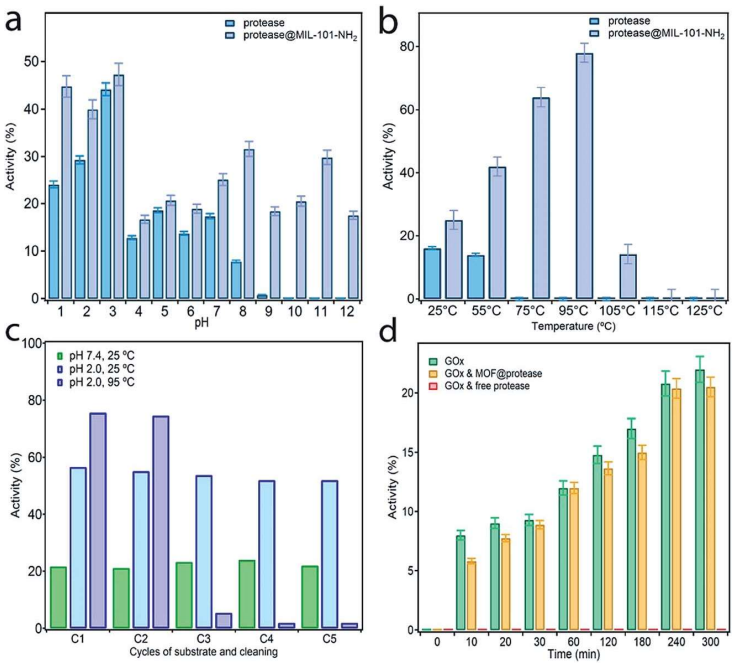

Fig. 4 Comparison of the activity of protease before and after encapsulation tested at variable (a) pH from 1 to 12, temperature fixed at 25 °C and (b) temperature from 25 to 125 °C, pH = 7.4. (c) Activity and recyclability of the dried biocomposite, stored at room temperature for two weeks, at 25 °C and pH 7 (green) and at pH 2 and 25 °C (blue) or 95 °C (purple), confirming long-term stability and excellent recyclability at room temperature. (d) Activity at room temperature in a buffered medium of GOx alone (red), in the presence of protease@MIL-101(Al)-NH_2 (yellow) and free protease (blue). MOF encapsulation prevents GOx digestion and retains its activity very similar to that of glucose oxidase alone.

(Fig. 4c). The activity remains constant after 5 cycles, ruling out enzyme leaching or partial denaturation. The PXRD of the material after recycling also confirms that its structure remains unchanged (Fig. S15†). Besides the protective shield offered by the MOF, we argue this excellent stability might be also linked to the surface chemistry of amino groups for stronger immobilization of the enzyme by supramolecular interactions. We decided to push the limits of the material at higher temperatures and performed, at pH 2, two equivalent tests at 25 °C and 95 °C. Although the initial boost in activity is consistent with the value recorded for the fresh material, we observe an abrupt decrease in performance after two catalytic cycles until the material becomes inactive after five rounds at high temperatures. This behaviour is not caused by ineffective encapsulation but the structural transformation of the MOF under these conditions. As shown in Fig. S15,† heating at 95 °C in an acidic medium favors the transformation of the MIL-101 phase into the MIL-53 one and thus the leaching of the enzyme. We argue the use of alternative MOFs, more stable at acidic pH, will allow for the preparation of biocomposites by using this same methodology with excellent recyclability also under extreme conditions.

Finally, to also prove the ability of MOF encapsulation to neglect the effect of inhibitors on the reactivity of the enzyme we tested the activity of protease@MIL-101(Al)-NH_2 in the presence of a second enzyme. The compatibility of Glucose Oxidase (GOx) with proteases is an important issue for biotechnological applications in food and health industries.[36] The small pore openings provided by MIL-101-NH_2 would be a promising alternative in this regard as they shall only enable the diffusion of small substrates, thus preventing the digestion of GOx. To confirm this possibility, we measured the activity of GOx in the presence of free protease and protease@MIL-101(Al)-NH_2 under buffered conditions at room temperature (Fig. 4d). However free protease cancels the activity of GOx immediately, and the activity of GOx in the presence of the encapsulated enzyme is very similar to that of glucose oxidase alone (Fig. S16†). This suggests that our encapsulation method also provides excellent compatibility with competing enzymes due to size exclusion.

Conclusions

In summary, we have demonstrated how the conformational flexibility of simple enzymes can be exploited to chemically induce the structural changes required for their infiltration into mesoporous hosts featuring comparatively smaller pore windows. Translocation into the host is enabled by using a non-polar medium and mild temperatures during enzyme incubation. Our proteolytic tests demonstrate that protease@MIL-101(Al)-NH_2 displays higher activity than the free enzyme in all cases but, more importantly, extends its usability to extreme conditions of pH (1–12) and temperatures up to 95 °C. MOF shielding is also effective in providing the biocomposite with long-term stability, recyclability and excellent compatibility with competing enzymes. The role of MOFs in the development of biocatalysts of interest for biotechnological applications is rapidly expanding. In this context, our methodology offers a simple approach for the preparation of new biocatalysts by encapsulation and stabilization of other enzymes for applications that demand ease of storage, good recyclability and tolerance to a broad range of operating conditions.

Conflicts of interest

There are no conflicts to declare.

Acknowledgements

This work was supported by the EU (ERC Stg Chem-fs-MOF 714122) and Spanish MINECO (Project CTQ2017-83486-P, RYC-2012-10894, RYC-2013-13114 and FPU16/04162), MINECO/FEDER (CTQ2015-74523-JIN(AEI/FEDER), Unit of Excellence Marí de Maeztu (MDM-2015-0538) and Generalitat Valenciana AICO/2018/238.

References

1 X. Lian, Y. Fang, E. Joseph, Q. Wang, J. Li, S. Banerjee, C. Lollar, X. Wang and H. C. Zhou, *Chem. Soc. Rev.*, 2017, **46**, 3386–3401.
2 R. Riccò, W. Liang, S. Li, J. J. Gassensmith, F. Caruso, C. Doonan and P. Falcaro, *ACS Nano*, 2018, **12**, 13–23.
3 C. Doonan, R. Riccò, K. Liang, D. Bradshaw and P. Falcaro, *Acc. Chem. Res.*, 2017, **50**, 1423–1432.
4 S. Jung, Y. Kim, S. J. Kim, T. H. Kwon, S. Huh and S. Park, *Chem. Commun.*, 2011, **47**, 2904–2906.
5 K. Liang, R. Ricco, C. M. Doherty, M. J. Styles, S. Bell, N. Kirby, S. Mudie, D. Haylock, A. J. Hill, C. J. Doonan and P. Falcaro, *Nat. Commun.*, 2015, **6**, 7240.
6 F.-K. Shieh, S.-C. Wang, C.-I. Yen, C.-C. Wu, S. Dutta, L.-Y. Chou, J. V. Morabito, P. Hu, M.-H. Hsu, K. C.-W. Wu and C.-K. Tsung, *J. Am. Chem. Soc.*, 2015, **137**, 4276–4279.
7 F. Lyu, Y. Zhang, R. N. Zare, J. Ge and Z. Liu, *Nano Lett.*, 2014, **14**, 5761–5765.
8 M. V. de Ruiter, R. Mejia-Ariza, J. J. L. M. Cornelissen and J. Huskens, *Chem*, 2016, **1**, 29–31.
9 P. Li, J. A. Modica, A. J. Howarth, L. E. Vargas, P. Z. Moghadam, R. Q. Snurr, M. Mrksich, J. T. Hupp and O. K. Farha, *Chem*, 2016, **1**, 154–169.
10 H. Deng, S. Grunder, K. E. Cordova, C. Valente, H. Furukawa, M. Hmadeh, F. Gándara, A. C. Whalley, Z. Liu, S. Asahina, H. Kazumori, M. O'Keeffe, O. Terasaki, J. F. Stoddart and O. M. Yaghi, *Science*, 2012, **336**, 1018–1023.
11 X. Lian, Y. P. Chen, T. F. Liu and H. C. Zhou, *Chem. Sci.*, 2016, **7**, 6969–6973.
12 P. Li, S. Y. Moon, M. A. Guelta, S. P. Harvey, J. T. Hupp and O. K. Farha, *J. Am. Chem. Soc.*, 2016, **138**, 8052–8055.
13 P. Li, Q. Chen, T. C. Wang, N. A. Vermeulen, B. L. Mehdi, A. Dohnalkova, N. D. Browning, D. Shen, R. Anderson, D. A. Gómez-Gualdrón, F. M. Cetin, J. Jagiello, A. M. Asiri, J. F. Stoddart and O. K. Farha, *Chem*, 2018, **4**, 1022–1034.
14 D. Feng, T. F. Liu, J. Su, M. Bosch, Z. Wei, W. Wan, D. Yuan, Y. P. Chen, X. Wang, K. Wang, X. Lian, Z. Y. Gu, J. Park, X. Zou and H. C. Zhou, *Nat. Commun.*, 2015, **6**, 1–8.

15 Y. Chen, V. Lykourinou, C. Vetromile, T. Hoang, L. J. Ming, R. W. Larsen and S. Ma, *J. Am. Chem. Soc.*, 2012, **134**, 13188–13191.
16 V. Daggett, *Acc. Chem. Res.*, 2002, **35**, 422–429.
17 S. E. Jackson and A. R. Fersht, *Biochemistry*, 1991, **30**, 10428–10435.
18 F. N. Zaidi, U. Nath and J. B. Udgaonkar, *Nat. Struct. Biol.*, 1997, **4**, 1016–1024.
19 P. Serra-Crespo, E. V. Ramos-Fernandez, J. Gascon and F. Kapteijn, *Chem. Mater.*, 2011, **23**, 2565–2572.
20 T. A. S. e Silva, A. Knob, C. R. Tremacoldi, M. R. Brochetto-Braga and E. C. Carmona, *World J. Microbiol. Biotechnol.*, 2011, **27**, 2491–2497.
21 R. J. S. de Castro and H. H. Sato, *J. Food Process. Technol.*, 2014, **2014**, 372352.
22 K. Liburdi, I. Benucci and M. Esti, *Food Biotechnol.*, 2010, **24**, 282–292.
23 S. W. Englander and L. Mayne, *Proc. Natl. Acad. Sci.*, 2014, **111**, 15873–15880.
24 K. A. Dill and H. S. Chan, *Nat. Struct. Biol.*, 1997, **4**, 10–19.
25 X. Lian, Y. Huang, Y. Zhu, Y. Fang, R. Zhao, E. Joseph, J. Li, J. P. Pellois and H. C. Zhou, *Angew. Chem., Int. Ed.*, 2018, **57**, 5725–5730.
26 F. X. Qin, S. Y. Jia, F. F. Wang, S. H. Wu, J. Song and Y. Liu, *Catal. Sci. Technol.*, 2013, **3**, 2761–2768.
27 J. L. England and G. Haran, *Annu. Rev. Phys. Chem.*, 2011, **62**, 257–277.
28 C. Férey, C. Mellot-Draznieks, C. Serre, F. Millange, J. Dutour, S. Surblé and I. Margiolaki, *Science*, 2005, **309**, 2040–2042.
29 *Principles of Fluorescence Spectroscopy*, ed. J. R. Lakowicz, Springer US, Boston, MA, 2006, pp. 29–575.
30 Y. Chen, S. Han, X. Li, Z. Zhang and S. Ma, *Inorg. Chem.*, 2014, **53**, 10006–10008.
31 V. Lykourinou, Y. Chen, X. S. Wang, L. Meng, T. Hoang, L. J. Ming, R. L. Musselman and S. Ma, *J. Am. Chem. Soc.*, 2011, **133**, 10382–10385.
32 S. Y. Venyaminov and N. N. Kalnin, *Biopolymers*, 1990, **30**, 1259–1271.
33 E. Goormaghtigh, V. Cabiaux and J. M. Ruysschaert, *Subcell. Biochem.*, 1994, **23**, 405–450.
34 Q. Sun, C. W. Fu, B. Aguila, J. Perman, S. Wang, H. Y. Huang, F. S. Xiao and S. Ma, *J. Am. Chem. Soc.*, 2018, **140**, 984–992.
35 N. Bombara, A. M. R. Pilosof and M. C. Añón, *J. Food Biochem.*, 1994, **18**, 31–41.
36 S. Patra, T. Hidalgo Crespo, A. Permyakova, C. Sicard, C. Serre, A. Chaussé, N. Steunou and L. Legrand, *J. Mater. Chem. B*, 2015, **3**, 8983–8992.

Supporting information

Translocation of Enzymes in a Mesoporous MOF for Enh Catalytic Activity Under Extreme Conditions

José Navarro-Sánchez,[a] Neyvis Almora-Barrios,[a] Belén Lerma-Berlanga,[a] J. Javier Ruiz-Pernía,[b] Victor A. Lórenz-Fonfría,[a] Iñaki Tuñón[b] and Carlos Martí-Gastaldo*[a]

[a] Instituto de Ciencia Molecular (ICMol) Universidad de Valencia Catedrático José Beltrán-2, 46980, Paterna (Spain)

[b] Departamento de Química Física Universidad de Valencia Doctor Moliner-50, 46100, Burjassot (Spain)

E-mail: carlos.marti@uv.es

Table of Content

S1. Experimental section

Materials and reagents.

All reagents and solvents used were of commercially available grade and used without any additional purification. Protease (f *Aspergillus s* Type XIII, ≥0.6 unit/mg solid), Glucose Oxidase *Aspergillus n* Type II, ≥15,000 units/g solid), Azocasein (protease substrate), Glycyl-L-tyrosine (Gly-Tyr), 2-Aminoterephthalic acid (99%), Aluminium chloride hexahydrate (≥98%), dimethyl formamide (DMF), buffers (TRIS base, HEPES, carbonate and PBS at 0.1 M) and other chemicals were used as acquired from commercial suppliers.

Experimental procedure.

Synthesis of MIL-101(Cr). The MOF was synthesized following a reported procedur [1]. The solid was cleaned by centrifugation three times with fresh DMF and ethanol. The polycrystalline powder was then activated by Soxhlet extraction with ethanol overnight and dried under vacuum.

Synthesis of MIL-101(Al) $_2$. The MOF was synthesized by following a reported procedure:[2] 2-aminoterephtalic acid (3.75 mmol was dissolved in DMF (150mL) and heated up to 110°C. Then 7.5 mmol of aluminium chloride hexahydrate were added. The temperature was maintained constant four hours with magnetic agitation. The flask was tightly sealed and placed in an oven at 110°C for 16 hours. After cooling down to room temperature, the yellow precipitate was isolated by filtration and washed thoroug ethanol and acetone. The polycrystalline powder was then activated by Soxhlet extraction with ethanol overnigh vacuum.

Synthesis of protease@MIL-101(Al)-NH_2. For the infiltration of the enzyme, 20 mg of protease were dissolved in (0.1 mol L^{-1}, pH 7.4) followed by the addition of 60 mg of the activated MOF with continuous stirring. Then, 30 mL of anhydrous hexan were added to the incubation medium, that was maintained at 60 °C overnight. The mixture was next cooled dow continuous stirring for 1 hour. Protease@MIL-101(Al)-NH_2 was then isolated by centrifugation and washed abundantl aliquots of TRIS in order to remove the excess of non-infiltrated enzyme. The total uptake of protease by the MOF was evaluated by correlating the disappearance of the UV-Vis band of the enzyme at 260 nm in the supernatant with its decreasing concentration in solution upon washing. The solid was dried at 50 °C under dynamic vacuum to obtain a yellowish powder that was stored at 4 activity test

Proteolytic activity test The catalytic activity of protease@MIL-101(A $_2$ was typically tested for 20 mg of the solid incubated at room temperature with 20 µmol of Glycyl-L-tyrosine (GlyTyr) in 3 ml of TRIS buffer (0.1M, pH 7.4) and compared to 1 m enzyme in the same medium, that was used as a reference. The evolution of the intensity of the UV-Vis band representative of peptide with time at 5, 10, 15, 30, 60, 120, 180 and 300 minutes was measured at 285 nm and plotted for the calculation of the catalytic activity and analysis of the enzyme kinetics. Aliquots of 100 µL were taken for the UV-Vis experiments. Variations in the cat with temperature and pH were analyzed by carrying out the same experiment. Temperature was controlled in a heating bath between 25 and 125 °C. pH was buffered between 1 and 12 by using a concentrated solution of HCl and NaOH. Reusability tests were perf by using 40 mg of protease@MIL-101(Al)-N $_2$ in a normal proteolytic procedure, followed by cleaning with aliquots of TRIS in eac cycle.

GOx (Glucose oxidase) interference t The compatibility of protease with competing enzymes like GOx before a encapsulation was studied by using either 20 mg of the biocomposite or 1 mg of the free enzyme incubated at room temperature with 20 µmoL of Glucose in 3 ml of TRIS buffer. The reduction of the intensity of the UV-Vis band representative of the glucose wa measured and plotted for the calculation of the catalytic activity from aliquots extracted from the reaction medium between 0 and 18 minutes. The reactions were performed at pH

Fluorescence spectroscopy. Solution emission studies of free protease and protease@M $_2$ were performed using 5 mg of fresh material suspended in 3 mL of TRIS buffer in a 1 cm quartz optical cuvette using a TI-Fluorimeter equipped with a GL-330 nitrogen laser, a GL-302 dye laser and a photomultiplier detection system. The sample was continuously stirred during the measurements. For the temperature with hexane-water experiments were used 2.85 mL of hexane and 0.15 mL of TRIS the samples were heated inside the tray and immediately measured. The excitation wavelength for all studies was 276 n

Raman spect . Solution emission studies of free protease and protease@MIL-101(Al)-NH_2 were performed using 5 m material over a glass slide. All experiments have been repeated at least five times to confirm reproducibility.

Physical characterization.

Dynamic light scattering (DLS) measurements were carried out with a Zetasizer Nano ZS instrument (M fresh solution of the enzyme in TRIS buffer (1 $g.L^{-1}$). The temperature was set ± 0.1 °C using a thermostat ba hydrodynamic diameter was determined by accumulative analysis. UV-Vis spectra were measured with a spectropolarimeter Jasco 810 and recorded from a temperature of 25°C. Ellipticity values were recorded every 0.5 nm at a wavelength scanning speed of 20 nm/min. The response time was set to 1s and the bandwidth was set to 1 nm. The final spectrum represented the accumulate avera of three consecutive scans. Powder X-ray diffraction (PXRD) was collected in a PANalytical X'Pert PRO diffractometer using radiation (Cu K_α = 1.5418 Å) with an X'Celerator detector, operating at 40 mA and 45 kV. Profiles were collected in the 2° 2θ < 40° range with a step size of 0.017°. Phase purity of the solid before/after enzyme infiltration was confirmed by Le Bail ref

FULLPROF software packa [3] Particle morphologies and dimensions were studied in a Hitachi S-4800 scanning electron microscope (SEM) at an accelerating voltage of 15 keV, over metalized samples with a mixture of gold and palladium during 30 s. Gas adsorptio measurements were recorded in a Micromeritics 3Flex at relative pressures up to 1 bar and performed ex-situ on activated solids. Samples were degassed overn [-6] Torr prior to analysis. Nitrogen adsorption-desorption isotherms were recorded at 77 K. Specific surface areas were calculated using the Brunauer–Emmett–Teller (BET) method in the relative pressure ran [0] = 0.05–0.30. The pore size distribution was analyzed by using a non-linear density functional theory (NLDFT) methods for the ads branch by assuming a cylindrical pore model. FT-IR was collected in the 4000–4 [−1] range from ground microcrystalline powder using an ATR Agilent Cary 630. Thermogravimetric analysis (TGA) was carried out with a Mettler Toledo TGA/SDTA 851e apparatus between 25 and 600 °C under ambient conditions [−1] scan rate and an air flo [−1]). All the Raman experiments were carried out using Confocal Raman Microscope puchased from Horiba-MTB Xplora in the range from 200 to 3600 cm^{-1}. A laser at 532 nm was used with a power of 0.0074mW at room temperature. The Raman shift was calibrated using silicon. All samples placed on a glass slide, with 40 accumulations of 2 seconds each. The spectrograph grating was 600 grooves/mm and a 10X objective was used.

S2. Enzyme size and MOF stability in different buffers.

Figure S1. Dynamic light scattering (DLS) of protease in the medium used for infiltration.

DLS measurements were carried out with a Zetasizer Nano ZS instrument (Malvern Instruments Ltd.) on a fresh solution in TRIS buffer (1 $g.L^{-1}$; pH 7.4) at 25 ºC. The mean hydrodynamic diameter of 2.85 nm was determined by statistic analysis of five different sa

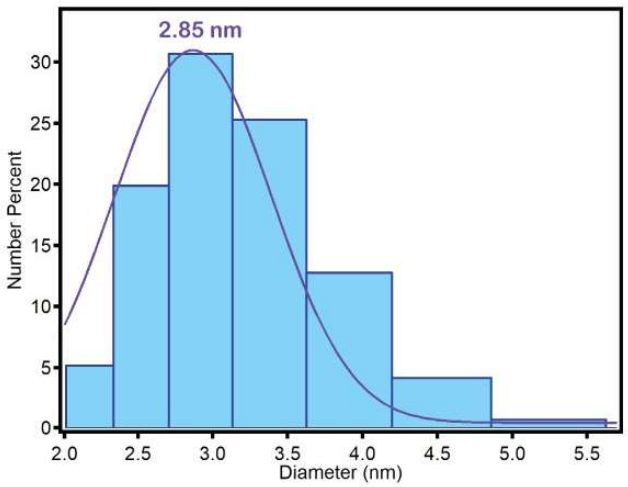

Figure S2. Effect of the buffer over the structure of MIL-101(Al)-NH_2 during enzyme infiltration.

Powder x-Ray diffraction (PXRD) of MIL-101(Al)-NH_2 displays important changes in presence of saline phosphate (PBS), sulphonate (HEPES) and carbonate buffers. Previous reports also confirm the negative influence of PBS over the structure of MIL-100(Fe) and the good of TRIS buffer.[4,5] In turn, the structure of the MOF is retained for an amine buffer (PBS), highlighting the importance of an adequat buffer to preserve the structural integrity of the MOF during enzyme infiltration. For comparison, the same experimental conditions described in the experimental section of the manuscript were used for the four different buffers. After thorough washing with fresh aliquots of the corresponding buffer, PXRDs of the solids isolated were collected in a PANalytical X'Pert PRO diffractometer copper radiation (Cu K_α = 1.5418 Å) with an X'Celerator detector, operating at 40 mA and 45 kV. Profiles were collected in the 2° 2θ < 45° range with a step size of 0.02°

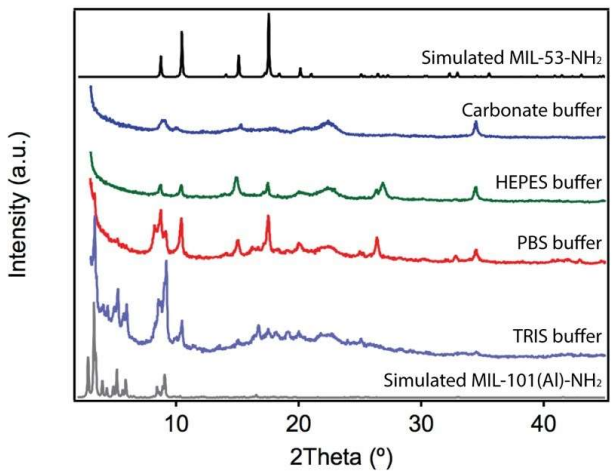

S3. Computational infor

The initial coordinates were taken from the X-ray crystal structure of Aspergillopepsin I (AP) from *Aspergillus saitoi* (also known *Aspergillus Phoeninci*). The structure employed can be f *Protein Data Bank* under the filename 1IBQ.[6] AP from *Aspergillus saitoi* is a monomer with one active site and a total of 325 residues. The protonation state of each residue was determined at pH=7 employing PROPKA 3.1 pr [7] Classically, all atom solvation was added explicitly with molecular dynamics simulation for the three systems: *i)* protein in water at 25 *ii)* protein in water at 60°C and *iii)* protein in a 3:1 mixture of hexane:water at 60°C were perfor using GPU version of PMEMD engine integrated with Am [8] The LEAP program of AMBER16 was used to generate topologies for the systems and add missed hydrogen ato The protein was then solvated in a cubic box of water molecules (aqueous systems) and hexane:water box (mixed system) with a 10 Å buffer region in all directions from the protein. 23 to neutralize the systems. The hexane:water mixture box was generated using PACKM [9] The protein, sodium ions and hexane were described using AMBER force field[10] while explicit water molecules were described by means of the TIP3P classic potential.[11,12] Energy was minimized by the steepest descent method with weak constraints for 10000 subsequently heated up to 25°C and 60°C for the aqueous systems and 60°C in the case of the hexane:water mixture. Afterwards, th three systems were equilibrated under 1 bar pressure over 100 ns in the isothermal-isobaric ensemble (NPT: a constant number of particles, constant pressure and constant temperature). Finally, 1 μs of production were performed on the three systems by periodic boundary conditions. The Particle Mesh Ewald (PME) method implemented in AMBER16, with direct space and a Van der Waals cut-off of 10 Å, was used to treat long–range electrostatic interactions. The SHAKE algorithm[13] was employed to constrai bonds involving hydrogen atoms, which allowed the use of a 2 fs timestep. The Langevin algor [14] was applied to couple systems to a 25 and 60°C external temperature bath. Finally, trajectories analysis including the Root Mean Square Deviation (RMSD), gyration and secondary structure analysis were carried out using CPPTRA [15] modules as implemented in AMBER1 Analysis of the secondary structure was carried out using the DSSP metho [16] The average number of residu unstructured regions (see Figure S3 below) was obtained as the difference between the total number of residues of the protein (325) and the average number of residues assigned to different secondary motifs by DSSP. Averages were taken in blocks of 100

Figure S3. Results of MD simulations of the Aspartic prot *Aspergillus* .

Average number of residues belonging to regions without secondary structure for the protein in hexane water at 25°C (black). As time passes, the number of residues that do not have a defined structure increases for hexane-water, wherea on only water remains unchanged. Only when hexane is added into the calculations there is a boost on randomly structured re

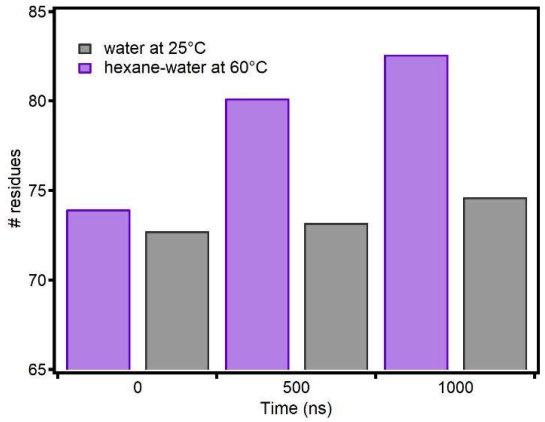

S4. Physicochemical characterization of the biocomposite.

Figure S4. Fluorescent spectrosco

Fluorescent spectra of the fully re-assembled protein (maintained overnight at 80°C, in purple) compared with the original free enzym (black). Also included the spectra of the MIL-101(Al)-N $_2$ to confirm that it does not interfere with the emission of the enzyme.

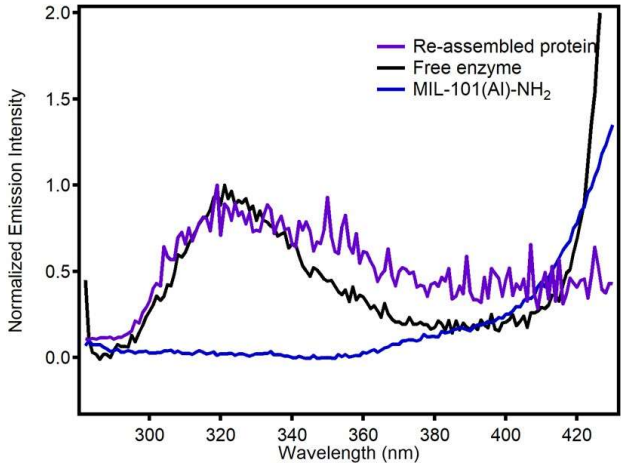

Figure S5. Raman spectra of protease, MIL-101(Al)-NH_2 and protease@MIL-101(Al)-NH_2.

Raman spectra of the free enzyme (purple), MIL-101(Al)-N $_2$ (black) and protease@MIL-101(Al) $_2$ (blue) in solid. The bands at 4 and 2430 cm^{-1} correspond to the vibration of disulfide bonds intrinsic to the cysteines in the polypeptide sequence of protease (UniPro code Q12567). a. Full spectra from 230 to 3600 cm^{-1} with the Raman peaks associated to the protein marked with grey bars. b. Zoom of the bands between 430- $^{-1}$. The signals at 470 and 2436 c $^{-1}$ in the enzyme are blue shifted close to 6 and 9 cm^{-1} after encapsulation as result of the interaction with the framework.

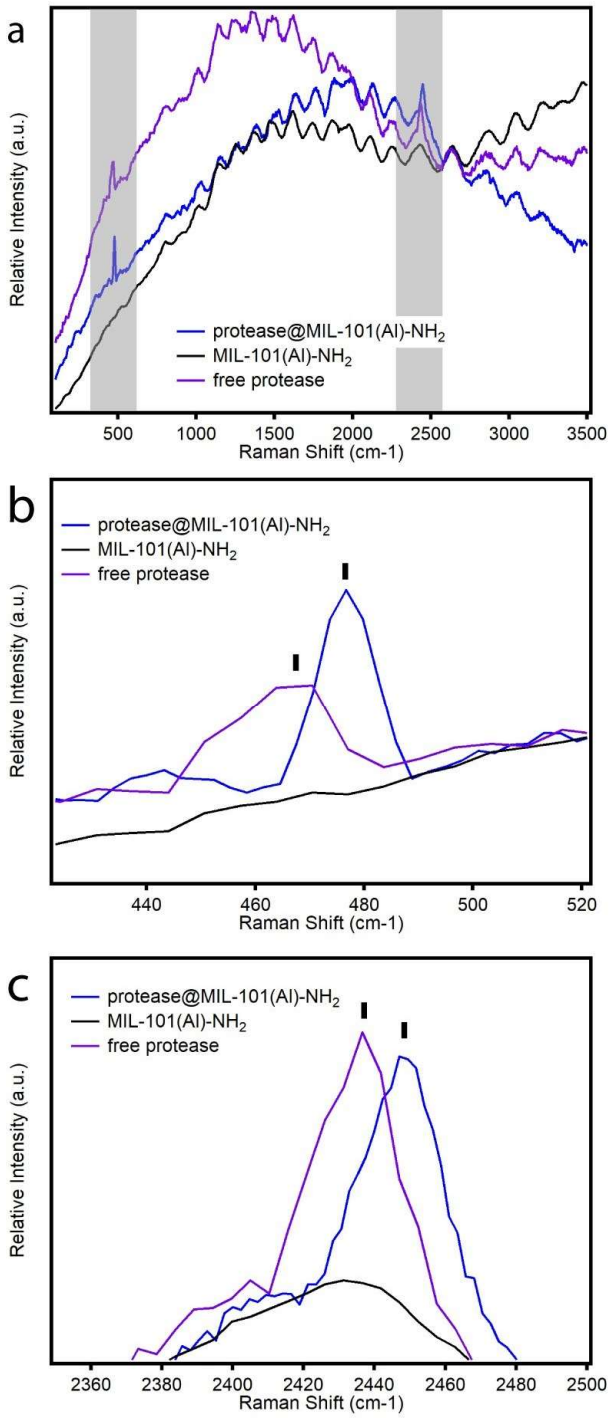

Figure S6. PXRD of non-functionalized MIL-101(Cr).

PXRDs of MIL-101(Cr) simulated (black) and as-synthesized material (gre

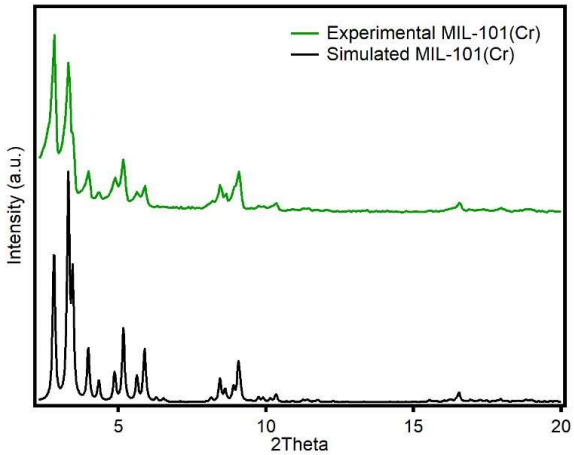

Figure S7. UV-Vis of MIL-101(Cr) after incubation with protease in presence of Gly-Tyr

Evolution of the proteolytic activity of MIL-101(Cr) after incubation with protease with time. Activity was followed with UV- monitoring the increase in absorption of the band intrinsic to the peptide (285 nm). For this essay we used 20 mg of the incubated solid (following the same procedure as for the MIL-101(Al)- $_2$) and 10 mg of GlyTyr dipeptide as substrate on 3 mL of TRIS buffer. As confirmed by the constant absorption value collected between 0 and 180 min, there was no measurable activity after the cleanings that could be linked to the presence of encapsulated enzyme. This confirms the importance of -NH2 groups in MIL-101(al)-NH2 to favou the translocation and subsequent regeneration of an active conformation of the enzyme into the MOF.

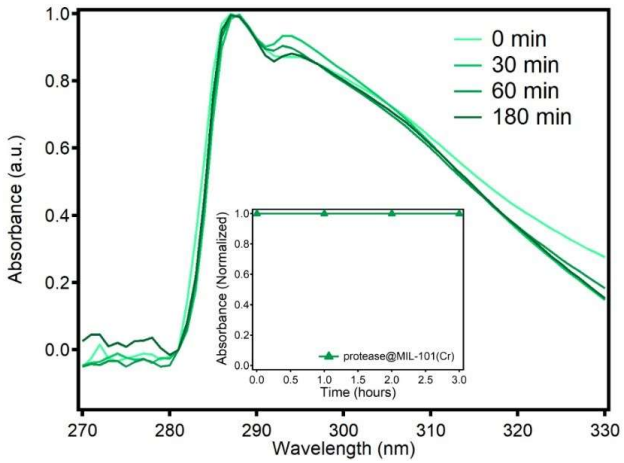

Figure S8. Thermogravimetric analysis of the MIL-101(Al)-NH_2, protease@MIL-101(Al)-$_2$ and free protease.

Thermogravimetric analysis (TGA) was carried out with a Mettler Toledo TGA/SDTA 851e apparatus between 25 and 600°C under ambient conditions (10°C·min^{-1} scan rate and an air flow $^{-1}$). The solids were measured after activation to minimize t effect of solvent loss over the TGA. Grey area stands for the decomposition of the protease inside the MOF. The decomposition of the free protease starts at 250°C, where protease@MIL-101(Al)-NH_2 also displays a slight weight loss, not present in the MOF before encapsulation, that corresponds approximately to 5% of mass loss.

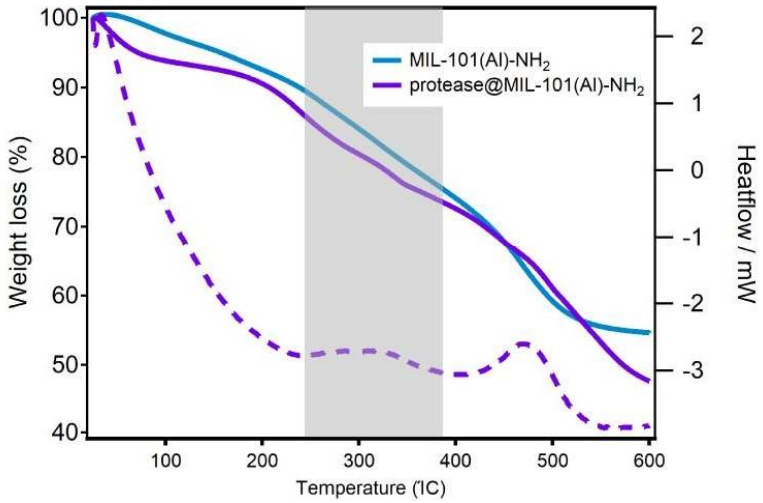

Figure S9. Evaluation of enzyme loading by UV-Vis spectroscopy of the supernatant after material washing.

UV-Vis spectra were measured with a spectropolarimeter Jasco J-810 and recorded at 25°C. Ellipticity values were recorded every 0.5 nm at a wavelength scanning speed of 20 nm/min. The response time was set to 1s and the bandwidth was set to 1 nm. The final spectrum represented the accumulate average of three consecutive scans. The uptake was calculated by correlating the drop in th absorption of the band intrinsic to protease, at 260 nm, with the concentrations of non-encapsulated enzyme in the supernatants after washing the material. The difference between the amount of enzyme detected in solution and the starting concentration accounts for close to 5% uptake.

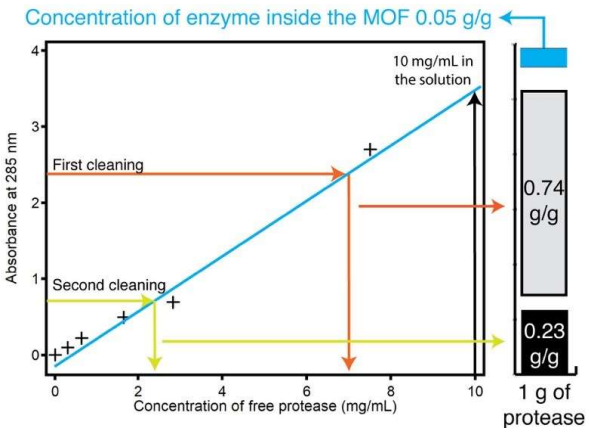

Figure S10. Powder x-Ray diffraction and Le Bail refinements of MIL-101(Al $_2$ and protease@MIL-101(Al)-NH_2.

Experimental (black line), calculated (red line), difference plot [*I*obs−*I*calcd)] (blue line, bottom panel) and Bragg positions (green ticks, bottom panel) for the refinement of experimental diffraction data collected at room temperature of MIL-101(Al)-NH_2 before and after enzyme infiltration. PXRDs were collected in a PANalytical X'Pert PRO diffractometer using copper radiation (Cu $_\alpha$ = 1.5418 Å) wi an X'Celerator detector, operating at 40 mA and 45 kV. Profiles were collected in the 2° < 2θ < 40° range with a step size of 0.017° and refineed with the FULLPROF software packag [17] by using CCDC605510 as a starting mo

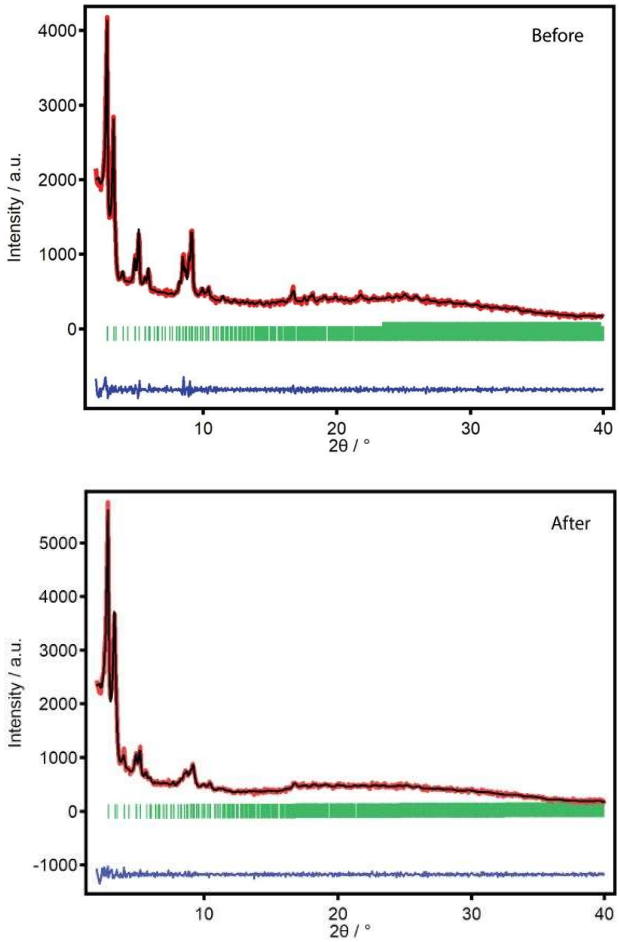

Table S1. Summary of the parameters obtained from the LeBail refinements.

	V [Å^3]	a [Å	$_e$ [%]	R_p [%]	R_{wp} [%]	gof
MIL-101(Al)-NH_2	680615.94	88.4	3.36	4.37	4.53	1.0
protease@MIL-101(Al)-NH_2	680039.75	87.9	3.48	4.52	4.22	1.0

Figure S11. Scanning Electron Microscopy (SEM)

SEM images of as-made MIL-101(Al $_2$ (*top r*) and protease@MIL-101(Al)-NH_2 (*bottom row*). Particle morphologies and dimensions were studied with a Hitachi S-4800 scanning electron microscope at an accelerating voltage of 20 keV, over metaliz samples with a mixture of gold and palladium during 30

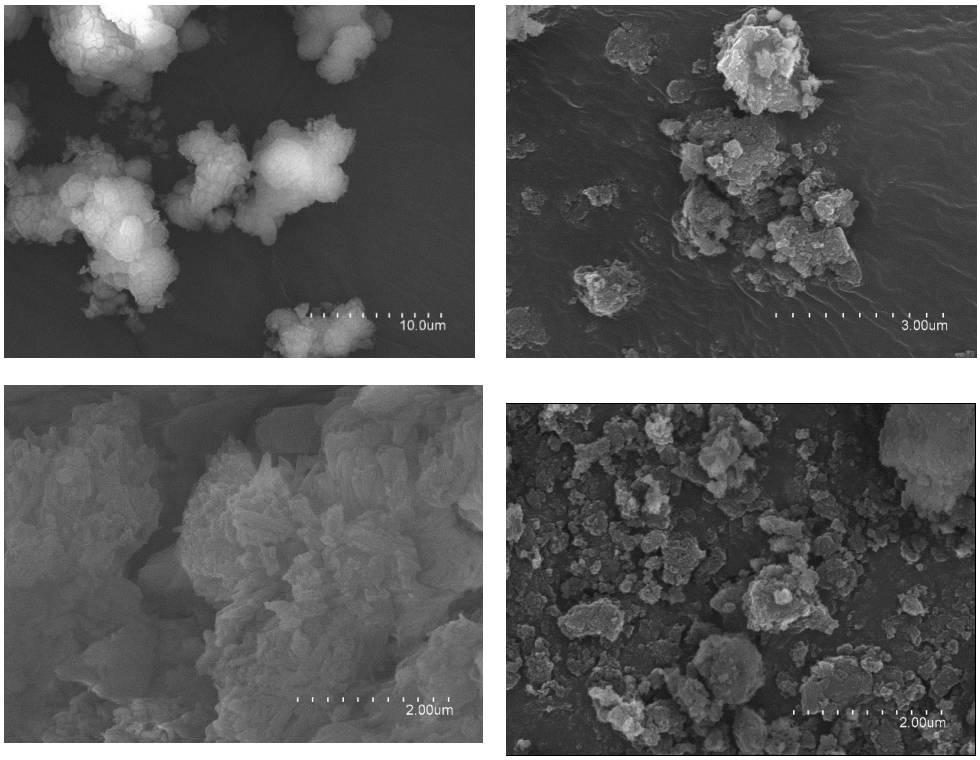

S5. Proteolytic activity tests.

Influence of the substrate concentration on the kinetics of peptide hydrolysis

Kinetics of the proteolytic activity was studied by using 20 mg of protease@MIL- 2 and 1 mg of free protease separately with 1, 2, 3, 4, 6 and 8 mM of GlyTyr. Kinetic parameters of the enzyme before and after encapsulation were determined by fitting th experimental data to the Hanes-Woolf equation:[18]

$$\frac{[S]}{v} = \frac{[S]}{V_{MAX}} + \frac{K_M}{V_{MAX}}$$

in which [S] represents the initial substrate concentration, v stands for the velocity of the reaction, V_{max} represents the maximum rat achieved by the system, at saturating substrate concentration, and K_M is the substrate concentration at which the reaction rate is half of the V_{max}. $k_{cat,}$ according to the equatio

$$k_{cat} = \frac{V_{max}}{[E_T]}$$

in which [T] represents the catalyst site concentration. It corresponds to the number of substrate molecules that each enzyme site converts to product per unit time (maximum efficiency). Finally, the rati k_{cat}/K_M stands for the catalytic efficienc [19]

Figure S12. Hanes-Woolf curve of proteolytic act

The evolution of the proteolytic activity with time was followed with UV-Vis by monitoring the increase in absorption of the band intrinsic to the peptide (285 nm). First, we analyzed the kinetics of enzyme reactivity for the hydrolysis at pH 3 and 25 °C of different q of Gly-Tyr, ranging from 0.8 to 8.4 µmol, in the presence of 1 mg of free protease (blue) and 20 mg of protease@MIL-1 2 (purple). These are the optimal working conditions for the alkaline protease used in this work.[20]

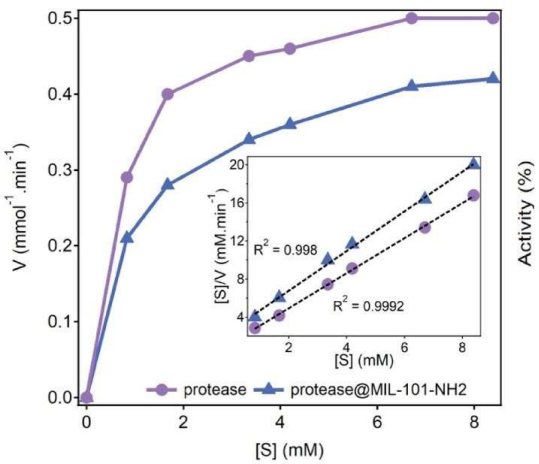

The comparison of the calculated kinetics parameters is summarized in **Table S2**. Compared to the free enzyme conditions, the initial hydrolysis rate of the peptide is slower for protease@MIL-101(Al)-NH_2 with a smaller k_M value. This is likely due to the slower diffusion of reactants and products in the MOF after loading. In turn, the biocomposite displays a higher K_{cat} value and k_{cat}/K_M ratios compared to the free enzyme, possibly due to the stability offered by the MOF. This suggests a change on the of the active site of the encapsulated enzyme, thus requiring a smaller Gly-Tyr concentration to achieve the maximum conversion This behavior is consistent with previous works that report a similar effect on enzymatic reactivity after encapsulation in mesopor MOFs.[21] This can be correlated with the subtle change observed in the fluorescent measurements, as the structure of the protease inside the MOF is different from the native. A different arrangement of the tryptophan and tyrosine residues might imply a diffe structure of the active site and thus a different specificity and velocity of the enzymatic reaction perfo

Table S2. Comparison of kinetic parameters for peptide hydrolysis of free and encapsulated protease in buffered conditions

Protease	K_M (mM)	k_{cat} (min^{-1})	k_{cat}/K_M ($min^{-1}mM^{-1}$)
Free	1.01	45	45
Encapsulated	0.66	55	83

Figure S13. Effect of the pH over the proteolytic activity of protease *a*) and protease@MIL-101(Al)-NH_2 (*b*) at 25°C

For these essays we used 20 mg of the solid incubated at room temperature with 20 μmol of GlyTyr in 3ml of TRIS buffer and compare to 1 mg of the free enzyme in the same medium, that was used as a reference. The evolution of the intensity of the band representative of the peptide (285 nm) with pH was measured and plotted for the calculation of the catalytic activit
from the reaction medium at 0, 60, 120 and 180 minutes, after dilution in 2.9 mL of TRIS buffer. The reactions were performed at pH 1-12 and 25°C. pH was monitored in a pH-meter GLP-20 from CRISON and controlled by addition of concentrated solution of HCl and NaOH.

a) Protease

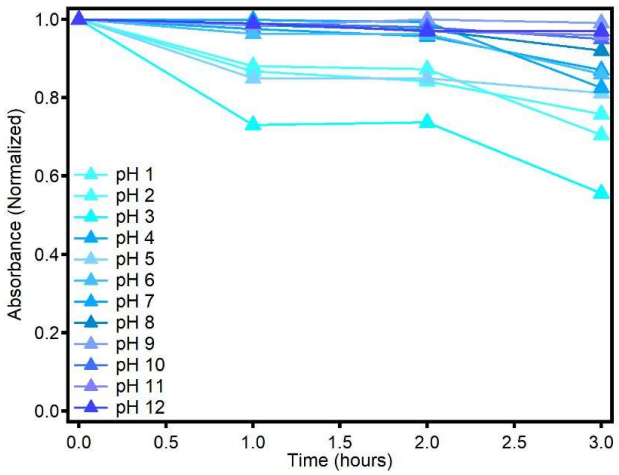

b) Protease@MIL-101(Al)-NH_2

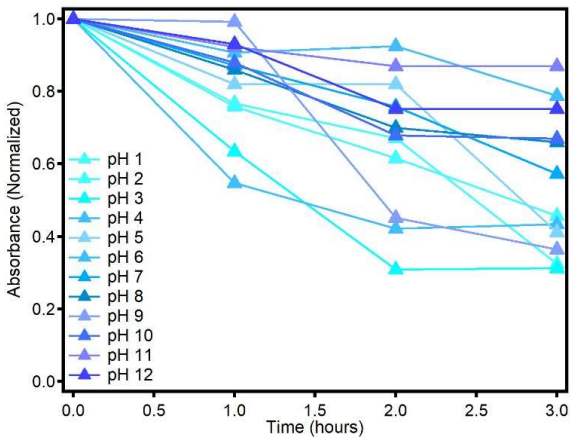

Figure S14. Effect of temperature over the proteolytic activity of protease (*top*) and protease@MIL-101-$_2$ (*bottom*) at pH 7.4

For these essays we used 20 mg of the solid incubated at room temperature with 20 μmol of GlyTyr in 3 ml of TRIS buffer and compar to 1 mg of the free enzyme in the same medium, that was used as a reference. The evolution of the intensity of the band represe of the peptide with temperature between 25 and 125°C was measured and plotted for the calculation of the catalytic activity from aliquots of 100 μL, extracted from the reaction medium at 0, 60, 120 and 180 minutes, after dilution in 2.9 mL of TRIS buffer. The reactions were performed at pH 7.4. Temperature was controlled with a thermostat in a heating bat

a) Protease

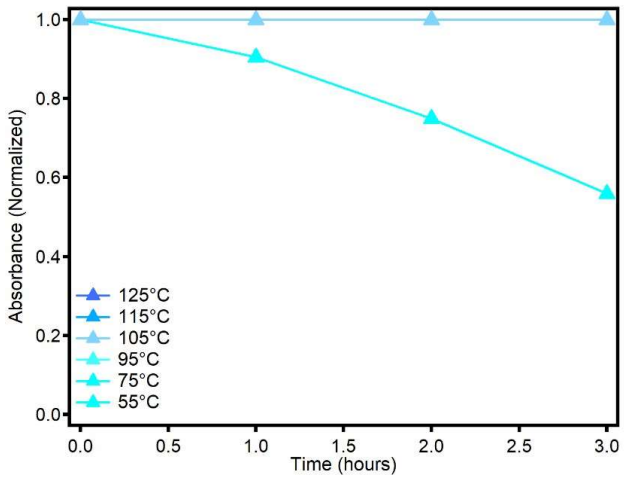

b) Protease@MIL-101(Al)$_2$

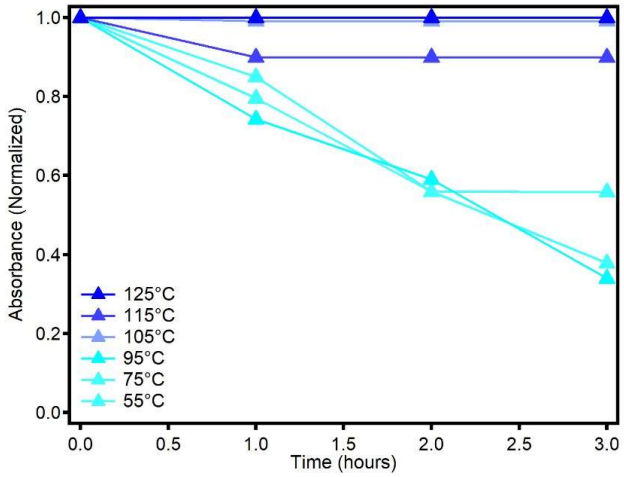

Figure S15. PXRD of protease@MIL-101($_2$ after the recyclability te

Comparison of the PXRD of protease@MIL-101(Al)-NH_2 after the recyclability tests run at 25°C, pH 7.4 (light blue) and 95°C, pH 2. (purple) with the simulated pattern of MIL-53-NH_2 (black; CCDC647506) and MIL-101-N $_2$ (grey, CCDC605510). The biocomposite retains its structural integrity at room temperature. However, heating at 95°C in an acid medium causes a structural transformation int the MIL-53 phase consistent with the appearance of characteristic Bragg peaks: [011], [020], [101] and [022]. This is possibly the reason for the gradual decrease in activity upon cycling as result of the leaching of the enzyme.

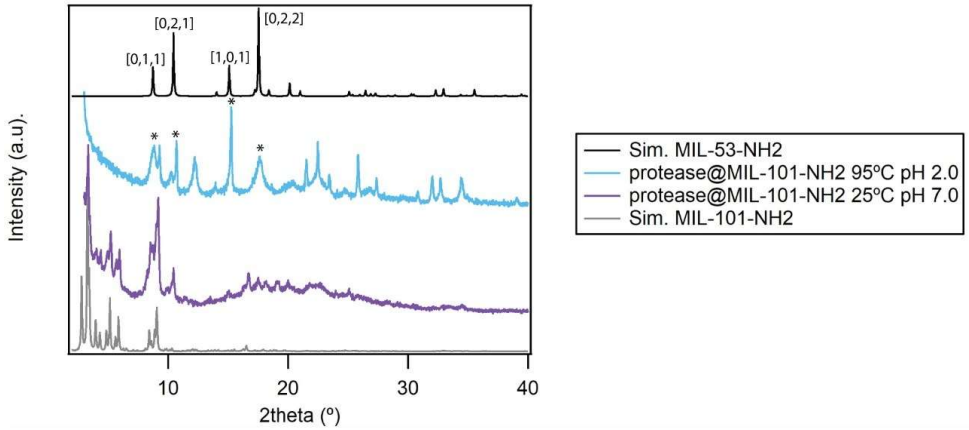

Figure S16. Activity of GOx alone (*top*), in presence of protease@MIL-101(Al $_2$ (middle) and free protease (*bottom*) at room temperature in a buffered medium.

For these essays we used 20 mg of the solid incubated at room temperatur μmoL of Glucose in 3 ml of TRIS buffer and compared to 1 mg of the free protease in the same medium, that was used as a reference. The reduction of the intensity of the UV-V band representative of the glucose was measured and plotted for the calculation of the catalytic activity from aliquots of 100 μ extracted from the reaction medium at 0, 60, 120 and 180 minutes, after dilution in 2.9 mL of TRIS buffer. The reactions were perf at pH 7.4.

a) GOx

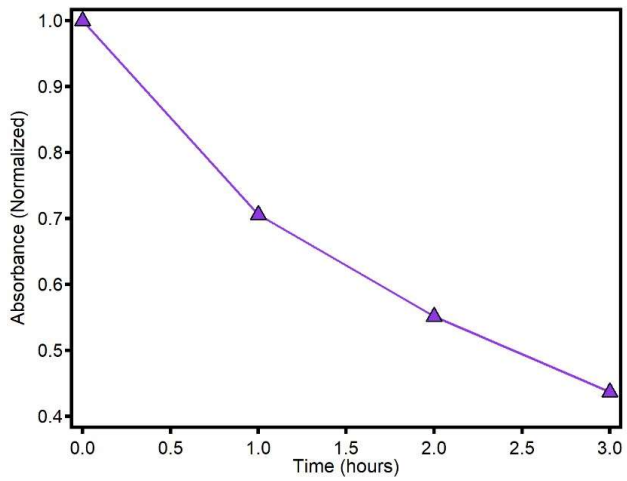

b) GOx & Protease@MIL-101(Al)-NH_2

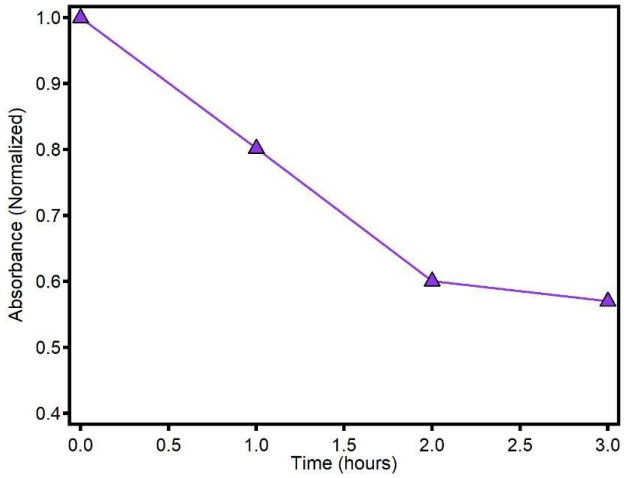

c) GOx & free proteas

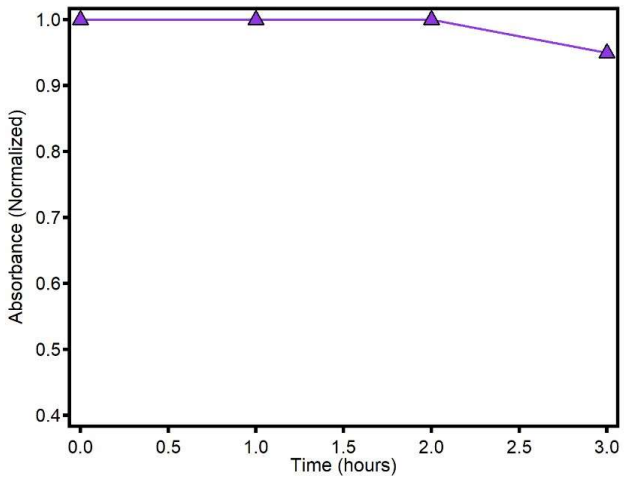

S6. Referen

1 C. Férey, C. Mellot-Draznieks, C. Serre, F. Millange, J. Dutour, S. Surblé and I. Margiolaki, *Science*, 2005, **309**, 2040–2042.
2 P. Serra-Crespo, E. V. Ramos-Fernandez, J. Gascon and F. Kapteijn *Chem. Mater.*, 2011, **23**, 2565–2572.
3 T. Roisnel and J. Rodríquez-Carvaja *Mater. Sci. F* , 2001, **378–381**, 118–123.
4 V. Agostoni, T. Chalati, P. Horcajada, H. Willaime, R. Anand, N. Semiramoth, T. Baati, S. Hall, G. Maurin, H. Chacun, K. Bouchemal, C. Martineau, F. Taulelle, P. Couvreur, C. Rogez-Kreuz, P. Clayette, S. Monti, C. Serre and R. *Adv. Healthc. Mater.*, 2013, **2**, 1630–1637.
5 R. Anand, F. Borghi, F. Manoli, I. Manet, V. Agostoni, P. Reschiglian, R. Gref and S. Monti, *J. Phys. Che* , 2014, **118**, 8532–8539.
6 Sang Woo Cho, N. J. Kim, M. U. Choi and W. Shin, *Acta Crystallogr. D Biol. Crystallog* , 2001, **57**, 948–956.
7 M. H. M. Olsson, C. R. SØndergaard, M. Rostkowski and J. H. Jensen, *J. Chem. Theory Comput* , 2011, **7**, 525–537
7 A. W. Götz, M. J. Williamson, D. Xu, D. Poole, S. Le Grand and R. C. Walker *J. Chem. Theory Compu* , 2012, **8**, 1542–1555.
9 L. Martinez, R. Andrade, E. G. Birgin and J. M. Ma *J. Comput. Ch* , 2009, **30**, 2157–2164.
10 W. D. Cornell, P. Cieplak, C. I. Bayly, I. R. Gould, K. M. Merz, D. M. Ferguson, D. C. Spellmeyer, T. Fox, J. W. Caldwell and P. A. Kollman, *J. Am. Chem. Soc.*, 1995, **117**, 5179–5197.
11 W. L. Jorgensen, J. Chandrasekhar, J. D. Madura, R. W. Impey and M. L. Klein, *J. Chem. Phys* , 1983, **79**, 926–935.
12 E. Neria, S. Fischer and M. Karplus *J. Chem. Phys* , 1996, **105**, 1902–1921.
13 V. Kräutler, W. F. Van Gunsteren and P. H. Hünenberger, *J. Comput. Ch* , 2001, **22**, 501–508.
14 X. Wu and B. R. Brooks, *Chem. Phys. L* , 2003, **381**, 512–518.
15 D. R. Roe and T. E. Cheatham *J. Chem. Theory Comput.*, 2013, **9**, 3084–3095.
16 W. Kabsch and C. Sander *Biopolymers*, 1983, **22**, 2577–2637.
17 J. Rodríguez-Carvajal, *Phys. B Phys. Condens. Matter*, 1993, **192**, 55–69.
18 J. Markwell, *Fundamental laboratory approaches for biochemistry and biotechnology, 2nd edit* , Fitzgerald Science Press, Bethesda Md., 2009,
18 A. Cornish-bowden, *Methods Study Mar. Benth* , 2013, **34**, 1-17.
20 S. R. Tello-Solis and A. Hernandez-Arana, *Biochem. J.*, 1995, **311**, 969–974
21 D. Feng, T. F. Liu, J. Su, M. Bosch, Z. Wei, W. Wan, D. Yuan, Y. P. Chen, X. Wang, K. Wang, X. Lian, Z. Y. Gu, J. Park, X. Zou and H. C. Zho *Nat. Commun.*, 2015, **6**, 1–8.

Chapter 5: Conclusions

MOFs can be considered as the ultimate synthetic examples of ordered 3D molecular spaced structures, capable of rational placement of metals and molecules in specific positions. It is naturally enticing to compare their custom-made properties with those of biological molecules such as proteins, for which the placement of the amino acids in the polypeptide chain determines their properties. This thesis originates from the multidisciplinary effort of making use of common nature biomolecules to construct MOFs and give them fitting applications, being described commonly as “bio-MOFs”. From a synthetic view, biomolecules are ideal MOF building blocks due to their accessibility and ability to coordinate metal ions, and from an implementation standpoint, their constituents proportionate opportunities for applications across biology and medicine.

In the first part of this work, we tried to study the mechanisms after the flexibility that peptidic chains bestow being incorporated inside MOFs. This type of linkers are capable of displaying a richer conformational landscape than common rigid constituents, resulting in more elastic structures for which the availability of low-energy conformation states would enable reversible conformation under stress. In order to study this phenomenon, was necessary the use of a dense peptide MOF, using *in situ* powder and single-crystal X-ray diffraction under high pressures, to allow a precise structural study on how this type of materials face compressibility. The synthetized crystals of the system $Zn(GlyTyr)_2$ were loaded in a DAC cell with varying pressures, and showed a reversible compression at 4 GPa of a 13% of its volume, showing the ability of the peptide linker to act as a flexible string for a cooperative response. The structural transformation was progressive and being controlled by changes in the conformation of the peptide, as it is capable of performing a sort of bond rearrangement in the coordination sphere of the Zn(II). Concretely, it was controlled through a cooperative rotation of the two amino acids and shortening the H-bond distances that dictate the interlayer separation. For that reason, the compressibility is dependent of the amino acids identity composing the peptidic chain of the ligand. This behavior was not affected by host/guest interactions nor solvent inside the pores, and relies exclusively on the conformational flexibility of the peptide and its side chain chemistry.

On the second part of the study of applications for bio-inspired MOFs, we employed a chiral framework based on the tripeptide GlyHisGly with Cu(II) for the enantioselective separation of two recreational drugs: methamphetamine and ephedrine. Monte Carlo simulations were employed to gain a better understanding of the role played by the functional groups of the peptide controlling the enantiomerical adsorption, that is, how are they able to stablish favorable binding

sites. This study suggested that the separation was linked to one of the enantiomers having stronger or simply more hydrogen bonds with the MOF, leading to an improved stability inside the scaffold and longer retention times inside the pores. To the formation of H-bonds between the amine and the imidazole group in the His side chain, there was a translation into a difference in adsorption energies of up to 13 kcal/mol. For the best results, a solid-phase extraction of a racemic mixture using Cu(GlyHisGly) permits isolating 54% of the (+)-ephedrine enantiomer in around 4 minutes. The column could be used at least for two runs without significant loss of crystallinity nor leaching. This combination of theory and experiment could allow to perform prediction studies, selecting chiral supports that best fit the separation of a certain chiral drug.

Finally, in the last approach we study how to improve enzymatic catalysis through the development of a new immobilization procedure, bypassing the limitations that the MOFs intrinsically bear. The scaffold selected was MIL-101(Al)-NH_2, as the pore size was ideal for the insertion of the enzyme, an aspartic proteinase from *Aspergillus saitoi*. We employed a mild heating coupled with the exposure to a non-polar solvent during the incubation, in order to cause a partial unfolding in the enzyme, allowing it to migrate inside the pores of the MOF. This was supported by molecular dynamic simulations and fluorescence spectroscopy, showing a structure change in the enzyme that allowed its translocation across the pore windows of the MOF, being 50% smaller in size. The MOF remained stable through the whole process and the pores were almost completely filled with the enzyme. Moreover, the proteolytic tests made with the composite show a sharp increase in the stability of the activity under extreme pH and temperature, protecting the enzyme from autolysis and external agents. The MOF immobilization is also effective in providing the protein with long-term stability, recyclability and compatibility with proteases in the outside medium. This simple, one-step infiltration strategy allows the development of a new variety of composite configurations.

Resumen de la tesis doctoral

La presente tesis doctoral ha sido realizada como compendio de publicaciones y lleva por título "*Biodiseño en adaptabilidad conformacional y reconocimiento de huéspedes en estructuras cristalinas*" (Biodesign for conformational adaptability and guest recognition in crystalline frameworks*)*. Se encuentra dividida en cuatro capítulos con unas conclusiones finales y resumen en castellano.

El primer capítulo se trata de una introducción a las redes metal-orgánicas (MOFs) basados en materiales biológicos, tanto su diseño a partir de éstos, como algunas de sus aplicaciones más notables. Inicialmente se habla del origen de este tipo de sistemas, que radica en la necesidad que tenían los químicos hace más de 30 años de poder racionalizar la obtención de estructuras periódicas, y convertir la química supramolecular en algo más predecible. Alrededor de esa fecha, muchos ya se dieron cuenta de que determinadas biomoléculas como los aminoácidos, péptidos, proteínas y nucleobases tenían potencial como ligandos, y de hecho existían varios ejemplos de incorporación a polímeros de coordinación. Siguiendo este orden, comenzamos la introducción hablando de cómo emplear materiales biológicos para el diseño de MOFs. Las primeras en ser nombradas son las nucleobases, de las cuales se han usado principalmente las bases púricas al ser las únicas con capacidad de conexión para la formación de redes. Éstas pueden proveer de uniones moleculares estables con cierta facilidad y varias posiciones para coordinar centros metálicos, teniendo cada una de esas bases una preferencia metálica única. Sin embargo, tienen muchas limitaciones al no ser elementos flexibles ni tener algún tipo de personalización. A diferencia de éstas, los péptidos suponen una mejora en el aspecto de la variedad, abriendo un abanico de posibilidades al poder combinarse varios aminoácidos en una secuencia peptídica para formar la cadena de un MOF. Además, son ligandos orgánicos excelentes y capaces de coordinar iones metálicos a través de sus grupos carboxilato y amino. La cadena lateral, al ser diferente en cada caso, puede impartir polaridad o apolaridad sobre el sistema del que forma parte. Finalmente se hayan las proteínas, el último escalón en complejidad, formadas por cadenas polipeptídicas asociadas de una forma predeterminada. La mayoría de las proteínas deben adoptar una conformación concreta, llamado plegado o estado nativo, para poder funcionar correctamente y desempeñar su función biológica. La energía necesaria para realizar ese plegado proviene principalmente de van der Waals, enlaces por puente de hidrógeno e interacciones electrostáticas que suceden entre elementos de esa cadena electrostática. Estas interacciones también se hayan en los aminoácidos más superficiales y permiten la formación de redes, otorgándoles una estructura periódica y la posibilidad de formar cristales. Posteriormente, se desarrollan algunas de las aplicaciones más importantes de dichos sistemas, teniendo en cuenta que el

diseño de los MOFs biológicos permite el emplazamiento de grupos funcionales en el sistema. Por ello, los entornos de poro personalizados a nivel molecular pueden ser obtenidos a través de este diseño específico. Gracias a esta posible personalización, los MOFs han sido estudiados para una gran variedad de aplicaciones entre las que se encuentran la catálisis heterogénea, separación, y aplicaciones biomédicas, entre otras. Sin embargo, cuando se aplican estos sistemas a campos relacionados con lo biológico, la toxicidad es uno de los puntos más importantes a considerar y hace al tipo de sistemas que tratamos más interesantes. El primer gran grupo de aplicaciones que saca partido de la funcionalización es el de la catálisis. Los catalizadores basados en bio-MOFs son especialmente interesantes ya que no solo tienen las características de estos materiales como la personalización y la existencia de grupos catalíticos, sino que además son extremadamente robustos y eficientes. Además del gran contenido en metal, una de sus mayores ventajas es que los sitios activos son todos exactamente iguales, dando lugar a una catálisis homogénea. El segundo grupo es la separación, pues estos materiales pueden obtener reconocimiento específico de forma muy efectiva y son sencillos de producir. Los MOFs poseen una gran porosidad y área superficial, lo que junto con la personalización del poro, la posibilidad de obtener sitios de coordinación metálicos libres y la regularidad de su estructura, proporcionan una base para la separación de una gran variedad de compuestos. El tercer y último gran grupo se basa en el confinamiento de moléculas dentro de los poros. En esta parte nos centramos en la incorporación de enzimas al interior de los MOFs, al poder proporcionarles dicha estabilidad y personalización a las proteínas huésped. Dentro del poro, las enzimas se hayan protegidas de toda interacción con el exterior que les pueda perjudicar, pudiendo seguir realizando su función. Durante este capítulo se ha tratado de recalcar por separado cada una de las tres partes fundamentales que poseen todos los MOF: metal, ligando y poro. Por ello, se ha dividido por nivel de complejidad biológica: nucleótidos, péptidos y enzimas; y también por aplicaciones principales de cada uno de ellos. Los nucleótidos se han empleado principalmente para catálisis al tener la mayoría de estructuras grupos metálicos libres, los péptidos al ser quirales han tenido mayor relevancia en el campo de la separación quiral y para las enzimas se trata de emplear a los MOFs como plataformas personalizables capaces de acomodarlas sin afectar a su estructura.

En el segundo capítulo se estudia la respuesta estructural a estrés por presión de un MOF compuesto por dipéptidos. Los dipéptidos nos ofrecen una gran variedad de combinaciones y son unos ligandos muy interesantes para la formación de MOFs, al dotar al complejo de la funcionalidad de dicha cadena. Es interesante estudiar cómo los sistemas flexibles actúan frente a presión externa ya que, precisamente una de las desventajas que poseen, es que tienen propiedades

mecánicas muy débiles pudiendo acabar en el colapso del poro o de la estructura una vez se le añade presión. Por tanto, este tipo de deformaciones estructurales también afectan a la función, pudiendo producir efectos no deseados. La flexibilidad estructural abre un abanico gigantesco de posibles respuestas a la presión, las cuales deben ser investigadas en detalle con el objetivo de predecirlas. Lamentablemente, no hay una gran cantidad de ejemplos de este tipo de estudios, ya que hasta la fecha se han basado en sistemas porosos. Estas estructuras al poder alojar en su interior moléculas de disolvente o huéspedes, no permiten saber si realmente lo que se mide es efecto de la estructura o de una influencia externa. Por ese motivo, nosotros usamos el MOF $Zn(GlyTyr)_2$ el cual se considera "denso" al no tener porosidad medible, esa imposibilidad de entrada de disolvente simplifica enormemente el refinamiento de la difracción de rayos X bajo presión.

La estructura del dipéptido está basada en interacciones por puente de hidrógeno entre las diferentes láminas que lo forman, produciendo una estructura que se empaqueta siguiendo a su cadena lateral. Pese a que se puede considerar no poroso, sigue siendo un material con un volumen de celda variable y su compresibilidad es mucho mayor que otros materiales basados en zeolitas. Con el objetivo de discernir qué técnicas y medio usar para los experimentos, primero debimos elegir qué medio emplear de entre los más usados medios transmisores de presión (*Pressure Transmitting Medium*) abreviado PTM, dentro de una celda de diamante (*Diamond Anvil Cell*) abreviado DAC. Esta técnica permite aplicar una presión constante y homogénea a todas las partes del cristal. Con el objetivo de permitir una recogida de datos lo más adecuada posible y evitar a la vez la amorfización de las muestras, decidimos empezar con experimentos de rayos X. Para conocer la presión de trabajo se empleó un cristal de rubí, y se comprobó que había una diferencia notable en las medidas a 3.7 GPa, atribuyéndose a una deterioración intrínseca de las condiciones quasi-hidrostáticas de los PTMs. La cristalinidad se pudo recuperar tras retirar la presión. Tras elegir al fluorinert y la mezcla metanol:agua como las que más respetaban la estructura, promoviendo una menor amorfización según aumentaba la presión, se comenzaron los experimentos bajo presión.

Para los experimentos de rayos X bajo alta presión, las estructuras se fueron refinando conforme se incrementaba la temperatura, teniendo algunas limitaciones al recogerse únicamente un 30% de las reflexiones. La celda del DAC está cerrada por ambos lados para poder ejercer la presión de forma controlada, y la única parte donde se podía enfocar era por la delantera. Por este motivo, tuvimos que emplear refinamientos estructurales para ser capaces de llegar a estructuras que pudiéramos comparar. Los cambios estructurales que observamos mostraban un cambio sobre los 2 GPa, indicando una transición de fase isoestructural de segundo orden. El grupo espacial, sin embargo, no cambiaba con el incremento de presión y

el volumen de la celda no mostraban ninguna discontinuidad. La información obtenida mostraba claramente que el sistema $Zn(GlyTyr)_2$ poseía una elevada resistencia anisotrópica a la compresión. Los mayores cambios en la estructura los pudimos observar de 0 a 4 GPa, donde la transición de fase del sistema se lleva a cabo gracias a una reorganización de la esfera de coordinación de los centros de Zn(II). Este fenómeno es controlado mediante la coordinación del grupo carboxilato de la glicina, haciendo que el clúster metálico cambie de configuración geométrica. El cambio en la conectividad general del sistema se lleva a cabo por igual por todo el MOF, mediante la relajación de las capas internas de la estructura, dependiendo de ajustes en las interacciones supramoleculares en el péptido. Esta información señala que el responsable real de esta capacidad del MOF de comprimirse sin degradarse es debida a los aminoácidos, pues son capaces de reducir la distancia del puente de H que separan las capas. El péptido es el responsable de los cambios cooperativos dentro del MOF, y concretamente, es la tirosina el aminoácido que más contribuye a esa relajación estructural y mantenimiento de la estructura. Como resumen se puede concluir que gracias al péptido junto con las interacciones no covalentes del MOF, éste puede soportar las presiones externas sin llegar a la amorfización. Gracias al hecho de ser un MOF denso, podemos descartar cualquier influencia de moléculas dentro del poro o de disolvente metiéndose en el poro.

En el tercer capítulo se continúa hablando de estructuras de MOFs basadas en péptidos, pero se sube un escalón en cuanto a complejidad se refiere. Así pues, se emplea el sistema Cu(GlyHisGly), basado en un tripéptido con enriquecimiento quiral y coordinado con Cu(II). Este tipo de materiales pueden ofrecer un reconocimiento quiral manteniendo simultáneamente una gran robustez, estabilidad química y porosidad. En este trabajo empleamos este sistema para separar dos fármacos frecuentemente empleados como drogas recreacionales: metanfetamina (MA) y efedrina (EP). Ambos son compuestos quirales y a nivel farmacéutico es imprescindible su separación para poder ser empleados. Para poder saber si habrá una separación verdaderamente relevante, llevamos a cabo un estudio teórico de la respuesta a los enantiómeros mediante el programa *Materials Studio Simulator* para realizar simulaciones con Monte Carlo. Esta aproximación nos permitió comprender verdaderamente qué rol juega el péptido al establecer una adsorción preferencial para el sito de unión más probable. Los dos enantiómeros (+,-) de la MA y EP fueron introducidos en la estructura tras haberla vaciado de disolvente. Después procedimos a estudiar las condiciones más energéticamente favorables de EP y MA, haciendo girar las moléculas de forma aleatoria y aceptando la estructura resultante sólo si era más estable que el paso anterior. Aunque la precisión del método empleado no permite hacer una predicción cuantitativa de la selectividad quiral, la simulación consiguió aproximarnos las energías indicando que la separación más efectiva sería la de EP, como resultado de las interacciones supramoleculares

cooperativas que lleva a cabo. La adsorción de la (+)-EP era pues preferencial y mucho mayor que en el caso de la (+)-MA, llegando a poseer energías cerca de 13 kcal/mol. Viendo que estos resultados eran prometedores de por sí, tratamos de trasladar estas energías al plano experimental para probar las capacidades predictivas de nuestro método. La explicación de este buen resultado radica en la interconexión de los canales, la cual da lugar a una decoración de la superficie del espacio vacío con grupos carboxilatos, amida e imidazol apuntando al interior de los canales.

Para realizar un primer estudio tentativo de las capacidades separativas de este MOF, comenzamos con una prueba de absorción simple en disolución. Es importante destacar que usualmente estos sistemas suelen evacuarse completamente de disolvente antes de realizar las pruebas, sin embargo, los MOFs constituidos de péptidos suelen poseer una baja estabilidad en ausencia de disolvente. Afortunadamente, el reconocimiento quiral es un proceso dinámico y la eliminación del disolvente ocupando los poros no es necesaria al ser sustituido por las moléculas a separar. Por tal motivo, nos abstuvimos de secar el MOF y se usó directamente tras un lavado para medir las retenciones. En esta primera prueba, decidimos simplemente calcular cuánto fármaco entraría dentro del MOF, midiendo el exceso enantiomérico en disolución tras un tiempo determinado. Por tanto, a una pequeña cantidad de MOF se le añadió fármaco en mezcla racémica y se midió el enriquecimiento de los enantiómeros a diferentes tiempos. Tras 1 hora en el caso de MA y 4 horas en el caso de EP se vio claramente que, mientras que la cantidad de (-)-MA y (-)-EP eran prácticamente la misma, la cantidad de (+)-MA y (+)-EP había sido reducida de manera notable. Atribuimos los largos tiempos de contacto a la composición polar de los disolventes. La retención preferencial se debe a que los fármacos quirales se estabilizan de forma diferente dentro del poro, concretamente se llega al máximo de retención que supone un 30% de exceso para la (+)-MA y 37% para la (+)-EP tras 4 y 2 horas, respectivamente. Los resultados del experimento coinciden perfectamente con las simulaciones teóricas que predicen esa diferenciación de los enantiómeros (+) en el poro quiral, ligado a las conformaciones específicas que las moléculas adoptan en el interior de los poros. Las simulaciones teóricas además predicen una separación más favorable de los enantiómeros de EP respecto a lo obtenido para la MA, y efectivamente son los resultados que muestran los experimentos.

Lamentablemente, el uso de MOFs como fase estacionaria posee una gran variedad de limitaciones debido a su baja estabilidad y heterogeneidad de partículas. Esto limita en gran medida las fases móviles que pueden ser usadas con analitos polares, e incrementa la dificultad para la obtención de un empacado de las partículas dentro de la columna. Una falta de control sobre el tamaño y forma de los cristales de MOF puede dar lugar a mayores tiempos de retención, un rendimiento

cromatográfico bajo y separaciones más largas. Por este motivo e inspirados por los buenos resultados hasta el momento, decidimos probar una de las separaciones más usadas en industria por su sencillez: extracción en fase sólida (*solid-phase extraction*) o SPE. A diferencia de las columnas usualmente más empleadas, las SPE permiten el aislamiento de los enantiómeros en lugar de una medición de la riqueza de la mezcla. El SPE permite obtener una medida cromatográfica mediante la eliminación de interferencias, además de un incremento en la concentración total y simplificación de la muestra. Empleamos esta técnica con el MOF como base en un cartucho de polipropileno de SPE y le hicimos pasar una disolución racémica de EP por el interior. En esta segunda parte decidimos concentrarnos en la EP y dejar de lado la MA ya que la primera nos dio mejor resultado en la prueba inicial, además de ser la que más sería retenida mediante la predicción teórica. En los test que llevamos a cabo, la columna quiral permitió llegar a un 54% de separación del enantiómero (+)-EP a partir de dichas muestras equimolares en 4 minutos, con una precisión totalmente satisfactoria y tiempos de retención cortos. La valoración sobre la precisión de la separación es una relación entre la distancia entre los picos y la anchura de los mismos. Estos resultados sugieren que el sistema Cu(GlyHisGly) ofrece un alto rendimiento en términos de reconocimiento estereoselectivo y de eficiencia en tiempo, para una columna de separación quiral de alta velocidad. Para acabar, con el objetivo de actuar como test de que verdaderamente es el MOF el que está actuando para establecer la separación entre enantiómeros, se realizó la misma prueba inicial pero directamente con la mezcla de Cu(II) y GlyHisGly en la misma proporción en que estaba presente en el MOF. Tras observar una diferencia inexistente en término a separación enantiomérica, pudimos concluir que ésta estaba basada en la distribución periódica de los canales quirales de la estructura del MOF, y que ésta era clave a la hora de separar ambos enantiómeros. La esencia del trabajo radica en el potencial que posee la mezcla entre teoría y experimento, permitiendo realizar tareas predictivas para maximizar las separaciones.

En el capítulo 4 se trata un tema completamente diferente. Este trabajo surge de la necesidad de idear un método de inmovilización de enzimas en MOFs diferente a lo ya reportado. Pese a que hay una gran cantidad de trabajos publicados sobre este tema, todos se centran en el contenedor y no en el contenido, modifican o alteran el MOF considerando a la enzima como un bloque inmóvil. Sin embargo, una de las propiedades más importantes de las enzimas y de la mayoría de las proteínas, es que tienen la capacidad de plegarse hacia su estructura terciaria sin ninguna asistencia. Este proceso se lleva a cabo mediante “saltos” energéticos, pues las enzimas siempre se pliegan hacia la formación energéticamente más favorable, y llegar a su estado nativo es un proceso de prueba-error a nivel de residuo. Basándonos en el único estudio donde esta peculiaridad se ha aprovechado para proteínas, decidimos llevarlo a un campo tan complejo como es

el de las enzimas, tratando de usar un desenhebrado parcial para introducir la enzima dentro del poro del MOF. Al permitir que una enzima cupiera por la ventana de un poro donde normalmente sería incapaz de entrar abriría un nuevo abanico de posibles MOFs y enzimas a usar, eliminamos una de las restricciones más importantes de este tipo de técnicas.

El proceso se inicia cuando la enzima lleva a cabo los cambios conformaciones bajo los cuales su estructura, y por tanto tamaño, van a variar permitiendo la migración a través de las ventanas del poro hacia la superficie del cristal. Empleando este proceso natural como concepto para desarrollar este nuevo tipo de inmovilización, decidimos atrapar a la enzima dentro del poro y provocar su replegado dentro de él, evitando su posterior salida. Usar enzimas obviamente supone un reto adicional, pues su estructura nativa es la que va a dar lugar a la función catalítica, por ello escogimos una familia de enzimas especialmente robusta y de tan solo una cadena. Se trata de una proteinasa aspártica de *Aspergillus saitoi*, la cual tiene propiedades biotecnológicas notables, habiendo sido estudiada previamente. Por otro lado, decidimos usar el poro del MIL-101(Al)-NH_2, pues sus cavidades mesoporosas son de 3.6 y 2.9 nm con ventanas hexagonales y pentagonales de 1.6 y 1.2 nm respectivamente. Esos tamaños son compatibles con el diámetro de la enzima, con un ratio cerca del 1.2, dejando un cierto espacio para que la enzima pueda volver a su estructura nativa por sí misma. El tamaño de la enzima se calculó mediante el uso de *Dynamic light scattering* o DLS, un aparato capaz de medir el radio de objetos en disolución, captando un diámetro medio de 2.85 nm. Además el MOF ha sido previamente empleado en aplicaciones compatibles con las condiciones biológicas y se puede adaptar a los requerimientos de las enzimas. También se comprobó que el sistema era estable en el tampón empleado durante el proceso (TRIS) y se empleó la versión funcionalizada con aminos, ya que la dicha decoración del interior de los poros ofrece un ambiente de hidrofilicidad que promueve la formación de puentes de hidrógeno. El incremento en polaridad también aumentó la dispersibilidad del MOF en la disolución acuosa.

Con el objetivo de permitir a la enzima entrar dentro de la estructura a través de esa desnaturalización parcial, pensamos en usar condiciones como un ligero incremento en la temperatura y el uso de un disolvente apolar. Estas son condiciones comúnmente empleadas con este propósito, ya que mediante ellas se puede reducir el efecto hidrofóbico e incrementar la energía cinética del sistema. La nueva disposición de péptidos con una estructura alterada, cambia de forma eficaz la distribución de energías asociadas con la selección de interacciones supramoleculares, con el disolvente y entre la proteína en si misma. Esto afecta a la estructura terciaria de la enzima. Para garantizar que toda la enzima se encuentra dentro del MOF, lavamos con detenimiento el sólido resultante del proceso, empleando buffer TRIS y midiendo en el UV-Vis hasta perderse la señal.

Para poder entender qué le sucede exactamente a la enzima durante este proceso, empleamos simulaciones con dinámica molecular. Se realizaron 1.0 μs de simulación donde se permitió a la enzima interactuar en los tres medios que tratamos: buffer TRIS, hexano-buffer, y el interior del MOF. Mientras pasa el tiempo, y empleando un valor estándar para el tamaño de la proteína como es la desviación media cuadrática (*root mean square deviation*) o RMSD, concluimos que efectivamente hay un despliegue parcial. El RMSD continúa incrementando con el tiempo hasta llegar a valores mayores en hexano que en el medio polar, tanto a 25°C como 60°C. Estos datos confirman que la enzima es únicamente capaz de ese cambio estructural mediante la combinación de ambos parámetros durante el proceso de inmovilización. En una comparación de esta estructura con la nativa, se ve claramente que la proteína sufre un despliegue en el disolvente apolar, implicando la apertura de una hendidura entre las dos subunidades enzimáticas. De hecho, estas pruebas mostraron una transformación progresiva entre hélice alfa y hojas beta hacia regiones no estructuradas con un aumento progresivo hacia regiones sin estructurar, consistiendo en aminoácidos que no forman parte de una estructura secundaria definida. Los resultados obtenidos en las simulaciones confirman que en estas condiciones somos capaces de provocar a la enzima un despliegue parcial para prepararla para esas condiciones de inmovilización.

Para apoyar estos cálculos, nos propusimos obtener resultados directos del estado de la enzima, empleando a tal efecto espectroscopía de fluorescencia. Esta técnica nos permite comparar los espectros de emisión de los tres estados: proteasa libre, proteasa en el medio de incubación y proteasa dentro del MOF. Esta proteína en particular consta de aminoácidos con fluorescencia como tirosina y triptófano, y por tanto podremos saber si ha habido algún cambio en su estructura siguiendo la señal que estos residuos proporcionan. Incubar la enzima en hexano provoca un desplazamiento de la señal hacia el rojo, que se asocia comúnmente a una desnaturalización proteica, correspondiente a un cambio en el entorno de los aminoácidos hacia lo apolar (siendo un cambio reversible). Por otro lado, cuando la proteína es introducida dentro del MOF hay un cambio diferente, llevando a un shift hacia el azul lo cual indicaría un cambio hacia la polaridad. Probablemente lo que ocurra es que al interaccionar con las cavidades del MOF, la enzima no esté verdaderamente plegada en su estructura nativa, sino en algo similar. Igualmente, la inmovilización de la enzima dio lugar a un incremento en su estabilidad, pudiéndose ver su inserción por TGA, Raman, Infrarrojo y experimentos de Adsorción. El MOF permaneció estable durante todo el proceso, sin variaciones notables en el tamaño de partícula.

La parte final del trabajo consistía en corroborar si ese estado intermedio en el que se encontraba la enzima era funcional, llevándose a cabo experimentos de catálisis. La reacción que se siguió consiste en la rotura del enlace peptídico de Gly-

Tyr, un sustrato que se puede medir en el UV-Vis con facilidad y puede entrar por las cavidades del MOF. Una primera tanda de medidas a condiciones óptimas para la enzima mostró que la enzima en disolución era más rápida que la que estaba dentro del MOF, explicándose ya que la velocidad de difusión del sustrato es mucho mayor estando fuera del composite. Sin embargo, cuando las condiciones fueron alejadas hacia extremos en pH y temperatura, la enzima inmovilizada mostró una notable estabilidad y eficiencia. En disolución, la enzima aguanta hasta los 55°C y pH 8 antes de perder toda actividad, mientras que la mezcla de MOF y enzima llega a 105°C y pH 12. Adicionalmente, se demostró dicho incremento en la actividad gracias a la unión, mediante el reciclaje y almacenaje a temperatura ambiente mostrando actividad tras 2 semanas y 5 ciclos de uso.